④

Applied Research Laboratory
The Pennsylvania State University

AD-A201 470
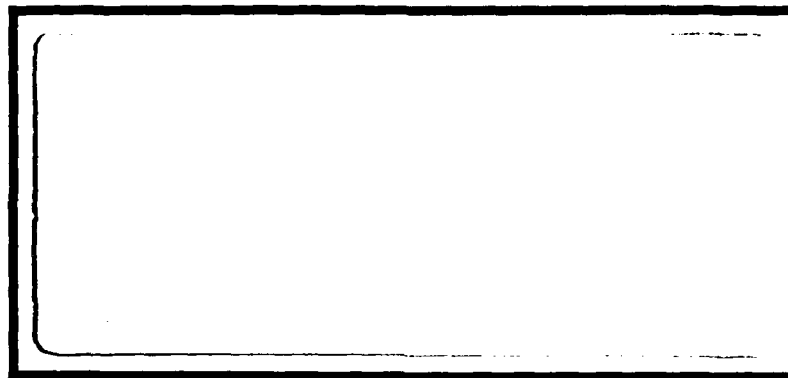
88 1026 038

(ARL/PSU) TECHNICAL REPORT

$N00024-85-C-6041$

The Pennsylvania State University
APPLIED RESEARCH LABORATORY
P. O. Box 30
State College, PA   16804

A COUPLED, PARABOLIC-MARCHING METHOD FOR THE
PREDICTION OF THREE-DIMENSIONAL VISCOUS
INCOMPRESSIBLE TURBOMACHINERY FLOWS

by

Kevin Richard Kirtley

DTIC
ELEC
OCT 2 7 1988
E

Technical Report No. TR 88-014

October 1988

SECURITY CLASSIFICATION OF THIS PAGE

REPORT DOCUMENTATION PAGE

1a. REPORT SECURITY CLASSIFICATION Unclassified		1b. RESTRICTIVE MARKINGS			
2a. SECURITY CLASSIFICATION AUTHORITY		3. DISTRIBUTION/AVAILABILITY OF REPORT Unlimited			
2b. DECLASSIFICATION/DOWNGRADING SCHEDULE					
4. PERFORMING ORGANIZATION REPORT NUMBER(S)		5. MONITORING ORGANIZATION REPORT NUMBER(S)			
6a. NAME OF PERFORMING ORGANIZATION Applied Research Laboratory The Pennsylvania State University	6b OFFICE SYMBOL (If applicable) ARL	7a. NAME OF MONITORING ORGANIZATION David Taylor Research Center Department of the Navy			
6c. ADDRESS (City, State, and ZIP Code) P. O. Box 30 State College, PA 16804		7b. ADDRESS (City, State, and ZIP Code) Bethesda, MD 20084			
8a. NAME OF FUNDING/SPONSORING ORGANIZATION Naval Sea Systems Command	8b. OFFICE SYMBOL (If applicable) NAVSEA	9. PROCUREMENT INSTRUMENT IDENTIFICATION NUMBER			
8c. ADDRESS (City, State, and ZIP Code) Department of the Navy Washington, DC 20362		10. SOURCE OF FUNDING NUMBERS			
		PROGRAM ELEMENT NO.	PROJECT NO.	TASK NO.	WORK UNIT ACCESSION NO.

11. TITLE (Include Security Classification)
A Coupled, Parabolic-Marching Method for the Prediction of Three-Dimensional
Viscous Incompressible Turbomachinery Flows (Unclassified)

12. PERSONAL AUTHOR(S)
Kevin Richard Kirtley

13a. TYPE OF REPORT Ph. D. Thesis	13b. TIME COVERED FROM _____ TO _____	14. DATE OF REPORT (Year, Month, Day) October 1988	15. PAGE COUNT 216

16. SUPPLEMENTARY NOTATION

17.	COSATI CODES		18. SUBJECT TERMS (Continue on reverse if necessary and identify by block number)
FIELD	GROUP	SUB-GROUP	laminar flow, three-dimensional fluid flow, turbomachinery
			two-phase fluid flow (J&S)

19. ABSTRACT (Continue on reverse if necessary and identify by block number)

A new coupled parabolic-marching method was developed to solve the

three-dimensional incompressible Navier-Stokes equation for turbulent

turbomachinery flows. Earlier space-marching methods were analyzed to

determine their global stability during multiple passes of the

computational domain. The methods were found to be unconditionally

unstable even when an extra equation for the pressure, namely the

Poisson equation for the pressure, was used between passes of the

20. DISTRIBUTION/AVAILABILITY OF ABSTRACT ☒ UNCLASSIFIED/UNLIMITED ☐ SAME AS RPT. ☐ DTIC USERS	21. ABSTRACT SECURITY CLASSIFICATION Unclassified		
22a. NAME OF RESPONSIBLE INDIVIDUAL	22b. TELEPHONE (Include Area Code)	22c. OFFICE SYMBOL	

D FORM 1473, 84 MAR	83 APR edition may be used until exhausted. All other editions are obsolete.	SECURITY CLASSIFICATION OF THIS PAGE Unclassified

domain. Relaxation of one constraint during the solution process was found to be necessary for the successful calculation of a complex flow. Thus, the method of pseudocompressibility was introduced into the partially parabolized Navier-Stokes equation to relax the mass flow constraint during the iterative process. This new method was found to be stable during a forward-marching integration as well as globally stable during successive passes of the domain. With consistent discretization, the new method was found to be convergent. *Keywords*

Also investigated was the splitting error which arises from the use of the LBI scheme in a three-dimensional parabolic-marching method. The splitting error was found to be extremely important for coarse grid computations and was analyzed and demonstrated for a strongly curved duct flow. A simple iterative solution method was developed which reduces the effect of the splitting error for three-dimensional computations.

Several turbulence models were introduced for the computation of turbulent flows. The three models used were the algebraic eddy viscosity model, the two equation $k-\epsilon$ model, and the algebraic Reynolds stress model (ARSM) which introduces the strong effect of rotation on the turbulence structure.

The new parabolic-marching method using the new solution method was used to compute several flows including the laminar and turbulent flow in an S-shaped duct and the turbulent flow in an end wall cascade and compressor rotor. For the laminar flow, the agreement with the analysis and the experimental data was excellent. For the turbulent flows, the pressure distributions were accurately predicted as were blade and end wall boundary layers and wakes. Prediction accuracy for the rotor flow was adequate with good resolution of the suction side boundary layers, secondary flow, and pressure losses at the rotor exit.

ABSTRACT

A new coupled parabolic-marching method was developed to solve the three-dimensional incompressible Navier-Stokes equation for turbulent turbomachinery flows. Earlier space-marching methods were analyzed to determine their global stability during multiple passes of the computational domain. The methods were found to be unconditionally unstable even when an extra equation for the pressure, namely the Poisson equation for the pressure, was used between passes of the domain. Relaxation of one constraint during the solution process was found to be necessary for the successful calculation of a complex flow. Thus, the method of pseudocompressibility was introduced into the partially parabolized Navier-Stokes equation to relax the mass flow constraint during the iterative process. This new method was found to be stable during a forward-marching integration as well as globally stable during successive passes of the domain. With consistent discretization, the new method was found to be convergent.

Also investigated was the splitting error which arises from the use of the LBI scheme in a three-dimensional parabolic-marching method. The splitting error was found to be extremely important for coarse grid computations and was analyzed and demonstrated for a strongly curved duct flow. A simple iterative solution method was developed which reduces the effect of the splitting error for three-dimensional computations.

Several turbulence models were introduced for the computation of turbulent flows. The three models used were the algebraic eddy viscosity model, the two equation k-ϵ model, and the algebraic Reynolds stress model (ARSM) which introduces the strong effect of rotation on

the turbulence structure.

The new parabolic-marching method using the new solution method was used to compute several flows including the laminar and turbulent flow in an S-shaped duct and the turbulent flow in an end wall cascade and compressor rotor. For the laminar flow, the agreement with the analysis and the experimental data was excellent. For the turbulent flows, the pressure distributions were accurately predicted as were blade and end wall boundary layers and wakes. Prediction accuracy for the rotor flow was adequate with good resolution of the suction side boundary layers, secondary flow, and pressure losses at the rotor exit.

Accession For	
NTIS GRA&I	☒
DTIC TAB	☐
Unannounced	☐
Justification	
By	
Distribution/	
Availability Codes	
Dist	Avail and/or Special
A-1	

TABLE OF CONTENTS

LIST OF FIGURES

LIST OF SYMBOLS

A,B,C

D,S   vectors in the governing equations

A^n Fourier coefficient matrix

a   pressure relaxation coefficient

c   chord length

C_p coefficient of pressure $2(p-p_I)/\rho Q_I^2$

I   imaginary unit $=\sqrt{-1}$

J   Jacobian of the grid transformation

k   turbulence kinetic energy

k_{sec} mass averaged secondary flow kinetic energy

n   normal direction

p   static pressure

p_o stagnation pressure $p + 1/2\rho Q^2$

P_k production of turbulence energy

Q   total velocity vector

q   dependent vector $(p,u,v,w)^T$

R   hub to tip ratio

Re   Reynolds number

S   streamwise distance non-dimensionalized by c

s   cascade blade spacing

Ti   turbulence intensity $\sqrt{k}/1.5$

u,v,w   non-dimensional velocity components

$\overline{u'},\overline{v'},\overline{w'}$ time-averaged turbulence velocity fluctuations

u*   friction velocity

U_s streamwise velocity component

U_n transverse velocity component

W_r radial velocity component

x-y-z   Cartesian coordinates

∂ partial derivative w-r-t subscript

ε turbulence dissipation

κ von Karman constant (=.41)

λ stagger angle, eigenvalue

λ^* complex conjugate of λ

μ,ν molecular, kinematic viscosity

ν_t non-dimensional eddy viscosity

Ω non-dimensional rotation rate

ϕ flow coefficient Q_m/Q_t

ξ-η-ζ body fitted coordinates

ρ density

γ space to chord ratio s/c

δ boundary layer thickness

θ harmonic frequency

θ_{11} streamwise momentum thickness

ψ_{loss} pressure-loss coefficient $2(p_{oI}-p_o)/(\rho\, Q_t^2)$

subscripts

B   bulk

$\mathcal{C}$ centerline

e   edge of shear layer

I   inlet

J   Jacobian

i,j,k   indices in ξ,η,ζ directions, respectively

m   mean

n   normal

p   first point from boundary

ps   pressure side

ss   suction side

s   streamwise

t   tip

superscripts

as   assumed

c   computed

m   iteration index at station i

n   global iteration level

ACKNOWLEDGMENTS

CHAPTER 1

INTRODUCTION

1.1 The Problem

The flow in turbomachinery is very complex. The description of the inviscid flow is generally all that is required to determine the gross properties of the geometry, such as blade loading. Some important features of the flow, however, are due to the viscous nature of the actual fluid flow, e.g., pressure losses and inefficiencies. Some of the viscous flow phenomena found in a typical axial flow turbomachine can be seen in Figure 1.1. These include the three-dimensional blade boundary layer, the three-dimensional wake, and overturning of the flow in the end-wall region. If the geometry in question is a rotor, the flow is further complicated by the tip leakage flow and the interaction of the leakage jet and the main flow.

For three-dimensional incompressible flow, three momentum transport equations and one mass conservation equation, collectively known as the Navier-Stokes equation, govern a continuous flow. The Navier-Stokes equation can be simplified to give algebraic relations for the dependent variables of static pressure and flow velocity or can be written as a single scalar Poisson equation for a potential function. Such forms cannot capture the above mentioned viscous flow phenomena. The full Navier-Stokes equation is a second order, non-linear partial differential equation that cannot be solved exactly. Thus, researchers have long used numerical methods to solve the equation on discrete

Figure 1.1 Nature of the Flow in a Turbomachine

points in the domain under consideration.

There are several methods for solving numerically the Navier-Stokes equation in full or simplified form. All have their advantages; some are economical yet less accurate while others are very accurate but require large amounts of computer time. A description of some of the more prominent methods for solving the three-dimensional Navier-Stokes equation follows.

1.2 Review of Related Studies

The number of different algorithms designed to predict viscous flows is vast. However, only methods developed to solve the three-dimensional Navier-Stokes equation are of interest here. The types of methods can be catagorized as time-marching methods, space-marching methods, parabolic-marching methods and fully elliptic methods. Time-marching methods are so called because the governing equations are integrated in the time coordinate. Likewise, space-marching methods use a streamwise integration procedure. Parabolic-marching methods are essentially multiple pass versions of space-marching methods whereby the domain is computed several times to relax residual errors. Finally, elliptic methods are relaxation techniques or inversion techniques which solve the entire matrix generated by the discretized equations.

1.2.1 Time-Marching Methods

The unsteady form of the incompressible Navier-Stokes equation seems well suited to a time integration procedure except that there is no time dependent term in the continuity equation. If the compressible form is used, the time-integration can proceed. Pulliam and Steger (1980) used

the implicit approximate factorization scheme of Beam and Warming (1978) to solve the compressible equation in three dimensions. Even though the important viscous terms were retained, the method required fourth order implicit and explicit artificial dissipation for convergence to be achieved. The method was used to compute various high Reynolds number supersonic and transonic flows. Computed pressure distributions compared favorably with the experimental data. If one were to use the above method to solve very low Mach number flows, difficulties would be encountered. At Mach numbers below 0.3 the energy equation tends to become weakly coupled to the momentum equations. This introduces large numerical errors and convergence of the system is not ensured. Briley, Buggeln, and McDonald (1985) replaced the energy equation with a constant enthalpy equation. An adiabatic equation of state was used to eliminate the pressure as a dependent variable. The resulting system is suitable for solving low Mach number flows. The Beam and Warming (1978) algorithm was used to solve the coupled system for a laminar horseshoe vortex generated by a wing-body juction. The inlet flow Mach number was 0.1. Only small amounts of artificial dissipation were required to achieve convergence. Also used to predict three-dimensional compressible flows is the MacCormick implicit method (1982) which is based on the author's explicit predictor-corrector method. It only requires the solution of bidiagonal matrices and so is very efficient. Recently, Dawes (1986) used a time-marching method to solve the flow in a compressor rotor. A finite volume formulation was used to discretize the governing equations. Computed Mach number contours compared well with the available experimental data.

The above methods use the compressible formulation which assumes a

perfect gas is being considered. If the fluid is water, a truly incompressible form of the equations must be used. Since no pressure term is present in the continuity equation, solution of the incompressible formulation is very difficult and the governing equations must be manipulated to yield a more tractible form. Following the ideas of Chorin (1967), Kwak et al. (1984) introduced a time derivative of the pressure into the continuity equation. For a steady flow, a time integration of the system yields a divergence free velocity field. The coupled system was solved using the Beam and Warming algorithm for several three-dimensional viscous flow problems including the flow in the space shuttle main engine power head. Both implicit and explicit fourth order artificial dissipation were necessary to achieve convergence which was seldom greater than two orders of magnitude.

In addition to the above implicit methods, explicit methods have been used to compute the three-dimensional viscous flow. Explicit schemes are generally limited to very small time steps due to the CFL condition and with this comes large computation times. However, with the advent of supercomputers, explicit methods are again finding favor among researchers. Shang et al. (1980) used MacCormack's explicit predictor-corrector scheme to study the shock/boundary layer interaction in a wind tunnel diffuser. The explicit scheme allowed for a high degree of vectorization and extremely fast computation times were reported. Results compared reasonably well with the experimental data. Chima (1986) used a vectorized two-step Runge-Kutta scheme to solve quasi-three-dimensional flows. A multigrid algorithm was used to efficiently compute the flow in a centrifugal impeller. Computed pressure distributions compared well with the experimental data.

Artificial dissipation was required to ensure convergence. Convergence to five orders of magnitude was enhanced by a factor of three when using the multigrid scheme over a single grid.

1.2.2 Space-Marching Methods

For some flows, solving the full elliptic form of the Navier-Stokes equation is not necessary. If a main flow direction can be identified, the governing equation can be "parabolized" and integrated in the time-like streamwise direction. The Navier-Stokes equation is parabolized by neglecting the streamwise diffusion of momentum and manipulating the streamwise flux vector such that the product of the inverse of its Jacobian and the Jacobian of the transverse flux vector has real eigenvalues. In supersonic flow, the eigenvalues are all real and positive if the streamwise velocity is non-negative. In the boundary layer, one eigenvalue becomes imaginary and the system becomes unstable for space-marching. In the boundary layer, retaining the streamwise pressure gradient in the implicit part of the streamwise flux vector yields an unstable system as the grid system is refined. Such departure solutions are well documented. Keeping the streamwise pressure gradient term explicit removes this instability but cannot account for any global interaction between the viscous and inviscid flows. Shiff and Steger (1979), following boundary layer theory, replaced the pressure in the viscous layer with the pressure in the outer supersonic flow. Vigneron, Rakich and Tannehill (1978) used a similar marching procedure, namely Beam and Warming (1978) scheme, yet split the streamwise pressure gradient into implicit and explicit parts. A weighted average was used based on the flow Mach number. Such a formulation can capture mild

pressure interaction between the inner and outer layers.

Govindan and Lakshminarayana (1987) later modified Shiff and Steger's (1979) method for internal subsonic flows. A special bulk pressure correction was required to conserve global mass flow. The method proved to be very sensitive to the value of the explicit assumed pressure gradient and had difficulty in low Mach number flows.

Along very different lines, Briley and McDonald (1979) based a new space-marching method on secondary flow theory. They split the velocity into four distinct parts namely, a known potential velocity, a potential secondary velocity, a solenoidal secondary velocity, and a viscous streamwise velocity correction. The governing equations were recast to give equations for each new component of the velocity. Elliptic effects were transmitted through the potential flow which was required a priori. The need for the potential flow a priori is a major drawback for the method although it has been used with good success on various curved duct geometries. Along similar lines, Dodge (1976) split the velocity into potential and rotational parts. The potential component was used to correct the pressure so that continuity was satisfied.

Patankar and Spalding (1972) developed the precusor to contemporary parabolic-marching methods. Their space-marching method for internal flows could solve with equal success the compressible or incompressible Navier-Stokes equation. The method used in the cross-plane was essentially the SIMPLE procedure which consisted of decoupling the continuity and momentum equations and solving for the velocity components on a staggered grid in the cross-plane. The streamwise momentum equation was solved for the streamwise velocity using an assumed streamwise pressure gradient. The transverse momentum equations

were solved in turn. A bulk passage averaged pressure correction was also included so that the global mass flow constraint was satisfied. A two-dimensional pressure correction was also included in order to correct the velocities to satisfy the continuity equation. This was accomplished by relating the gradients of the pressure correction to the velocity corrections. In this way, a two-dimensional Poisson equation for the pressure correction could be written in place of the continuity equation. Once converged at a particular streamwise station, the pressure correction tended to zero and thus the velocity corrections tended to zero giving a divergence free velocity field. The process was iterated to convergence at each streamwise station before the procedure was advanced to the next station. The marching scheme could be used only for parabolic flows yet was a major breakthrough.

Briley (1974) and later Ghia and Sokhey (1977) used the same pressure split scheme and similar approaches to solve the incompressible equations on a regular grid. Ghia and Sokhey (1977) introduced an extra inviscid mean pressure which was a function of the streamwise direction only. The inviscid mean pressure was assumed known and its presence allowed for the computation of mildly elliptic flows. Conservation of global mass flow was used to determine the viscous mean pressure and the cross-plane pressure was computed from a Poisson equation which was generated by taking the divergence of the transverse momentum equations. Most importantly, the system did not in general satisfy continuity. Thus, irrotational velocity corrections were introduced to satisfy continuity. Being irrotational, a potential function could be written for the velocity corrections and when substituted into the continuity equation, yielded a second Poisson equation to be solved in the cross-

plane. Thus, at a particular streamwise station, the streamwise momentum equations were solved for their respective velocities and the pressure was corrected to satisfy global mass flow through iterations. The cross-plane pressure was computed from the Poisson equation and the velocities were corrected to satisfy continuity by solving the second Poisson equation. The process was repeated until convergence was achieved and the procedure was advanced to the next streamwise station. With so many Poisson equations, the method proved to be cumbersome and thus not widely used.

To remove the need for Poisson equations, Pouagare and Lakshminarayana (1986) kept the pressure gradients implicit and solved the entire incompressible formulation in a coupled fashion using the LBI scheme of Briley and McDonald (1980). Thus, local continuity and the global mass flow constraint were satisfied without the need for solving extra equations. An eigenvalue analysis showed that the system could be space-marched if the coefficient of the streamwise pressure gradient was less than zero. This result could be inferred from the work of Vigneron, Rakich and Tannehill (1978) for a Mach number of zero. Thus, the streamwise pressure gradient was split into implicit and explicit parts with the implicit part multiplied by a small negative coefficient. For small values of the coefficient, the method was relatively insensitive to the explicit assumed pressure gradient when applied to parabolic flows. This is not suprising since the streamwise pressure gradient is closely tied to the conservation of global mass flow. The implicit pressure gradient corrected the explicit part in order to conserve global mass. The method was very fast and extremely accurate for straight and curved ducts; however, several problems were

encountered when the method was used in a multi-pass mode. These problems will be discused extensively in Chapter II.

Recently, due to the speed of supercomputers, explicit methods have been used to solve the parabolized Navier-Stokes equation. Spradley and Stalnaker (1981) developed an interesting procedure which used the time-dependent, parabolized Navier-Stokes equation. The authors termed this a Quasi-Parabolic system and used their General Interpolants Method (GIM) to discretize the equation. At a particular streamwise station, using the solution at the previous station as initial conditions, the equation was iterated to convergence using MacCormack's predictor-corrector scheme in the cross-plane. At convergence, the solution procedure was advanced to the next streamwise station until the entire domain was computed. Gielda and McRae (1986) solved the steady, parabolized Navier-Stokes equation using MacCormack's two step predictor-corrector scheme, marching in the streamwise direction. Small marching steps were required due to CFL conditions yet no minimum step size requirement, common to implicit schemes, had been encountered. Due to its high degree of vectorization, the method proved to be computationally efficient even with the fine mesh used. It should be noted that the fine grid resulted in increased accuarcy for hypersonic flow over ogive cylinders at an angle of attack. Also, less numerical damping was required compared to implicit methods.

1.2.3 Parabolic-Marching Methods

Pratap and Spalding (1976) extended Patankar and Spalding's (1972) scheme to allow for a multi-pass solution procedure. The domain was computed several times using the previously computed pressure field as a

new assumed pressure. The procedure was repeated until the pressure corrections dropped to zero. In this way, more strongly elliptic flows could be computed since downstream pressure effects could be transmitted upstream.

Moore and Moore (1979) used a very similar procedure to compute the viscous compressible flow in ducts. A finite volume method was used with the pressure corrections located at the center of the control volumes. The equations were integrated in the streamwise direction and a one-dimensional pressure correction was used to conserve global mass flow. A three-dimensional pressure correction equation was written based on force residuals found in the momentum equations. This pressure correction equation was solved after each integration of the momentum equations until the force residuals dropped to zero. Moore and Moore (1981) later improved the method by using only one three-dimensional pressure correction. The gradients of these corrections were manipulated in such a way that large changes in the transverse gradients did not yield large changes in the streamwise gradient. This method could be used on non-orthogonal grids whereas the earlier method had great difficulty with such grids. The three-dimensional pressure correction equation based on force residuals was retained and the method was used to compute the flow in a ghost impeller. The computed static pressure compared well with the experimental data, however, the computed velocity field did not compare well.

Rhie (1983) extended Pratap and Spalding's (1976) multiple pass marching scheme to generalized coordinates. The method employed a finite volume integration and pressure corrections to conserve local and global mass. Averaging was used on control volume boundaries to give a

finite difference expression much like the SIMPLE scheme. Numerical diffusion was introduced to avoid instabilities associated with central differencing of the convective terms. The computational procedure is very similar to Pratap and Spalding's procedure except that once a forward-marching pass was completed, a three-dimensional elliptic pressure correction equation was solved to accelerate the propagation of downstream pressure corrections upstream. The method was used to compute the viscous flow in curved ducts and diffusers and in impellers by Rhie, Delaney, and McKain (1984). In all cases, the results compared favorably with the experimental data. Khalil and Weber (1984) used a procedure very similar to Rhie's accept that special attention was paid to the satisfaction of a compatibility relation when solving the pressure correction equation. The compatibility relation is based on Green's divergence theorem and must be satisfied exactly if a converged solution is to be obtained for any Poisson equation. The method was used on various curved duct flows with very good results.

1.2.4 Elliptic Methods

Elliptic methods solve the Navier-Stokes equations with no parabolizing assumptions made. Usually, a finite volume form of the uncoupled equations is employed which is relaxed until the residuals drop to some small level. Hah (1984) solved the uncoupled equations on a staggered grid. The staggered grid is generally difficult to use on a curvilinear coordinate system, however, Hah overcomes these dificulties by using a quadratic upstream interpolation scheme and a skew upwinding scheme. A complex algebraic Reynolds stress model was used to model the effects of the turbulence. This method was used to compute the viscous

flow in a turbine end-wall cascade and recently in a compressor rotor with tip clearance (Hah (1986)). Results compared extremely well to the experimental data for all test cases. Velocity profiles and flow angles compared almost exactly to the experimental data in the tip clearance region even with as few as five grid points in the clearance region. Moore and Moore (1985) used nearly the same procedure as Hah but incorporated an algebraic eddy viscosity model for the turbulence. The predicted pressure losses were in better agreement with the experimental data than Hah's prediction for a turbine end-wall cascade.

Vanka (1985) solved the governing equations in a coupled fashion using a direct solver. Such a solver requires large amounts of computer storage but can be very efficient. The method was used on a strongly curved duct with very good results.

Recently, Rhie (1986) developed a full elliptic solver which employs the Pressure Implicit Split Operator (PISO) concept. Several levels of pressure corrections are used to correct for mass flow imbalances and the method can be used for all Mach numbers were the flow remains a continuum. The density is treated implicitly in the pressure correction procedure. A predictor-corrector type algorithm was employed and a multigrid procedure was included to enhance convergence. The method was tested on a wide range of flows including a three-dimensional driven cavity and a turbine end-wall cascade. Results agree very well with the experimental data.

1.3 Objectives and Method of Approach

The major objective of this work is to develop a new parabolic-marching method to solve the three-dimensional incompressible Navier-

Stokes equation. The method must be stable, convergent, and accurate for the computation of a wide range of turbomachinery flows. The new method will be used to compute blade and end wall boundary layers and three-dimensional wakes in rotating and stationary blade rows. A secondary objective is to discuss drawbacks of a few earlier methods and to include high order turbulence models. Also, some of the idiosyncracies of forward-marching the Navier-Stokes equation will be discussed.

In order to develop a new method, the difficulties associated with existing techniques must be discussed. A technique recently developed to overcome these difficulties will be analyzed using Fourier stability theory to determine its global stability characteristics as a multiple pass method. Next a simple modification to the technique will be analyzed to see if convergence can be ensured with a multiple pass scheme. Also, an eigenvalue analysis will be performed to determine if the modified method is stable during the forward-marching integration process. Finally a new parabolic-marching method will be developed which is convergent when multiple passes are made and which overcomes some of the difficulties with the afore mentioned methods. An eigenvalue analysis will be performed to ensure stability during the forward-marching process and a Fourier analysis will be performed to ensure global stability during the iteration process for a wide range of flow conditions. A new solution procedure will also be explored which improves predictions for coarse grids. The new method employing the new solution procedure will be calibrated by computing the developing flow in a straight duct with square cross-section. Proper transmission of pressure ellipticity will be tested by computing the laminar flow in an

S-shaped duct. Finally, to complete the validation, various turbulent turbomachinery flows will be computed and the results compared to the available experimental data.

CHAPTER 2

ANALYSIS AND MODIFICATION OF EXISTING TECHNIQUES

2.1 Introduction

The equation which governs fluid flow is the Navier-Stokes equation. The components of this vector equation are the continuity equation and the three momentum equations. If the flow is compressible, an energy equation is added to the set. Only incompressible internal flow is considered here. Thus, the Navier-Stokes equation is written in non-dimensional form as:

$$\partial_x A + \partial_y B + \partial_z C - 1/Re \; (\partial_{xx} D + \partial_{yy} D + \partial_{zz} D) = S$$

$$(2.1)$$

$$A = \begin{bmatrix} u \\ u^2+p \\ uv \\ uw \end{bmatrix} \qquad B = \begin{bmatrix} v \\ vu \\ v^2+p \\ vw \end{bmatrix} \qquad C = \begin{bmatrix} w \\ wu \\ wv \\ w^2+p \end{bmatrix}$$

$$D = \begin{bmatrix} 0 \\ u \\ v \\ w \end{bmatrix} \qquad S = \begin{bmatrix} 0 \\ 0 \\ \Omega^2 y + 2\Omega w \\ \Omega^2 z - 2\Omega v \end{bmatrix}$$

where Re is the Reynolds number and all velocities are normalized by some bulk inlet velocity and the pressure by the dynamic head.

Equation 2.1 is written for geometries which rotate about the x axis with non-dimensional rotation Ω. The equation is second order elliptic

due to the diffusion terms. If a main flow direction can be identified, as with most turbomachinery flows, the streamwise diffusion of momentum can be neglected. For the sake of example, x is assumed to be the streamwise direction and so neglect the diffusion in x which gives equation 2.2.

$$\partial_x A + \partial_y B + \partial_z C - 1/Re \, (\partial_{yy} D + \partial_{zz} D) = S$$

(2.2)

This reduces the order of ellipticity and the resulting system is termed 'partially parabolic'. With such a system, efficient spacially marching solution procedures may be used. However, the streamwise pressure gradient term introduces first order ellipticity and thus requires special treatment.

2.2 Difficulties With Existing Techniques

The forward-marching procedures available, whether single pass space-marching or multiple pass parabolic-marching methods, have various drawbacks associated with them. The following methods either remove the pressure completely from the formulation or split the pressure into a two-dimensional transverse pressure and a one-dimensional bulk streamwise pressure. These modifications are useful in overcoming the traditional difficulties associated with unmodified pressure terms. Briley and McDonald's (1979) method removes the pressure from the formulation and requires the specification of the potential flow for the geometry and flow conditions under consideration. For simple straight and constant curvature ducts, the potential flow is almost trivial. However, for complex flows, a full potential solver must be used

initially to establish the potential field. This may require a large expenditure of computation time in addition to the viscous flow solver. Also, the viscous pressure field is not a computed quantity and so viscous pressure losses cannot be computed. Patankar and Spalding's (1972) method solves the parabolized Navier-Stokes equation on a staggared grid in an uncoupled fashion using a pressure split scheme. The staggared grid is difficult to implement in complex geometries using generalized coordinates. Rhie (1983) later recast the equations for a non-staggared grid but like Patankar and Spalding, must solve a Poisson equation in the transverse plane for the pressure corrections in order to indirectly satisfy continuity. Due to the large amount of computer time required to reach a converged solution, a Poisson equation should be avoided in the formulation. For this reason, Briley's (1974) and Ghia and Sokhey's (1977) methods are not recommended, in fact both methods use two Poisson equations in the cross plane, one for the pressure and another for irrotational velocity corrections which indirectly satisfy the continuity equation. That is, the continuity equation in the above methods is satisfied only through an iterative process and not satisfied directly. Pouagare and Lakshminarayana (1986) sought to remove these Poisson equations from the formulation. To do so, the flux vectors in the governing equation must be manipulated to achieve a stable forward-marching procedure.

In the following, several modifications to equation 2.2 are described which manipulate the pressure terms to allow for stable forward-marching. The global stability of multiple passes of the flow field using these modifications is investigated and drawbacks are described. For the sake of example, the two-dimensional form of

equation 2.2 is used to simplify the analysis, however, the extension to three dimensions is straightforward albeit laborious.

2.3 Method of Pouagare and Lakshminarayana (PL)

In an attempt to develop an efficient single pass space-marching method to solve the partially parabolized Navier-Stokes equation, Pouagare and Lakshminarayana (1986) modified the streamwise pressure gradient term. The modification was motivated by the following eigenvalue analysis performed by them. It is the intent of this author to show, through a Fourier stability analysis in section 2.3.2, that this method is globally unstable when multiple passes of the flow field are made.

2.3.1 Eigenvalue Analysis

For simplicity, the following analysis is performed for a two-dimensional system. The results are applicable to three dimensions as well. First, the streamwise pressure gradient in the flux vector A is tagged with the coefficient σ giving:

$$A = \begin{bmatrix} u \\ u^2 + \sigma p \\ uv \end{bmatrix} \tag{2.3}$$

The two-dimensional form of equation 2.2 is then linearized and written in frozen coefficient form as:

$$A_J \, \partial_x q + B_J \, \partial_y q - D_J \, \partial_{yy} q = S \tag{2.4}$$

where A_J, B_J, and D_J are the Jacobians of the vectors A, B, and D, respectively and q is the dependent vector $(p, u, v, w)^T$.

$$A_J = \begin{bmatrix} 0 & 1 & 0 \\ \sigma & 2u & 0 \\ 0 & v & u \end{bmatrix} \qquad B_J = \begin{bmatrix} 0 & 0 & 1 \\ 0 & v & u \\ 1 & 0 & 2v \end{bmatrix}$$

$$D_J = \begin{bmatrix} 0 & 0 & 0 \\ 0 & 1/Re & 0 \\ 0 & 0 & 1/Re \end{bmatrix} \tag{2.4a}$$

The terms on the left-hand side of equation 2.4 and all other equations are treated implicitly in the computation while terms on the right are treated explicitly. For stable forward-marching, the eigenvalues of the matrix $A_J^{-1}D_J$ must be real and non-negative for proper damping. Also, the eigenvalues of the matrix $A_J^{-1}B_J$ must be real. For the modified flux vector A in equation 2.3, the characteristic equation of $A_J^{-1}D_J$ is:

$$\lambda^2(\lambda - 1/u) = 0 \tag{2.5}$$

The solution of equation 2.5 gives the following eigenvalues:

$$\lambda_{1,2} = 0 \quad , \quad \lambda_3 = 1/u \tag{2.6}$$

Therefore, if the streamwise velocity is positive, the scheme is naturally dissipative and the first condition for stable forward-marching is satisfied. For $A_J^{-1}B_J$, the characteristic equation is:

$$\lambda^3 - (v/u)\lambda^2 + (1/\sigma)\lambda - v/(\sigma u) = 0$$

(2.7)

thus, the eigenvalues are:

$$\lambda_1 = v/u \ , \ \lambda_{2,3} = \pm I/\sqrt{\sigma}$$

(2.8)

where $I = \sqrt{-1}$. Therefore, if σ is less than zero, the eigenvalues are all real. In such a case, forward-marching is stable.

Pouagare and Lakshminarayana set σ to some small negative value (-0.01). With this, the authors modified the source vector S for consistency in the following manner (with no rotation):

$$S = \begin{bmatrix} 0 \\ -\partial_x p^{as} + \sigma \partial_x p \\ 0 \end{bmatrix}$$

(2.9)

where $\partial_x p^{as}$ is an assumed pressure gradient and is forward differenced for proper transmission of elliptic effects and $\sigma \partial_x p$ is differenced in the same manner as the implicit part namely:

$$\sigma \partial_x p = \sigma(p_i - p_{i-1})/\Delta x$$

(2.10)

where i is the streamwise index at which the solution is desired. Since S is a source term, p_i is not yet known and so must be replaced by p^{as}_i. Thus, equation 2.10 becomes:

$$\sigma \partial_x p = \sigma(p^{as}_i - p_{i-1})/\Delta x$$

(2.11)

The final system is inconsistent unless $p^{as} = p$. The equation was discretized and solved using the LBI scheme of Briley and McDonald (1980). Pouagare and Lakshminarayana used a very small σ, i.e., -0.01. This relaxes the streamwise pressure gradient condition so that the global mass flow constraint, through the satisfaction of the continuity equation coupled to the momentum equations, can be satisfied directly.

2.3.2 Global Stability Analysis

With the modifications described in section 2.3.1, the system of equations can be space-marched. It is apparent that if the assumed pressure field is not correct, the computed pressure field will adjust so that the governing equations will be satisfied. One must now ask whether multiple passes of the domain will relax the residual errors due to an incorrect assumed pressure such that $p \rightarrow p^{as}$. The following global stability analysis will answer this question.

To perform the analysis, equation 2.2 must be discretized in the way in which it is to be solved. Two point backward differences are used for streamwise derivatives while three point central differences are used for transverse derivatives giving:

$$A_J (q_{i,j}-q_{i-1,j})^n/\Delta x + B_J (q_{i,j+1}- q_{i,j-1})^n/2\Delta y$$
$$- D_J (q_{i,j+1}-2q_{i,j}+q_{i,j-1})^n/(\Delta y)^2 = S_J q^{n-1}_{i,j}$$

(2.12)

where n is the global iteration index (pass number) and j is the transverse index.

The multiple pass stability or global stability of the method can be checked using a von Neumann stability analysis. The underlying premise of this analysis according to Smith (1978) is that the error function at any point in the domain satisfies the partial differential equation under consideration. Thus, it is assumed that any error $e^n_{i,j}$ satisfies equation 2.12. The error is also separable into a function of space and a function of iteration level. With this, the error can be decomposed in a Fourier series. The necessary and sufficient condition for the global stability of a two level system is that the error due to the iteration level must not increase with increasing iterations. Therefore, the following relation is introduced substituting the error function for the dependent vector q in equation 2.12.

$$q^n_{i,j} \rightarrow e^n_{i,j} = A^n \exp I(i\theta_x + j\theta_y)$$

$$(2.13)$$

where A^n is a Fourier coefficient and I is the imaginary unit. Then, equation 2.12 becomes:

$$P_J \, A^n = H_J \, A^{n-1}$$

$$(2.14)$$

where

$$P_J = \begin{bmatrix} 0 & \ell_1 & \ell_2 \\ \sigma(\ell_1+\ell_4) & 2u\ell_1+v\ell_2-\ell_3 & u\ell_2 \\ \ell_2 & v\ell_1 & u\ell_1+2v\ell_2-\ell_3 \end{bmatrix}$$

and

$$H_J = \begin{bmatrix} 0 & 0 & 0 \\ \sigma+1-\ell_5 & 0 & 0 \\ 0 & 0 & 0 \end{bmatrix}$$

with

$$\ell_1 = 1 - \cos\theta_x + I\sin\theta_x$$

$$\ell_2 = (\Delta x/\Delta y)\, I\sin\theta_y$$

$$\ell_3 = 2\Delta x\,(\cos\theta_y - 1)/\{Re\,(\Delta y)^2\}$$

$$\ell_4 = \cos\theta_x - I\sin\theta_x$$

$$\ell_5 = \cos\theta_x + I\sin\theta_x$$

(2.15)

The amplification matrix G is now defined as:

$$G = P_J^{-1}\, H_J = \begin{bmatrix} M_1 & 0 & 0 \\ M_2 & 0 & 0 \\ M_3 & 0 & 0 \end{bmatrix}$$

(2.16)

where

$$M_1 = (\sigma+1-\ell_5)(v\ell_1\ell_2 - \ell_1(u\ell_1+2v\ell_2-\ell_3))/|P_J|$$

$$M_2 = (\sigma+1-\ell_5)(-\ell_2^2)/|P_J|$$

$$M_3 = (\sigma+1-\ell_5)\ell_1\ell_2/|P_J|$$

$$|P_J| = -\ell_1(\sigma(\ell_1+\ell_4)(u\ell_1+2v\ell_2-\ell_3)-u\ell_2^2))$$

$$+\ell_2(\sigma(\ell_1+\ell_4)v\ell_1-\ell_2(2u\ell_1+v\ell_2-\ell_3))$$

such that

$$A^n = G A^{n-1}$$

$$(2.17)$$

In order to achieve a convergent system, the absolute value of the eigenvalues of G must be less than or equal to unity. The eigenvalues of G were found to be:

$$\lambda_1 = (\sigma+1-\ell_5)\{v\ell_1\ell_2-\ell_1(u\ell_1+2v\ell_2-\ell_3)\}/|P_J|$$

$$(2.18)$$

$$\lambda_{2,3} = 0$$

$$(2.19)$$

One can check the maximum value of the eigenvalues by setting $\theta_x=\theta_y=\pi$. This gives:

$$|\lambda_{1max}| = |1 + 2/\sigma|$$

$$(2.20)$$

which for $\sigma=-0.01$ (as used by Pouagare and Lakshminarayana (1986)) is 199. Note that equation 2.20 is not a function of the velocity ratio nor the grid aspect ratio; thus, the PL method is unconditionally unstable when used in a global marching procedure. However, it is apparent that the scheme is globally stable when σ is set to -1. A close inspection of the PL equations reveals that this gives a simple forward difference for the streamwise pressure gradient which is essentially the same as the Rubin and Reddy (1983) scheme on a regular grid.

For completeness, the global stability for all wave numbers must be investigated. Recall that if the absolute value of λ must be less than

or equal to unity for global stability, then the absolute value of $\lambda^*\lambda$ must also be less than or equal to unity where λ^* denotes the complex conjugate of λ. With u and v set to one, $\Delta x = \Delta y$ and Re arbitrarily set to 1000, the global stability for all wave numbers for $\sigma=-0.01$ and -1.0 can be reviewed in Figures 2.1 and 2.2, respectively. The hatched area indicates the region where the scheme is unstable. One can see that for high wave numbers, the original PL method with $\sigma=-0.01$ is unstable but with $\sigma=-1.0$, the scheme is stable everywhere. When the velocity ratio is changed, there is no change in the stability characteristics. There is, however, a large change when the grid aspect ratio is changed. The effect of the ratio of $\Delta x/\Delta y$ on the stability can be seen in Figures 2.3 and 2.4 for $\sigma=-0.01$. When the aspect ration of the grid is changed to $\Delta x/\Delta y=0.01$ from unity, the system of equations becomes ustable for a wider range of wave numbers but the level of the eigenvalues remains essentially unchanged. The stable region is confined to wave numbers of $\theta_y/\pi < 0.04$. This is consistent with the well known stability limitation on a minimum Δx when solving incompressible flow with a space-marching method. As Δx is decreased, the instability becomes greater. Likewise, when Δx is increased, stability is enhanced since the zone of ellipticity is overstepped. This can be seen for $\Delta x/\Delta y=100$. For this aspect ratio, there appears to be a wider range of wave numbers where the global iteration procedure is stable. The region of stability is confined to values of θ_x/π between 0.1 and 0.9. At $\theta_x=\theta_y=\pi$, the eigenvalue still reaches its maximum of 199. If the absolute value of the eigenvalue is greater than unity for any wave number then stability cannot be assured. Variation of the Reynolds number from 10 to 10^6 produces no change in the global
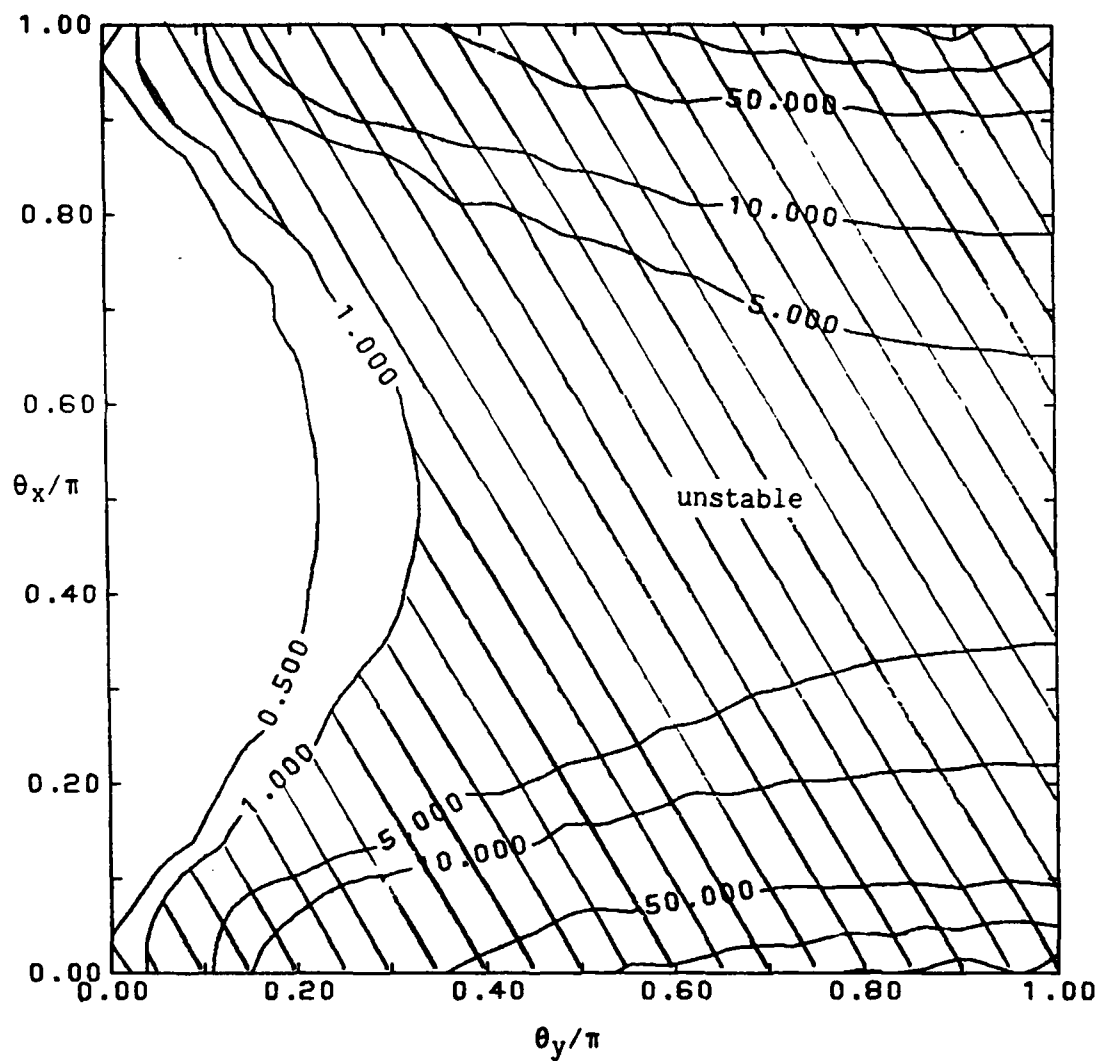
Figure 2.1   Real Part of $\lambda^*\lambda$, $\sigma=-0.01$ for All Wave
Numbers for the PL method ($u=v=1, \Delta x=\Delta y=1, Re=1000$)
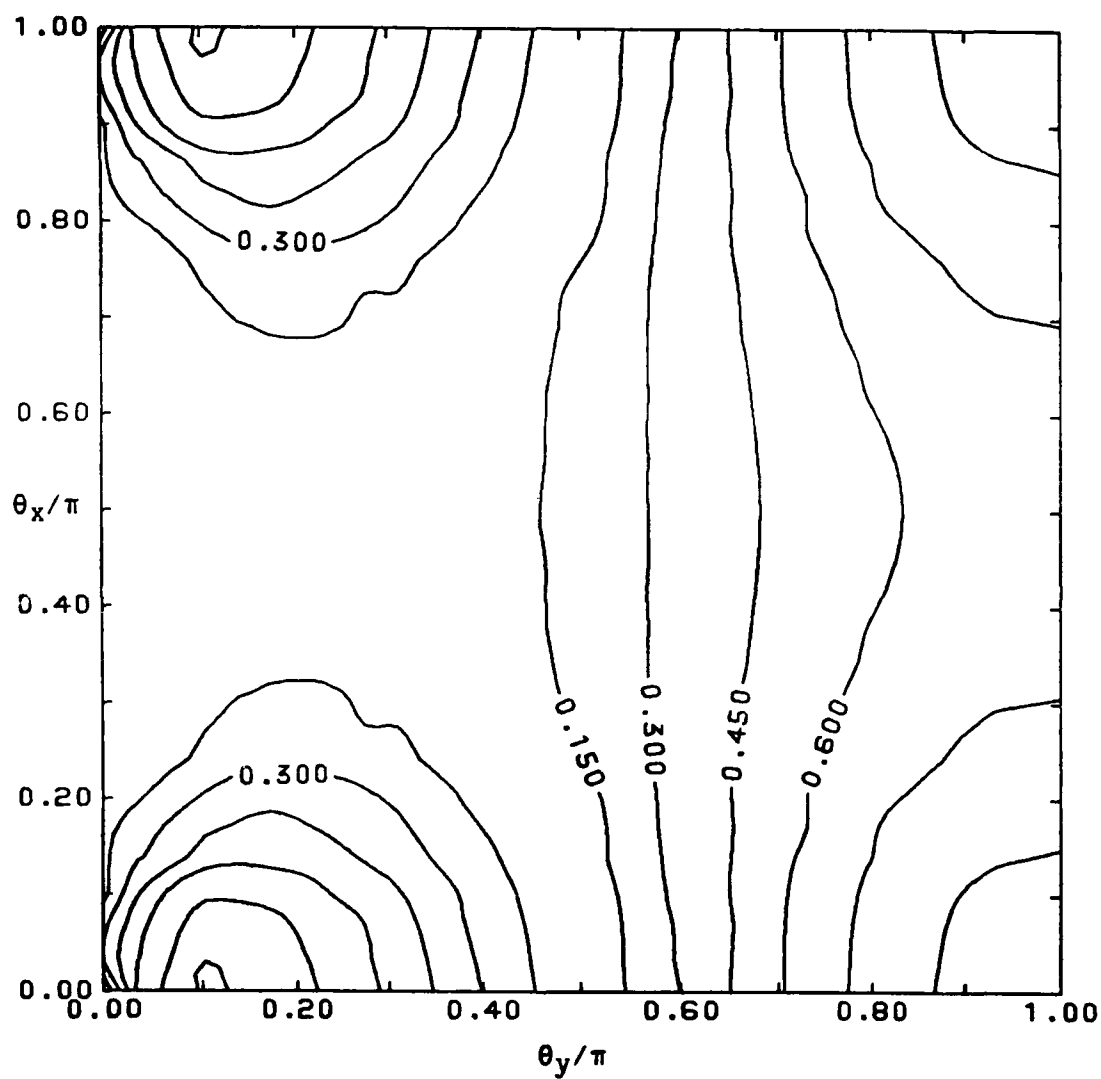
Figure 2.2 Real Part of $\lambda^*\lambda$, σ=-1.00 for All Wave
Numbers for the PL method (u=v=1,Δx=Δy=1,Re=1000)
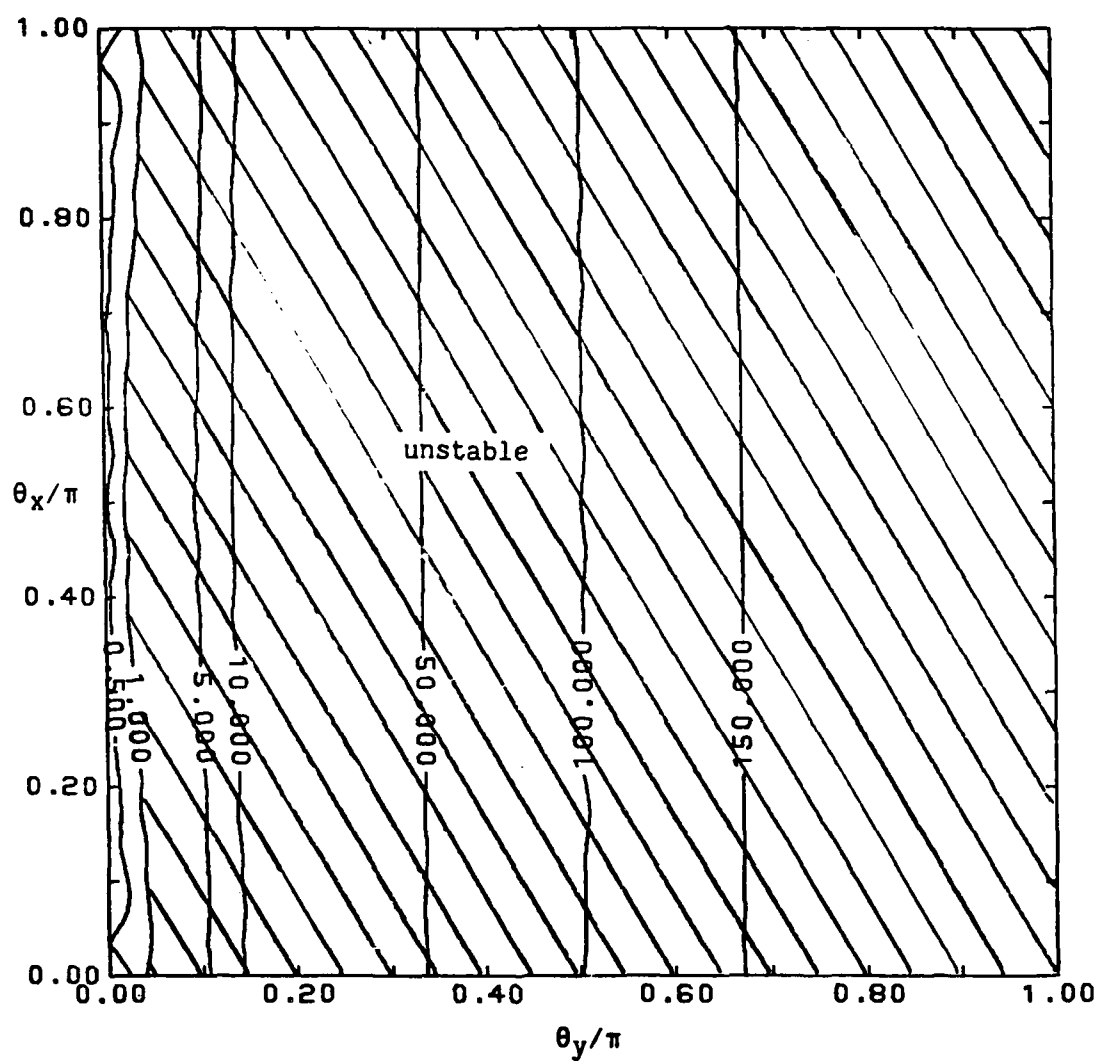
Figure 2.3 Real Part of $\lambda^{*}\lambda$, $\sigma=-0.01$ for All Wave

Numbers for the PL method ($u=v=1, \Delta x=0.01\ \Delta y=1, Re=1000$)
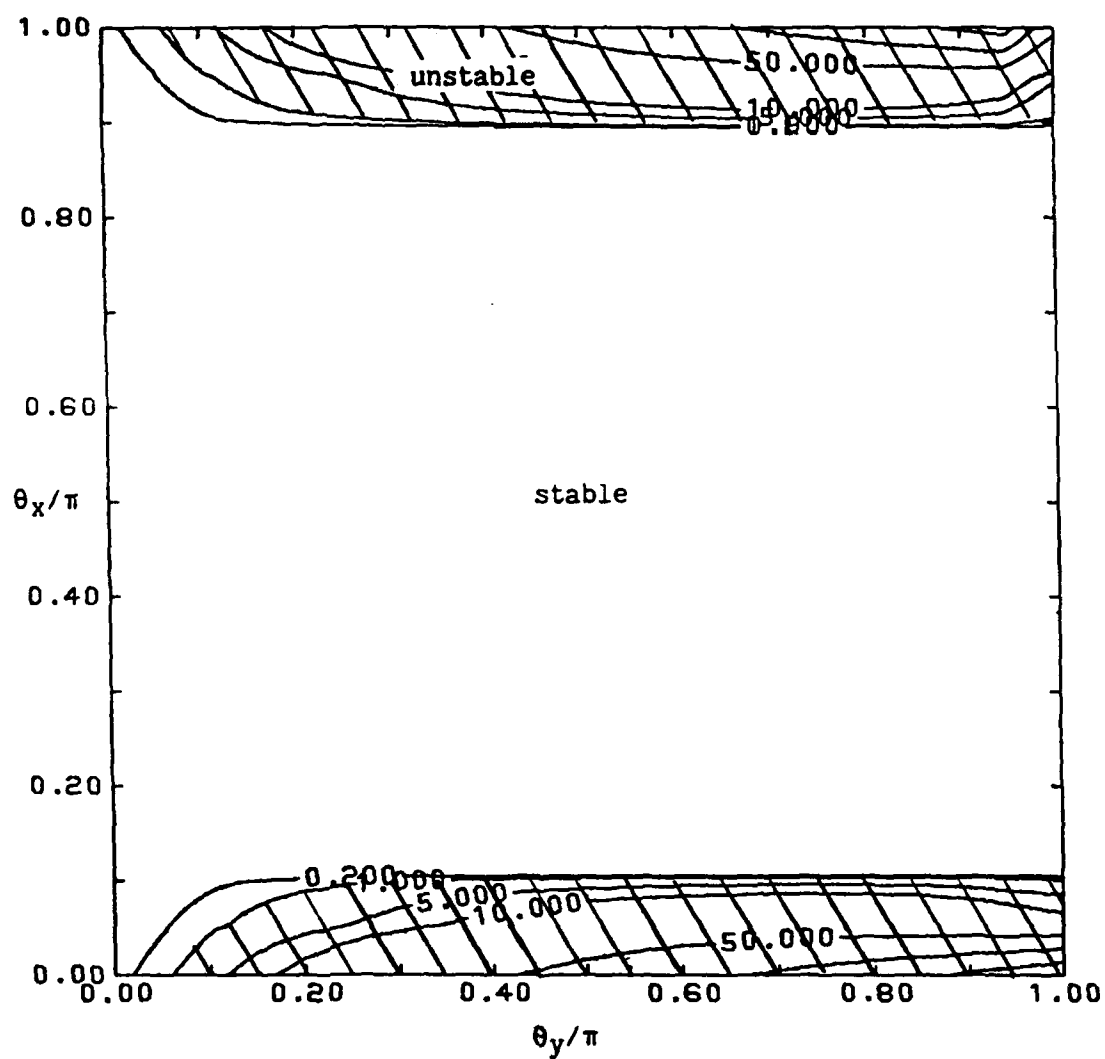
Figure 2.4   Real Part of $\lambda^*\lambda$, $\sigma=-0.01$ for All Wave
Numbers for the PL method ($u=v=1$, $\Delta x=100$ $\Delta y=1$, $Re=1000$)

stability characteristics. Thus, it is apparent that only when $\sigma=-1.0$ is the PL scheme stable for multiple passes of the flow field. Unfortunately, the small value of σ is the most attractive feature of the PL method since this allows for very good viscous flow predictions when the inviscid pressure is given as the assumed pressure (see Pouagare and Lakshminarayana (1986)). With $\sigma=-1.0$, viscous predictions of complex flows become difficult since the streamwise pressure gradient condition is nolonger relaxed and the coupling of the continuity equation to the momentum equations stiffens the solution process.

2.3.3 Remarks on the Method

The PL method was found to be relatively insensitive to the assumed pressure distribution for strongly parabolic flows, e.g., developing flow in a constant curvature duct with constant cross-sectional area. This is no surprise since the satisfaction of the global mass flow constraint should set the proper streamwise pressure gradient for an internal flow. For parabolic flows, the transverse pressure gradients are essentially constant or change only slightly in the streamwise direction. Thus, their effect can be introduced as some source term in the transverse momentum equations leaving the pressure as a dependent variable in only one equation, the streamwise momentum equation. With continuity satisfied exactly, the proper velocity field is always computed regardless of how the streamwise pressure gradient is treated. The pressure is always adjusted during the computation in response to the assumed pressure. Combining the assumed and computed pressure through a simple functional relationship yields an integral equation for the actual pressure as was done by Pouagare and Lakshminarayana (1986).

When the transverse pressure gradients vary with the streamwise direction, as in cascades, the actual pressure cannot be obtained from a simple relationship. When using the PL method for complex flows, while good viscous velocities are obtained, the viscous pressure cannot be determined easily. One alternative is to use the Poisson equation for the pressure which uses only the viscous velocity field to compute a new viscous pressure field (see Kirtley and Lakshminarayana (1985)). The question of whether the Poisson equation can be coupled to the PL method to yield a convergent system is defered to section 2.5.

The method is very useful for obtaining the viscous velocity field in a complex geometry if a fairly accurate presciption of the inviscid pressure field is used as the assumed pressure. It should also be noted that, due to the small value of σ, the uncoupling of the odd and even points in the computation is severe.

It is useful to comment that the computation of complex flows is successful with the PL method because one condition, namely the streamwise pressure gradient condition, is relaxed during the computation. It should also be noted that most methods described in chapter I also relax some condition, usually the continuity condition.

Regarding the stability of the multiple pass mode, a look at a one-dimensional system as suggested by Abdallah (1987a) leads to the same conclusion as the von Neumann analysis. The one-dimensional system is:

$$\partial_x u = 0$$
$$\partial_x u^2 + \sigma \partial_x p = -\partial_x p^{as} + \sigma \partial_x p$$

$$(2.21)$$

where the second term on the right side of the momentum equation is

differenced as in equation 2.11. Inversion of the system shows that:

$$u_i = u_{i-1}$$

$$p_i = 1/\sigma \, (\partial_x p^{as}) + p^{as}_i$$

$$(2.22)$$

Thus, regardless of the value of p^{as}, the correct velocity is always computed. On the otherhand, the difference between the computed and assumed pressure is equal to the assumed pressure gradient divided by σ. Thus, any error in the assumed pressure gradient will be multiplied by a very large number since σ is very small. If σ was large, the system would be stable but physically unrealistic. Thus, the same conclusion of unconditional instability of the PL method can be made. One wonders whether a similar modification to the pressure gradients could be made in such a way as to give results as good as the PL scheme in single pass mode yet be stable in multiple pass mode.

2.4 Modified PL Method (MPL)

In an attempt to overcome some of the drawbacks of the PL technique, a modified PL method is developed in this section based on the pressure corrections of Moore and Moore (1981). The pressure is split into an assumed pressure and a pressure correction.

$$p = p^{as} + p^c$$

$$(2.23)$$

The gradients of p are split as follows:

$$\partial_x p = \partial_x p^{as} + \partial_x p^c$$

$$\partial_y p = \partial_y p^{as} + b \partial_y p^c$$

$$\partial_z p = \partial_z p^{as} + b\partial_z p^c$$

(2.24)

Where as Moore and Moore solve an uncoupled set of equations, the present MPL method solves a coupled system of equations. Thus, in two dimensions, vectors A, B, and S in equation 2.4 become:

$$A = \begin{bmatrix} u \\ u^2 + p^c \\ uv \end{bmatrix} \quad B = \begin{bmatrix} v \\ uv \\ v^2 + bp^c \end{bmatrix} \quad S = \begin{bmatrix} 0 \\ -\partial_x p^{as} \\ -\partial_y p^{as} \end{bmatrix}$$

(2.25)

So that as $p^c \to 0$, the exact equation is solved within the accuracy of the discretization. It is hoped that if the absolute value of b is large then the global instability characteristic of the PL method may not arise and global convergence of the MPL method may be achieved. Moore and Moore use the notation 1/e which is equivalent to b and use a value of e equal to -0.01.

2.4.1 Eigenvalue Analysis

The stability of the forward-marching procedure of the MPL method can be studied in a manner similar to that in section 2.3.1. The Jacobians of the modified vectors A and B are:

$$A_J = \begin{bmatrix} 0 & 1 & 0 \\ 1 & 2u & 0 \\ 0 & v & u \end{bmatrix} \quad B_J = \begin{bmatrix} 0 & 0 & 1 \\ 0 & v & u \\ b & 0 & 2v \end{bmatrix}$$

Again, for stable forward-marching, the eigenvalues of the matrix $A_J^{-1}D_J$ must be real and non-negative for proper damping and the eigenvalues of

the matrix $A_J^{-1}B_J$ must also be real. For the flux vector A in 2.25, the characteristic equation of $A_J^{-1}D_J$ is:

$$\lambda^2(\lambda - 1/u) = 0$$

<div align="right">(2.26)</div>

thus, the eigenvalues are:

$$\lambda_{1,2} = 0 \quad , \quad \lambda_3 = 1/u$$

<div align="right">(2.27)</div>

Therefore, if the streamwise velocity is positive, the scheme is naturally dissipative. For $A_J^{-1}B_J$, the characteristic equation is:

$$\lambda^3 - (v/u)\lambda^2 + b\lambda - vb/u = 0$$

<div align="right">(2.28)</div>

Solving equation 2.28 gives the following eigenvalues:

$$\lambda_1 = v/u \; , \; \lambda_{2,3} = \pm\sqrt{-b}$$

<div align="right">(2.29)</div>

Therefore, if b is less than zero, the scheme is stable for forward-marching. One should also notice that the eigenvalues in 2.29 are the same as those of the PL method in equation 2.8 if b is equal to $1/\sigma$. Therefore, the MPL method should give very similar results to those of the PL method if b is set to -100. So now there is a large coefficient multiplying the implicit pressure correction gradient. As seen from the analysis for the PL method, global convergence is expected with the MPL method with the absolute value of b large.

2.4.2 Global Stability Analysis

The question now arises whether the MPL scheme can be used in a multiple pass mode to reduce residual errors. Using the procedure outlined in section 2.3.2 with the Fourier decomposition in equation 2.13 gives:

$$P_J \ A^n = H_J \ A^{n-1}$$

(2.14)

where

$$P_J = \begin{bmatrix} 0 & \ell_1 & \ell_2 \\ \ell_1 & 2u\ell_1+v\ell_2-\ell_3 & u\ell_2 \\ b\ell_2 & v\ell_1 & u\ell_1+2v\ell_2-\ell_3 \end{bmatrix}$$

and

$$H_J = \begin{bmatrix} 0 & 0 & 0 \\ 0 & 0 & 0 \\ \ell_2(b-1) & 0 & 0 \end{bmatrix}$$

This gives the following amplification matrix G:

$$G = \begin{bmatrix} M_1 & 0 & 0 \\ M_2 & 0 & 0 \\ M_3 & 0 & 0 \end{bmatrix}$$

(2.30)

where

$$M_1=(b-1)\ell_2(u\ell_1\ell_2-\ell_2(2u\ell_1+v\ell_2-\ell_3))/|P_J|$$

$$M_2=(b-1)\ell_1\ell_2^2/|P_J|$$

$$M_3 = (1-b)\ell_2\ell_1^2 / |P_J|$$

$$|P_J| = -\ell_1(\ell_1(u\ell_1 + 2v\ell_2 - \ell_3) - ub\ell_2^2))$$

$$+\ell_2(v\ell_1^2 - b\ell_2(2u\ell_1 + v\ell_2 - \ell_3))$$

and $\ell_{1,2,3,4}$ are defined as before in equation 2.15.

The eigenvalues of G are then:

$$\lambda_1 = M_1$$

$$\lambda_{2,3} = 0$$

$$(2.31)$$

Previously, the maximum value of λ_1 was found for $\theta_x = \theta_y = \pi$. For this combination of wave numbers, $\lambda_1 = 0$ which would indicate that the system is stable for multiple passes. This is not the case as a plot of the absolute value of $\lambda^*\lambda_1$ in Figure 2.5 will attest. Again the hatched area indicates regions of instability. For a value of $b = -100$, $u = v = 1$ and $Re = 1000$, the values of the eigenvalues are much less than those of the PL technique. In fact, the eigenvalues are only slightly higher than unity and are less than unity for most wave numbers. However, by definition, the system is not stable if $|\lambda^*\lambda_1| > 1$ for any wave number. As with the PL method, the stability characteristics remain unchanged when the velocity ratio is changed. However, when the grid aspect ratio is changed from $\Delta x/\Delta y = 1$ to 0.01, it seems apparent from Figure 2.6 that the scheme is globally stable. Unfortunately, there is a small unstable region confined to the area where $\theta_y/\pi = 0$ at which location the maximum eigenvalue equals 1.01 for this combination of parameters. Again, this indicates that global stability is not ensured. As with the PL method, when the ratio of $\Delta x/\Delta y = 100$ (see Figure 2.7), the region

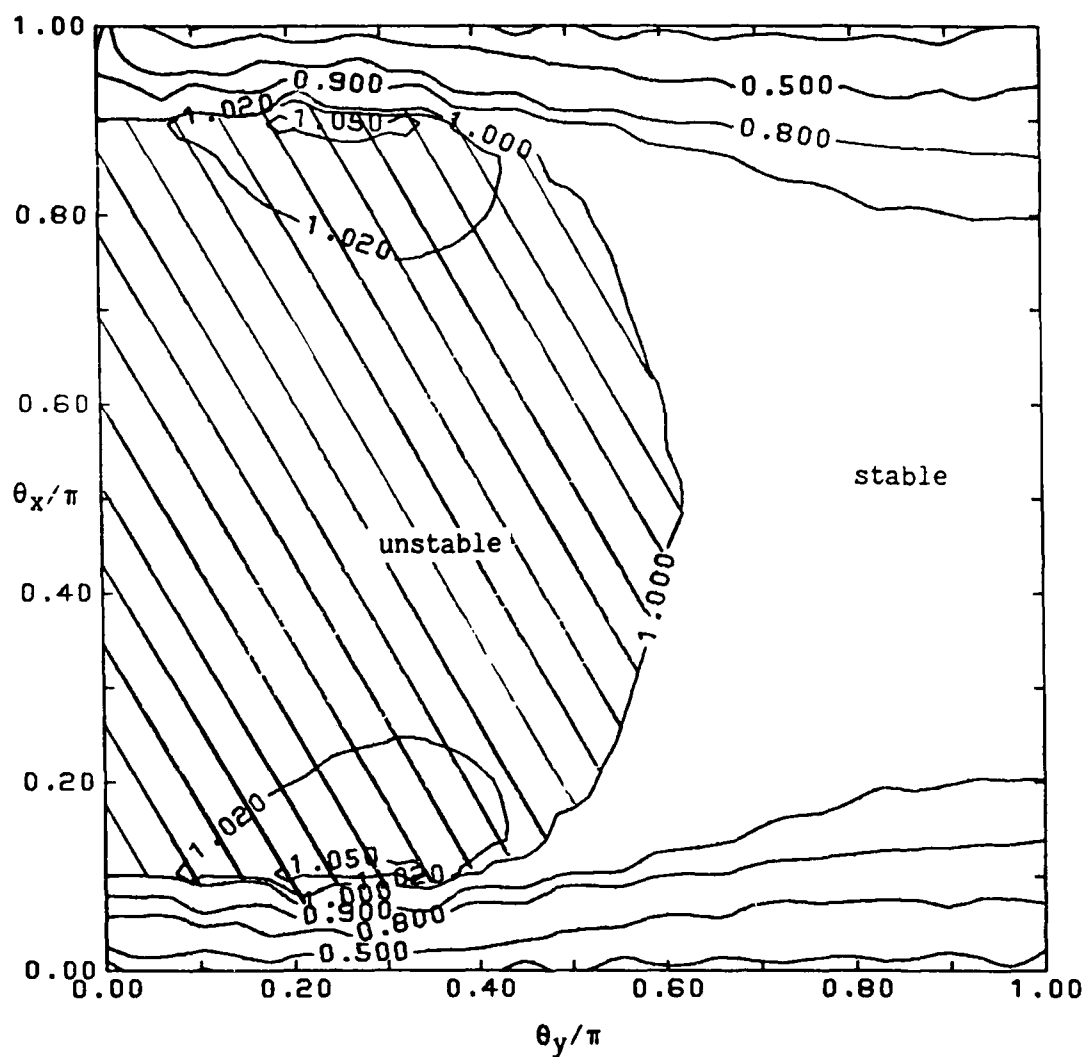Figure 2.5   Real Part of $\lambda^{*}\lambda$, b=-100 for All Wave
Numbers for the MPL method (u=v=1,Δx=Δy=1,Re=1000)

Figure 2.6 Real Part of $\lambda^*\lambda$, b=-100 for All Wave
Numbers for the MPL method (u=v=1,Δx=0.01 Δy=1,Re=1000)

where the global marching procedure is stable is greater, i.e., for 0.1 < θ_x/π < 0.9. Still, the maximum eigenvalue is 1.01 at $\theta_x=\pi$ and $\theta_y=0$. Therefore, the MPL method is unstable for a multiple pass procedure. It is interesting to note that, for the same combination of parameters, the MPL method is stable for the combination of wave numbers where the PL method is unstable and vice versa. A possible explanation for this is that the streamwise momentum equation is manipulated in the PL method whereas the transverse momentum equations are manipulated for the MPL method.

The above analysis is not exact since the actual equation is not solved in frozen coefficient form and the treatment of the boundary conditions has not been included in the analysis. This leads one to believe that the system may be stable after all. Therefore, it seems worthwile to persue this technique.

2.4.3 Remarks on the Method

The MPL method appears to be very promising. The forward-marching eigenvalue analysis indicates that the single pass results may be as good as those of the PL technique. Indeed, it can be used efficiently as a single pass method as can the PL method. Unfortunately, the method is not stable for multiple passes of the domain even though the pressure gradient is multiplied by a large coefficent which seemed to be appropriate for global convergence as mentioned in section 2.3.3. A computation of the developing flow in a straight duct with a square cross-section shows a slow divergence when multiple passes are made. Figure 2.8 gives the convergence history for this test case. Due to the large value of b, the same uncoupling of odd and even points is present
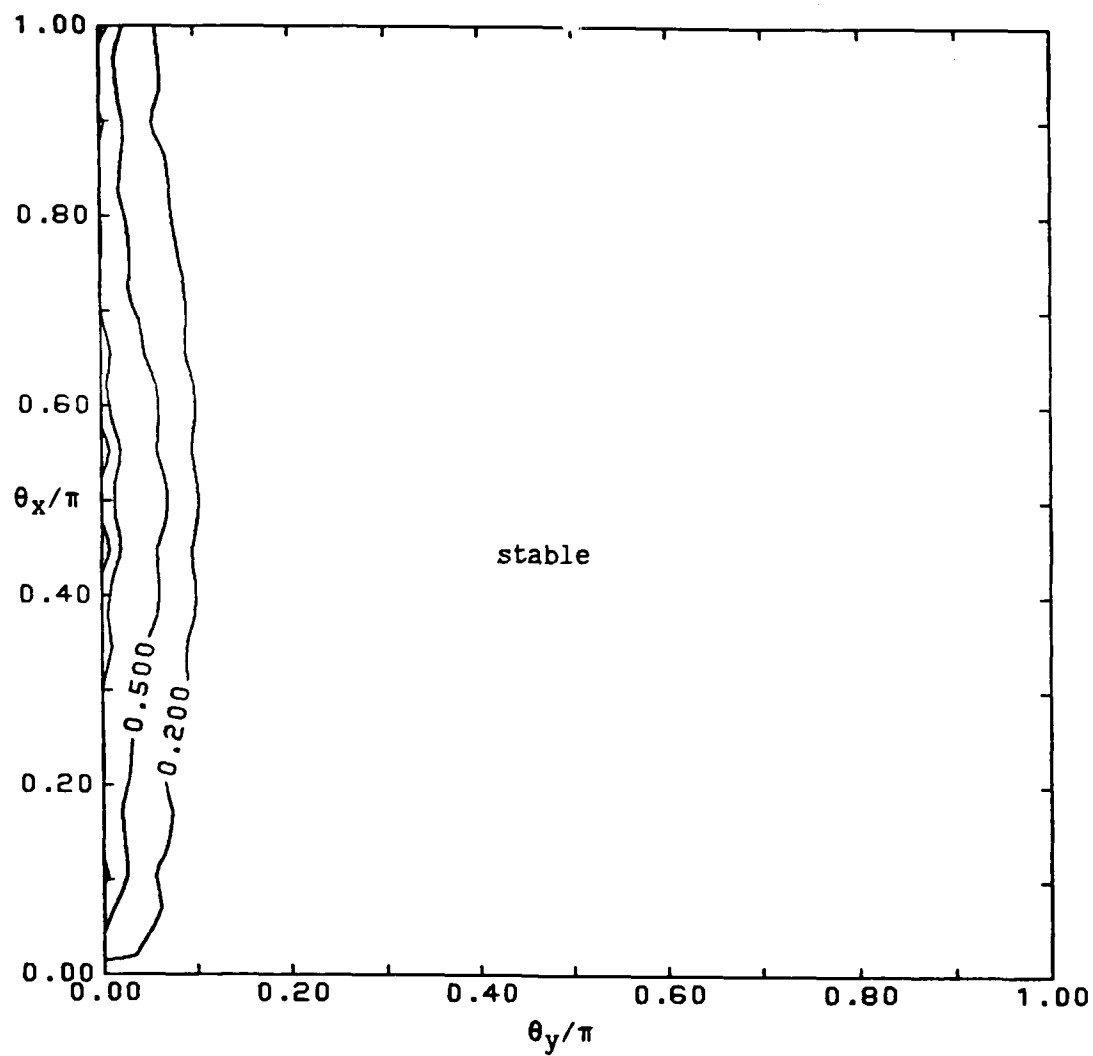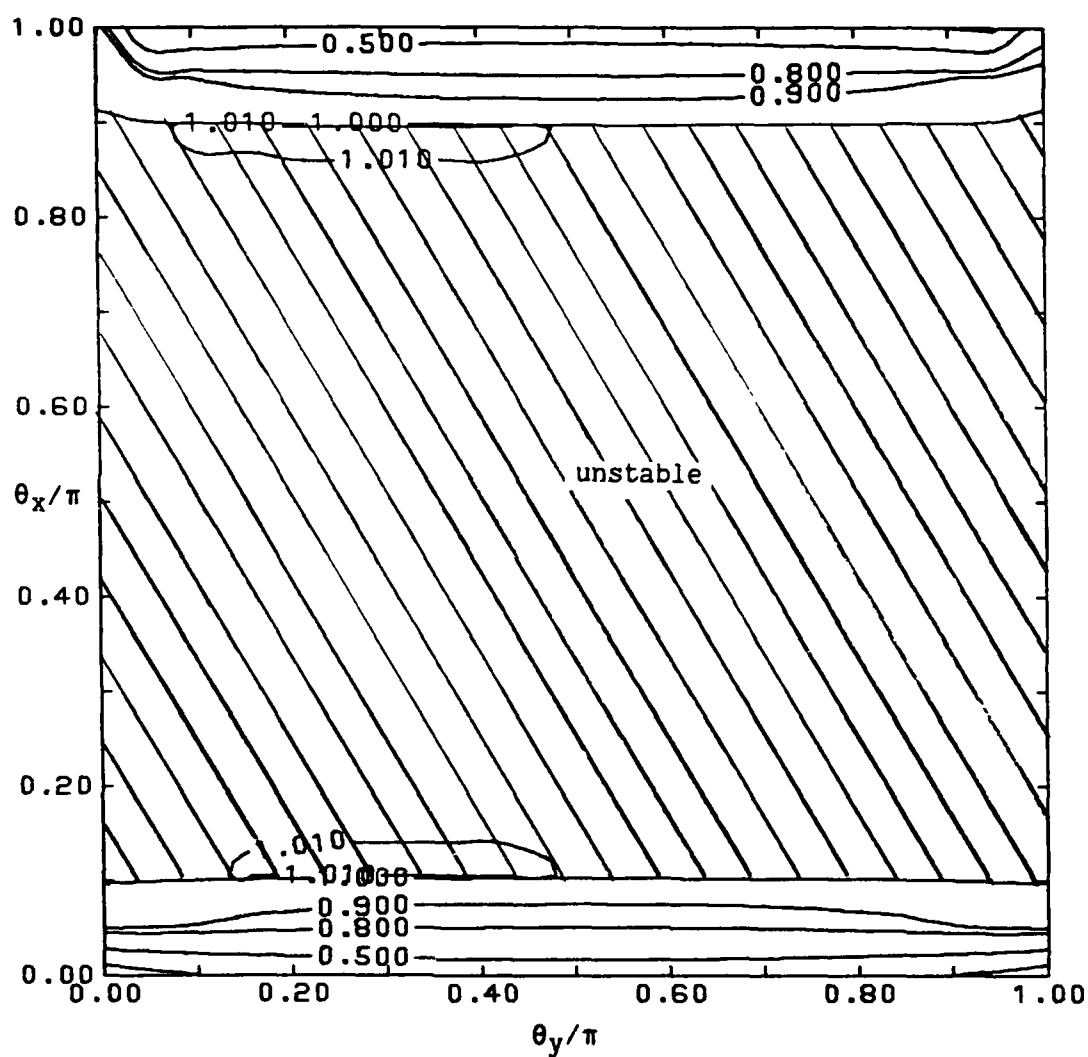
Figure 2.7   Real Part of $\lambda^*\lambda$, b=-100 for All Wave

Numbers for the MPL method (u=v=1,Δx=100 Δy=1,Re=1000)
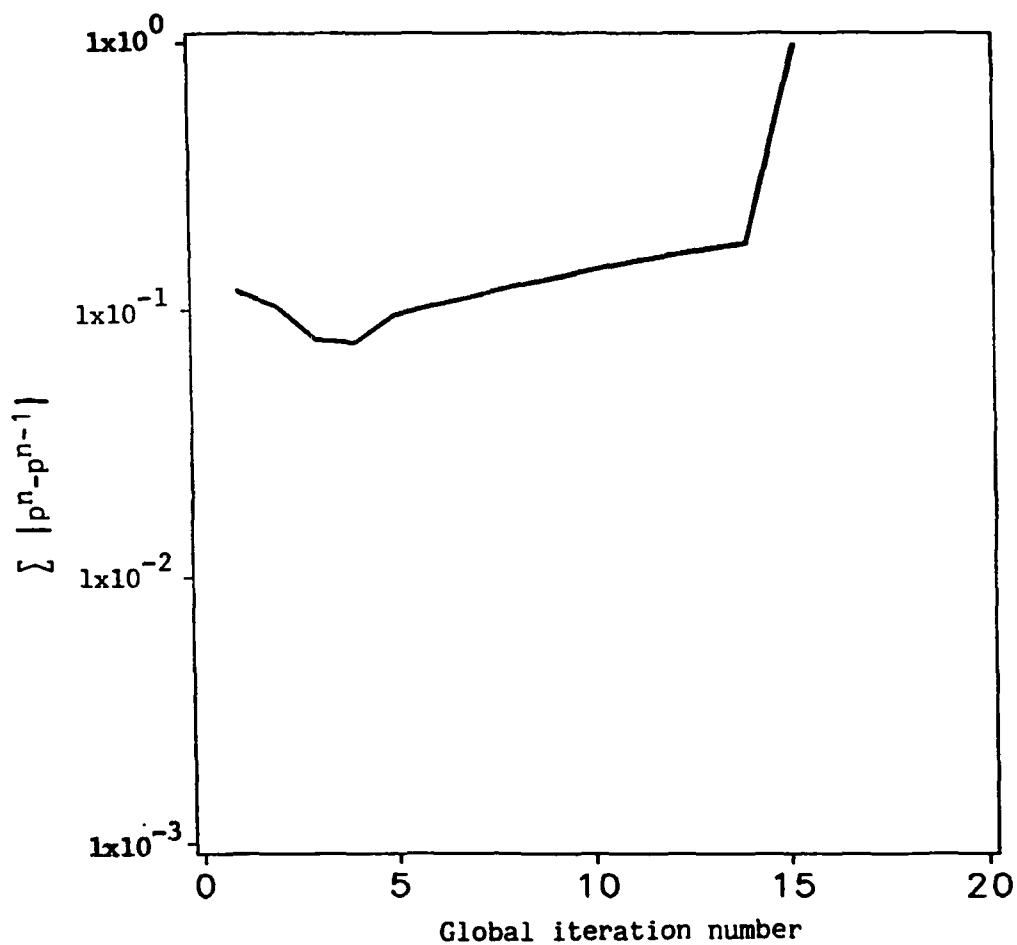
Figure 2.8 Convergence History for the MPL method for Developing

Flow in a Square Duct, Re=100

as with the PL scheme. This also leads to great difficulty in computing spacially periodic flows. The scheme has been used for a zonal equation method developed by Warfield and Lakshminarayana (1987). In their scheme, the MPL method is used in parabolic regions of the flow and a time-marching method is used in the elliptic regions and to correct the pressure field in the entire domain. With another equation determining the new pressure field, the MPL method in essentially a multiple pass mode and is shown to be convergent. The question then arises whether both the PL and MPL techniques could be used in a multiple pass mode and be stable if a separate equation for the pressure is used to determine a new pressure field between passes of the domain. The obvious choice for the separate equation is the Poisson equation for the pressure.

2.5 Poisson Equation for the Pressure

The Poisson equation for the pressure is obtained by taking the divergence of the momentum equation. For the three-dimensional system, the equation looks like:

$$\nabla^2 p = \Sigma_p$$

(2.32)

$$\Sigma_p = -(2(\partial_x v \partial_y u + \partial_x w \partial_z u + \partial_y w \partial_z v) + (\partial_x u)^2 + (\partial_y v)^2 + (\partial_z w)^2)$$

(2.33)

There is no analytical solution to equation 2.32 since the source term Σ_p is not separable. Equation 2.32 can be inverted directly for p, however, this requires immense amounts of computer storage for three-dimensional computations. Relaxation techniques are the most efficient way to solve 2.32 but a convergent solution requires the satisfaction of

a compatibility relation which arises from Green's divergence theorem, namely:

$$\int\int_V \Sigma_p \, dV = \int_S \partial_n p \, dS$$

(2.34)

where V is the volume of the domain, S is the area enclosing the domain and ∂_n is the derivative normal to S.

Equation 2.32 was coded, solved using a semi-implicit method, and coupled to the MPL technique. In order to test the convergence of this system, the turbulent flow in an S-shaped duct was computed. The geometry is given in Figure 2.9 along with the measurement locations. The flow was measured by Taylor et al. (1982) at a flow Reynolds number of 40000 based on the duct width. More details about this particular flow are given in section 3.8.2.

With no assumed pressure field, the MPL method could not compute past the second bend of the duct. Here, the computed flow separated and the turbulence model introduced instabilities. Thus, the computation was restarted using an assumed pressure field derived from a sine function with the measured bulk pressure drop imposed. This assumed pressure was both smooth and close to the experimental data. With this, the MPL successfully computed the entire domain. The results are presented in Figures 2.10 through 2.13.

The computed streamwise and transverse velocity profiles are compared to the experimental data at station 2 in Figures 2.10 and 2.11, respectively. Here, the streamwise boundary layer thickness is reasonably well predicted but the secondary flow, while having the proper sense, is not large enough. This may be due to inlet conditions

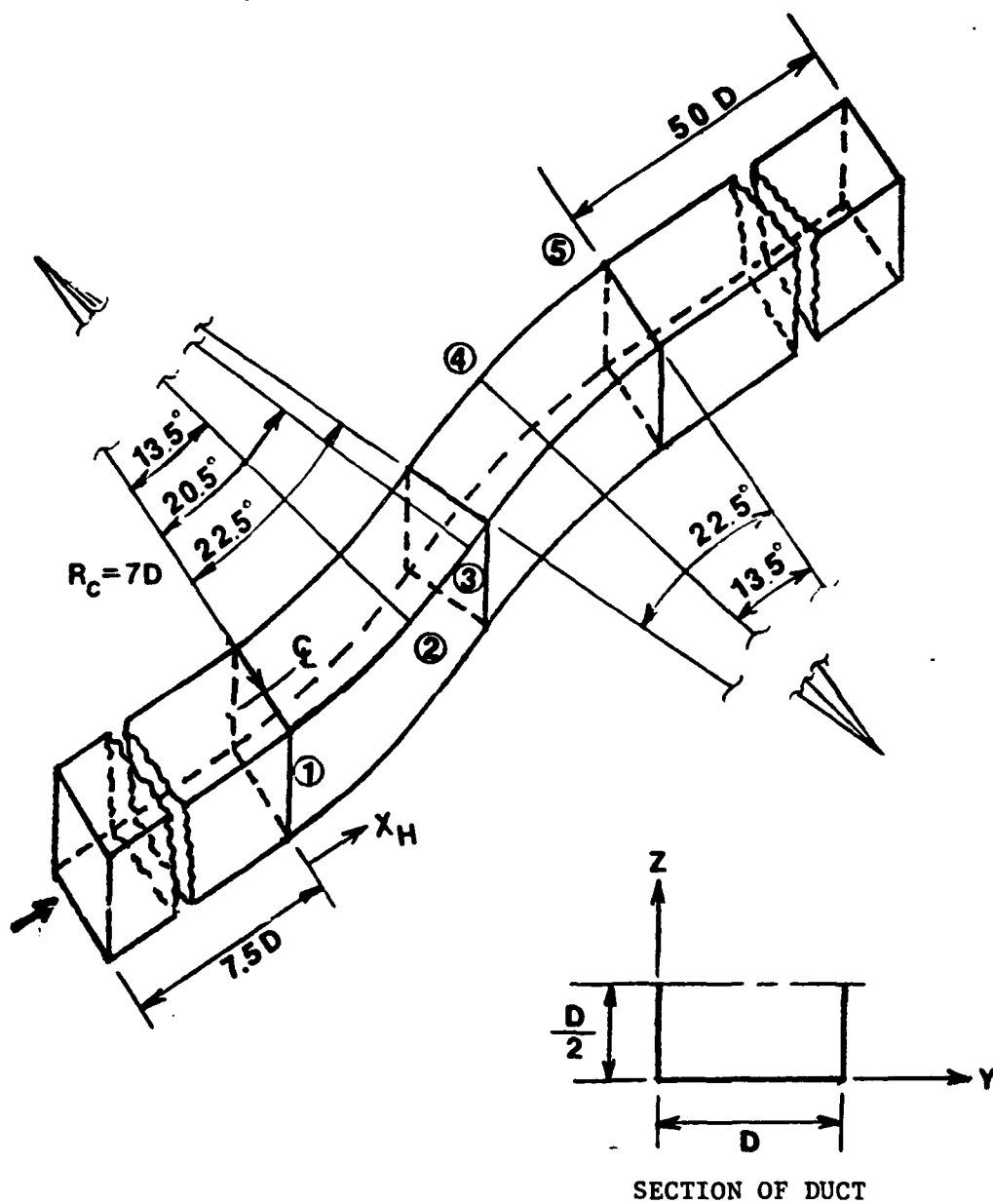Figure 2.9 Geometry of the S-shaped Duct

Figure 2.10 Streamwise Velocity Profiles for the S-Duct,
Station 2, MPL method, Re=40000.
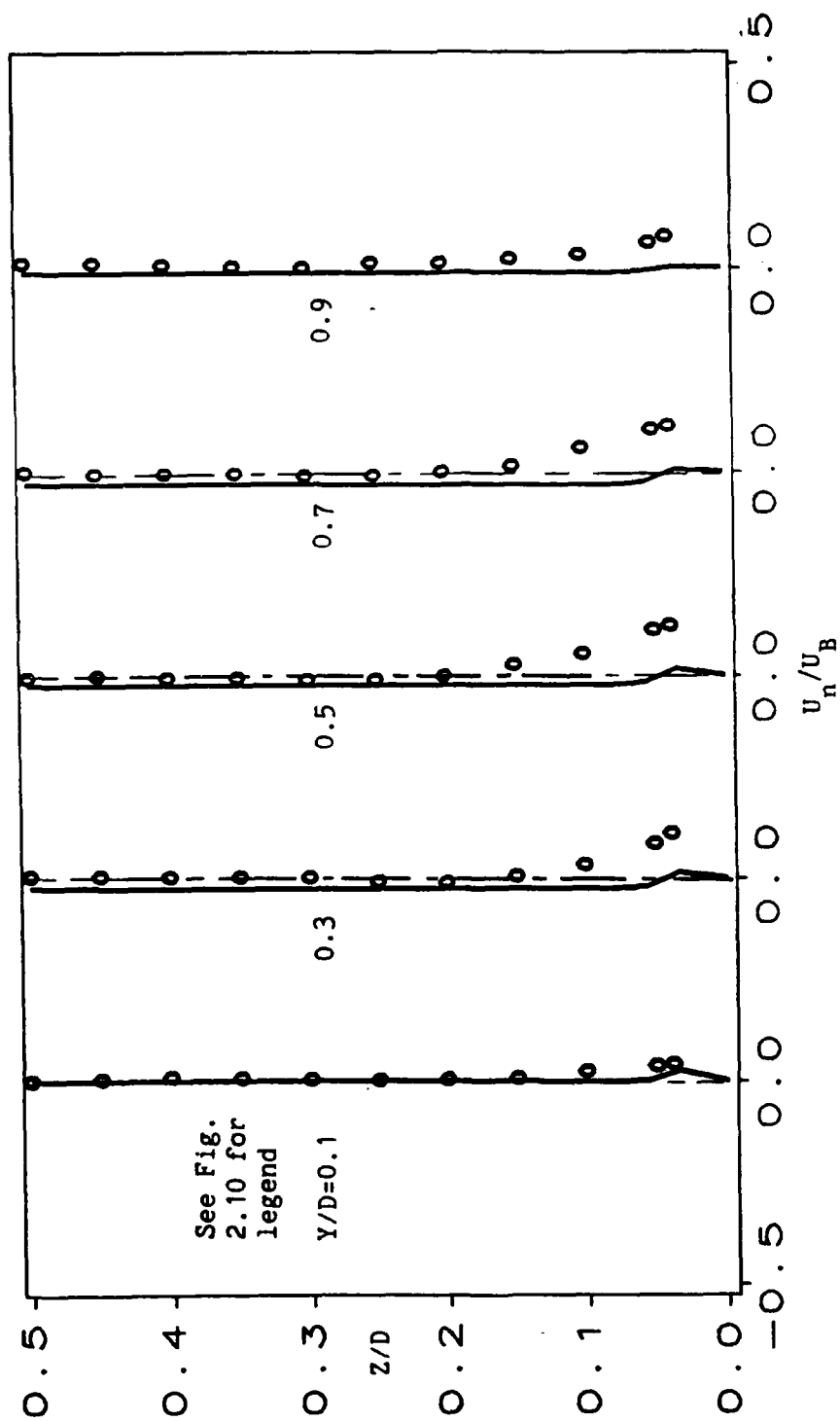
Figure 2.11 Transverse Velocity Profiles for the S-Duct,
Station 2, MPL method, Re=40000.
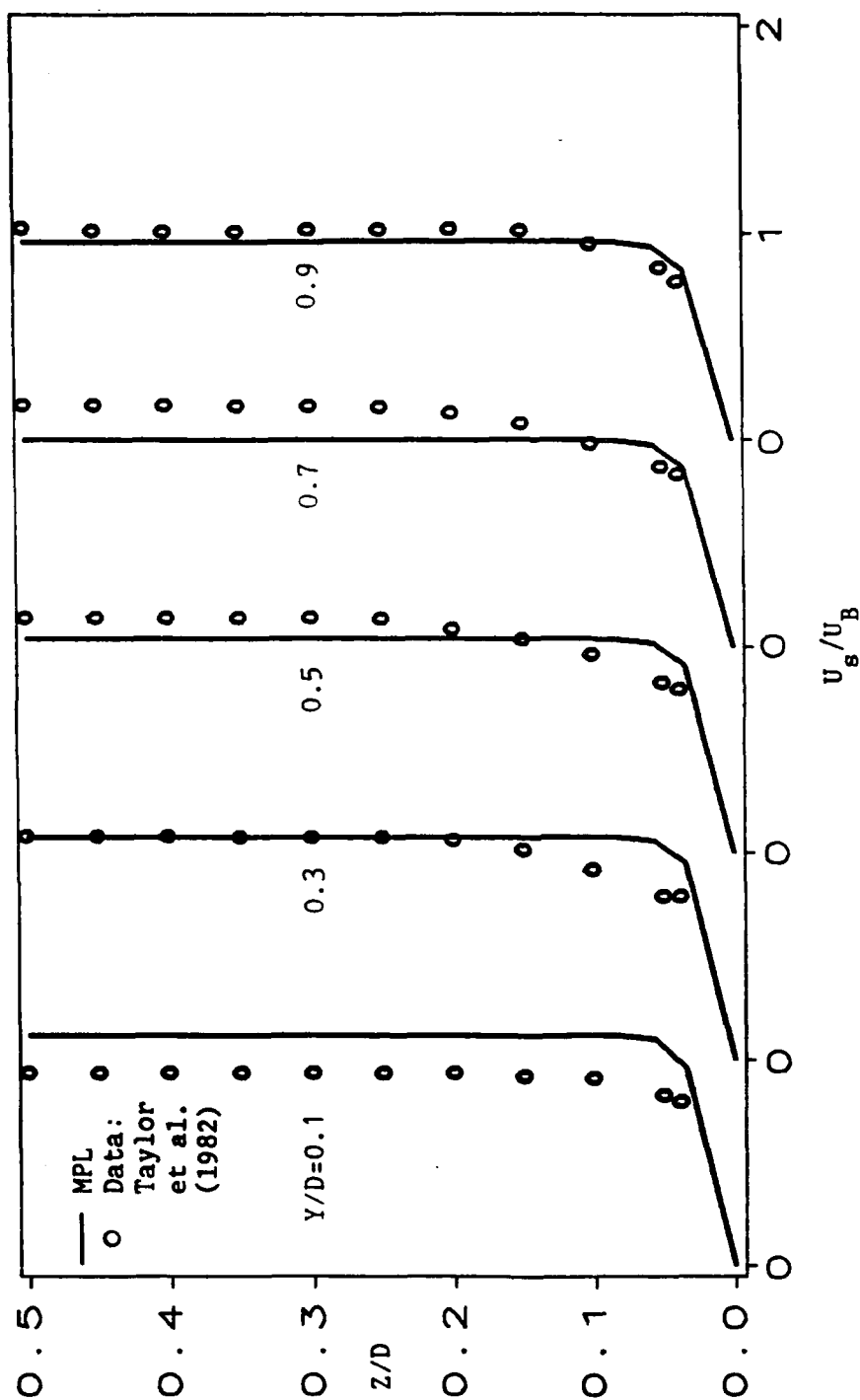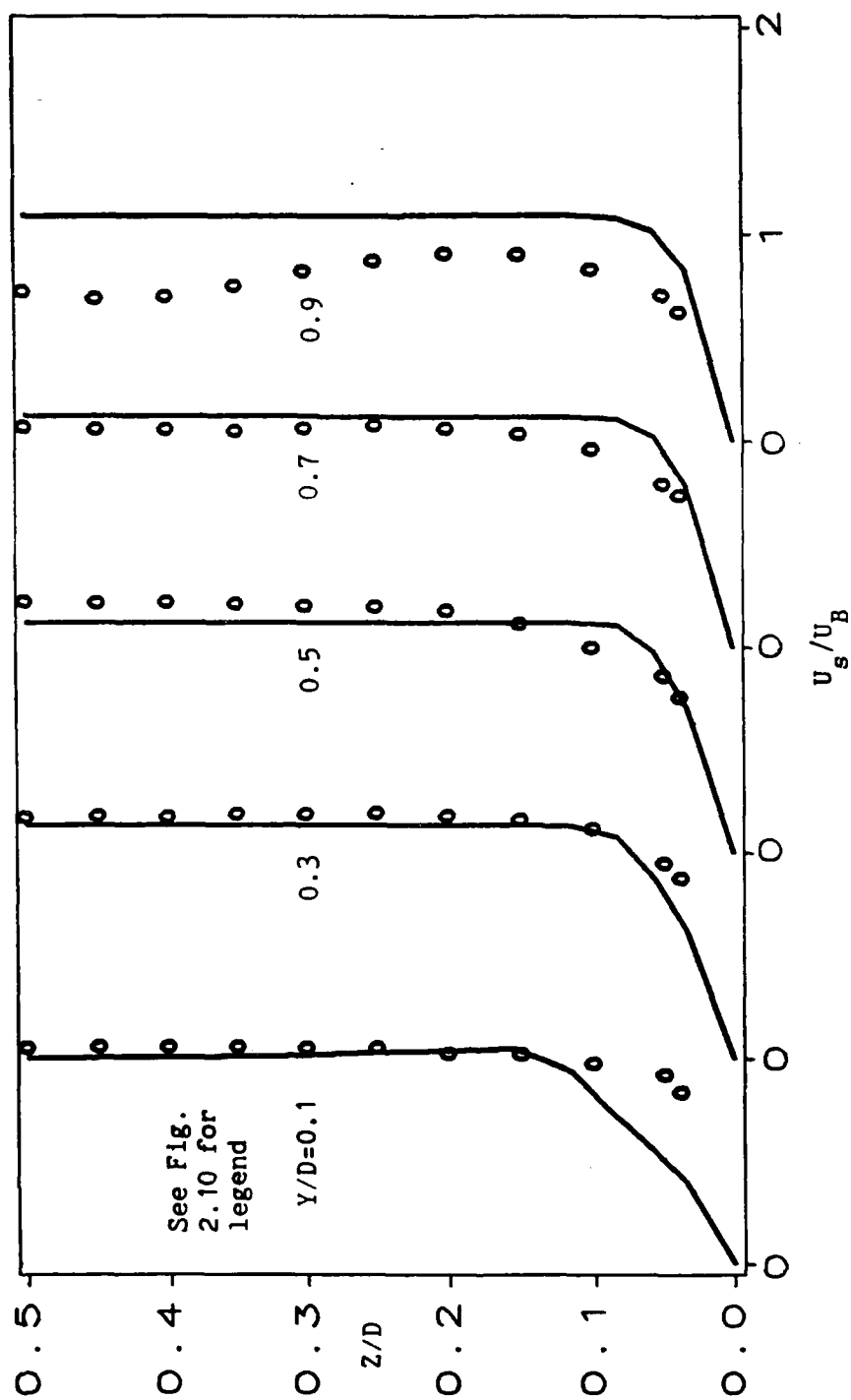
Figure 2.12 Streamwise Velocity Profiles for the S-Duct,

Station 5, MPL method, Re=40000.
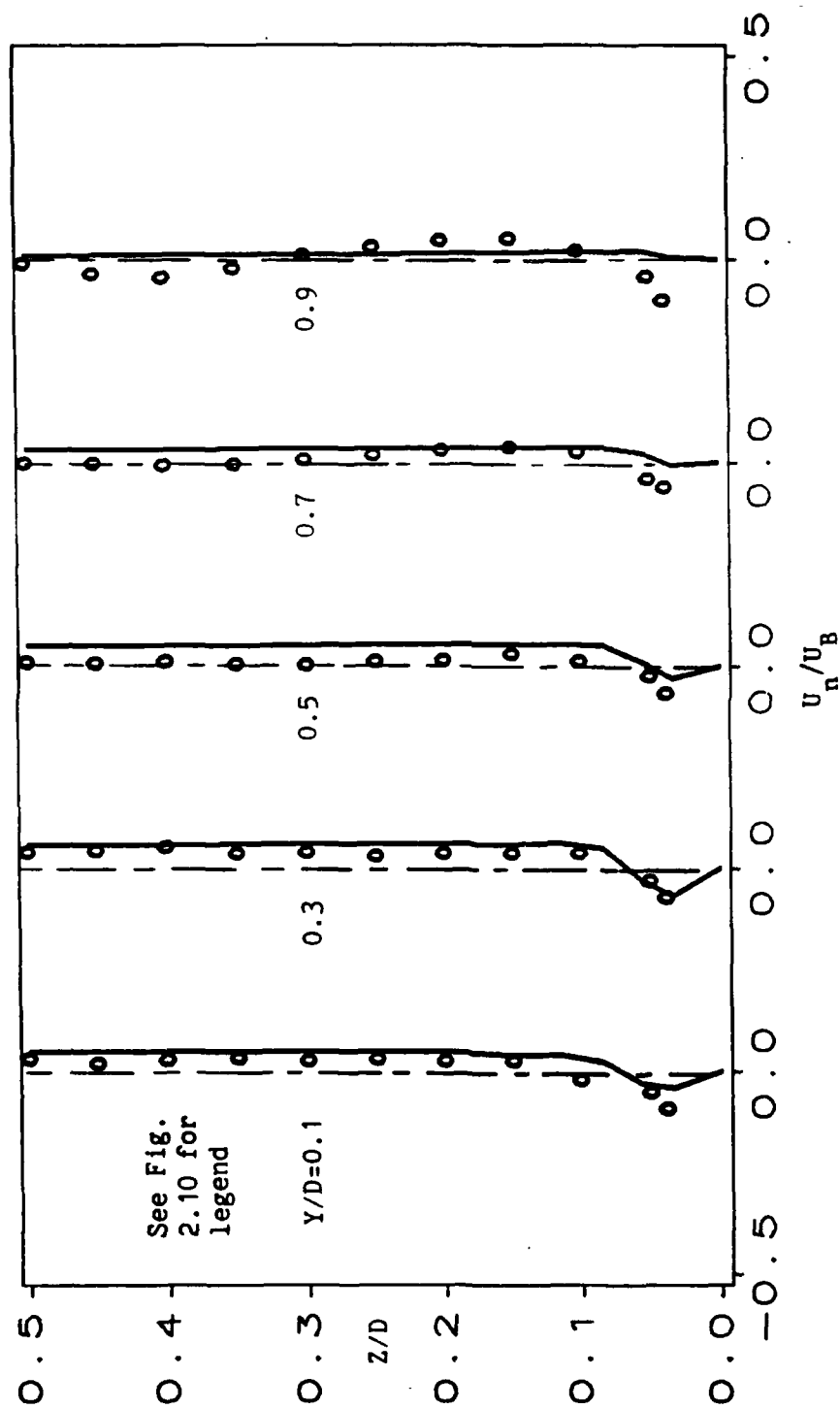
Figure 2.13 Transverse Velocity Profiles for the S-Duct,
Station 5, MPL method, Re=40000.

with a lower than measured vorticity or a poor resolution of the transverse pressure gradient. The streamwise and transverse velocities are again compared to the experimental data at station 5 in Figures 2.12 and 2.13, respectively. Station 5 is perceived to be the location where elliptic influences are the greatest. Near the side walls, the predictions of the streamwise velocity are not good. The secondary flow is well predicted at all transverse locations except at Y/D=0.9. At this location, almost no secondary flow is computed which is not consistent with the data. These below average predictions should not be worrysome, however, since this is the first pass of what is hoped to be a multiple pass procedure in which the solution converges to the correct solution after several global iterations with the Poisson equation used to update the pressure.

The viscous pressure was computed from equation 2.32 and is given in Figure 2.14. Neumann boundary conditions based on the momentum equations were used on all boundaries save the downstream boundary where a Dirichlet condition was used. One can see from Figure 2.14 that the new computed pressure field, while qualitatively correct, does not match the experimental data near Y/D=0.1 and 0.5. When this pressure was used as the new assumed pressure and the marching process repeated with the MPL technique, the computation exhibited divergent behavior near the begining of the second bend. Manipulation of the boundary conditions for the pressure solver did not improve the convergence. When the laminar flow was computed, which has much stronger secondary flows and pressure gradients, the same divergent behavior was observed. From this, one may conclude that the Poisson equation coupled to the MPL method as outlined above, does not yield a globally stable system of
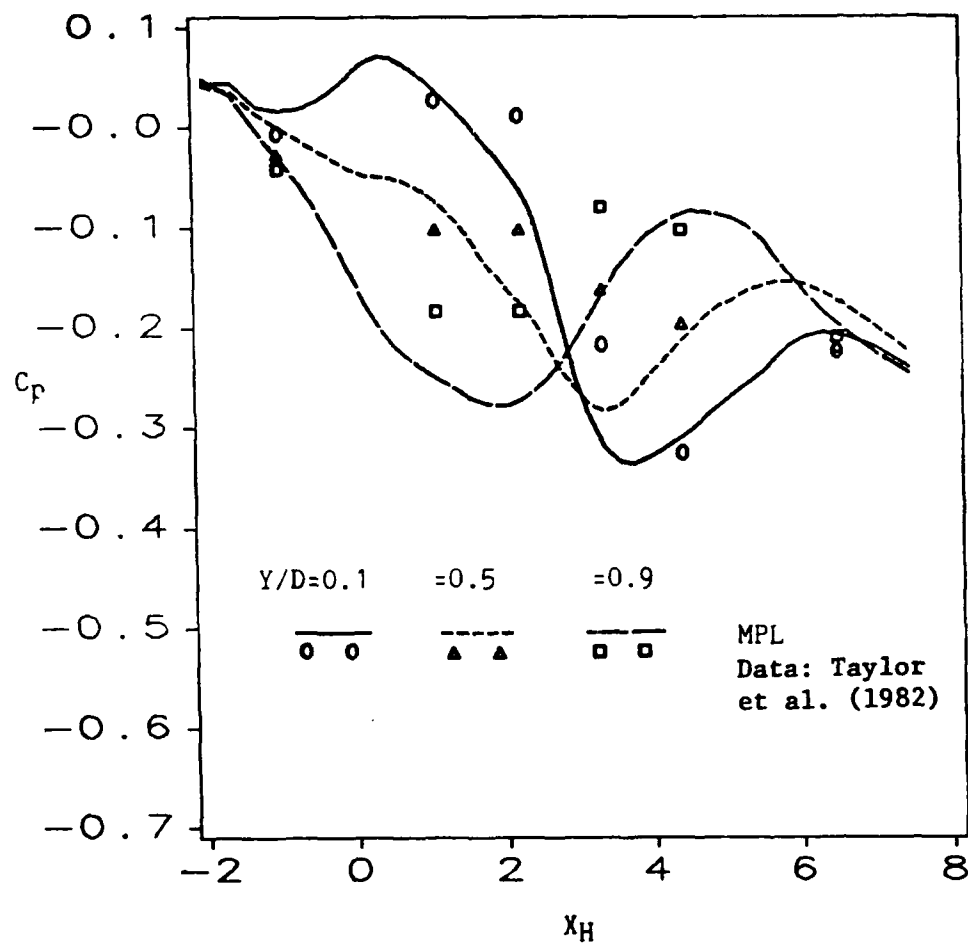
Figure 2.14 Pressure Computed from the Poisson Equation Using
MPL method, Re=40000.

equations. There appears to be no mechanism in the system, of equations to relax the pressure errors. Another problem may be due to the following. When using Neumann boundary conditions, equation 2.34 is seldom satisfied by the discretized form of equation 2.32. This leads to a divergent solution of the Poisson equation. If one Dirichlet boundary condition is used then equation 2.34 will be satisfied exactly and a convergent solution will result. This is because $\partial_n p$ on the boundary with the Dirichlet condition will adjust such that equation 2.34 is satisfied as it must. Unfortunately, this pressure gradient may not satisfy the normal momentum equation with the velocity field used in equation 2.33. This inconsistency will not affect the relaxation solution of equation 2.32 but may infect the pressure field in such a way that a global iteration procedure between the PL or MPL equation system and equation 2.32 will not converge.

In other words, $\partial_n p$ based on the momentum equations cannot be used on all boundaries because the compatibility relation is not satisfied by the discretized form of equation 2.32. A Dirichlet condition on one boundary cannot be used because the $\partial_n p$ arising from the solution of equation 2.32 and satisfaction of the compatibility relation will not be consistent with the $\partial_n p$ as determined from the normal momentum equation with the computed velocity field.

Recently, Abdallah (1987) developed a discretization scheme for the Poisson equation such that the compatibility condition is satisfied exactly by the discretized equations. Equation 2.32 was shown to converge using Neumann boundary conditions based on the momentum equations. The Navier-Stokes equation used in this analysis was discretized using a central difference scheme. The me.tod has not been

extended to the backward difference scheme adopted here for the forward-marching solution of the Navier-Stokes equation.

2.6 Conclusion

The PL method was shown to be unconditionally unstable in a multiple pass marching procedure with σ equal to any value other than -1.0. With $\sigma=-1$, a standard forward difference scheme for the streamwise pressure gradient results which has been shown to be globally stable as other investigators have found (see Rubin and Reddy, 1983). The advantage of the standard PL method ($\sigma=-0.01$) is that complex flows can be computed with a single pass of the domain provided a good assumed pressure is given a priori. The success can be directly attributed to the fact that one condition, namely the streamwise pressure gradient condition, was relaxed, due to the small value of σ, in favor of satisfying the global mass flow constraint. This was accomplished by coupling the continuity equation directly to the momentum equations during the solution process.

The global stability of the PL method suffered due to the small value of σ, thus, a modified version of the method (MPL) was developed in an attempt to overcome this lack of global stability. Even with a large coefficient multiplying the pressure gradients, the MPL method was found to be globally unstable. When the Poisson equation for the pressure was introduced, global stability was not assured as the computations proved. It should be noted that the solution of the Poisson equation in three dimensions requires large amounts of computer storage and computation time. This seems to reduce the advantages gained by using parabolic-marching algorithms over time-marching

algorithms. It is evident that a new parabolic-marching method is in order which overcomes the most important hurdle, that of global stability.

CHAPTER 3

NEW PARABOLIC-MARCHING METHOD (NPM)

3.1 Introduction

It was found in the preceeding analysis that the PL method was unconditionally unstable for a global, multiple pass, marching procedure for all σ other than -1. However, if σ is equal to -1, a simple forward difference for the streamwise pressure gradient is recovered with the downstream pressure known from a previous pass of the domain. The maximum eigenvalue of the amplification matrix is unity; thus, the system is stable. This yields a method very similar to that of Rubin and Reddy (1983) except that it is on a regular grid. The problem with such a method is that it is very difficult to compute the first pass of a complex flow unless a very good prescription of the pressure field is given initially. The PL and MPL methods generally have little trouble computing the first pass since one condition is relaxed during the marching process. Recall that in the PL method the streamwise pressure gradient is relaxed and in the MPL method the transverse pressure gradients are relaxed. This allows for a more stable forward-marching process with the continuity equation coupled to the momentum equations.

What is apparent is that the pressure gradients cannot be relaxed in order to achieve a multiple pass procedure that is stable. Yet some condition must be relaxed during the computation in order to solve complex flows. The only condition left to be relaxed in a practical way is continuity.

The method of Chorin (1967), developed for incompressible flow, relaxes the continuity constraint while keeping the equation coupled to the momentum equations. In Chorin's method, an artificial time derivative of the pressure is added to the continuity equation as in the following:

$$1/\beta \ \partial_t p + \nabla \cdot Q = 0$$

(3.1)

where Q is the total velocity vector. This relaxes the continuity constraint during a time-marching integration of the Navier-Stokes equation (see Kwak et. al 1984). At convergence, for steady flows, the computed velocity field is divergence free since $\partial_t p \rightarrow 0$.

Since a parabolic-marching scheme is under consideration here, and no time derivatives are present, the continuity equation must be written in a form other than that in equation 3.1. Successive passes of the domain may be thought of as an advancement in time. With this in mind, the continuity equation is rewritten as:

$$a(p^n - p^{n-1}) + \nabla \cdot Q = 0$$

(3.2)

where n is a global iteration index and a is a coefficient analagous to $1/\beta \Delta t$ in Chorin's method where β is some positive constant. As determined from the eigenvalue analysis performed in section 2.3.1, the streamwise pressure gradient must be forward differenced for stable forward-marching. Therefore, forward differencing of the streamwise pressure gradient and the replacement of the continuity equation with equation 3.2 yields the following form of the governing equation:

$$\partial_x A + \partial_y B + \partial_z C - 1/Re \ (\partial_{yy} D + \partial_{zz} D) = S$$

$$(3.3)$$

$$A = \begin{bmatrix} ap+u \\ u^2+p \\ uv \\ uw \end{bmatrix} \quad B = \begin{bmatrix} v \\ vu \\ v^2+p \\ vw \end{bmatrix} \quad C = \begin{bmatrix} w \\ wu \\ wv \\ w^2+p \end{bmatrix}$$

$$D = \begin{bmatrix} 0 \\ u \\ v \\ w \end{bmatrix} \quad S = \begin{bmatrix} a\partial_x p^n - p_i{}^n + p_i{}^{n-1} \\ 0 \\ \Omega^2 y + 2\Omega w \\ \Omega^2 z - 2\Omega v \end{bmatrix}$$

It should be noted that without the implicit pressure term in the streamwise flux vector, a globally unstable system results.

3.2 Eigenvalue Analysis

The question now arises whether equation 3.3 can be forward-marched in a stable fashion. Using the analysis described in section 2.3.1, for a model two-dimensional problem, the flux vectors A and B are written as:

$$A = \begin{bmatrix} ap+u \\ u^2-p \\ uv \end{bmatrix} \quad B = \begin{bmatrix} v \\ uv \\ v^2+p \end{bmatrix}$$

$$(3.4)$$

The negative sign of the pressure term in A is due to the forward differencing procedure used for the streamwise pressure gradient. With this, the two-dimensional form of equation 3.3 is linearized and written

in frozen coefficient form as:

$$A_J \ \partial_x q + B_J \ \partial_y q - D_J \ \partial_{yy} q = S$$

(3.5)

where A_J, B_J, and D_J are the Jacobians of the vectors A, B, and D, respectively and q is the dependent vector $(p, u, v, w)^T$.

$$A_J = \begin{bmatrix} a & 1 & 0 \\ -1 & 2u & 0 \\ 0 & v & u \end{bmatrix} \qquad B_J = \begin{bmatrix} 0 & 0 & 1 \\ 0 & v & u \\ 1 & 0 & 2v \end{bmatrix}$$

$$D_J = \begin{bmatrix} 0 & 0 & 0 \\ 0 & 1/Re & 0 \\ 0 & 0 & 1/Re \end{bmatrix}$$

For stable forward-marching, the eigenvalues of the matrix $A_J^{-1}D_J$ must be real and non-negative for proper damping. In addition, the eigenvalues of the matrix $A_J^{-1}B_J$ must be real. For the modified flux vector A in equation 3.4, the characteristic equation of $A_J^{-1}D_J$ is:

$$\lambda^3 - \lambda^2 \{1/u + a/(1+2ua)\} + \lambda(1/u)a/(1+2ua) = 0$$

(3.6)

The solution of equation 3.6 gives the folowing eigenvalues:

$$\lambda_1 = 0 \quad , \quad \lambda_2 = 1/u \quad , \quad \lambda_3 = a/(1+2ua)$$

(3.7)

It is apparent that a can be negative and still give a system which is naturally dissipative if u is positive. Since the analogy was drawn to time-marching methods where a looks like $1/\beta \Delta t$, a negative value for a

is not physically realistic. The global stability analysis performed in section 3.3 indicates that a must be non-negative for global stability and convergence. For $A_J^{-1}B_J$, the characteristic equation is:

$$\lambda^3(1+2ua) - \lambda^2\{2av+v/u(1/(1+2ua))\} + \lambda(2av^2/u-1)+v/u = 0$$

$$(3.8)$$

Solution of equation 3.8 gives the following eigenvalues:

$$\lambda_1 = v/u$$

$$\lambda_{2,3} = \{av\pm\sqrt{(av)^2+(1+2ua)^2}\}/(1+2ua)$$

$$(3.9)$$

One can see that the radicand of equation 3.9 is always positive regardless of the value of a; thus, the eigenvalues are all real and forward-marching will be a stable solution technique.

3.3 Global Stability Analysis

The motivation for making the above modification to the governing equation is to develop a marching scheme which is stable in multiple pass mode; thus, the following stability analysis must be performed. Using the Fourier decomposition in equation 2.13 for the discretized equation in 2.12 with the modifications made in equation 3.4, the following relationships result:

$$P_J A^n = H_J A^{n-1}$$

$$(2.14)$$

where

$$P_J = \begin{bmatrix} a(\ell_1+\ell_4) & \ell_1 & \ell_2 \\ -(\ell_1+\ell_4) & 2u\ell_1+v\ell_2-\ell_3 & u\ell_2 \\ \ell_2 & v\ell_1 & u\ell_1+2v\ell_2-\ell_3 \end{bmatrix}$$

and

$$H_J = \begin{bmatrix} a & 0 & 0 \\ -\ell_5 & 0 & 0 \\ 0 & 0 & 0 \end{bmatrix}$$

with

$$\ell_1 = 1 - \cos\theta_x + I\sin\theta_x$$

$$\ell_2 = (\Delta x/\Delta y)\, I\sin\theta_y$$

$$\ell_3 = 2\Delta x\,(\cos\theta_y - 1)/(Re(\Delta y)^2)$$

$$\ell_4 = \cos\theta_x - I\sin\theta_x$$

$$\ell_5 = \cos\theta_x + I\sin\theta_x$$

(3.10)

The amplification matrix G is:

$$G = P_J^{-1}\, H_J = \begin{bmatrix} M_1 & 0 & 0 \\ M_2 & 0 & 0 \\ M_3 & 0 & 0 \end{bmatrix}$$

(3.11)

where

$$M_1 = (a((2u\ell_1+v\ell_2-\ell_3)(u\ell_1+2v\ell_2-\ell_3)-uv\ell_1\ell_2)$$
$$+\ell_5(\ell_1(u\ell_1+2v\ell_2-\ell_3)-v\ell_1\ell_2))/|P_J|$$

$$M_2 = (a((\ell_1+\ell_4)(u\ell_1+2v\ell_2-\ell_3)+u\ell_2^2)$$

$$-\ell_5(a(\ell_1+\ell_4)(u\ell_1+2v\ell_2-\ell_3)-\ell_2^2))/|P_J|$$

$$M_3 = (a(-(\ell_1+\ell_4)v\ell_1-\ell_2(2u\ell_1+v\ell_2-\ell_3))+\ell_5(a(\ell_1+\ell_4)v\ell_1-\ell_1\ell_2))/|P_J|$$

$$|P_J| = a(\ell_1+\ell_4)((2u\ell_1+v\ell_2-\ell_3)(u\ell_1+2v\ell_2-\ell_3)-uv\ell_1\ell_2)$$

$$+\ell_1((\ell_1+\ell_4)(u\ell_1+2v\ell_2-\ell_3)+u\ell_2^2)$$

$$-\ell_2((\ell_1+\ell_4)v\ell_1+\ell_2(2u\ell_1+2v\ell_2-\ell_3))$$

The eigenvalues of G are then:

$$\lambda_1 = M_1$$

$$\lambda_{2,3} = 0$$

$$(3.12)$$

The maximum value of λ_1 can be determined by setting $\theta_x = \theta_y = \pi$ which gives:

$$|\lambda_1| = |1-2/[a(2u+c)+1]|$$

$$(3.13)$$

where $c = 2\Delta x/Re/(\Delta y)^2$

Therefore, if a is non-negative, the maximum eigenvalue is always less than unity regardless of the value of c. Thus, the scheme appears to be unconditionally stable in multiple pass mode. From equation 3.13, one can determine that the lower bound for a is zero. For a less than zero, the maximum eigenvalue is greater than unity and the error will grow without bound. This is not surprising since a is analagous to $1/\beta\Delta t$ in time-marching methods. For completeness, the stability characteristics for all wave numbers for various combinations of parameters should be studied. Again let $u=v=1$ and $Re=1000$ and plot the real part of $\lambda^*\lambda_1$ for all wave numbers in Figure 3.1 for a arbitrarily
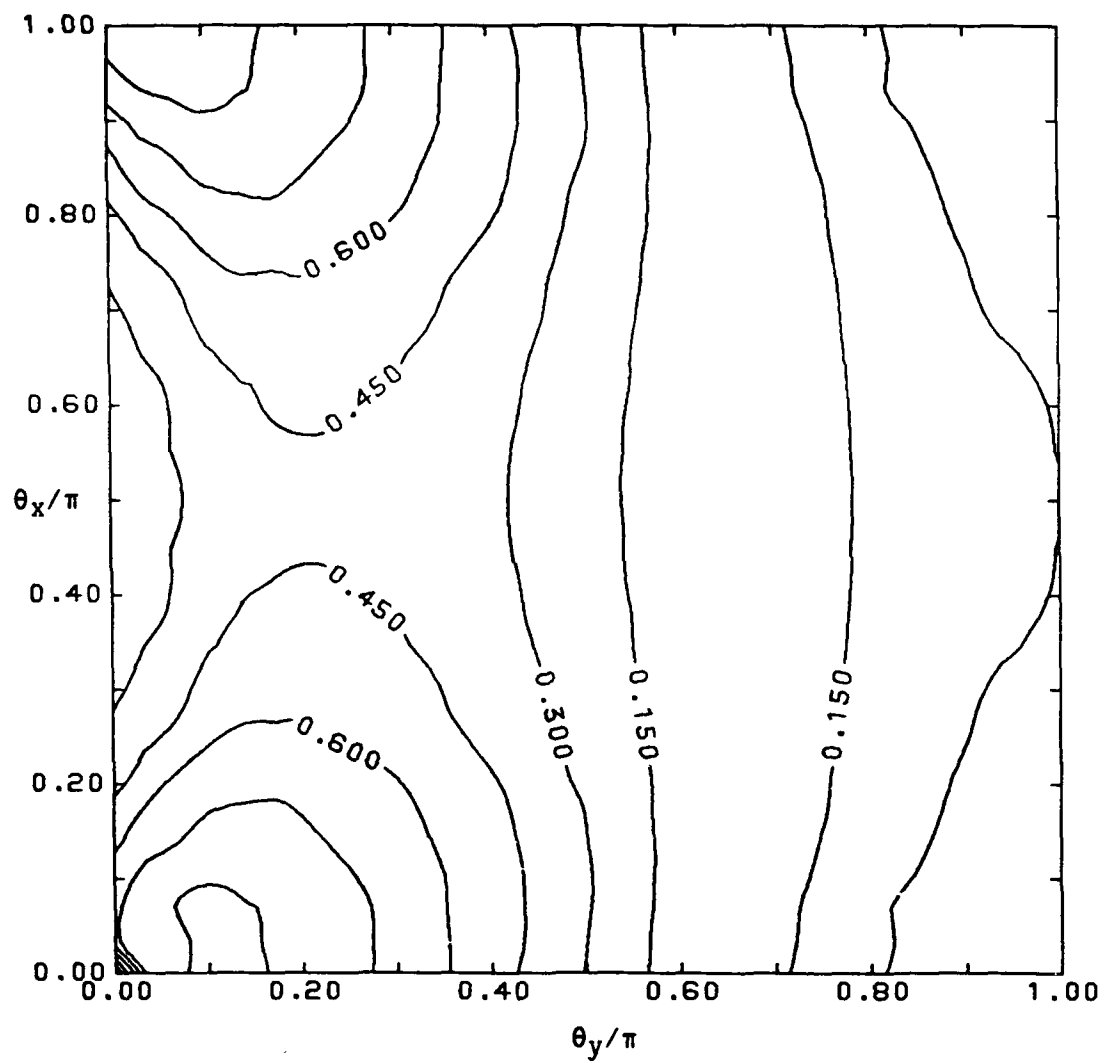
Figure 3.1 Real part of $\lambda^*\lambda_1$, a=0.2, for all wave numbers for the NPM method (u=v=1,Δx=Δy=1,Re=1000)

set to 0.2. With this set of parameters, one can see that the method is stable for all wave numbers. The maximum values of $\lambda^*\lambda_1$ occur at the limits of the frequency spectrum. The minimum values are found near $\theta_y/\pi \approx 0.6$. With the ratio u/v changed from unity, the stability characteristics do not change. Also not an important parameter is the Reynolds number which was changed from 10 to 10^6 with no significant difference in the stability characteristics. With the ratio $\Delta x/\Delta y = 0.01$, the stability characteristics are plotted in Figure 3.2. It is evident that the maximums are now confined to $\theta_y/\pi = 0$ and 1, however, the scheme is stable everywhere. The minimums are still found near $\theta_y/\pi \approx 0.6$. With $\Delta x/\Delta y$ set to 100, the stability characteristics are much different (see Figure 3.3). The maximum values of $\lambda^*\lambda_1$ are now confined to a very thin region for θ_x/π less than 0.01 and greater than 0.99. Large values of a should severely underrelax the dependent variables as does a small Δt in a time-marching method. The value of a was varied from 1 to 100 and the differences in the global stability characteristics are given in Figure 3.4. One can see that there is no value of $\lambda^*\lambda_1$ greater than unity so that the system is stable for a multiple pass solution procedure.

The above analysis was performed for a two-dimensional system and it was assumed that the results were applicable to three-dimensions. For completeness, the stability analysis should be performed for three-dimensions. Recall that:

$$P_J A^n = H_J A^{n-1}$$

$$(2.14)$$

where P_J and H_J are now given as:

Figure 3.2 Real part of $\lambda^*\lambda_1$, a=0.2, for all wave
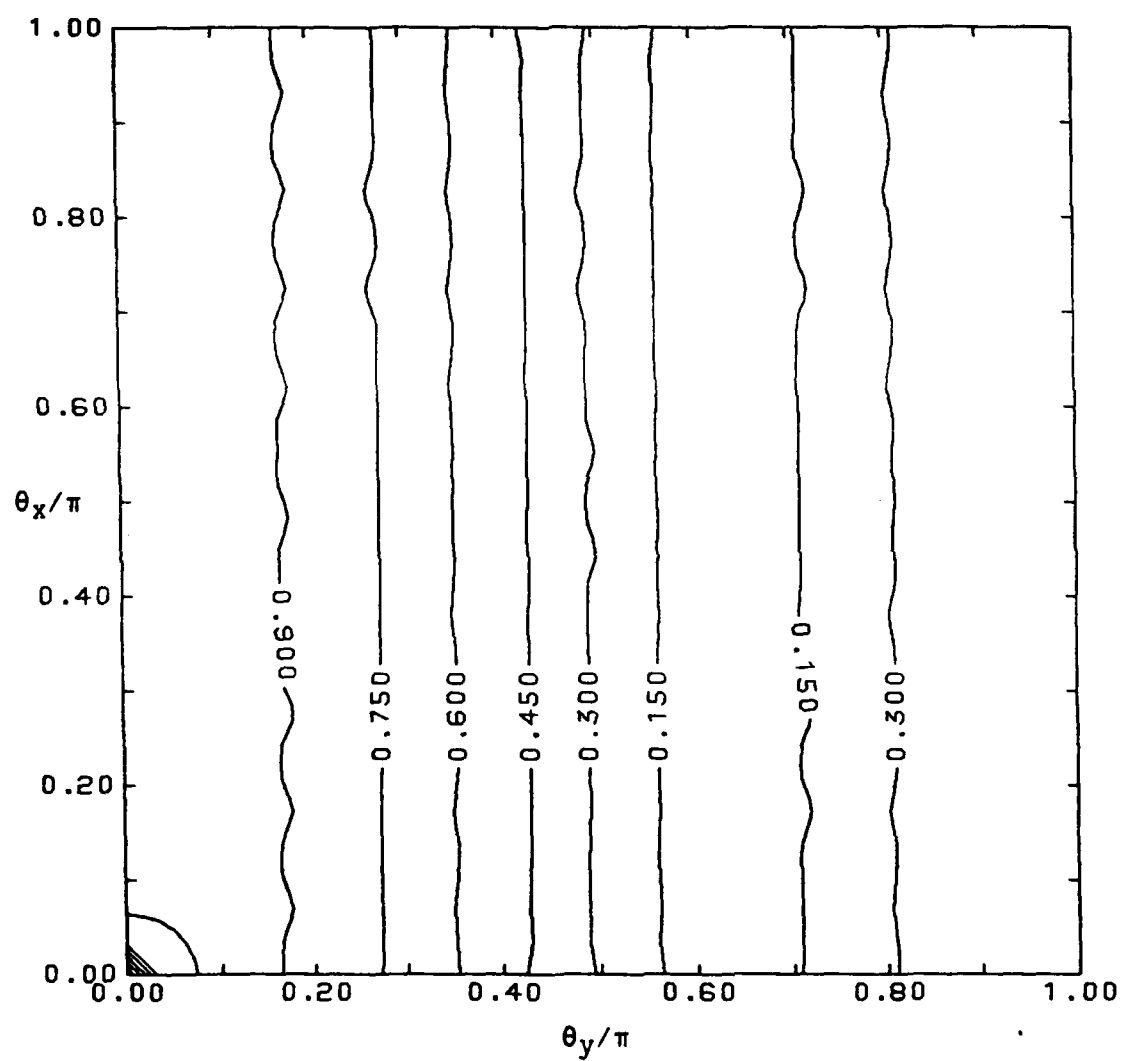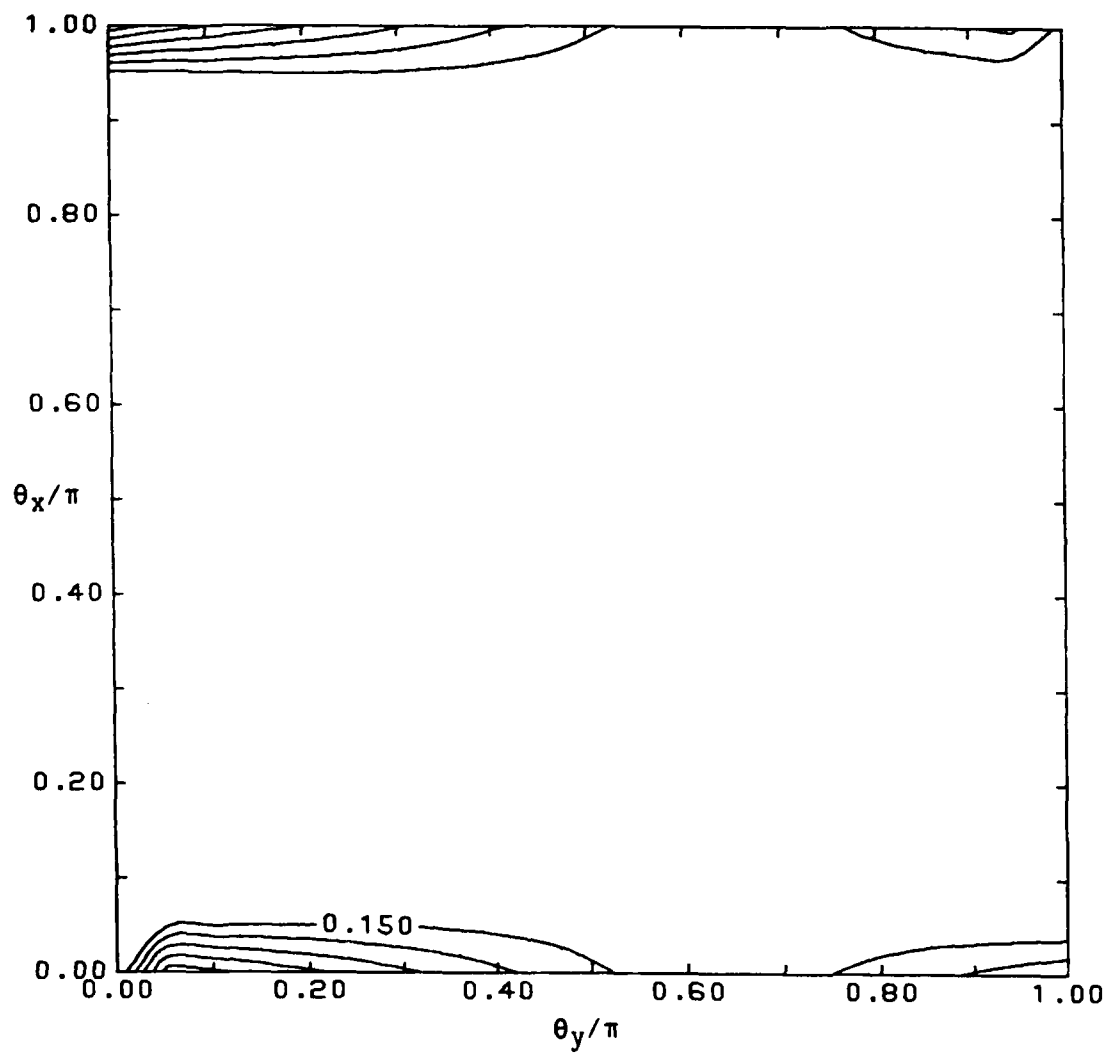numbers for the NPM method (u=v=1,Δx=0.01 Δy=1,Re=1000)

Figure 3.3 Real part of $\lambda^*\lambda_1$, a=0.2, for all wave numbers for the NPM method (u=v=1,Δx=100 Δy=1,Re=1000)

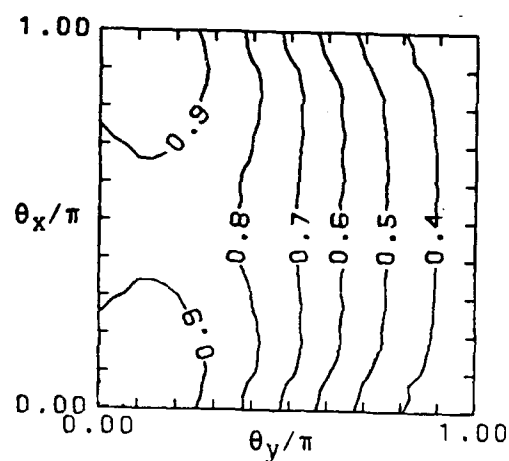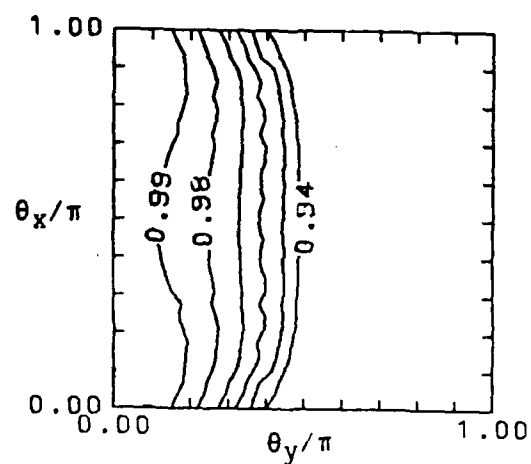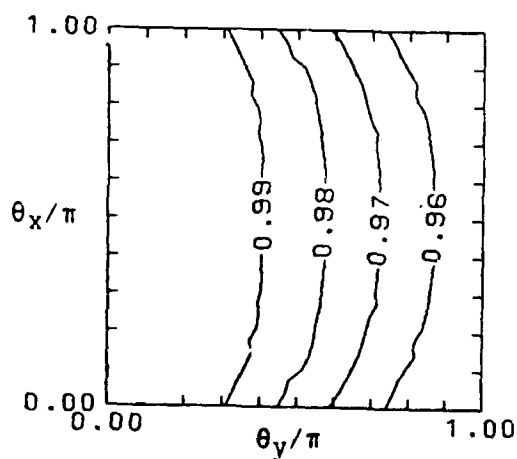a) a= 1

b) a= 5

c) a= 20
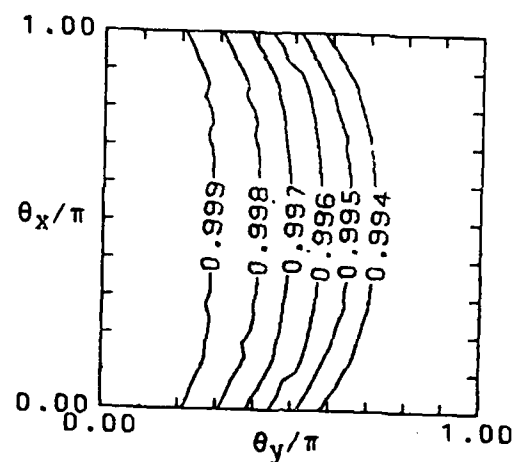
d) a= 100

Figure 3.4 Real part of $\lambda^{*}\lambda_1$ for various values of a, for all wave numbers for the NPM method ($u=v=1, \Delta x=\Delta y=1, Re=1000$)

$$H_J = \begin{bmatrix} a & 0 & 0 & 0 \\ -\ell_5 & 0 & 0 & 0 \\ 0 & 0 & 0 & 0 \\ 0 & 0 & 0 & 0 \end{bmatrix}$$

and

$$P_J = \begin{bmatrix} a & \ell_1 & \ell_2 & \ell_6 \\ -1 & 2u\ell_1+v\ell_2+w\ell_6-\ell_3-\ell_7 & u\ell_2 & u\ell_6 \\ \ell_2 & v\ell_1 & u\ell_1+2v\ell_2+w\ell_6-\ell_3-\ell_7 & v\ell_6 \\ \ell_6 & w\ell_1 & w\ell_2 & u\ell_1+v\ell_2+2w\ell_6-\ell_3-\ell_7 \end{bmatrix}$$

where $\ell_{1,2,3,4,5}$ are defined in equation 2.15 and

$$\ell_6 = (\Delta x/\Delta z) \ I \sin \theta_z$$

$$\ell_7 = 2\Delta x \ (\cos \theta_z - 1)/(Re(\Delta z)^2)$$

For $\theta_x = \theta_y = \theta_z = \pi$ the maximum value of λ_1 is

$$|\lambda_1| = |1 - 2/[a(2u+c+d)+1]|$$

(3.13a)

where $c = 2\Delta x/Re/(\Delta y)^2$ and $d = 2\Delta x/Re/(\Delta z)^2$. Thus, if a is positive, the system in three-dimensions is stable for multiple passes. Since the discretization of the governing equation is consistent, by Lax's theorem one may state that the system is also convergent. In actual practice, no method is always convergent for complex turbulent flows, however, confidence is high that the new method will outperform both the PL and MPL methods.

3.4 Convergence of the Method

It is important to show that the method is able to converge to machine precision to show that artificial energy losses are not introduced with the introduction of the pressure term in the continuity equation. The developing laminar flow in a straight duct with square cross section was computed on a coarse grid with a=0.01. The resulting convergence history is given in Figure 3.5. Convergence to machine precision (1 x 10^{-16} on the IBM 3090-200) is achieved and no divergent behavior is apparent. Regarding convergence rates, it is known that the value of the maximum eigenvalue sets the convergence rate of the global iteration process. That is,

$$e^n/e^{n-1} \simeq 1/|\lambda_1| = 1/\rho(G)$$

$$(3.14)$$

where $\rho(G)$ is the spectral radius of the amplification matrix G. Thus, if λ_1 is minimized, the rate of convergence will be maximized. It is apparent that equation 3.13 can be minimized if:

$$a = 1/(2u+c)$$

$$(3.14a)$$

For u=v=1, Re= 1000, $\Delta x=\Delta y=1$, the optimum value of a is 0.5. This may reduce the largest value of the eigenvalue but comparison of Figures 3.1 and 3.6 shows that for other wave numbers, the eigenvalues for a=0.5 are generally higher than for a=0.2. Therefore, the apparent optimum value of a may not yield the fastest convergence. Similarly for three-dimensions, the optimum value for a is:

Figure 3.5   Convergence History to Machine Precision

Figure 3.6 Real part of $\lambda^{*}\lambda_1$, a=0.5, for all wave numbers for the NPM method (u=v=1, $\Delta x=\Delta y=1$, Re=1000)

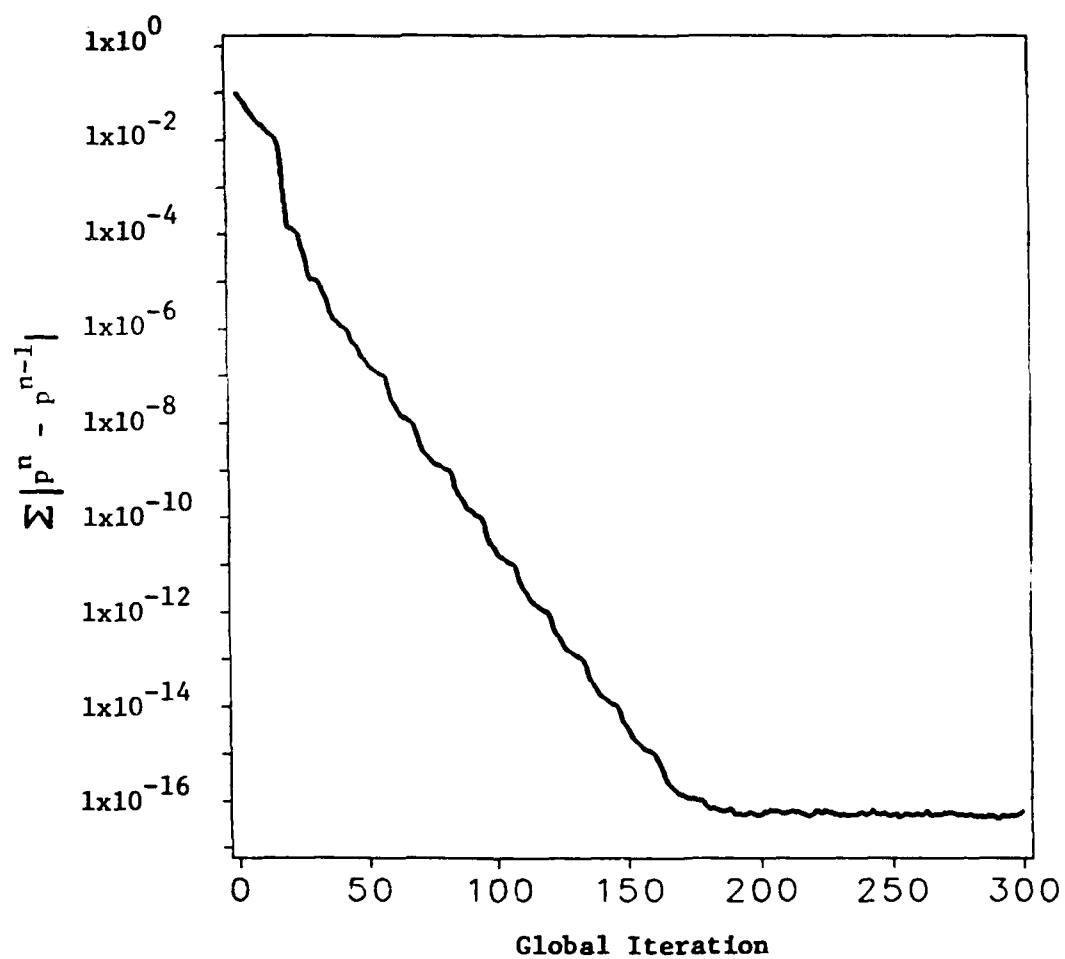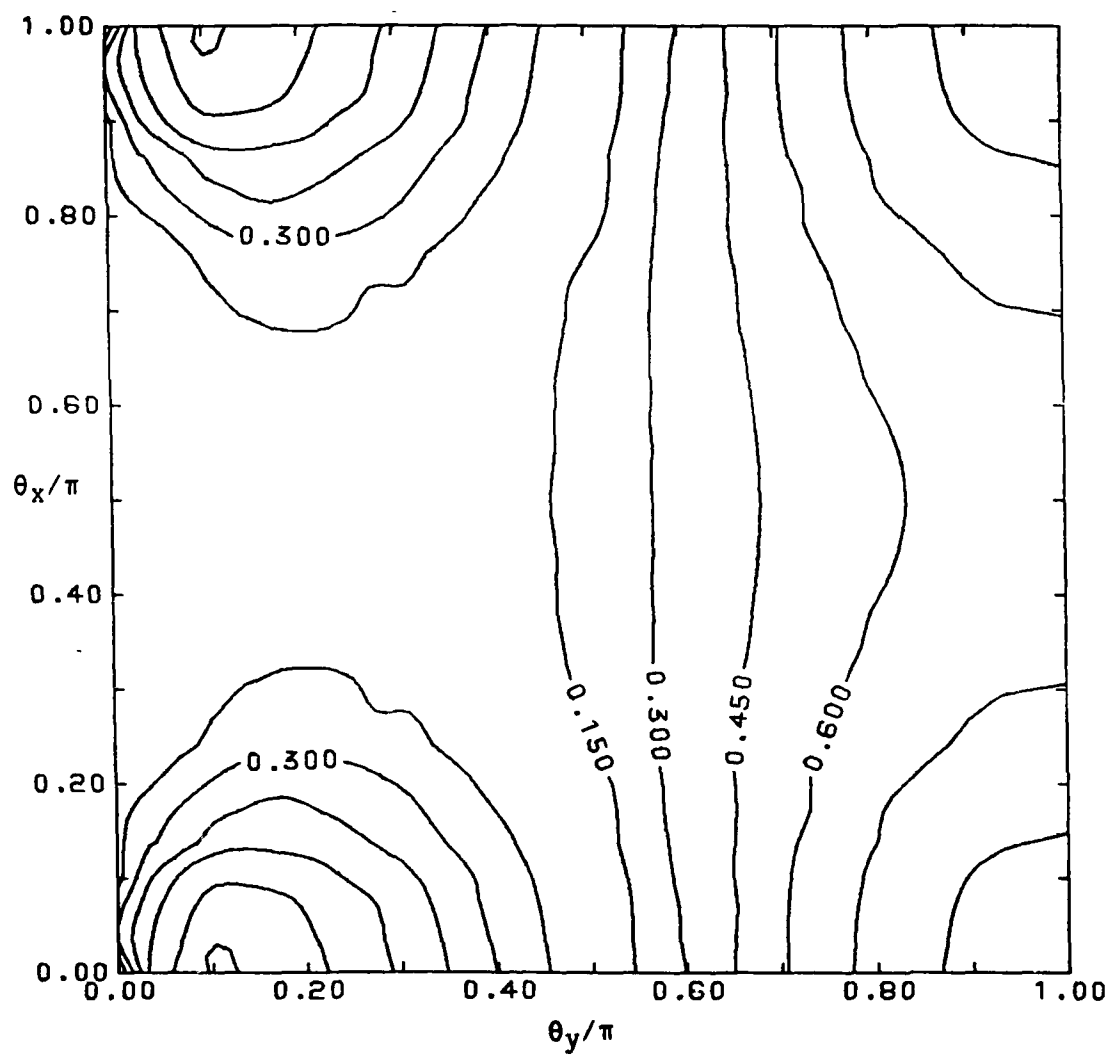$$a = 1/(2u+c+d)$$

<div align="right">(3.14b)</div>

A problem with parabolic-marching methods in general is that, since pressure information propagates upstream only one streamwise step per global pass, the downstream pressure boundary condition will not influence the inlet flow until the same number of passes as streamwise steps is made. Also, small wave length errors, order Δx, are damped out quickly while large wave length errors, order $N\Delta x$, are damped out at a much slower rate rate or not at all. Because of this, convergence of any parabolic-marching method is very slow and the NPM method is no different.

One technique for accelerating the convergence of the numerical method is the multigrid procedure of Brandt (1977). In incorporating this into the NPM technique, the multigrid procedure would be applied in the streamwise direction only. The coarse grid equations would be solved on grids with a progressively increasing aspect ratio. While this does not reduce the stability of the NPM method as seen in section 3.3, it may severely decrease accuracy if the prolongation operation of the multigrid is not performed perfectly. Rubin and Reddy (1983) have used multigrid with their parabolic-marching method but the improvement in convergence does not seem to be worth the extra computational effort.

Another method for accelerating the convergence of a parabolic-marching method was recently developed by Tenpas and Pletcher (1987). Their method solves a modified Poisson equation for a pressure correction with a single backward pass of the domain after each forward-marching pass of the mean flow equations. A variable coefficient multiplies the transverse pressure gradient in the Poisson equation

which is different for each case. The increase in convergence is impressive but results for a flow with large transverse pressure gradients have not been published by them and one must wonder what the influence is of the modified transverse pressure gradient in the Poisson equation.

3.5 Transformation and Discretization of the Equation

In order to implement boundary conditions in a straightforward fashion for complex geometries, it is desirable to solve the governing equation on a generalized coordinate system. Therefore, the equations solved must be recast into the generalized coordinates using the following transformation:

$$\xi = \xi(x,y,z)$$
$$\eta = \eta(x,y,z)$$
$$\zeta = \zeta(x,y,z)$$

The full equation, 2.1, is transformed using a chain rule conservative formulation. The Cartesian velocity components and the pressure are still the dependent variables, however, the equation is now solved on a generalized coordinate system. The modifications made to equation 2.1 in the x-direction which yielded equation 3.3 are now made in the streamwise ξ-direction giving the following relation:

$$L_\xi + L_\eta + L_\zeta - 1/(J\ Re)\ (\ L_{\eta\eta} + L_{\zeta\zeta}) = -1/(J\ Re)\ I_{\eta\zeta} + S'/J$$

$$(3.15)$$

where

$$L_\xi = (\xi_x \partial_\xi A' + \xi_y \partial_\xi B' + \xi_z \partial_\xi C')/J$$

$$L_\eta = (\eta_x \partial_\eta A + \eta_y \partial_\eta B + \eta_z \partial_\eta C)/J$$

$$L_\zeta = (\zeta_x \partial_\zeta A + \zeta_y \partial_\zeta B + \zeta_z \partial_\zeta C)/J$$

$$L_{\eta\eta} = \eta_x \partial_\eta \{(1+\nu_t)\eta_x \partial_\eta D\} + \eta_y \partial_\eta \{(1+\nu_t)\eta_y \partial_\eta D\} + \eta_z \partial_\eta \{(1+\nu_t)\eta_z \partial_\eta D\}$$

$$L_{\zeta\zeta} = \zeta_x \partial_\zeta \{(1+\nu_t)\zeta_x \partial_\zeta D\} + \zeta_y \partial_\zeta \{(1+\nu_t)\zeta_y \partial_\zeta D\} + \zeta_z \partial_\zeta \{(1+\nu_t)\zeta_z \partial_\zeta D\}$$

$$L_{\eta\zeta} = \eta_x \partial_\eta \{(1+\nu_t)\zeta_x \partial_\zeta D\} + \eta_y \partial_\eta \{(1+\nu_t)\zeta_y \partial_\zeta D\} + \eta_z \partial_\eta \{(1+\nu_t)\zeta_z \partial_\zeta D\}$$
$$+ \zeta_x \partial_\zeta \{(1+\nu_t)\eta_x \partial_\eta D\} + \zeta_y \partial_\zeta \{(1+\nu_t)\eta_y \partial_\eta D\} + \zeta_z \partial_\zeta \{(1+\nu_t)\eta_z \partial_\eta D\}$$

where J is the Jacobian of the transformation given by:

$$J = \xi_x(\eta_y \zeta_z - \eta_z \zeta_y) - \eta_x(\xi_y \zeta_z - \xi_z \zeta_y) + \zeta_x(\xi_y \eta_z - \xi_z \eta_y)$$

$$(3.16)$$

and ν_t is the eddy viscosity described in chapter IV. Also notice that the cross derivative term $L_{\eta\zeta}$ is held explicitly since the Linearized Block Implicit (LBI) solution procedure of Briley and McDonald (1980) cannot treat such terms implicitly.

The vectors in equation 3.15 are:

$$A' = \begin{bmatrix} ap+u \\ u^2-p \\ uv \\ uw \end{bmatrix} \qquad B' = \begin{bmatrix} v \\ vu \\ v^2-p \\ vw \end{bmatrix} \qquad C' = \begin{bmatrix} w \\ wu \\ wv \\ w^2-p \end{bmatrix}$$

$$A = \begin{bmatrix} u \\ u^2+p \\ uv \\ uw \end{bmatrix} \qquad B = \begin{bmatrix} v \\ vu \\ v^2+p \\ vw \end{bmatrix} \qquad C = \begin{bmatrix} w \\ wu \\ wv \\ w^2+p \end{bmatrix}$$

$$D= \begin{bmatrix} 0 \\ u \\ v \\ w \end{bmatrix} \qquad S'= \begin{bmatrix} \xi_x a(p_i^{n-1}-p_{i-1}^n) \\ -\xi_x(p_{i+1}^{n-1}-p_{i-1}^n) \\ -\xi_y(p_{i+1}^{n-1}-p_{i-1}^n) + \Omega^2 y + 2\Omega w \\ -\xi_z(p_{i+1}^{n-1}-p_{i-1}^n) + \Omega^2 z - 2\Omega v \end{bmatrix}$$

Equation 3.15 is discretized using a two point backward difference scheme for streamwise derivatives and a three point central difference scheme for all transverse derivatives. A linearized form of the governing equation is obtained by using truncated Taylor series about i-1 as follows:

$$A_i = A_{i-1} + \partial_q A \, \Delta q$$

$$(3.17)$$

where $\partial_q A$ is the Jacobian denoted by A_J and Δq is the streamwise change in the dependent vector.

$$\Delta q = [\Delta p, \Delta u, \Delta v, \Delta w]^T$$

$$(3.18)$$

$$\Delta q = q_i - q_{i-1}$$

$$(3.19)$$

When equation 3.17 is applied to all the vectors in equation 3.15 except S, the standard delta form of the discretized equation results giving:

$$(L_\xi \cdot + L_\eta \cdot + L_\zeta \cdot) \, \Delta q_i = R$$

$$(3.20)$$

where

$$L_\xi = \text{convection terms in } \xi\text{-direction}$$

L_η = convection and diffusion terms in η-direction

L_ζ = convection and diffusion terms in ζ-direction

R = terms from Euler implicit differencing and cross
derivative diffusion terms

The operator on the left side of equation 3.20 is split into two components which yields block tridiagonal matrices which can be solved easily. Solving for Δq in this way is the basic LBI scheme of Briley and McDonald (1980) which is essentially ADI for a vector system. The method is second order accurate in the transverse plane but first order accurate in the streamwise direction. Full second order accuracy can be obtained using three-point backward differences for the streamwise gradients. Since truncated Taylor series are used to discretize the governing equation and no averaging is used, the discretization is consistent by definition. The method does, however, introduce an inconsistency in the form of a splitting error.

3.6 New Solution Procedure

3.6.1 Splitting Error in LBI Scheme

The discretized Navier-Stokes equation appears to be second order accurate. However, when using the LBI scheme of Briley and McDonald (1980), a splitting error arises which may reduce the overall accuracy of the method. When the LBI scheme is applied to a space-marching method, the splitting error not only reduces accuracy but may destroy the solution due to an inconsistency in the splitting error. This error can be examined by using the PL method. Equation 2.2 can be written in frozen coefficient form as:

$$(A_J \cdot + \Delta\xi B_J \partial_\eta \cdot + \Delta\xi C_J \partial_\zeta \cdot) \Delta q = R$$

(3.21)

The diffusion terms are neglected to simplify the analysis. Equation 3.21 is generated using an Euler implicit differencing technique and the operator on the left-hand side must be split to obtain matrices which can be inverted easily. The split can be carried out in one of the following two ways.

System one

first solve $(A_J \cdot + \Delta\xi B_J \partial_\eta \cdot) \Delta q^* = R$

then solve $(A_J \cdot + \Delta\xi C_J \partial_\zeta \cdot) \Delta q = A_J \Delta q^*$

(3.22)

which is the system used by Pouagare and Lakshminarayana (1986), or

System two

first solve $(A_J \cdot + \Delta\xi C_J \partial_\zeta \cdot) \Delta q^* = R$

then solve $(A_J \cdot + \Delta\xi B_J \partial_\eta \cdot) \Delta q = A_J \Delta q^*$

(3.23)

When system one and two are recombined, their respective splitting errors are:

System one

The splitting error $= \Delta\xi^2 (B_J A_J^{-1} C_J) \partial_\eta \cdot \partial_\zeta \cdot \Delta q$

(3.24)

System two

The splitting error $= \Delta\xi^2 (C_J A_J^{-1} B_J) \partial_\eta \cdot \partial_\zeta \cdot \Delta q$

$$(3.25)$$

The splitting errors in equations 3.24 and 3.25 are equivalent if and only if the matrices B_J and C_J are commutative matrices which they are not in general. This was recognized by Briley and McDonald (1980) but was not considered to be a problem since, for time-marching methods, the splitting errors are multiplied by a time change in the dependent vector which tends to zero for steady flows. For parabolic-marching methods, the splitting error is multiplied by the streamwise change in the dependent vector which seldom goes to zero. Thus, the splitting error goes to zero only if the streamwise grid is refined. Refining the grid by one order of magnitude will give a two order reduction in the splitting error. Recall though, that adding ten times more streamwise grid lines could increase the number of global iterations of a parabolic-marching scheme by as much as thirty times. Also, a more refined grid, while giving increased accuracy will require much more computer time per global iteration. The magnitude of this error is unknown and so should be investigated.

The matrix multiplication found in equations 3.24 and 3.25 can be performed for the PL method.

For system one

$$
B_J \, A_J^{-1} C_J =
\begin{bmatrix}
0 & 0 & w/u & 0 \\
0 & 0 & w & v \\
0 & w/\sigma & 2wv/u & -u/\sigma \\
v/u & 0 & w^2/u & vw/u
\end{bmatrix}
$$

$$(3.26)$$

For system two

$$
C_J \, A_J^{-1} B_J =
\begin{bmatrix}
0 & 0 & 0 & v/u \\
0 & 0 & w & v \\
w/u & 0 & wv/u & v^2/u \\
0 & v/\sigma & -u/\sigma & 2vw/u
\end{bmatrix}
$$

(3.27)

Recall that the order of the equations is continuity, x-, y-, z-momentum; thus, the error is the same for the x-momentum equation and very similar for the y- and z-momentum equations. However, the error in the continuity equation is much different between the two systems.

With the elements of Δq being roughly the same, if v is much larger than w as would be the case for a duct curving in the x-y plane, then one expects system one to give a smaller error in the continuity equation than system two and thus better results. This observation will be born out in section 3.6.3. One other problem that should be noted is that, since a forward-marching procedure is under consideration, the error will build up with each marching step. There is no mechanism to reduce the error as the computation progresses.

3.6.2 New Solution Method

The error can be significantly reduced by iterating equation 3.21 at each streamwise station. For convenience the equation under consideration, i.e., equation 3.20, is repeated here.

$$
(\, L_\xi{}^\bullet \, + L_\eta{}^\bullet \, + L_\zeta{}^\bullet \,) \, \Delta q_i = R
$$

(3.28)

An iterative form of 3.28 can be written as:

$$(L_{\xi} \cdot + L_{\eta} \cdot + L_{\zeta} \cdot) \Delta s_i{}^m = R'$$

$$R' = R - (L_{\xi} \cdot + L_{\eta} \cdot + L_{\zeta} \cdot) \Delta q_i{}^{m-1}$$

$$(3.29)$$

where $\Delta s_i{}^m = \Delta q_i{}^m - \Delta q_i{}^{m-1}$ with m as an iteration index and R' being the solution to the Navier-Stokes equation within the formal accuracy of the discretization.

The operator on the left side of equation 3.29 can now be split as in the LBI scheme, however, the splitting error is reduced with each iteration at streamwise station i since $\Delta s_i{}^m$ tends to zero. To improve convergence, $\Delta q_i{}^m$ is updated using the following relationship.

$$\Delta q_i{}^m = \Delta q_i{}^{m-1} + \omega \, \Delta s_i{}^m$$

$$(3.30)$$

where ω is an underrelaxation parameter which usually is set to a value of 0.7.

The solution procedure for equation 3.29 is as follows. At streamwise station i, the operator in equation 3.29 is split using either system one or two using R' as determined from the previous streamwise station and the value of $\Delta q_i{}^{m-1}$; for the first iteration this is the converged value of Δq at i-1. With the right-hand side known, equation 3.29 is solved for $\Delta s_i{}^m$ which is used to update $\Delta q_i{}^m$ using equation 3.30. The procedure is repeated until Δs drops at least two orders of magnitude. Such convergence is usually achieved in five iterations. After convergence, the procedure is advanced to the next streamwise station and repeated until the entire domain is computed. In short, the splitting error is iterated out of the solution at each streamwise station and thus the discretized system retains its formal

second order accuracy.

3.6.3 Error in Curved Duct Flow

In order to examine the effect of the splitting error and the ability of the new solution method to reduce it, the laminar flow in Taylor et al.'s (1981) strongly curved duct was computed. The geometry is given in Figure 3.7. The radius of curvature R_c is 2.3D and the flow Reynolds number based on D and the bulk inlet velocity is 790. The inlet velocity field was interpolated from the available experimental data and a radial pressure gradient based on simple radial equilibrium was used as the assumed pressure for the PL method. The marching procedure was started at the inlet plane $\phi = 0^0$ and progressed to $\phi = 78^0$. The computational grid included 21 points in the radial direction, 11 points from the lower wall to the symmetry plane and $\Delta\phi = 2^0$. Recall that the major motivation for the new solution method is to maintain a high degree of accuracy with a coarse grid for improved convergence of the parabolic-marching method. The afore mentioned splitting error is small for fine grids. Indeed, the prediction of this flow by Pouagare and Lakshminayana (1986), reprinted in Figure 3.8, is very accurate for a grid of 41 by 21 in the cross plane and $\Delta\phi = 0.5^0$, nearly 15 times as many points as the present computation. The method used by Pouagare and Lakshminarayana is equation 3.28 using the system one splitting procedure. This method was used as well as that using the splitting procedure of system two on the coarse grid and compared to the results obtained by the new iterative solution method.

Computed streamwise and transverse velocity profiles at $\phi = 77.5^0$ are presented in Figures 3.9 and 3.10, respectively. Careful
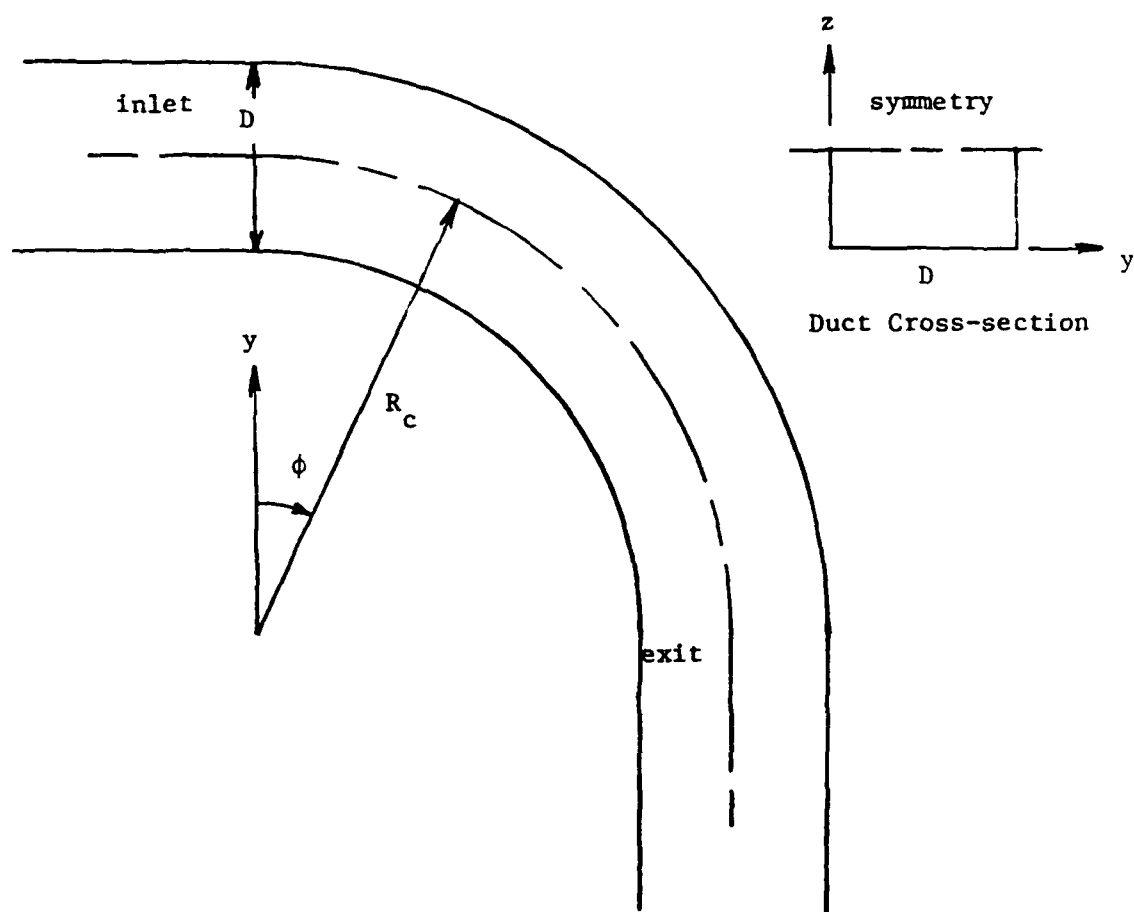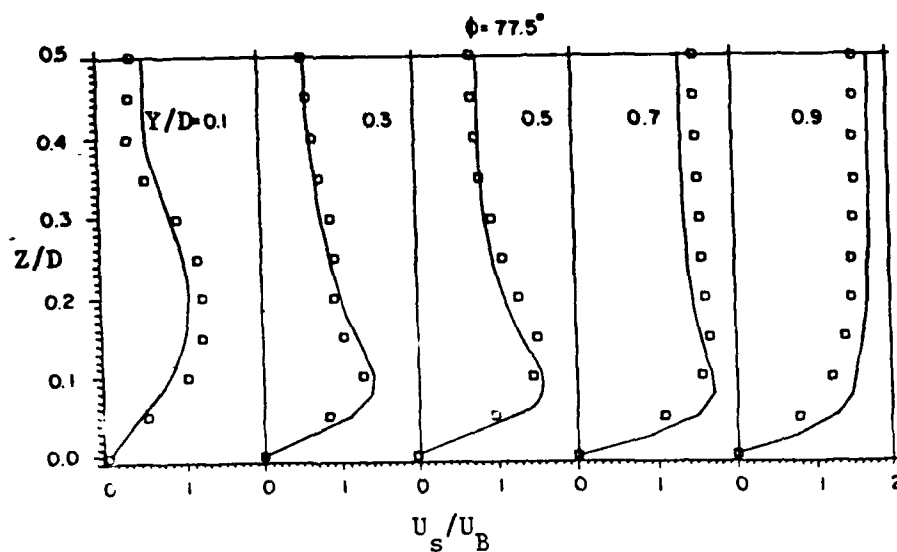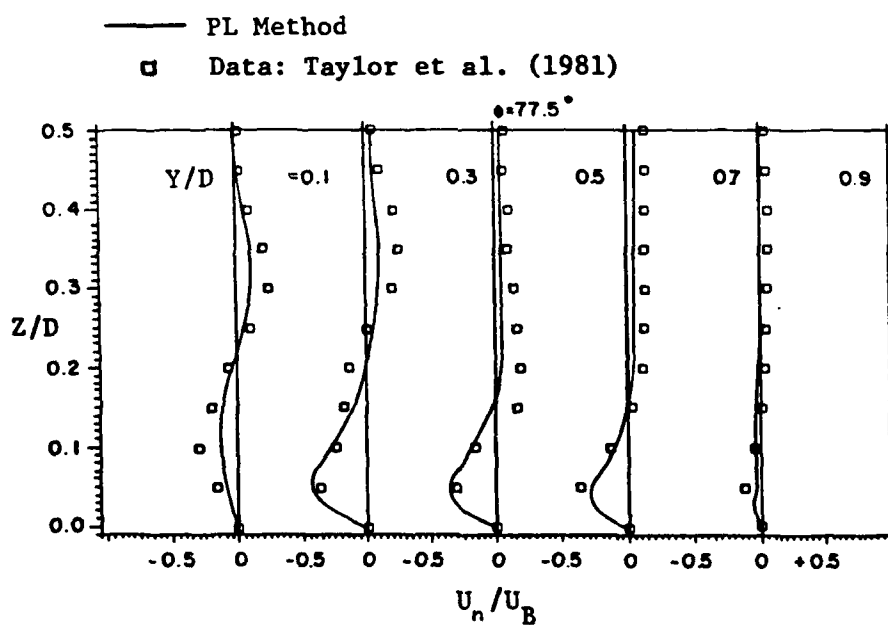
Figure 3.7 Strongly Curved Duct Geometry

a) Computed streamwise velocity profiles

——— PL Method

◻ Data: Taylor et al. (1981)

b) Computed transverse velocity profiles

Figure 3.8 Fine Grid Results of Pouagare and Lakshminarayana (1986)
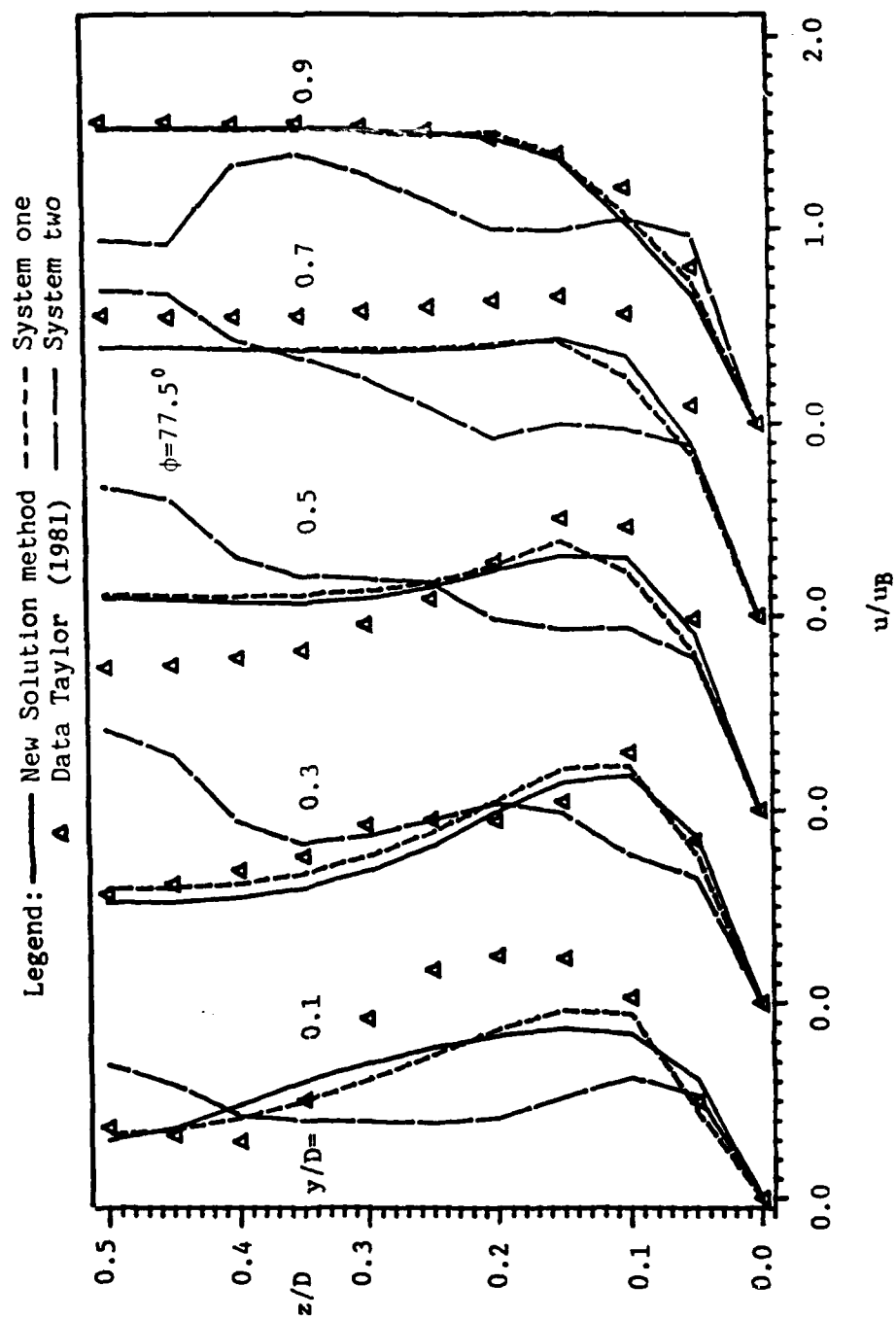for the Strongly Curved Duct Flow

Figure 3.9 Computed Streamwise Velocity Profiles for the Strongly
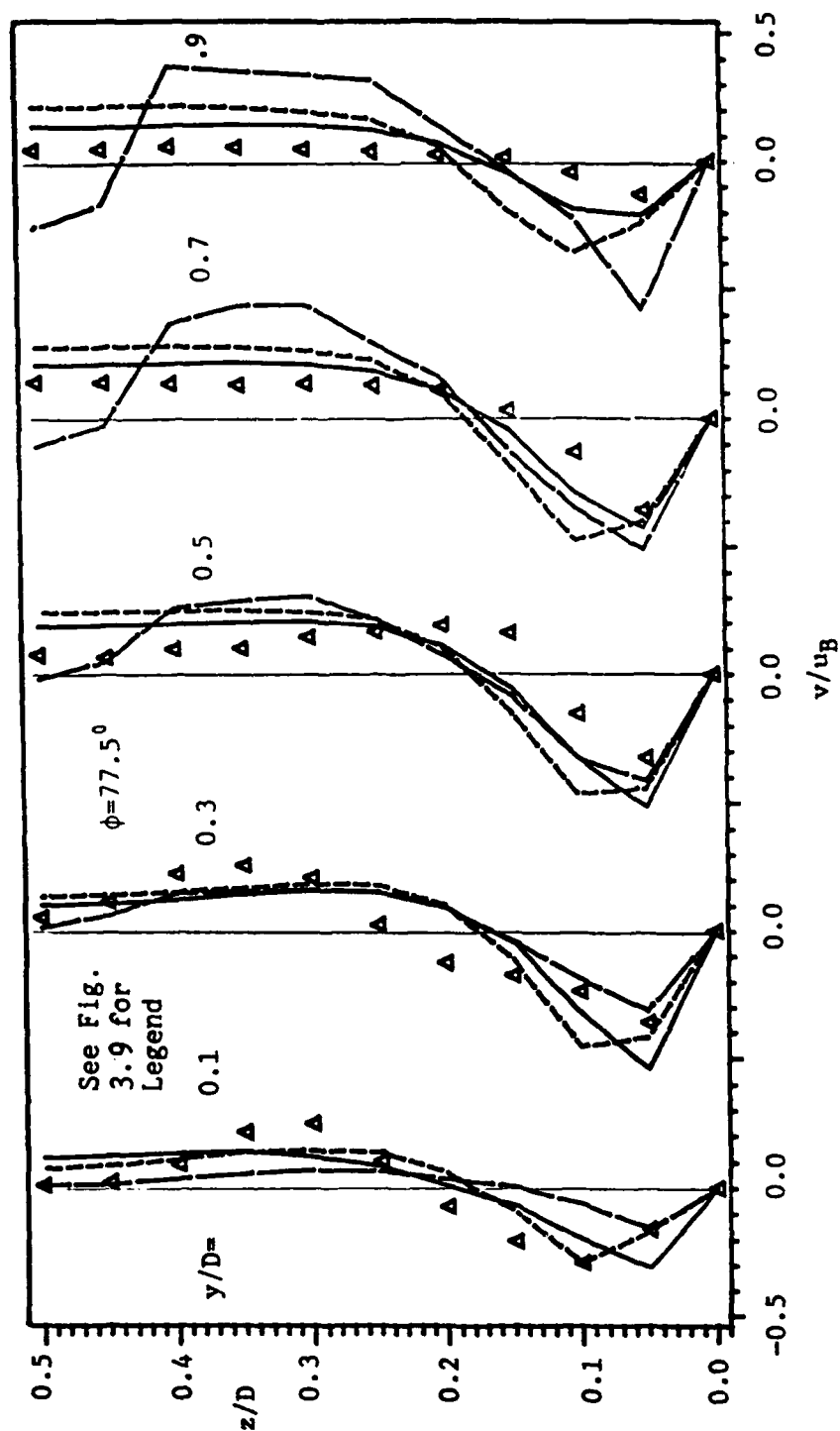
Curved Duct Flow, PL method

Figure 3.10 Computed Transverse Velocity Profiles for the Strongly
Curved Duct Flow, PL method

examination of the results shows the pronounced effect of the splitting error. The results using system one agree reasonably well with the experimental data as does those cf the new solution method. The results from using system two are very poor as was predicted from the analysis in the previous section. The difference between the two systems is quite dramatic and is due soley to the effect of the splitting error. The new solution method produces results closer to the experimental data especially in the secondary flow predictions. Note the large deviation from the data at $y/D = 0.9$ in Figure 3.10 for system one while the results of the new solution procedure compare very well.

The residual in the continuity equation is plotted in Figure 3.11 verses the streamwise station for the three methods of splitting the operator. Notice that the residual for system one is much less than for system two as anticipated, however, the error is clearly unbounded as the computation is carried farther downstream. On the other hand, the error in the continuity equation using the new iterative solution method is much lower and remains low. It is evident from this result that the extra computational effort required by the new solution method is justified.

The convergence history of the iterative LBI scheme at a typical streamwise station for this flow is given in Figure 3.12. Strong convergence is exhibited for all variables. It should be noted that system one and two were used in alternative iterations and is the reason for the small spikes in the convergence history. Clearly, one splitting system is better suited to this flow but the iterative scheme still converges.
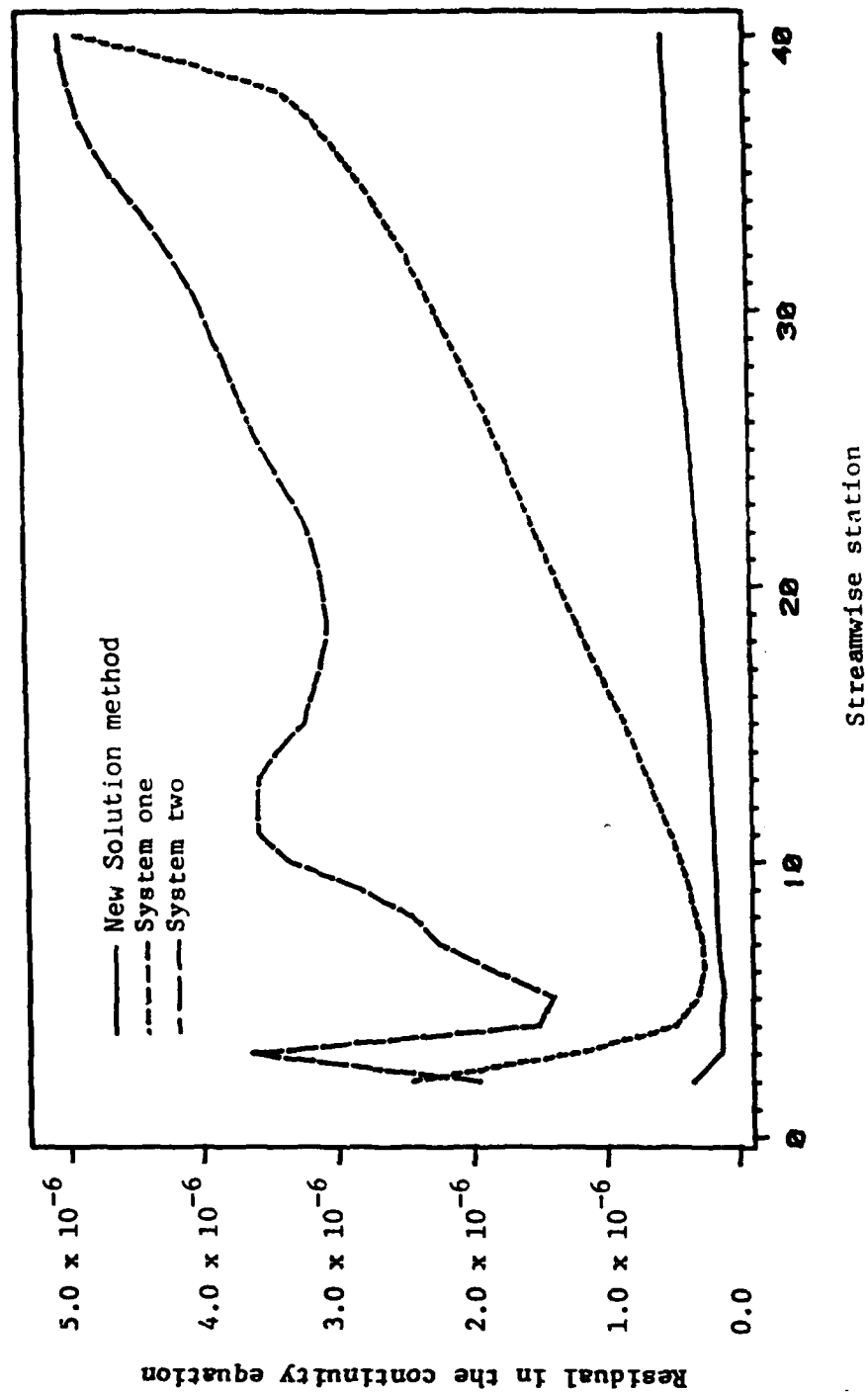
Figure 3.11 Computed Residual in the Continuity Equation
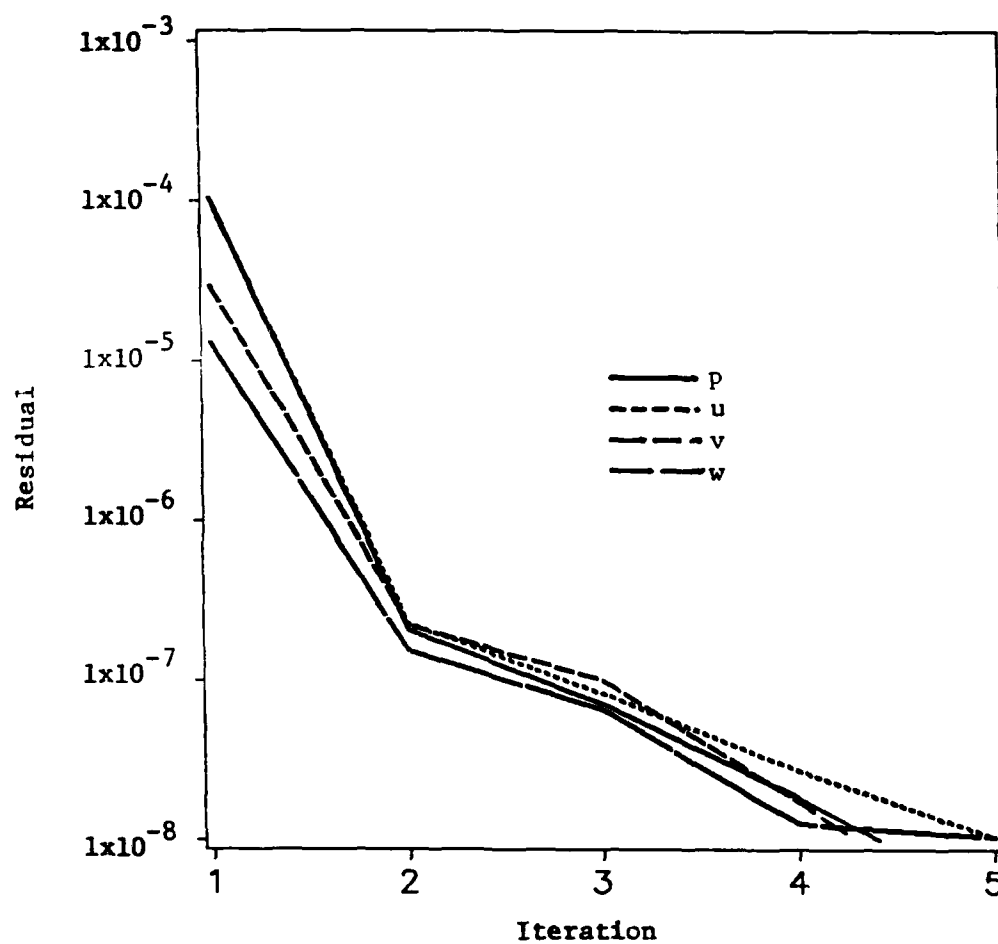
for the Three Solution Methods

Figure 3.12 Convergence History for the Iterative LBI Scheme

3.7 Boundary Conditions

For the internal turbomachinery problems for which the NPM method was developed, only four different boundary conditions are considered. First, the no-slip boundary condition is the proper boundary condition for viscous flow near a solid boundary. For such a condition, all velocities are set to zero on the boundary with the normal gradient of the pressure set to zero following boundary layer theory. A two point backward difference scheme is used for the pressure gradient condition in order to couple the odd and even points more strongly (see Pouagare and Lakshminarayana (1986)). This condition is always used for laminar flows. Second, for turbulent flows, the no-slip condition may also be used. However, under special circumstances, namely high turbulance intensities with a coarse grid, a turbulent slip velocity must be used. This slip velocity is based on the log law-of-the-wall and is determined as follows:

$$Q_{wall} = Q_p - u*/\kappa$$

$$(3.31)$$

where Q is the total velocity, κ is the von Karman constant, and u* is the friction velocity determined from the following relationship:

$$Q_p/u* = 5.8 \log y^+ + 5.0$$

$$(3.32)$$

where $y^+ = Re\ u*\ n_p$

$$(3.33)$$

n_p is the normal distance from the boundary to the first grid point. This condition is carefully applied so that the resultant velocity

component is tangent to the boundary surface.

Third, on a symmetry plane, the normal gradient of the velocities tangent to the plane, one of which is the streamwise component, is set to zero. The velocity component normal to the plane of symmetry is also set to zero. The normal pressure gradient is set to zero across the symmetry boundary. A two point backward difference scheme is employed for these gradient conditions both implicitly and explicitly.

Finally, for most of the turbomachinery flows investigated here, there are substantial regions of the flow which are spacially periodic. Thus, a periodic boundary condition is used upstream and downstream of a blade row. This condition can be enforced in several ways. First, the condition can be enforced implicitly. This requires the solution of a periodic matrix which can be solved using a recursive formula. The matrix has the form:

$$
\begin{bmatrix}
b & c & & & & a \\
a & b & c & & & \\
& & \cdot & \cdot & \cdot & \\
c & & & & a & b
\end{bmatrix}
$$

Without artificial dissipation, central difference schemes notoriously produce uncoupled solutions. The solution of the equations with implicit periodic boundary conditions exacerbates the odd even uncoupling.

Second, the periodic condition can be applied explicitly. The computational domain can be extended to include the periodic line on both sides of the domain. The value of q computed at the previous iteration in the transverse plane is used as boundary conditions outside

the periodic lines. Thus, two different values of q might be computed on the periodic line, an upper and a lower value. To maintain periodicity, the upper and lower values are averaged to give the value of q on the periodic line. This slows convergence of the iterative scheme in the transverse plane but periodicity must be enforced. Uncoupling of the odd and even points is not as severe when the explicit condition is applied. It should be noted that for coupling purposes, the normal pressure gradient equals zero condition is always applied implicitly regardless of which boundary condition is used. Experience has shown that there is no great loss in accuracy, even in periodic regions, when this condition is used, however, the coupling of the odd and even points is greatly enhanced.

At the inlet plane, only the velocity components are needed as inlet boundary conditions. This inlet field can be generated from available experimental data. Downstream, only the pressure is used as a boundary condition and so needs to be specified. Since the flow is incompressible, the level of pressure is not important but the transverse pressure gradients downstream should be correct, i.e., match the experimental data or analysis.

3.8 Algorithm Verification

The NPM algorithm must be calibrated for convergence and accuracy on a simple laminar flow before one can have faith in its ability to predict the complex, turbulent flow in a turbomachine. The most simple yet non-trivial laminar flow that can be computed is the developing flow in a straight duct with a square cross-section. Once a successful computation of this flow has been achieved, the laminar flow in an S-

shaped duct of square cross-section is computed since this flow is characterized by large streamwise variations in the transverse pressure gradients as well as large secondary flows. These characteristics are also found in most turbomachinery flows.

3.8.1 Developing Laminar Flow in a Straight Duct

For this case the Reynolds number based on the duct width was set to 50. The domain was extended to 6 duct widths downstream where fully developed flow should be present. A grid density of 21x21 points was used in the cross-plane while 25 points were used in the streamwise direction. Exponential stretching was used to pack grid points near the entrance region. A uniform inlet profile was used to start the marching process and a unifrom pressure field was used as the downstream pressure boundary condition. For these conditions, the optimum value for a is computed by equation 3.14b is a=0.2. The value of a was varied from 0 to 0.4 in order to study its effect on the rate of convergence. Figure 3.13 shows the convergence history for a = 0, 0.01, 0.2 and 0.4. It is evident that for the initial passes, convergence is faster for a not equal to zero as the analysis professed. Overall, the fastest convergence was achieved with a=0.0. This is not suprising since the normal pressure gradients are essentially zero and the satisfaction of the global mass flow constraint, through continuity, is the driving mechanism in this particular flow. Therefore, with a=0.0, convergence should be achieved in as many global iterations as there are streamwise points which is indeed the case. Still, with a not equal to zero, convergence is achieved (initially at a faster rate) but clearly a=0.2 is not the optimum value. This gives credence to the observation that,
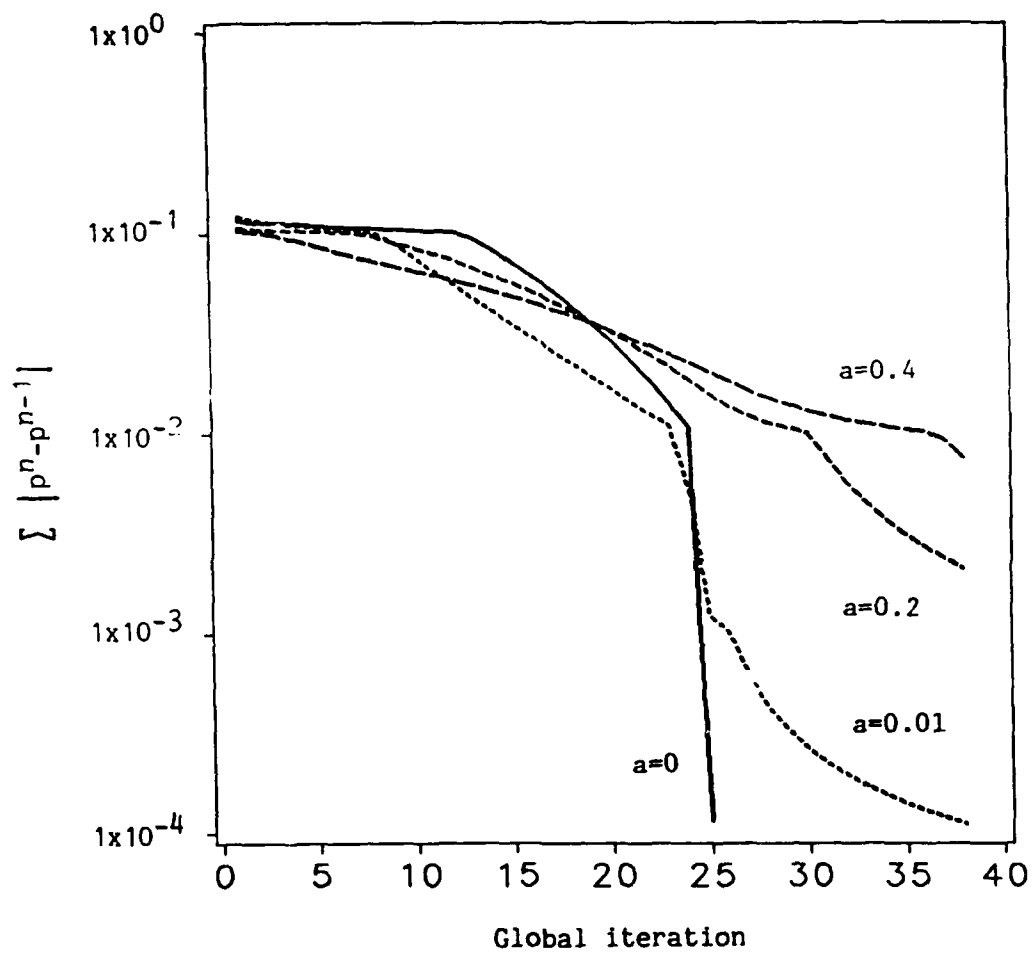
Figure 3.13 Convergence History for the Straight Duct

while an optimum value for a apparently can be computed for one set of wave numbers in the spectrum, it may not be the optimum value for all wave numbers.

The computed centerline coefficient of pressure and the centerline velocity are compared to the analytical results (see White (1974)) in Figures 3.14 and 3.15, respectively. One can see that the computed coefficient of pressure compares favorably with the analytical results except very near the duct entrance. The computed centerline velocity compares well with the analytical results only far from the entrance. In the entrance region, the velocity profiles tend to bulge near the walls of the duct reducing the momentum in the center of the duct. This is most likely due to the development of spurious transverse pressure gradients which suppress the diffusion of momentum from near the wall to the center of the duct. This did not occur when the PL technique was used by Pouagare and Lakshminarayana (1986). This is because in the PL technique, the small value of σ essentially removes the effect of the transverse pressure gradients from the computation. These spurious transverse pressure gradients are not large and diminish to zero past the entrance region. Grid refinement in the entrance region should be all that is necessary to reduce this problem. In the fully developed flow region, the exact centerline velocity is computed and the computed velocity profiles compare very well to the analytical results in Figure 3.16. These results did not change for the various values of a. This proves that at convergence, the continuity equation is satisfied within the accuracy of the discretization everywhere and the global mass flow is conserved.
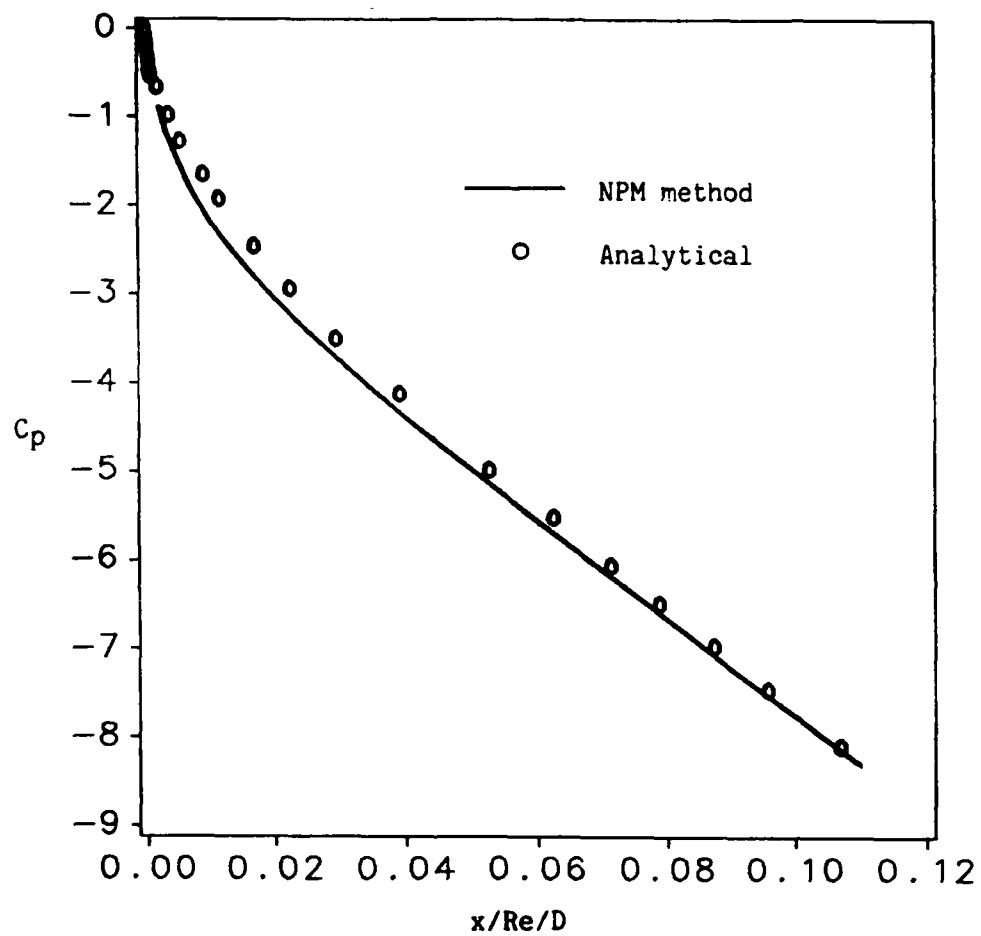
Figure 3.14   Computed Centerline Coefficient of Pressure
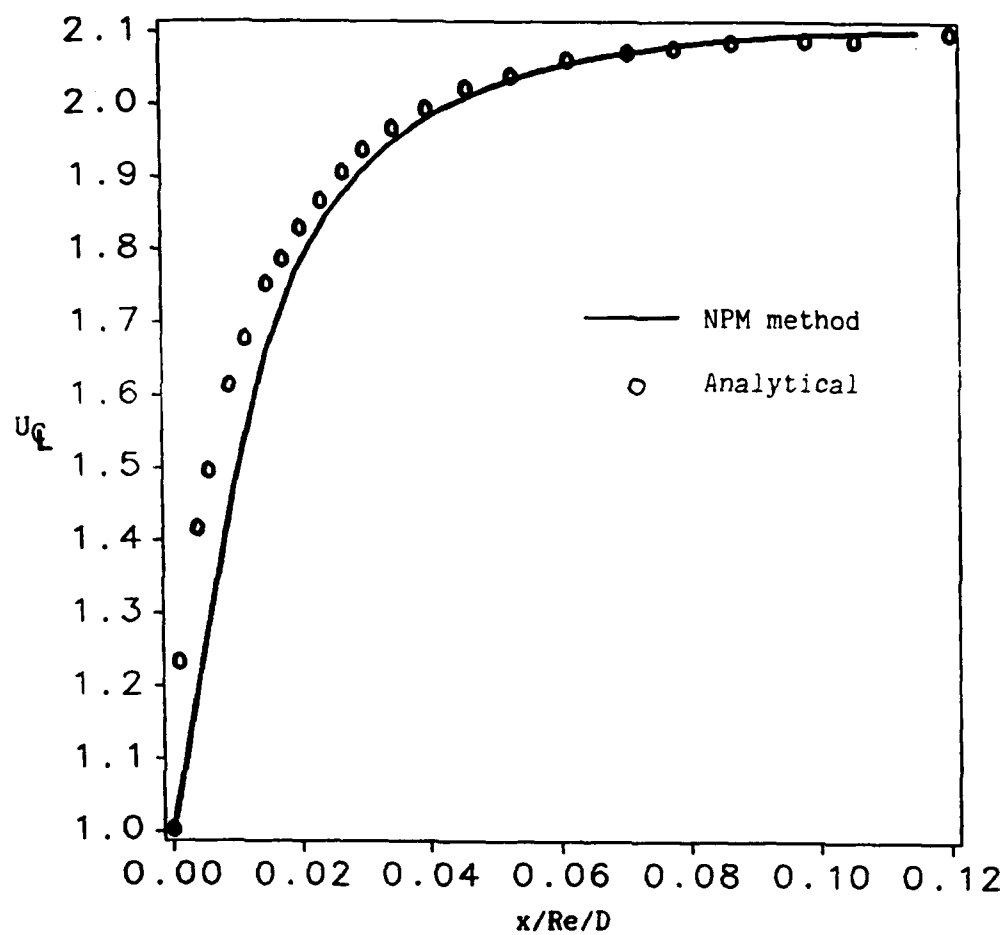
for the Straight Duct

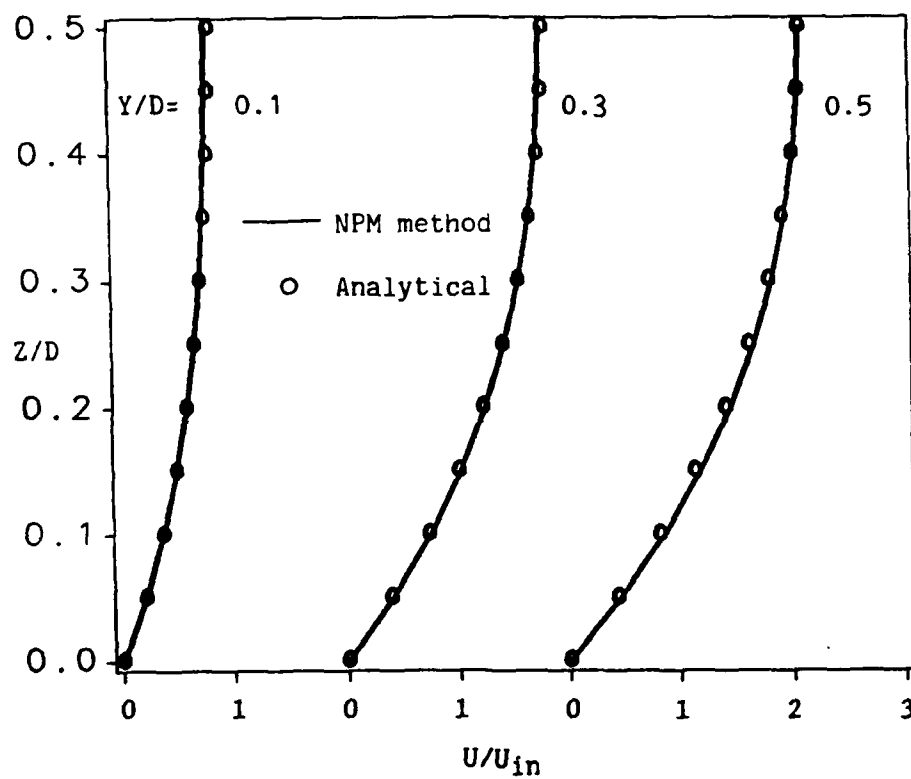Figure 3.15   Computed Centerline Velocity for the Straight Duct

Figure 3.16   Computed Fully Developed Velocity Profiles

for the Straight Duct

3.8.2 Laminar Flow in an S-Shaped Duct

The entry flow in a straight duct, while not trivial, is not characterized by a streamwise variation in the transverse pressure gradients as is a typical turbomachinery flow. Thus, the laminar flow in an S-shaped duct was computed to determine the NPM method's ability to resolve the large variations in the transverse presure gradients as well as the strong secondary flows present. The flow was measured by Taylor et al. (1982) using a laser Doppler velocimeter. The geometry is given in Figure 2.9 along with the measurement locations. The radius of curvature was 7D to the center of the duct. The Reynolds number based on the bulk inlet velocity U_B and the duct width D was 790. The computational domain extended from $X_H = -2.5$ to 8.0 and from zero to D in both the Y and Z directions. The comptuational grid consisted of 47 points in the streamwise direction spaced evenly and a 25 by 21 grid was used in the cross-plane with exponential stretching included to pack the grid points near the walls. The inlet conditions were determined by computing the developing flow in the entrance region up to $X_H=-2.5$ using the PL technique.

Recall that for the developing flow in a straight duct, the best convergence was achieved with a=0.0. With a=0.0, the governing equation is essentially unmodified and the method is no different than the PL method with $\sigma=-1.0$. However, with no assumed pressure distribution, the computation could not progress to the end of the domain successfully with a=0.0. With a set to 5.0, however, the computation was successful. Figure 3.17 shows the convergence history for a=5.0. Convergence to two orders of magnitude were achieved in 140 global iterations. Total CPU time on the IBM 3090-200 at The Pennsylvania State University was 1.87
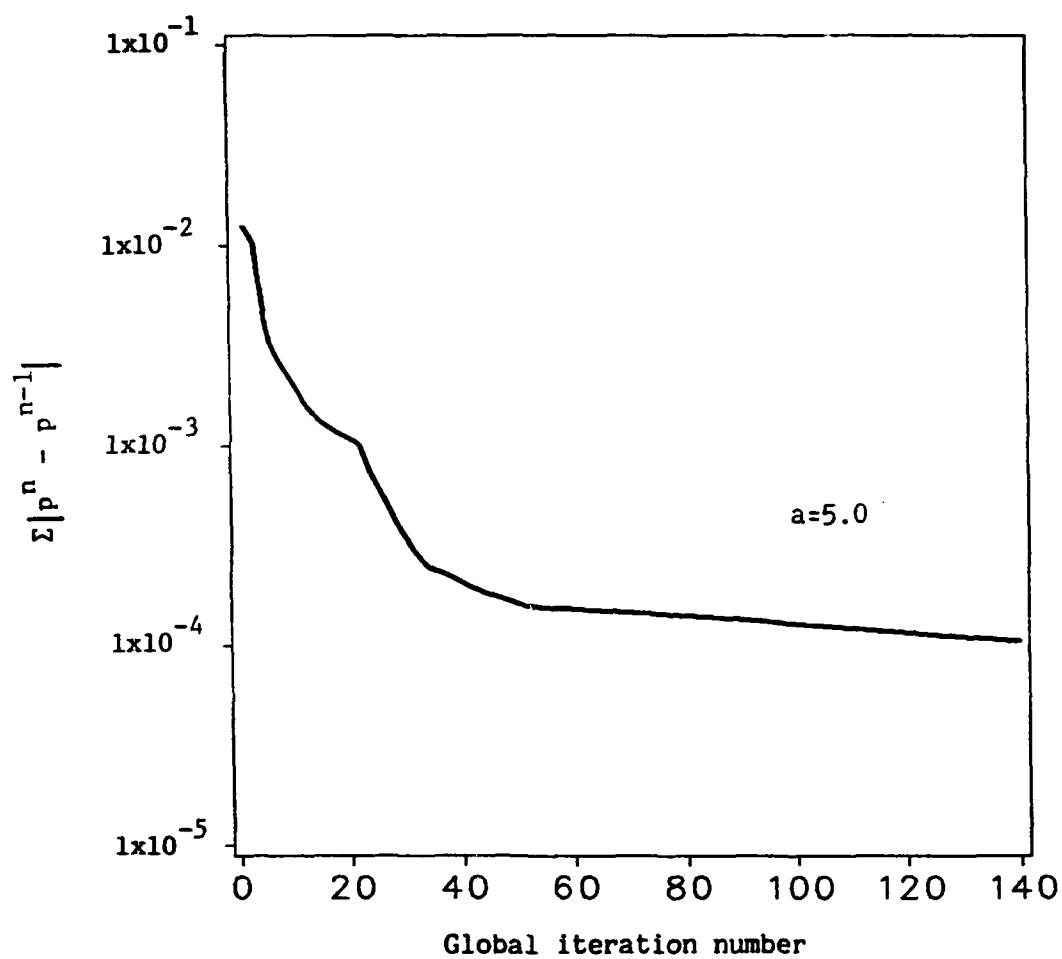
Figure 3.17   Convergence History for the S-Duct

hours or 0.00195 seconds per point per global iteration.

Figure 3.18 shows the computed pressure distribution for the S-duct. No experimental data is available for the C_p distribution for the laminar flow but the computed head loss is very close to that for the developing flow in a straight duct with the same inlet conditions. The results are certainly qualitatively correct with a negative transverse pressure gradient in the upward curving region switching to a positive gradient as the duct turns back. Indeed, when comparing the computed C_p to that measured for turbulent flow (see Figure 2.14), the fine details of the distribution agree very well qualitatively.

The computed velocity profiles are compared to the experimental data in Figures 3.19 through 3.26. The agreement between the computation and the experimental data is excellent in all regions of the flow. At station 1, just upstream of the initial bend, the computed velocity field is no longer symmetric and a small secondary velocity exists owing to the transverse pressure gradient effect. Since streamwise ellipticity was reduced to first order in the NPM method, it is apparent that the pressure ellipticity is sufficient for an accurate prediction for this type of flow. At station 2, a strong secondary flow is developing due to the influence of the centrifugal force and the end wall boundary layer. This is typical in turbomachinery blade rows. Again, agreement with the experimental data is excellent at all measurement locations. At station 4, the reversal of the secondary flow due to the change in sign of the transverse pressure gradient has begun. Also apparent is the bulge in the streamwise velocity profile at $Y/D=0.7$ indicating the center of the secondary vortex. Again the method accurately predicts all these flow phenomena. Finally at station 5, the
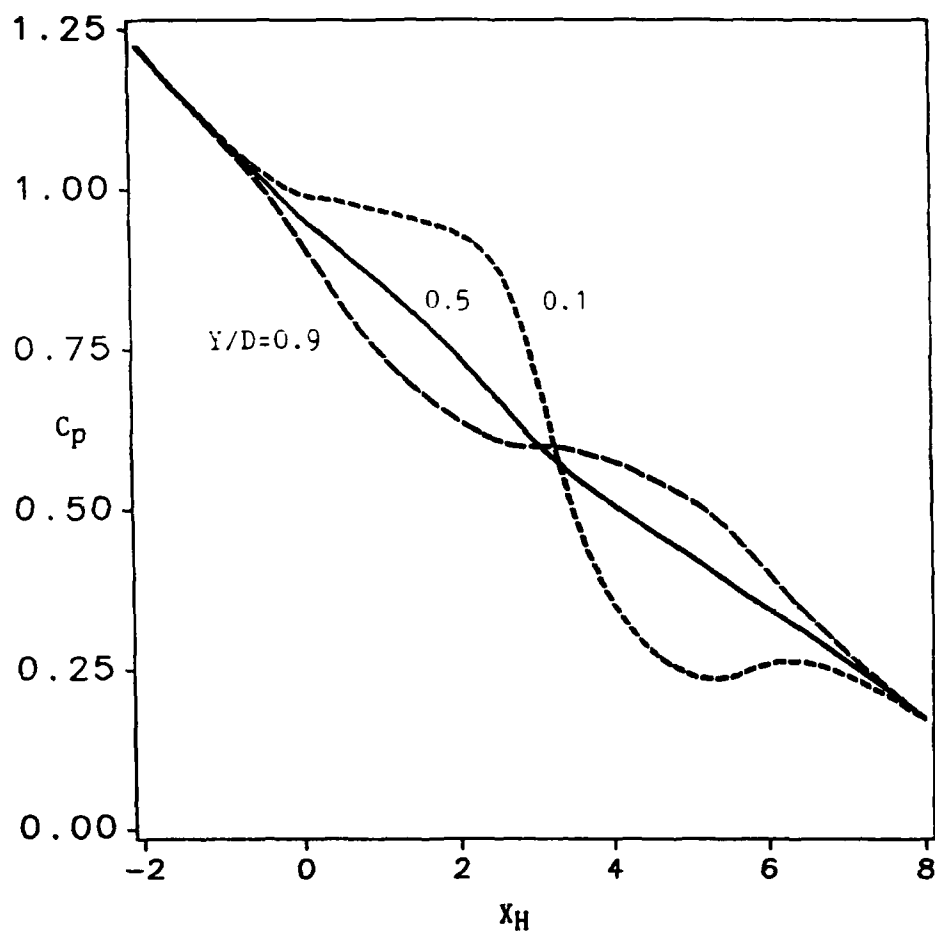
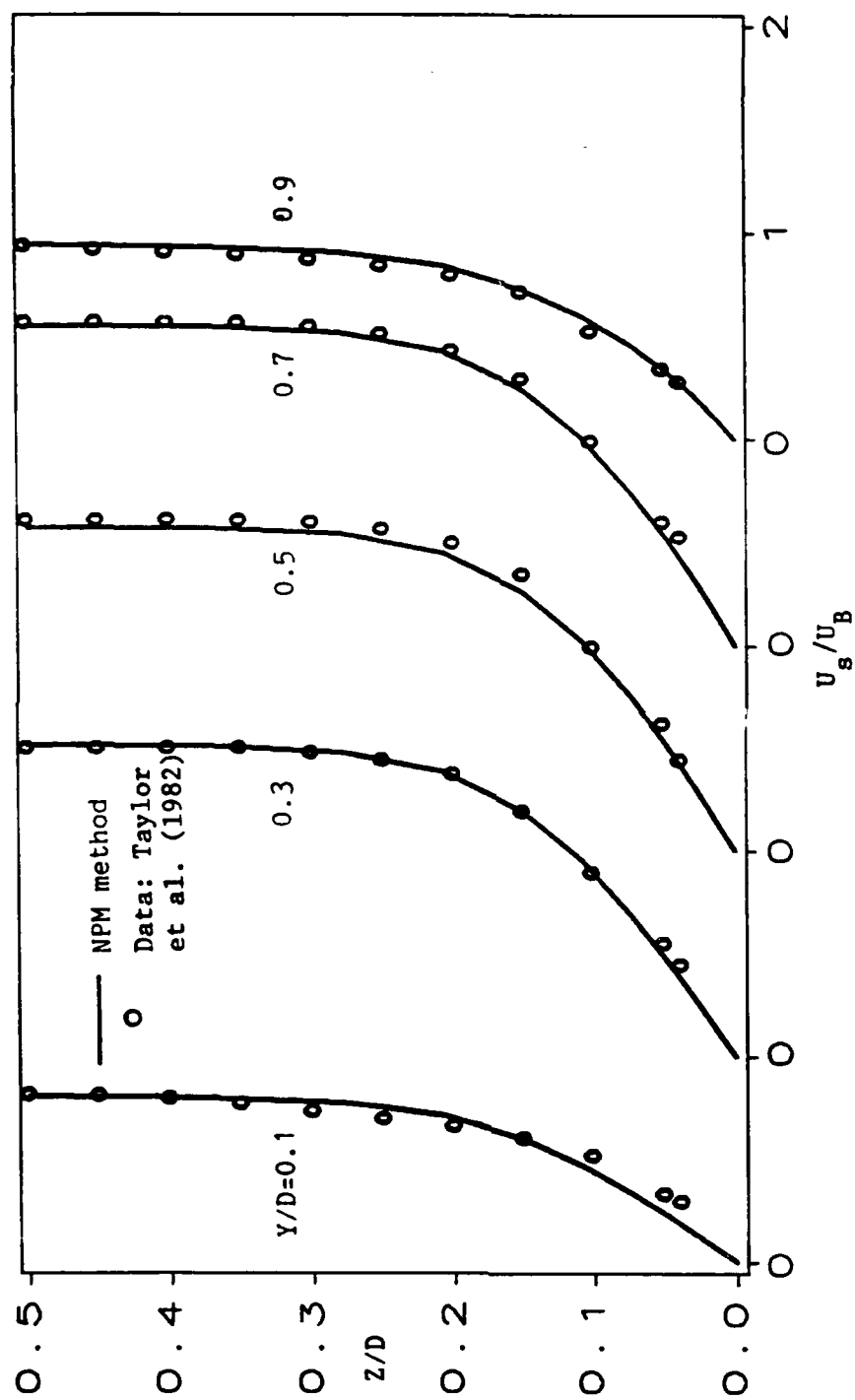Figure 3.18 Computed Coefficient of Pressure for the S-Duct

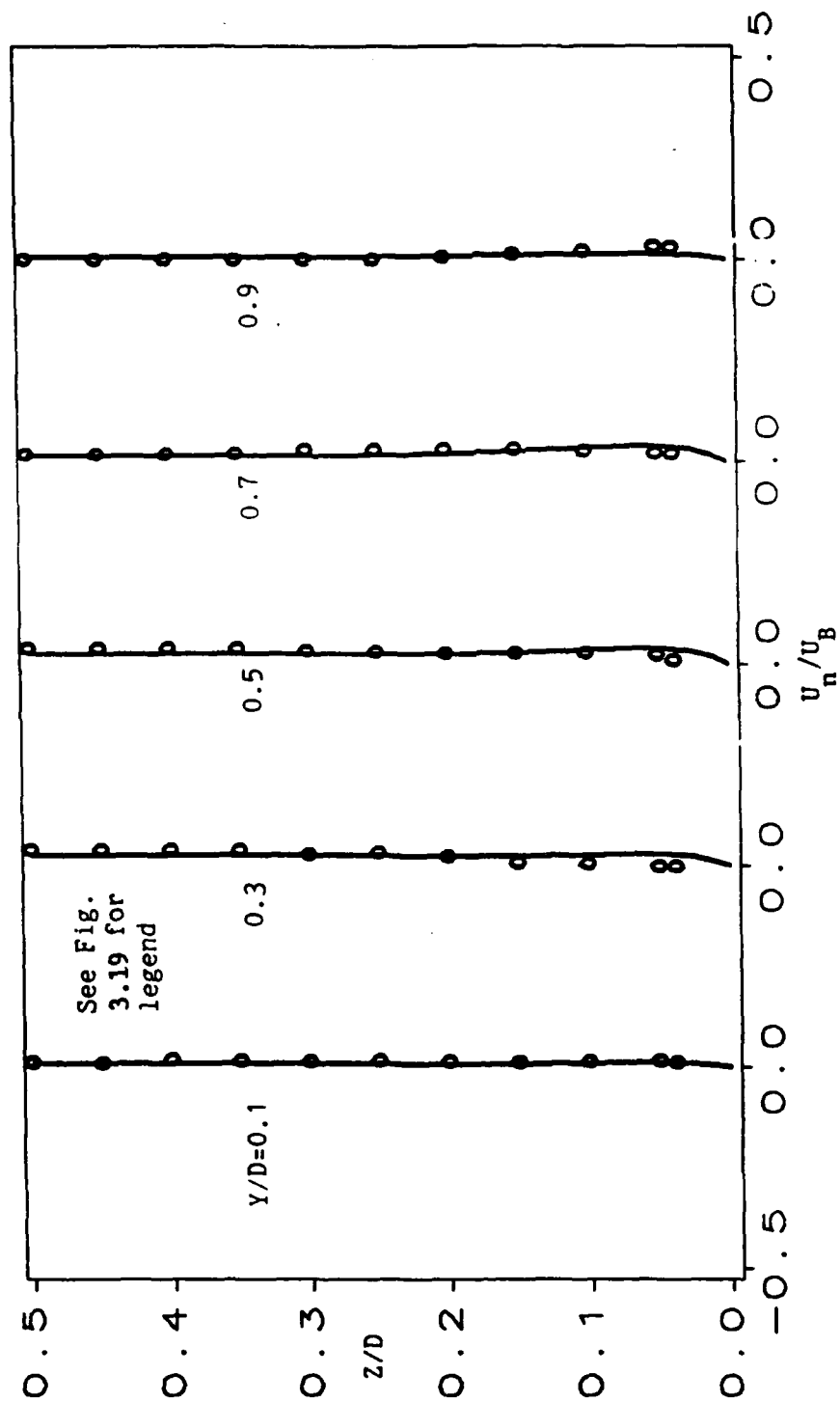Figure 3.19 Streamwise Velocity Profiles for the S-Duct at

Station 1

Figure 3.20 Transverse Velocity Profiles for the S-Duct at
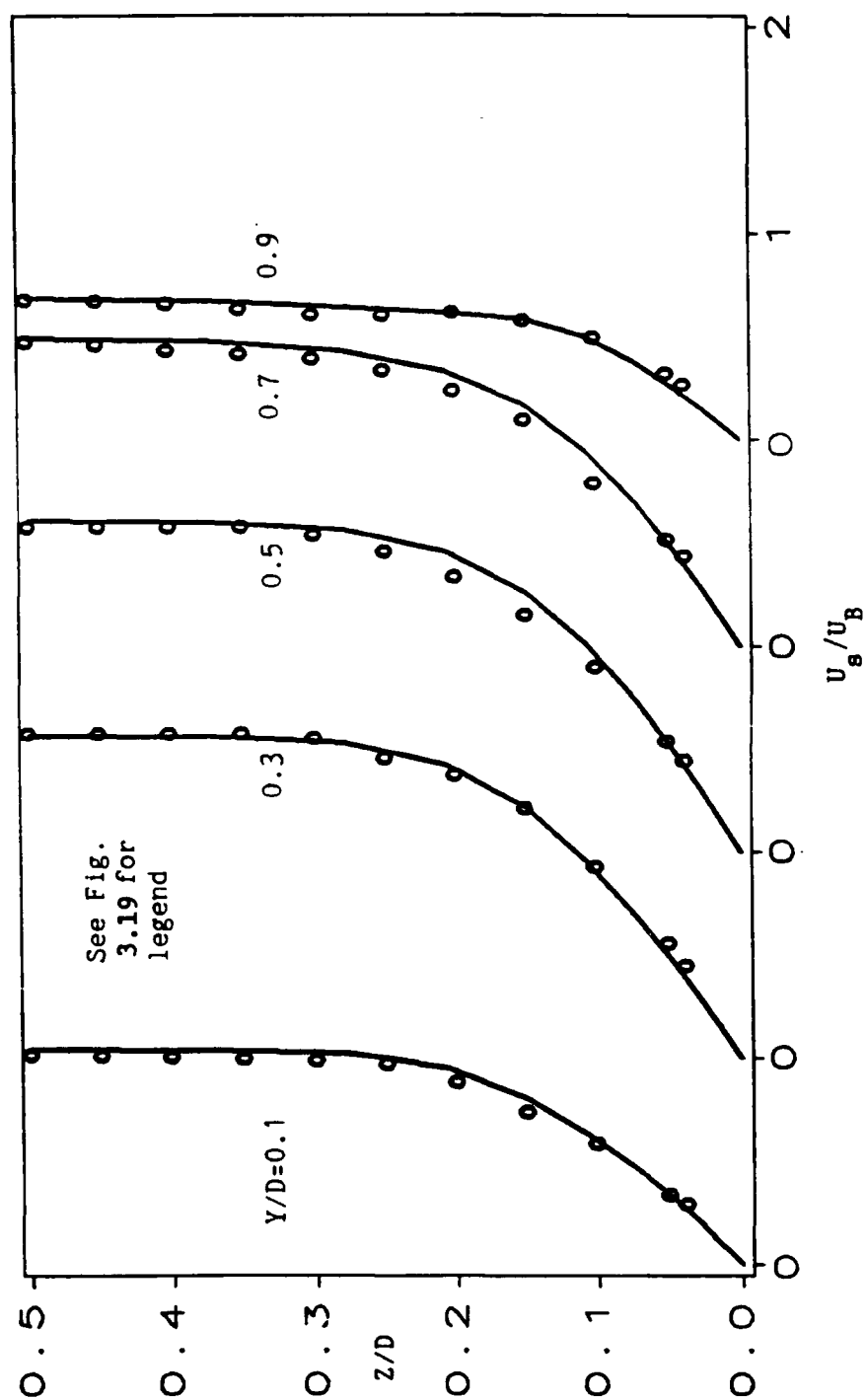Station 1

Figure 3.21 Streamwise Velocity Profiles for the S-Duct at
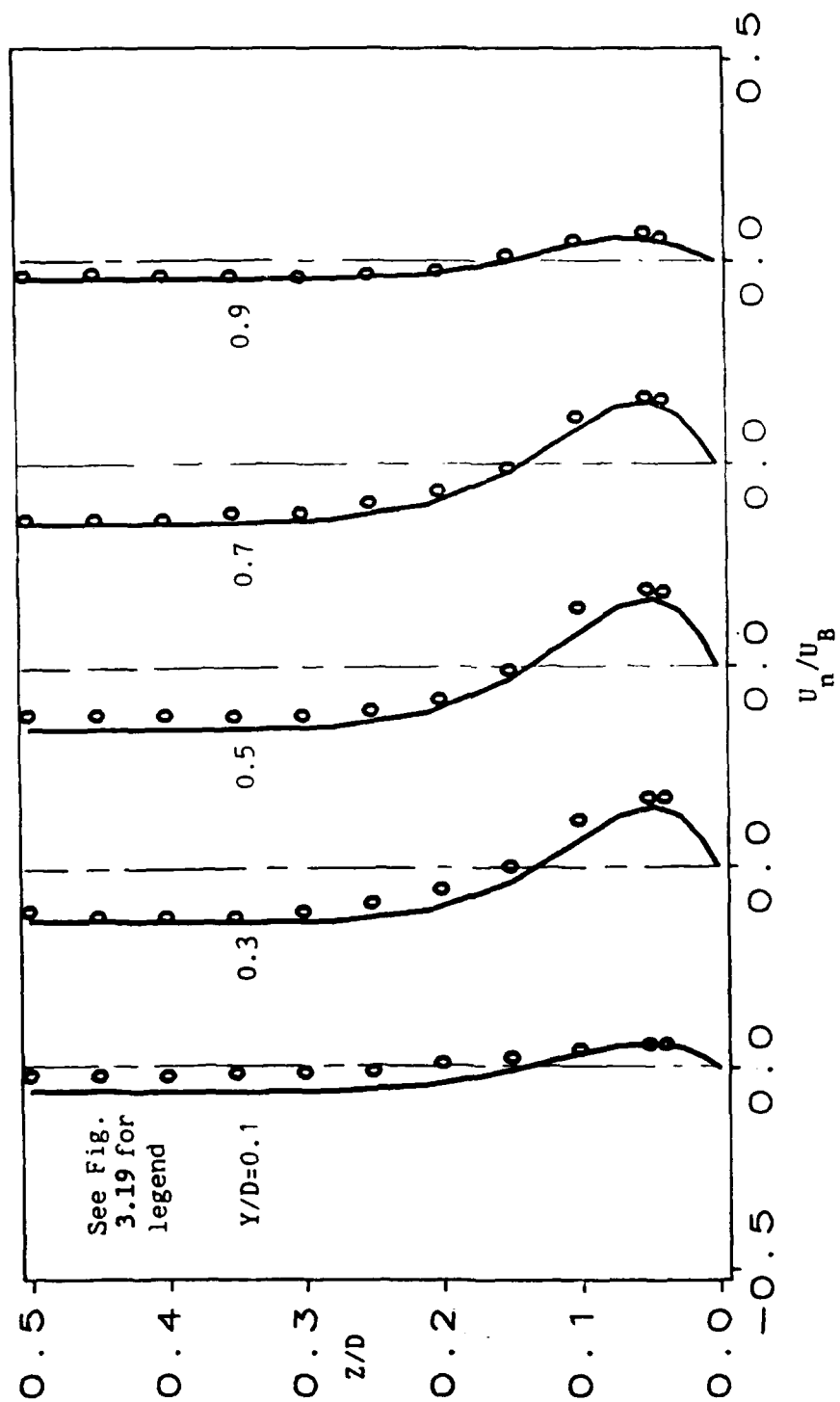Station 2

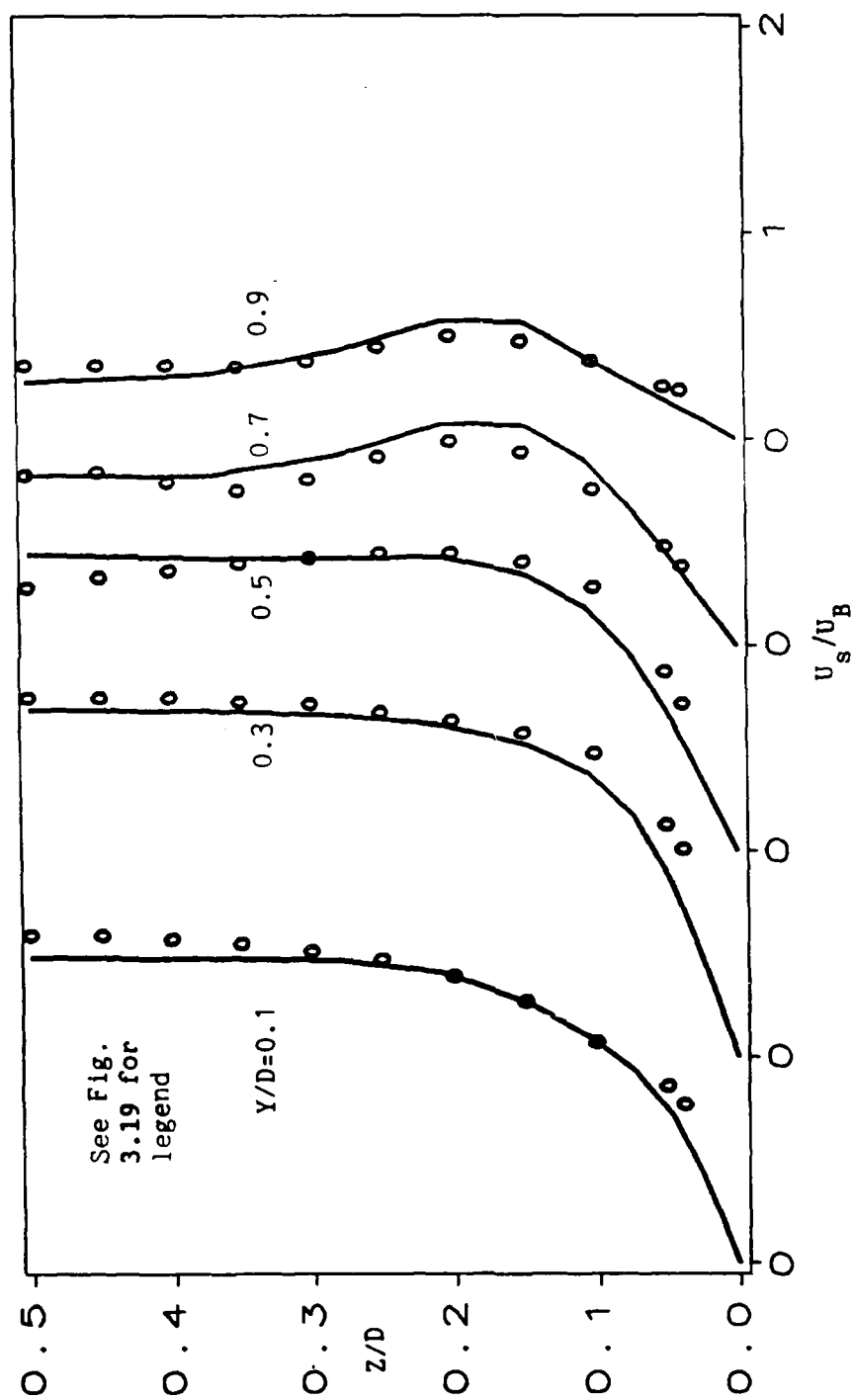Figure 3.22 Transverse Velocity Profiles for the S-Duct at

Station 2

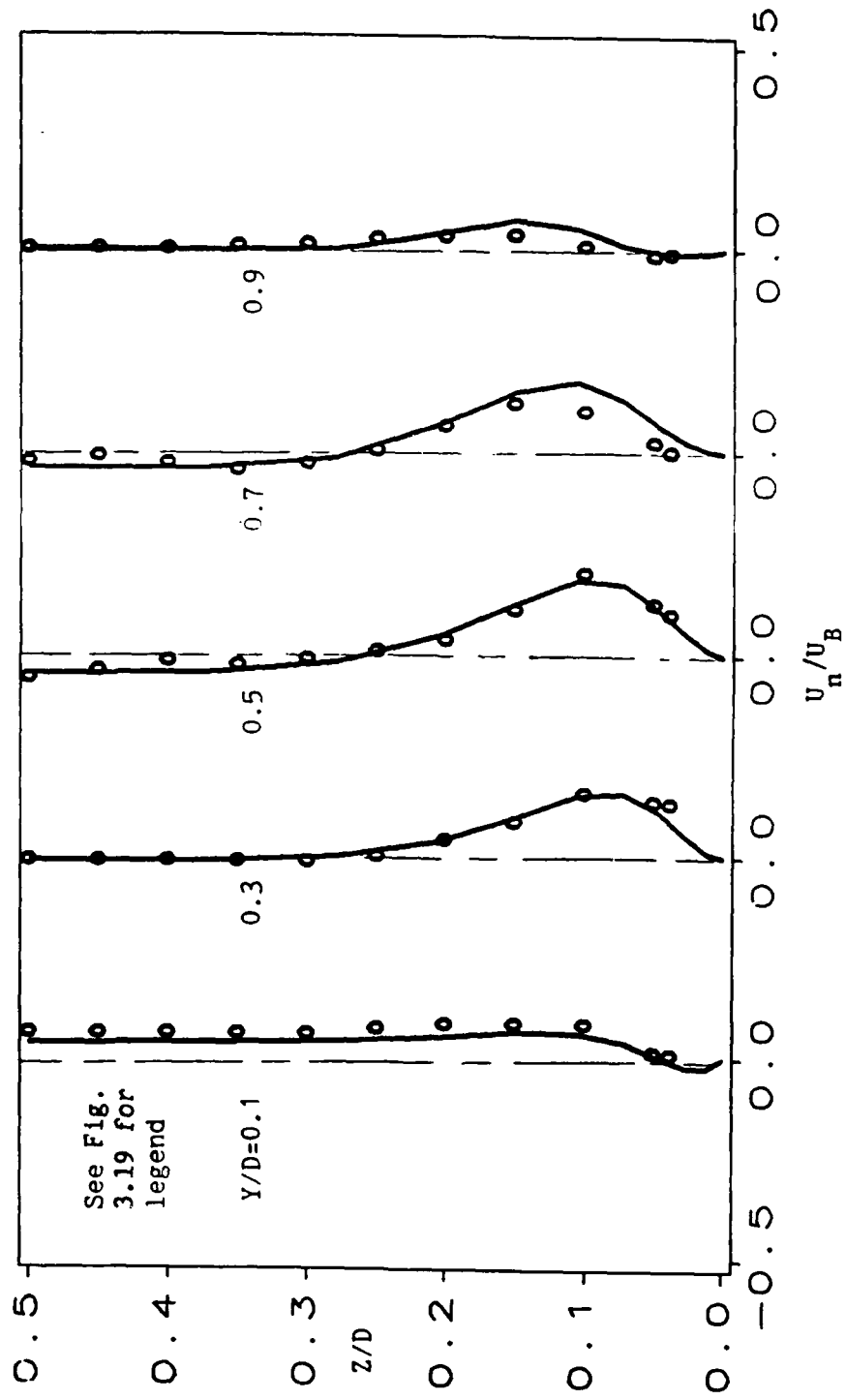Figure 3.23 Streamwise Velocity Profiles for the S-Duct at Station 4

Figure 3.24 Transverse Velocity Profiles for the S-Duct at Station 4

secondary flow reversal is complete and the influence of the straight portion of the duct outlet, through the streamwise pressure gradient, has begun to straighten out the flow at Y/D=0.9. At this location, the streamwise profile is not well predicted near the symmetry plane. It should be noted that the grid is sparse in this region and may have led to the poor prediction. This exemplifies one of the major obstacles hindering a true prediction of the flow. If experimental data were not present, the secondary vortex that generates the odd profile at Y/D=0.9 would not be anticipated and a fine grid would normally not be placed in that region.

Overall, the agreement with the experimental data for the S-duct was excellent. This case proved that multiple passes of the partially parabolized Navier-Stokes equation as a solution procedure is capable of transmitting downstream pressure effects upstream albeit slowly and that the NPM method converges even when all the pressure gradients are substantial. Also, the case proved that the NPM method is superior to multiple pass methods which only forward difference the streamwise pressure gradient with no other modifications since the flow could not be computed with a=0.0.

3.9 Closing Remarks

In the most general terms the NPM method is a line relaxation of Chorin's method with no unsteady velocity terms. With the inclusion of the pressure term in the continuity equation, it has been shown that convergence is improved over a partially parabolic system with no modifications. Also, the extra term tends to improve the coupling of the odd and even points. In addition, with a non-zero element in the
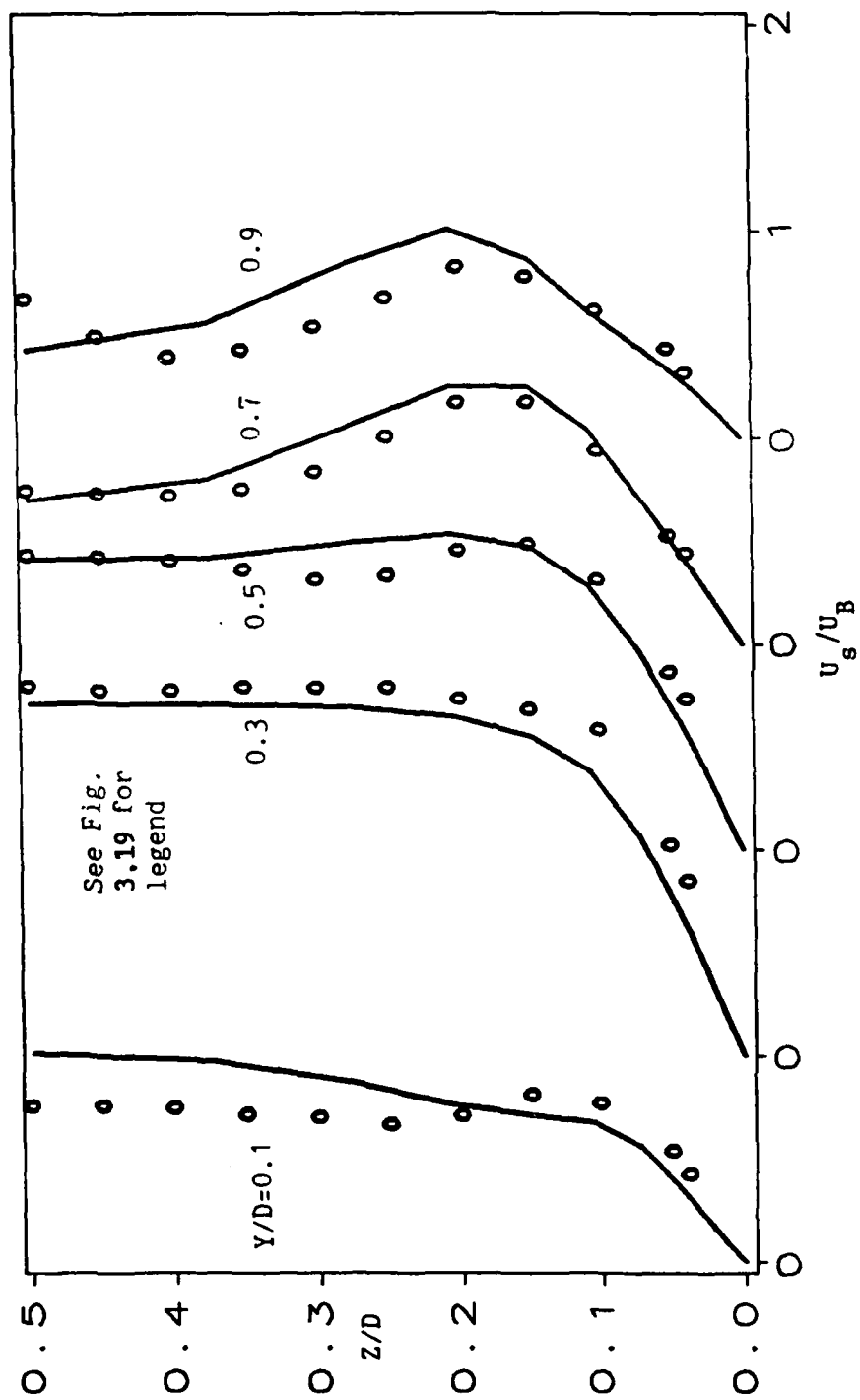
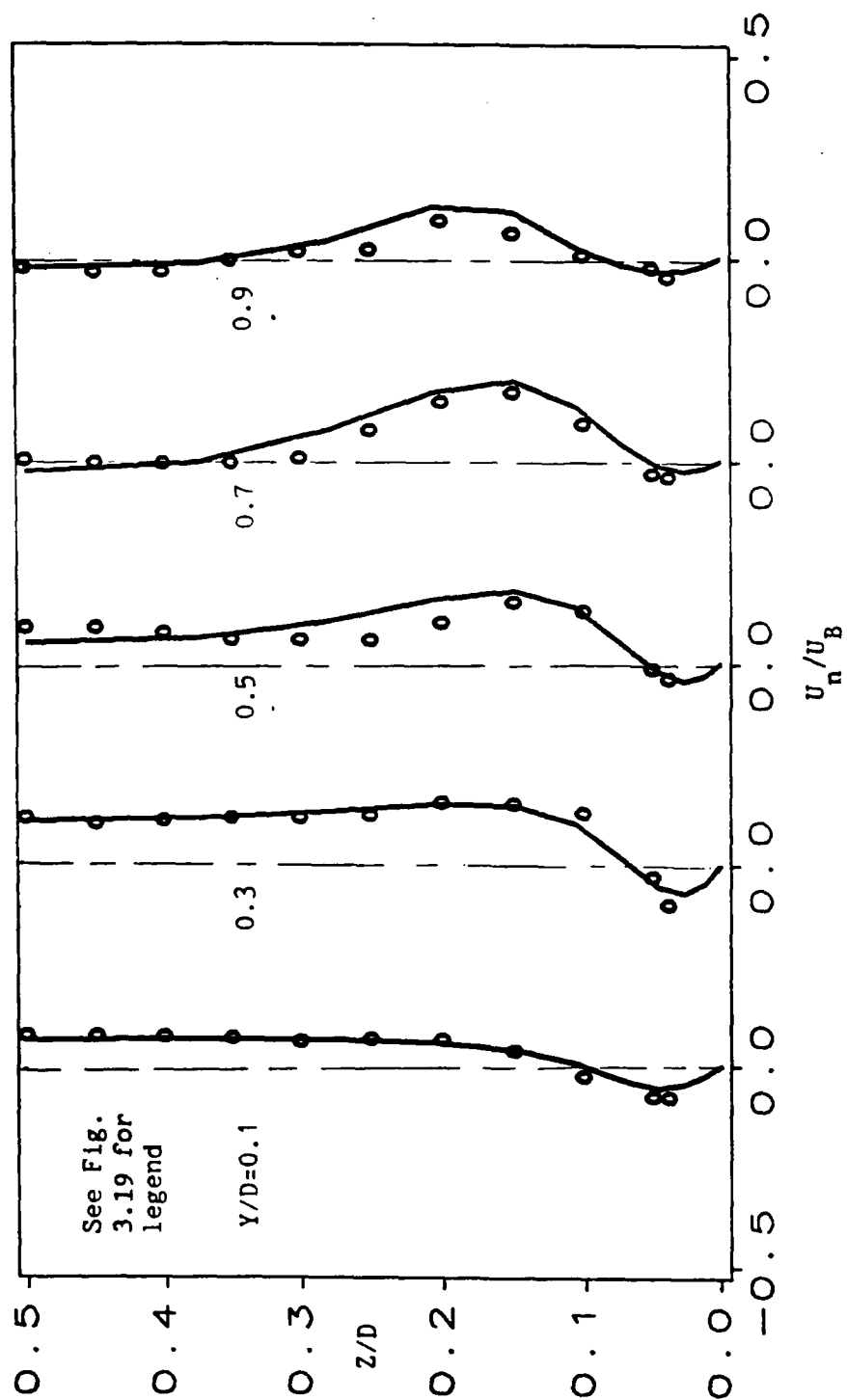Figure 3.25 Streamwise Velocity Profiles for the S-Duct at

Station 5

Figure 3.26 Transverse Velocity Profiles for the S-Duct at
Station 5

1,1 position of A_J, diagonal dominance is assured and the amount of pivoting required in the solution of the block tridiagonal matrices is reduced considerably with a saving of computation time. It should be noted that no implicit or explicit smoothing is required for good results. Due to the one-sided differencing of the pressure gradient boundary condition and the one-sided differencing of all streamwise derivatives, there is a small amount of artificial dissipation introduced.

The method has been shown to accurately introduce the streamwise ellipticity due to the pressure as seen in the S-duct results. This is the most important feature of the method since strong pressure ellipticity is the reason one cannot use the PL or MPL method with success. The method has been used to compute laminar flows with excellent results and so it should be able to compute complex turbulent flows with success with the inclusion of turbulence models.

Due to the parabolizing assumptions made in the governing equation, only H-type computational grids can be used. A description of this type of grid and an algorithm for generating them is described in the appendix. Also, the flow near blunt leading edges cannot be computed accurately due to the lack of streamwise diffusion in the governing equation.

CHAPTER 4

TURBULENCE CLOSURE SCHEMES

4.1 Introduction

Direct simulation of the turbulence by solving the unsteady Navier-Stokes equation at the Kolmogorov scales is a monumental task for complex turbomachinery flows. Thus, a simplified form of the equation, namely the Reynolds averaged Navier-Stokes equation, is used which is similar to equation 2.1 with the variables being time averages. The Reynolds averaging also introduces time averaged products of velocity fluctuations called Reynolds stresses. These Reynolds stresses can be interpreted as apparent additional shear stresses and related, using the Boussinesq approximation, to a mean velocity gradient with some constant of proportionality. This constant is termed the eddy viscosity since it mimics the kinematic viscosity but is associated with the turbulence eddies. With this model, the governing equation is in a closed form provided the eddy viscosity is known. Here lies the difficulty in modelling turbulence. The eddy viscosity must somehow be modelled using our knowledge and intuition about the nature of turbulence.

Various models have been proposed with varying degrees of simplification and empericism. The most simple model is the algebraic eddy viscosity model which relates the eddy viscosity to some length scale and a mean velocity gradient. The two-equation k-ε model relates the eddy viscosity to the turbulence kinetic energy and the turbulence energy dissipation. Both of these models do not include the effects of

the anisotropy of turbulence. Unfortunately, turbulence in general is not isotropic. Flow curvature, rotation and bouyancy all introduce anisotopy which should be modelled appropriately. The best way to do this is to use the full Reynolds stress model where partial differential equations are solved for each Reynolds stress. Some of the terms in these equations must be modelled themselves which tends to complicate matters greatly. A compromise between the k-ε model and the full Reynolds stress model is the algebraic Reynolds stress model or ARSM. The ARSM uses algebraic equations for the various Reynolds stresses and includes some degree of anisotropy. The ARSM along with the algedraic eddy viscosity model and the k-ε model will be discussed.

4.2 Algebraic Eddy Viscosity Model

From a purely dimensional argument, the eddy viscosity can be related to some turbulence length scale ℓ and a mean velocity gradient. Thus, the equation for the eddy viscosity is

$$\nu_t = \ell^2 \, \partial_n Q$$

$$(4.1)$$

A two layer algebraic model developed by Baldwin and Lomax (1978) has been used here for all shear layers where:

$$\nu_t = \begin{cases} \nu_t \text{ inner} & 0 < n < n_c \\ \\ \nu_t \text{ outer} & n_c < n < \delta \end{cases}$$

$$(4.2)$$

where n is the distance normal to the boundary, δ is the edge of the

shear layer and n_c is the point where the eddy viscosity is switched from the inner to the outer formula. The length scale for the inner formulation includes the van Driest damping function and the total vorticity replaces the mean velocity gradient in equation 4.1. Thus, the non-dimensional inner eddy viscosity is written as:

$$\nu_{t\ inner} = [\kappa\ n\ (1-\exp(-y^+/A^+))]^2 |\omega| Re$$

(4.3)

where

$$\omega = \sqrt{(\partial_y u - \partial_x v)^2 + (\partial_z v - \partial_y w)^2 + (\partial_x w - \partial_z u)^2}$$

(4.4)

and

$$y^+ = u* \ n\ Re$$

$$\kappa = 0.4$$

$$A^+ = 26$$

$u* = $ friction velocity defined in equation 3.32

The outer formulation is based on several emperical constants, the Klebenov intermittancy factor, and the total mean vorticity.

$$\nu_{t\ outer} = K\ C_{cp}\ F_{wake}\ F_{kleb}\ Re$$

(4.5)

where

$$F_{wake} = minimum\ of \begin{cases} n_{max}\ F_{max} \\ \\ C_{wk}\ n_{max}\ Q_D^2/F_{max}\ , \end{cases}$$

n_{max} is the distance where F is a maximum from:

$$F = \kappa \, n \, (1 - \exp(-y^+/A^+)) \, |\omega|$$

$$F_{kleb} = [\, 1 + 5.5(\, C_{kleb} \, n/n_{max})^6]^{-1}$$

and

$$Q_D = Q_{max} - Q_{min}$$

The following emperical constants are applied.

$$C_{cp} = 1.6$$
$$C_{kleb} = 0.3$$
$$C_{wk} = 0.25$$
$$K = 0.0168$$

In determining the crossover location n_c, it has been found to be more computationally efficient to compute both the inner and outer components of the eddy viscosity and using the smaller of the two. In three dimensions, the above formulations were used for the nearest boundary. It should also be noted that the distribution of F has two peaks. Experience has shown that taking F_{max} to be the second peak yields the best results. For wakes, only the outer formulation of ν_t is used.

The advantage of the Baldwin and Lomax model over other algebraic eddy viscosity models is that the edge of the shear layer need not be computed directly. Rather, the shear layer edge is determined from the vorticity. This is important for internal flows since the freestream or the inviscid core is not uniform but characterized by some non-zero gradient. Thus, using the traditional determination of the shear layer

edge, i.e., at $Q = .99\ Q_{freestream}$, becomes difficult.

This model can be used for a wide variety of flows with very good results. Difficulties arise in large interaction regions , e.g., separated flows, and highly three-dimensional flows. The algebraic model contains no 'history' effects of the turbulence and is based on two-dimensional shear layers only. In order to include more physics in the model, a two-equation k-ε turbulence model can be used.

4.3 Two-equation model

The greatest difficulty with the above algebraic model is that the turbulence length scale must be determined in an ad hoc fashion. It is desirable to determine the turbulence length scale and velocity scale from partial differential equations derived from physical considerations. The turbulance velocity scale can be found from the scalar turbulence kinetic energy. An equation for the turbulence length scale does not exist but the turbulence dissipation in combination with the turbulence kinetic energy does yield a length scale and a partial differential equation can be written for the turbulence dissipation. From dimensional analysis, the eddy viscosity can be related to the turbulence kinetic energy and dissipation.

$$\nu_t \propto k^2/\varepsilon$$

$$(4.6)$$

in non-dimensional form, equation 4.6 is written as:

$$\nu_t = C_\mu\ k^2/\varepsilon\ Re$$

$$(4.7)$$

The equation for the turbulence kinetic energy can be derived from the Reynolds stress equation and has the following form:

$$\partial_x uk + \partial_y vk + \partial_z wk - 1/Re \; [\; \partial_x(\nu_k \partial_x k) + \partial_y(\nu_k \partial_y k)$$
$$+ \partial_z(\nu_k \partial_z k) \;] = P_k/Re - \epsilon$$

(4.8)

where

$$\nu_k = 1 + \nu_t/\sigma_k.$$

The turbulence dissipation equation can be derived by taking the derivative of the unsteady Navier-Stokes equation with respect to the coordinates, time average, then subtract the mean flow equation and multiply the result by the unsteady strain rate and the kinematic viscosity. Taking the time average gives an equation for the isotropic turbulence dissipation. The equation includes several terms which must be modelled. The final form of the equation has the following form:

$$\partial_x u\epsilon + \partial_y v\epsilon + \partial_z w\epsilon - 1/Re \; [\; \partial_x(\nu_\epsilon \partial_x \epsilon) + \partial_y(\nu_\epsilon \partial_y \epsilon)$$
$$+ \partial_z(\nu_\epsilon \partial_z \epsilon) + C_{\epsilon 1}\epsilon/k \; P_k - C_{\epsilon 2}\epsilon^2/k \; Re \;] = 0$$

(4.9)

where

$$\nu_\epsilon = 1 + \nu_t/\sigma_\epsilon.$$

The various constants were set to match experimental data for free and bounded shear layers and dissipation of turbulence in gradient free flow. The standard values are (see Rodi (1982)):

$$C_{\epsilon 1} = 1.44 \qquad\qquad C_{\epsilon 2} = 1.92$$

$$\sigma_k = 1.0 \qquad\qquad \sigma_\varepsilon = 1.3$$

$$C_\mu = 0.09$$

The production of turbulence is given by the following simplified relationship:

$$P_k = \nu_t[(\partial_\eta Q)^2 + (\partial_\zeta Q)^2]$$

(4.10)

The k-ε equations must be recast into generalized coordinates in a manner similar to the mean flow equations. Thus, the k-equation becomes:

$$L_\xi + L_\eta + L_\zeta - 1/(J\ Re)\ (\ L_{\eta\eta} + L_{\zeta\zeta}) = -\ 1/(J\ Re)\ L_{\eta\zeta} + S_T/J$$

(4.11)

where

$$L_\xi = (\xi_x \partial_\xi uk + \xi_y \partial_\xi vk + \xi_z \partial_\xi wk)/J$$

$$L_\eta = (\eta_x \partial_\eta uk + \eta_y \partial_\eta vk + \eta_z \partial_\eta wk)/J$$

$$L_\zeta = (\zeta_x \partial_\zeta uk + \zeta_y \partial_\zeta vk + \zeta_z \partial_\zeta wk)/J$$

$$L_{\eta\eta} = \eta_x \partial_\eta \{\nu_k \eta_x \partial_\eta k\} + \eta_y \partial_\eta \{\nu_k \eta_y \partial_\eta k\} + \eta_z \partial_\eta \{\nu_k \eta_z \partial_\eta k\}$$

$$L_{\zeta\zeta} = \zeta_x \partial_\zeta \{\nu_k \zeta_x \partial_\zeta k\} + \zeta_y \partial_\zeta \{\nu_k \zeta_y \partial_\zeta k\} + \zeta_z \partial_\zeta \{\nu_k \zeta_z \partial_\zeta k\}$$

$$L_{\eta\zeta} = \eta_x \partial_\eta \{\nu_k \zeta_x \partial_\zeta k\} + \eta_y \partial_\eta \{\nu_k \zeta_y \partial_\zeta k\} + \eta_z \partial_\eta \{\nu_k \zeta_z \partial_\zeta k\}$$
$$+ \zeta_x \partial_\zeta \{\nu_k \eta_x \partial_\eta k\} + \zeta_y \partial_\zeta \{\nu_k \eta_y \partial_\eta k\} + \zeta_z \partial_\zeta \{\nu_k \eta_z \partial_\eta k\}$$

$$S_T = P_k/Re - \varepsilon$$

Similarly, the ε-equation becomes:

$$L_\xi + L_\eta + L_\zeta - 1/(J\ Re)\ (\ L_{\eta\eta} + L_{\zeta\zeta}) + S_T/J = -\ 1/(J\ Re)\ L_{\eta\zeta}$$

$$(4.12)$$

where

$$L_\xi = (\xi_x \partial_\xi u\epsilon + \xi_y \partial_\xi v\epsilon + \xi_z \partial_\xi w\epsilon)/J$$

$$L_\eta = (\eta_x \partial_\eta u\epsilon + \eta_y \partial_\eta v\epsilon + \eta_z \partial_\eta w\epsilon)/J$$

$$L_\zeta = (\zeta_x \partial_\zeta u\epsilon + \zeta_y \partial_\zeta v\epsilon + \zeta_z \partial_\zeta w\epsilon)/J$$

$$L_{\eta\eta} = \eta_x \partial_\eta\{\nu_\epsilon \eta_x \partial_\eta \epsilon\} + \eta_y \partial_\eta\{\nu_\epsilon \eta_y \partial_\eta \epsilon\} + \eta_z \partial_\eta\{\nu_\epsilon \eta_z \partial_\eta \epsilon\}$$

$$L_{\zeta\zeta} = \zeta_x \partial_\zeta\{\nu_\epsilon \zeta_x \partial_\zeta \epsilon\} + \zeta_y \partial_\zeta\{\nu_\epsilon \zeta_y \partial_\zeta \epsilon\} + \zeta_z \partial_\zeta\{\nu_\epsilon \zeta_z \partial_\zeta \epsilon\}$$

$$L_{\eta\zeta} = \eta_x \partial_\eta\{\nu_\epsilon \zeta_x \partial_\zeta \epsilon\} + \eta_y \partial_\eta\{\nu_\epsilon \zeta_y \partial_\zeta \epsilon\} + \eta_z \partial_\eta\{\nu_\epsilon \zeta_z \partial_\zeta \epsilon\}$$
$$+ \zeta_x \partial_\zeta\{\nu_\epsilon \eta_x \partial_\eta \epsilon\} + \zeta_y \partial_\zeta\{\nu_\epsilon \eta_y \partial_\eta \epsilon\} + \zeta_z \partial_\zeta\{\nu_\epsilon \eta_z \partial_\eta \epsilon\}$$

$$S_T = C_{\epsilon 1}\epsilon P_k/(k\ Re) - C_{\epsilon 2}\epsilon^2/k$$

The k-ϵ equations are weakly coupled and so are solved in an uncoupled fashion with the k equation solved first. Equations 4.11 and 4.12 are discretized in the same manner as the mean flow equations and solved in the cross plane using the alternating direction implicit (ADI) algorithm. The solution of the equations is lagged one streamwise station behind the mean flow equation using the velocities previously computed.

4.3.1 Boundary Conditions

Since the k-ϵ equations are valid only in regions where the turbulence Reynolds number is high, wall functions are used to give

boundary conditions for the turbulence kinetic energy and dissipation which avoids having to solve the k-ε equations in the viscous sublayer and buffer region of a bounded shear layer. The boundary conditions are those proposed by Rodi (1982). At the first point from a solid boundary, the following values of k and ε are applied and the k-ε equations are solved in the rest of the domain.

$$k_p = u*^2/\sqrt{C_\mu}$$

(4.13)

$$\varepsilon_p = u*^3/(\kappa \ n_p)$$

(4.14)

where u* is the friction velocity defined in equation 3.32. For these wall functions to apply, the first point from the solid boundary must be no closer than at $y^+ = 20$. Although the use of these wall fuctions implies the use of a turbulent slip velocity as a boundary condition for the mean flow, the no-slip boundary condition is generally used except for extremely thin boundary layers.

At a symmetry boundary the normal gradients of k and ε are set to zero. For periodic boundaries, the periodicity condition is enforced implicitly using a periodic matrix solver.

4.3.2 Initial Conditions

Two methods can be employed to generate initial conditions for the k-ε equations. First, when experimental data is available for the turbulence intensities, the turbulence kinetic energy is determined from:

$$k = 1/2(\overline{u'^2} + \overline{v'^2} + \overline{w'^2})$$

$$(4.15)$$

With the Reynolds shear stress measured, the definition of the eddy viscosity can be used along with the previously computed turbulence kinetic energy to give the turbulence dissipation in the following way (two dimensions are used for example):

$$\overline{u'v'} = - C_\mu k^2/\epsilon \; Re \; \partial_\eta Q$$

then

$$\epsilon = -C_\mu k^2 \; Re \; \partial_n Q \; / \; \overline{u'v'}$$

$$(4.16)$$

Thus, k and ϵ are known at the inlet plane and the equations can be forward-marched behind the mean flow equations.

If the experimental data is not available, the algebraic eddy viscosity model is used to give the eddy viscosity. Then equilibrium is assumed so that production equals dissipation or:

$$\epsilon = P_k/Re$$

$$(4.17)$$

and

$$k = \sqrt{\nu_t \epsilon/(C_\mu Re)}$$

$$(4.18)$$

A major problem associated with the k-ϵ model is that the constants in the equations are based on simple two-dimensional shear layers. In addition, the turbulence length scale is generally over predicted which artificailly suppresses boundary layer detachment in the computation.

Another problem with the model is that it assumes the turbulence is isotropic. True anisotropy can only be introduced by solving the full Reynolds stress equations and not use the eddy viscosity hypothesis. This is computationally inefficient especially for complex geometries. It is unfortunate that in the field today, the most simple models are used on the most complicated flows and the most complex models are used on the simplest of flows. An efficient way of introducing anisotropy in an approximate fashion is to assume that the transport of the Reynolds stresses is very similar to the transport of the turbulence kinetic energy. In this way, algebraic relations can be written for the Reynolds stresses.

4.4 Algebraic Reynolds Stress Model (ARSM)

For the turbomachinery type flows under consideration here, the major generator of anisotropy is rotation of the flow. The rotation effects the various Reynolds stresses in an unequal way. The Coriolis force arising from using a rotating coordinate system stabilizes or destabilizes the turbulence in shear layers. This cannot be captured by the standard k-ϵ model. By relating the transport of Reynolds stresses to the transport of k, Rodi (1976) developed the following algebraic relation for non-rotating systems.

$$\overline{u'_i u'_j} = k[2/3\delta_{ij} + (P_{ij} - 2P\delta_{ij}/3)(1-C_2)/(P+\epsilon(C_1-1))]$$

$$(4.19)$$

where δ_{ij} is the Kronecker delta, P_{ij} is the production tensor and $P = 1/3 \, P_{ii}$. Also, $C_1 = 1.8$ and $C_2 = 0.6$. Along similar lines, Warfield and Lakshminarayana (1986) developed an algebraic relation for rotating

flows.

$$\overline{u'_i u'_j} = k[2/3\delta_{ij} + \{(R_{ij}(2-C_2)/2 + P_{ij} - 2P\delta_{ij}/3)(1-C_2)\}/(P+\epsilon(C_1-1))]$$

(4.20)

where

$$R_{ij} = -2\Omega_p[\epsilon_{ipk}\overline{u'_j u'_k} + +\epsilon_{jpk}\overline{u'_i u'_k}]$$

(4.21)

and Ω_p is the rotation vector and ϵ_{ijk} is the permutation tensor.

Warfield and Lakshminarayana manipulated equation 4.21 to give the variable C_μ Prandtl-Kolmogorov form found in equation 4.22.

$$C_\mu = -(2/3)(C_2-1)(C_2 P_k/\epsilon + C_1 - 1)/(D_1 + D_2)$$

(4.22)

where

$$D_1 = \{(P_k/\epsilon) + (C_1-1)\}^2$$

$$D_2 = [4R_1(2-C_2)/2]^2 + 4(C_2-1)(2-C_2)R_2 R_1^2$$

The following natural groups appeared in their analysis:

$$(P_k/\epsilon) \qquad R_1 = (k\Omega/\epsilon) \qquad R_2 = \partial_n Q /\Omega$$

Here, R_2 looks like a gradient Richardson number. Equation 4.22 for equilibrium conditions with zero rotation gives a value of C_μ other than the standard 0.09 thus it is multiplied by a scale factor to recover the standard value in such conditions. Also, when the ARSM is applied, upper and lower limits are placed on C_μ of 0.2 and 0.025, respectively.

The variable C_μ method for applying the ARSM is stable and very easy to apply to existing k-ϵ models and is capable of modelling the physical nature of rotation effects on turbulence according to Warfield and Lakshminarayana (1986).

4.5 Methods of Solution

Integration of the above turbulence models into the mean flow equations is straightforward. With the solution to the mean flow equations known at station i, the eddy viscosity is determined from one of the various models. This new eddy viscosity is then incorporated implicitly in the mean flow equations at station i+1. Therefore, the eddy viscosity is lagged one streamwise station behind the mean flow equations. The k-ϵ equations are solved in an uncoupled form using ADI and are marched in a fashion similar to the mean flow equations. If the ARSM is used, the k-ϵ equations are computed at station i using the value of C_μ determined at i-1. With k and ϵ now known, a new value of C_μ is determined from the ARSM and used to find the new value of the eddy viscosity. For applications where the eddy viscosity changes drastically from one streamwise station to the next, an iterative scheme may be adopted, however, this will prolong the computation time.

CHAPTER 5

COMPUTATION OF COMPLEX TURBOMACHINERY FLOWS

5.1 Introduction

In order to test the prediction accuracy of the new parabolic-marching method (NPM), the flow in several different geometries are computed to test the NPM method's ability to compute various flow phenomena. Initially, the turbulent flow in an S-shaped duct is computed since it is characterized by a strong variation in the transverse pressure gradient. Next, the turbulent flow in an end wall cascade is computed to determine how well the pressure distribution and end wall boundary layer growth is captured as well as the passage vortex. Since the wakes of turbomachinery blades are very important to the designer, the turbulent wake of a cascade of airfoils is computed. This is also a good validation of the various turbulence models incorporated into the NPM code since the wake spreading is a strong function of the turbulence. Finally, the flow in an axial flow compressor rotor is computed to study the combined effects of the blade and end wall boundary layers, strong secondary flow and rotation on the flow field.

5.2 Flow in an S-Shaped Duct

The turbulent flow in an S-shaped duct was computed using the NPM method and results compared to the LDV data acquired by Taylor et al. (1982). The geometry is shown in Figure 2.9. No assumed pressure was

used as initial conditions and the inlet flow was determined in the manner described in section 3.8.2. The computaional domain and grid used here is the same as for the laminar case presented in section 3.8.2. The flow Reynolds number based on the bulk inlet velocity and the duct width was 40,000. This Reynolds number proved to be too low for successful application of the k-ε turbulence model described in chapter IV, thus the algebraic eddy viscosity model was used.

For this case, initial passes of the domain required values of a larger than for the laminar flow. This trend was observed for all turbulent flow computations. The convergence history for a=30.0 is shown in Figure 5.1. The chosen value of a was the minimum value with which a convergent solution was obtained. Typically, the more complex a flow, the larger the value of a. Nearly two orders of magnitude were achieved after 130 global iterations. CPU time on the IBM 3090-200 was 0.00201 seconds per point per iteration. The convergence was not as strong as with the laminar flow, however, the same characteristics are present, i.e., fastest convergence for initial sweeps as small wavelength errors were damped out.

At the initial measurement location, the computed streamwise velocity profiles compare very well with the experimental data, especially near the side walls (see Figure 5.2). Near the end walls, the velocity gradients do not match the data which for internal flows portends an incorrect computed bulk pressure drop. In Figure 5.3. the computed secondary velocities at station 1 is compared to the experimental data with very good agreement. Thus the inlet conditions, so important for parabolic-marching methods, is accurately captured.

At station 2, the computed streamwise flow does not compare well to
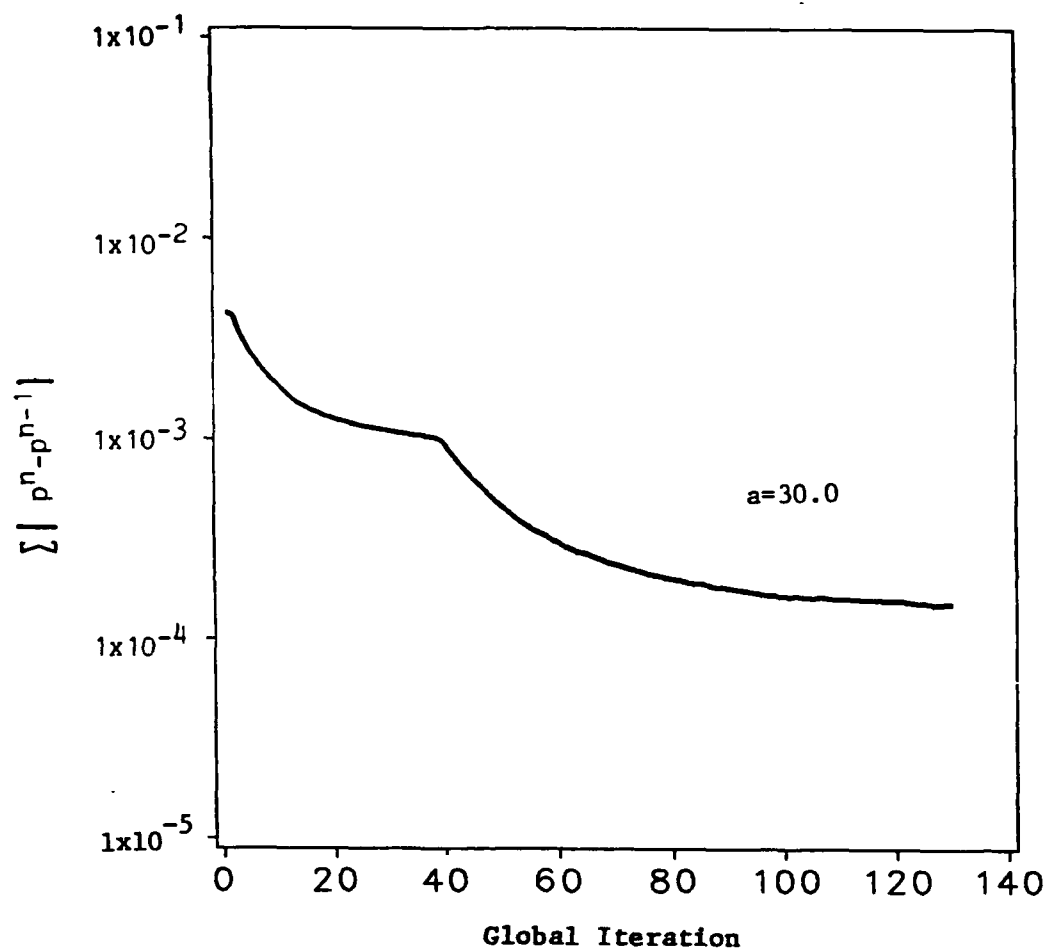
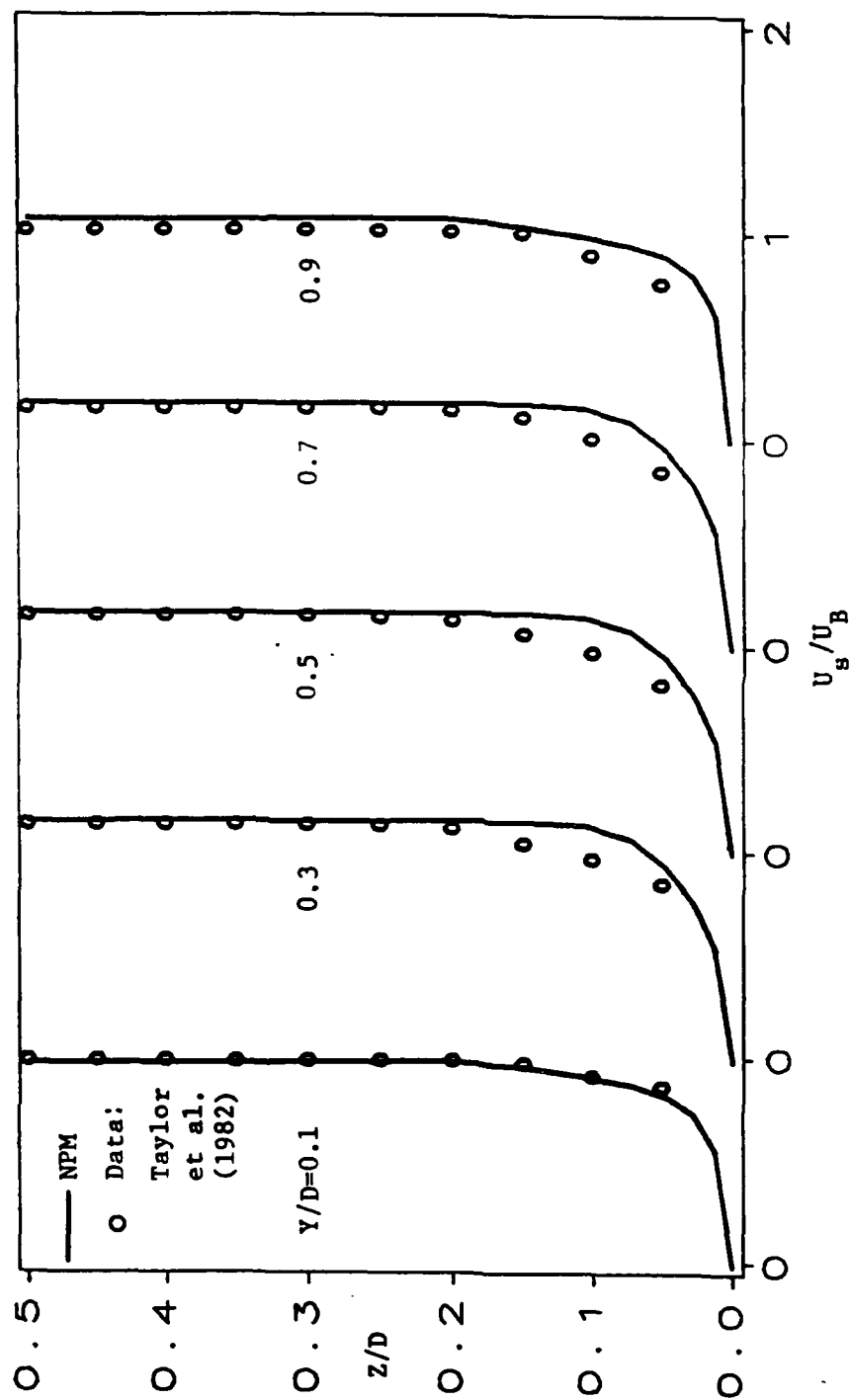Figure 5.1 Convergence History for the Turbulent S-Duct

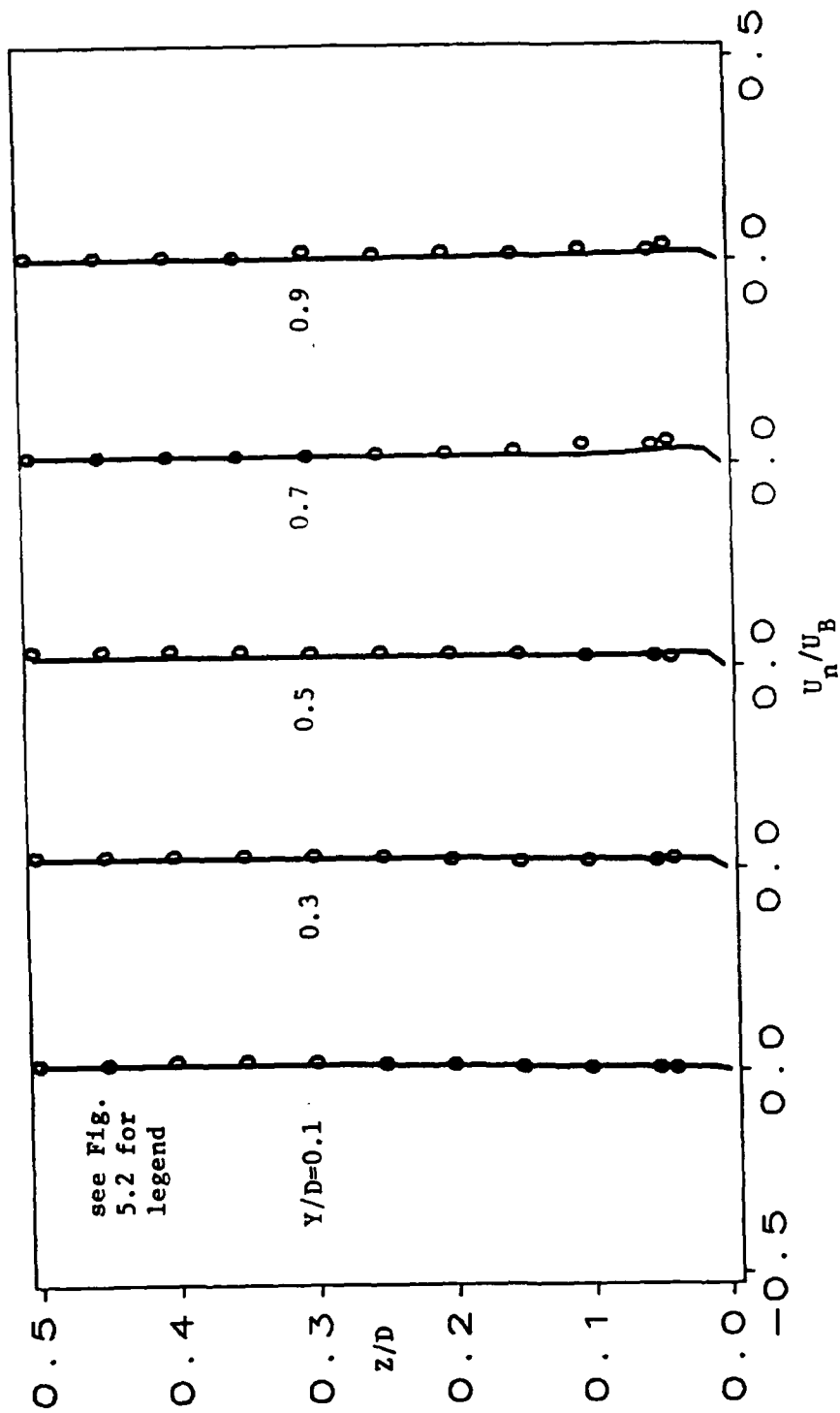Figure 5.2 Streamwise Velocity Profiles for the Turbulent S-Duct

at Station 1

Figure 5.3 Transverse Velocity Profiles for the Turbulent S-Duct
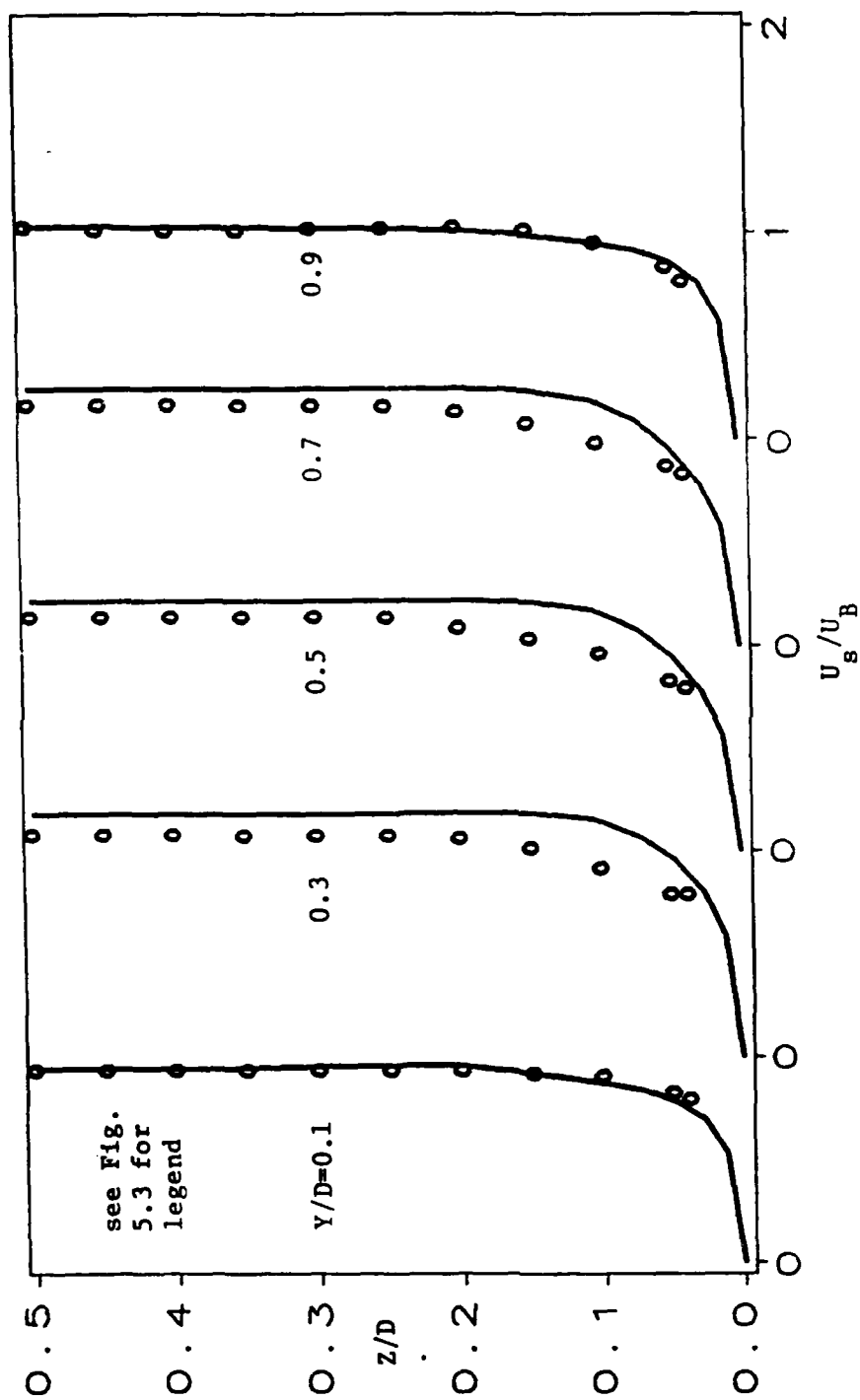at Station 1

Figure 5.4 Streamwise Velocity Profiles for the Turbulent S-Duct

at Station 2

the experimental data near the center of the duct in Figure 5.4. Inspection of the profiles leads one to believe that there may be some computed mass surplus, however, the profiles very near the side walls were not measured and so a conclusion regarding this cannot be drawn. The computed mass flow did remain constant at each station at convergence with less than a 3% variation.

The secondary flow at station 2 has developed properly as seen in Figure 5.5. The inviscid secondary flow is slightly overpredicted yet the maximum flow turning in the end wall viscous region is well predicted. At station 4 in the second bend of the duct, see Figure 5.6, the computed streamwise velocity profiles compare as well to the data as at station 2. At Y/D=0.1, however, the computed profile does not match the data qualitatively but at Y/D=0.9 there is excellent agreement between the computation and the experimental data of Taylor et al. (1982). The computed secondary flow at this station, shown in Figure 5.7, is in excellent agreement with the data at all measurement locations. Finally in Figure 5.8, the computed streamwise velocity profiles at station 5 continue to show only adequate agreement with the data near the center of the duct. The best predictions come near the side walls. In Figure 5.9, the computed secondary flow profiles compare well to the experimental data except near the side walls especially at Y/D=0.9. Here, the measured transverse velocity has an s-shaped profile and the magnitude of the velocity near the end wall is large. The computed velocity profile does not exhibit this behavior. This strong secondary flow may have been missed due to the coarse nature of the computational grid. Again it should be noted that the velocity gradients very near the wall do not compare well to the data which may
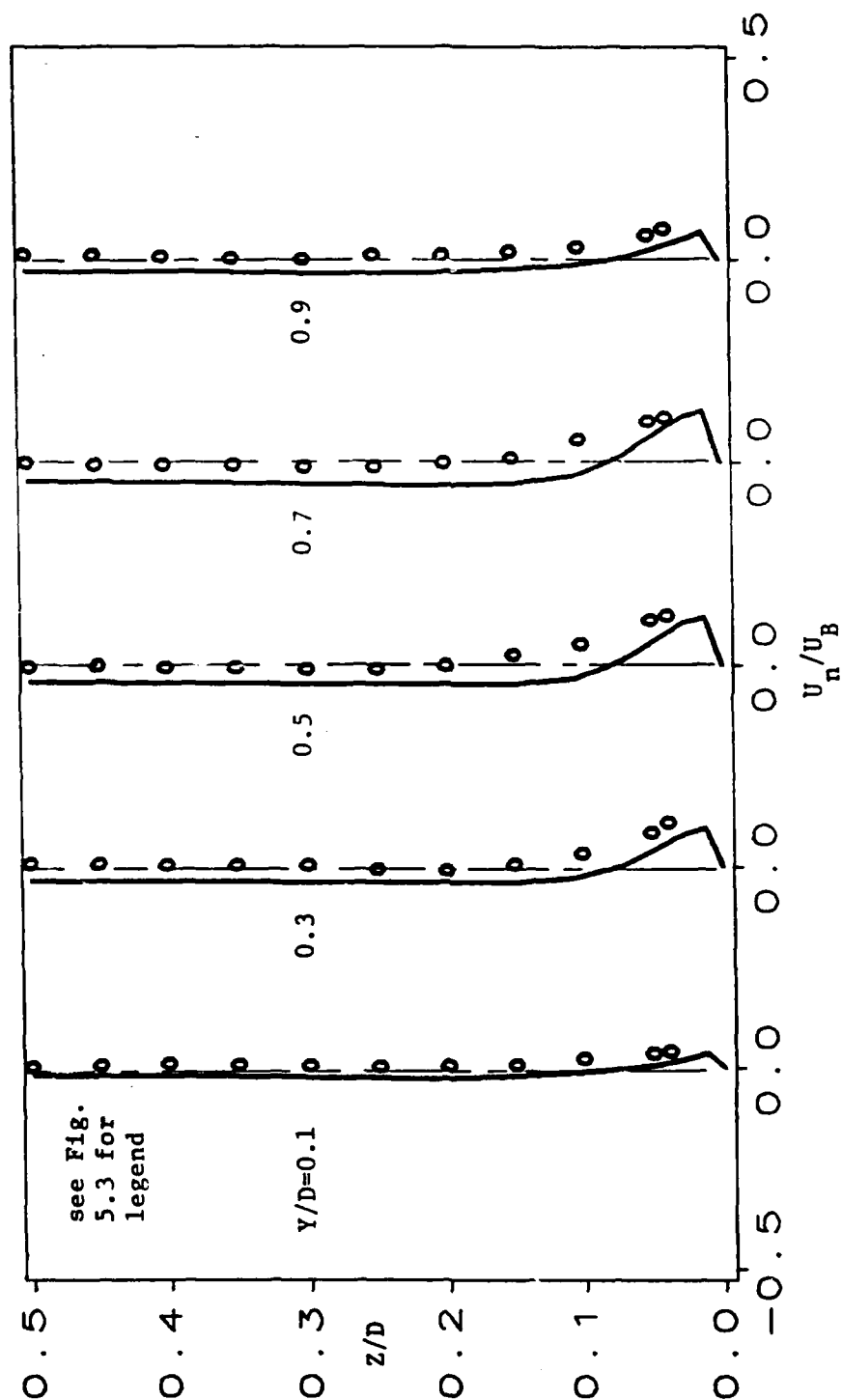
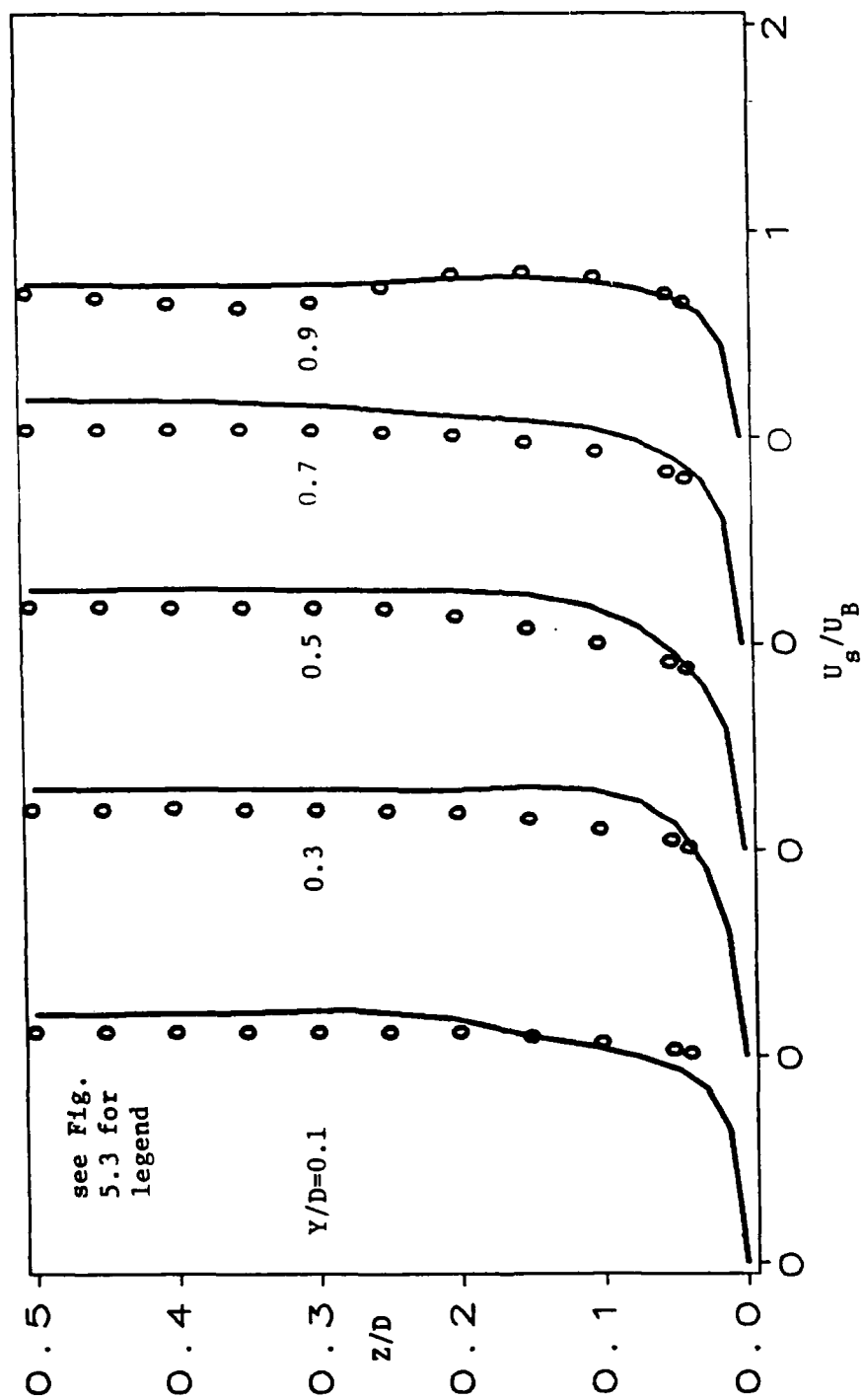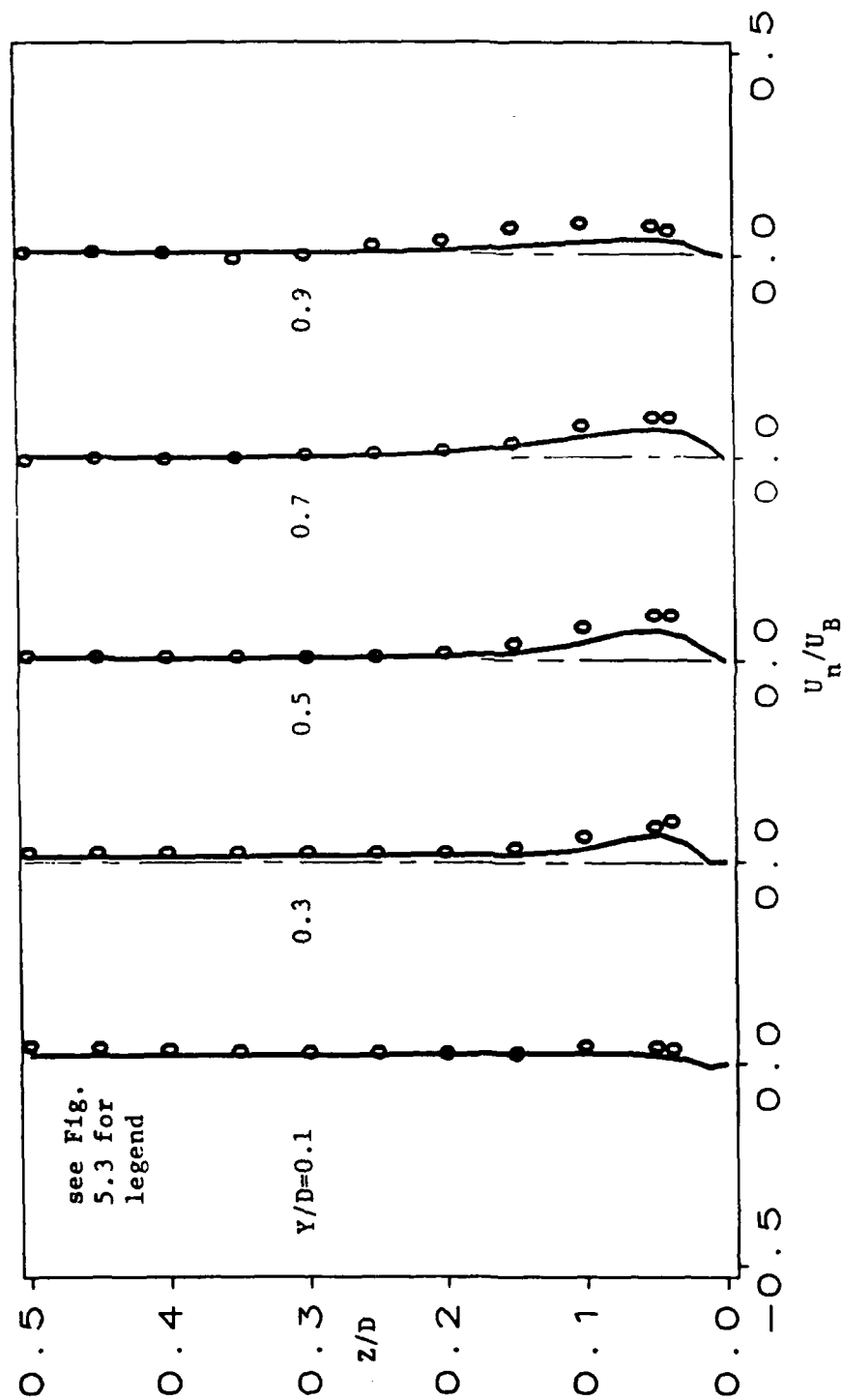Figure 5.5 Transverse Velocity Profiles for the Turbulent S-Duct

at Station 2

Figure 5.6 Streamwise Velocity Profiles for the Turbulent S-Duct

at Station 4

Figure 5.7 Transverse Velocity Profiles for the Turbulent S-Duct
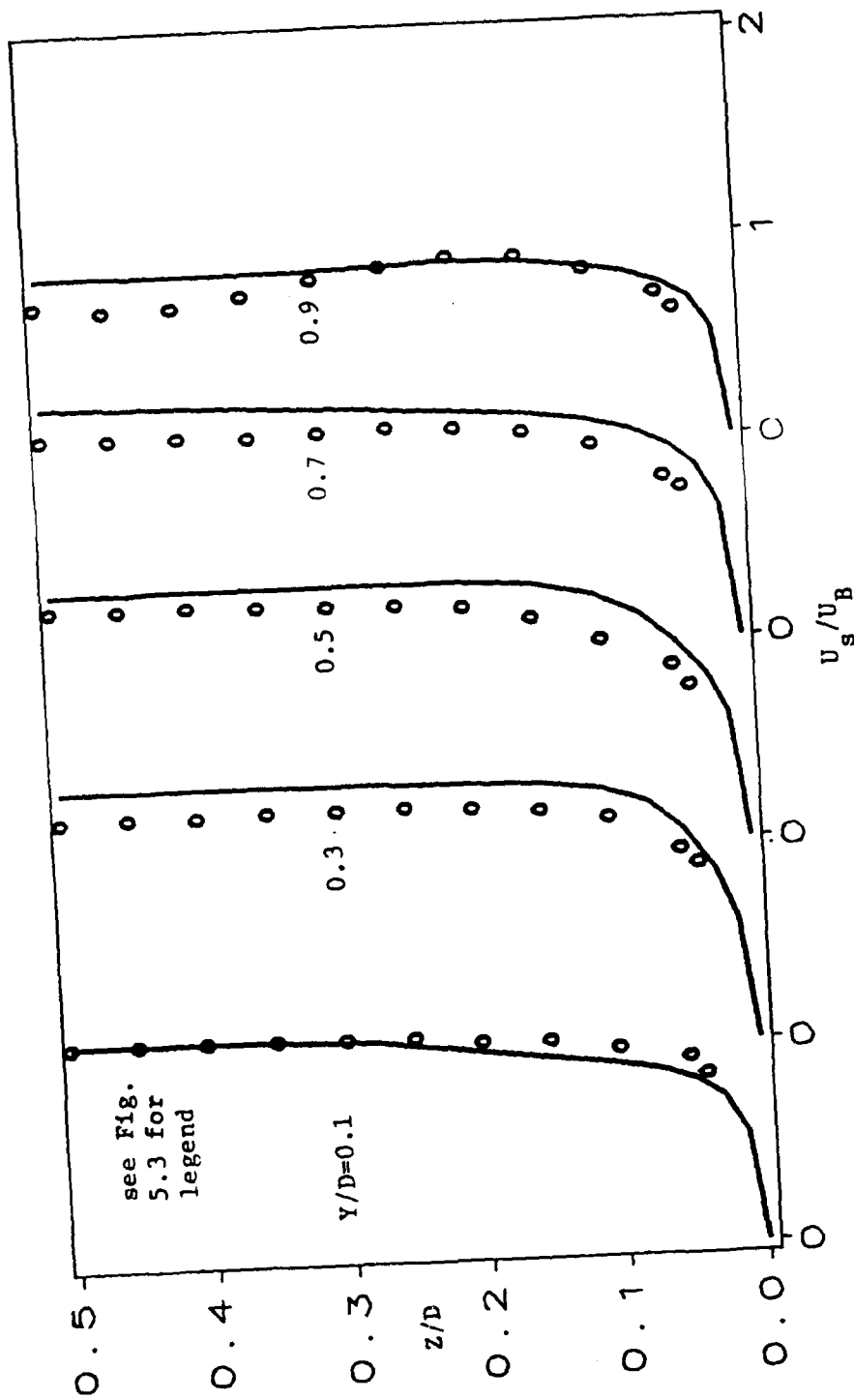at Station 4

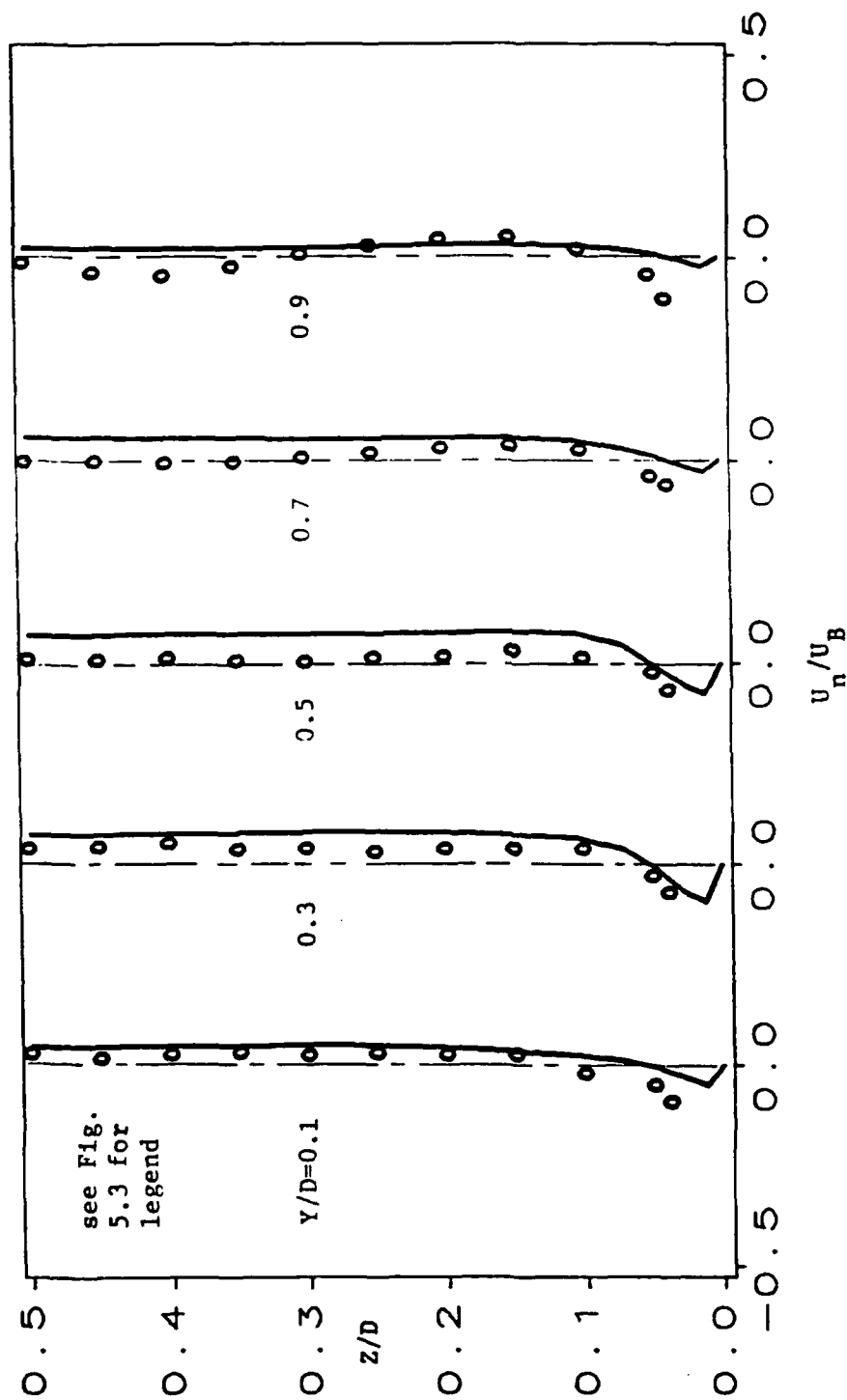Figure 5.8 Streamwise Velocity Profiles for the Turbulent S-Duct
at Station 5

Figure 5.9 Transverse Velocity Profiles for the Turbulent S-Duct
at Station 5

give rise to a poor prediction of the bulk pressure drop. Indeed, the computed transverse pressure gradient is well predicted everywhere while the bulk pressure drop is not well predict as seen in Figure 5.10. With the excellent agreement with the data for the laminar case for this same geometry, the less than stellar prediction of the turbulent flow implicates the turbulence model. The value of the near wall velocity gradient is strongly dependent upon the turbulence model. Good predictions of the skin friction in two dimensions have been achieved by many users of the Baldwin and Lomax (1978) algebraic model. Therefore, simple extension of the two-dimensional model to three dimensions without regard for the actual physics of a three-dimensional boundary layer may be the reason for the reduced accuracy. The next challenge then is to compute the turbulent flow in a turbomachinery blade row.

5.3 Flow in an End Wall Cascade

The three-dimensional turbulent flow in a turbine end wall cascade was computed using the NPM method. The flow was measured using a hot wire probe by Flot and Papailiou (1975). The cascade was made up of NACA 65-12-A_{10}-10 blades with a stagger angle of -15°. The span to chord ratio was 2.1, the pitch to chord ratio was 0.8 and the flow Reynolds number was 389,000. The geometry and measurement locations are given in Figure 5.11. Only the blade region was computed and the computational grid consisted of 30 points in the streamwise direction and a 23x23 grid in the cross plane. Both the algebraic eddy viscosity model and the k-ϵ turbulence model were used to compute this flow. There was very little difference in computational results between the two models but the use of the k-ϵ model required more computation time.
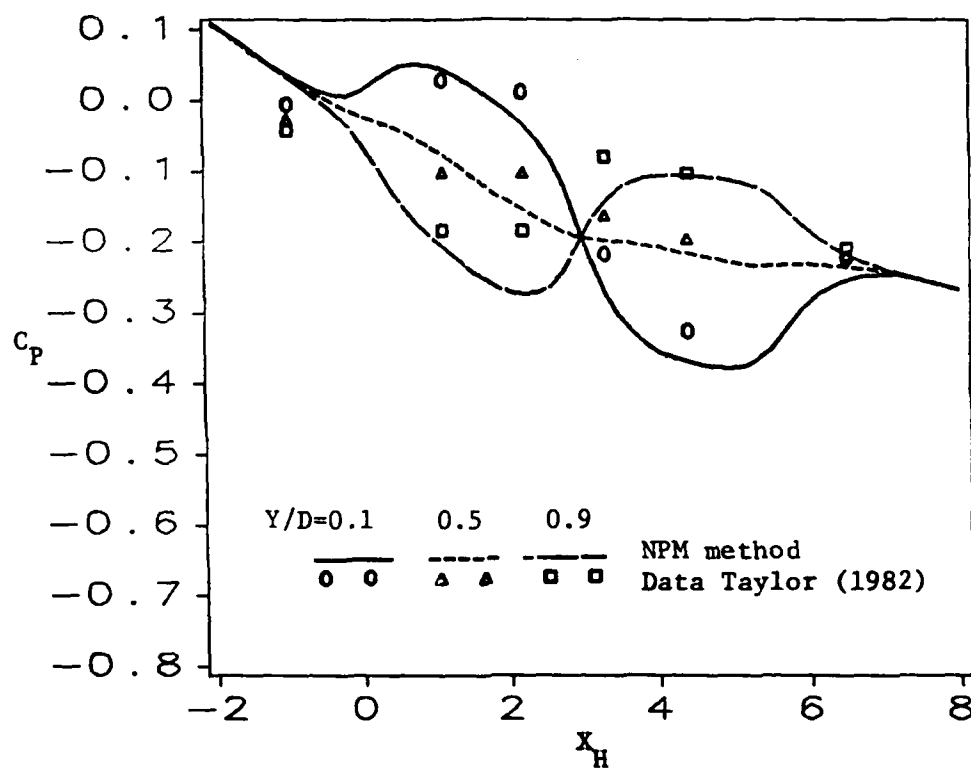
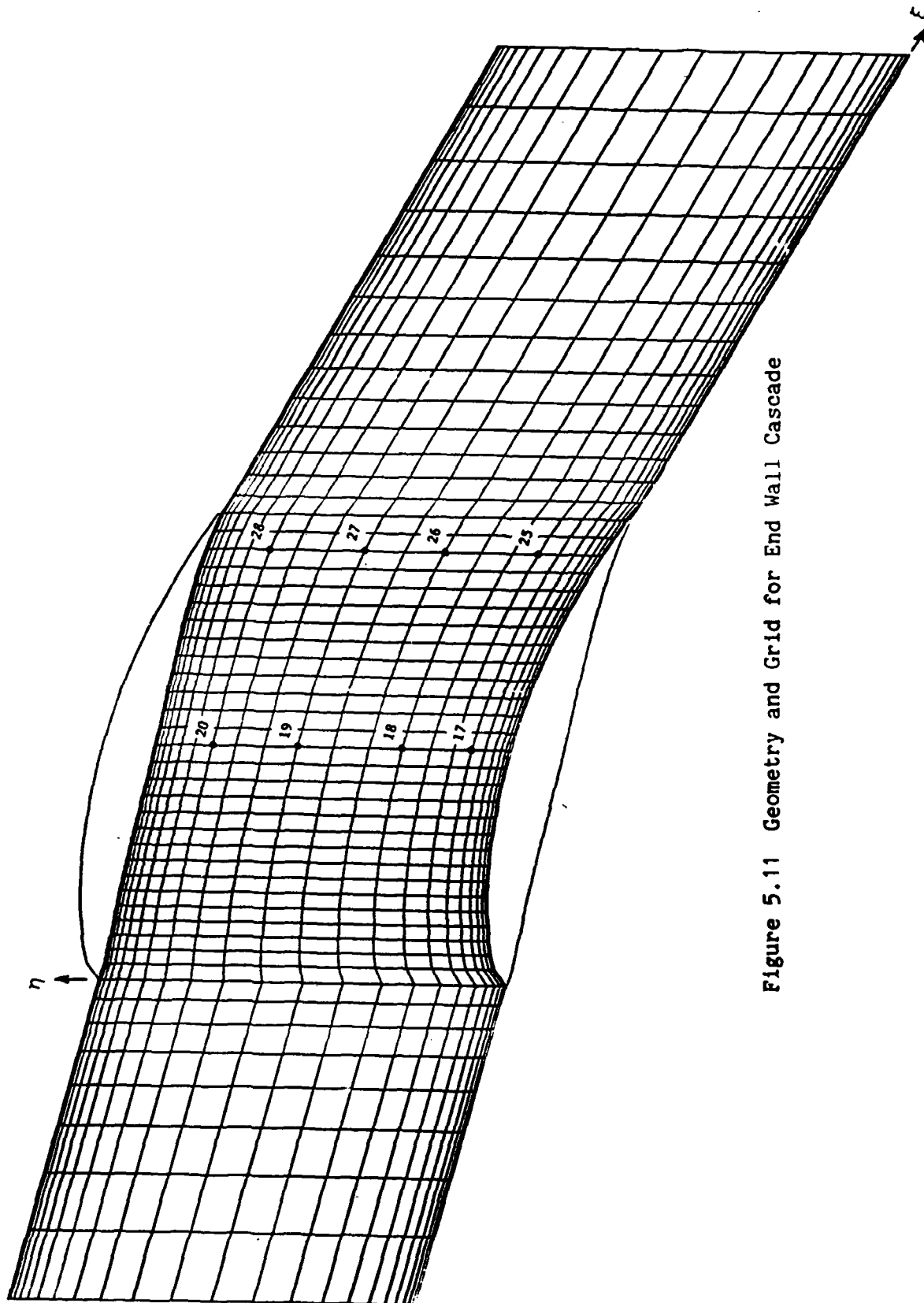Figure 5.10 Computed Coefficient of Pressure for the Turbulent

S-Duct

Figure 5.11 Geometry and Grid for End Wall Cascade

The following results were from the two-equation model. The no-slip boundary condition was used on the blade surfaces as well as on the end wall boundary. A symmetry boundary condition was applied at the mid-span. The inviscid velocity distribution was used as inlet conditions at the blade leading edge to start the computation.

The convergence history is presented in Figure 5.12. For this case, a was set to 20 and the pressure residuals dropped one and one half orders of magnitude in 50 global iterations. At this point, the convergence flattened out and the computation was stopped in order to conserve CPU time.

The computed pressure distribution at the mid-span is compared to the experimental data in Figure 5.13 with excellent agreement. The inviscid pressure distribution computed from the panel code of Giesing (1964), used as the initial pressure distribution, is also presented in Figure 5.13. The pressure near the end wall is very similar to that at the mid-span which gives creedence to the assumption that the normal gradient of pressure is zero following classical boundary layer theory. The good agreement with the experimental data indicates that the NPM method is capable of computing the viscous pressure field accurately unlike the PL method and various other space-marching methods.

The computed streamwise end wall velocity profiles at 44% chord and 88% chord are compared to the experimental data in Figures 5.14 and 5.15, respectively. The agreement with the data is very good near the suction side and near mid pitch at both streamwise locations. Near the pressure side, the results are not as good and this may be due to a poor prediction of the pressure side blade boundary layer. Unfortunately, no blade boundary layers were measured to verify this. Figure 5.16 shows
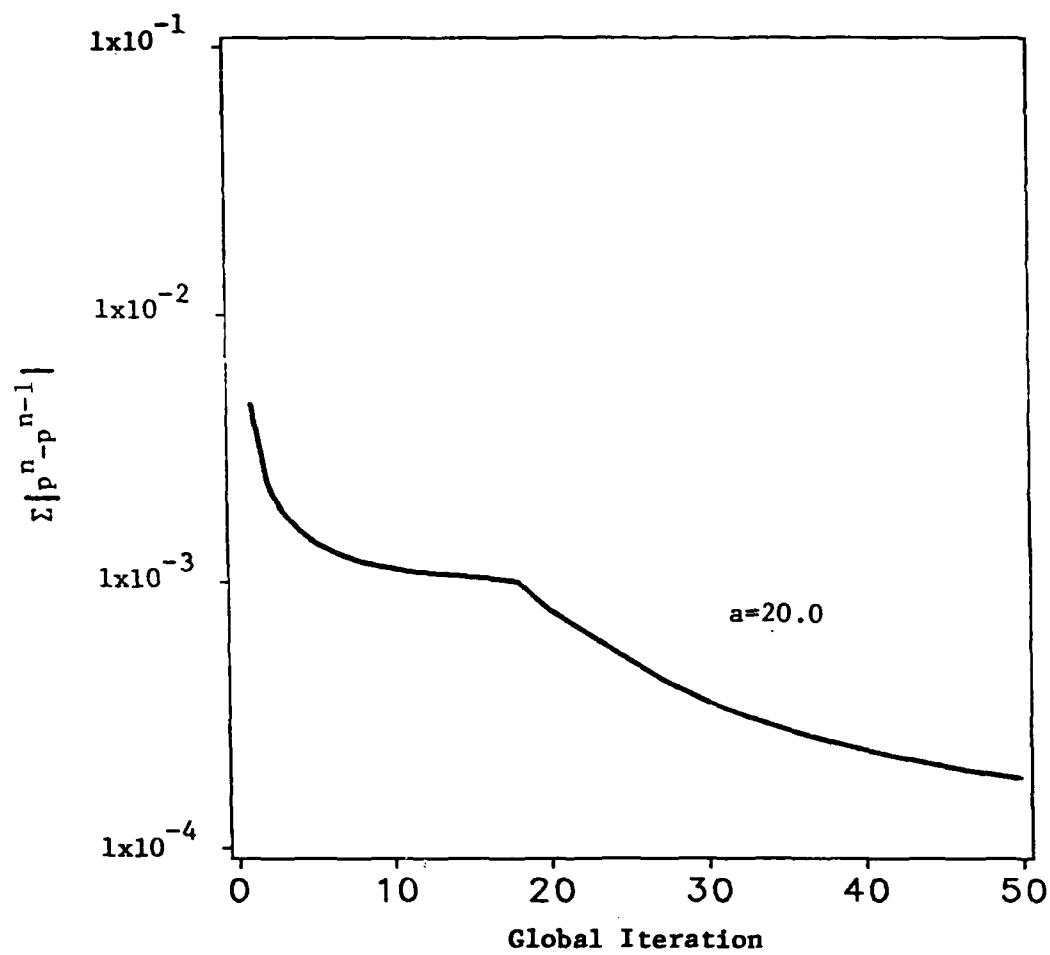
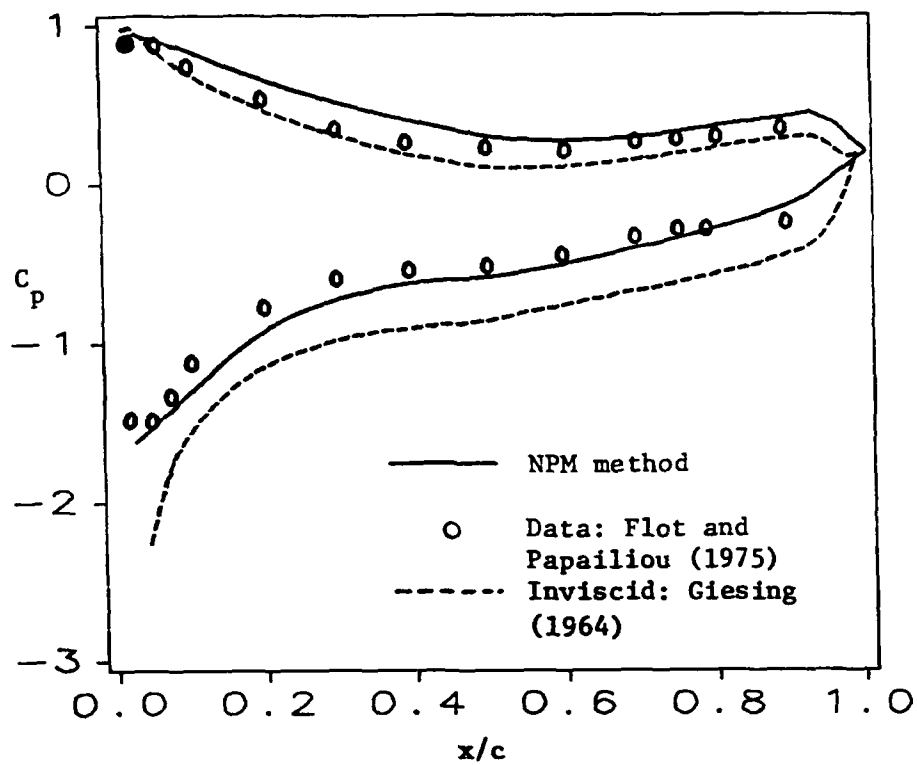Figure 5.12 Convergence History for the End Wall Cascade

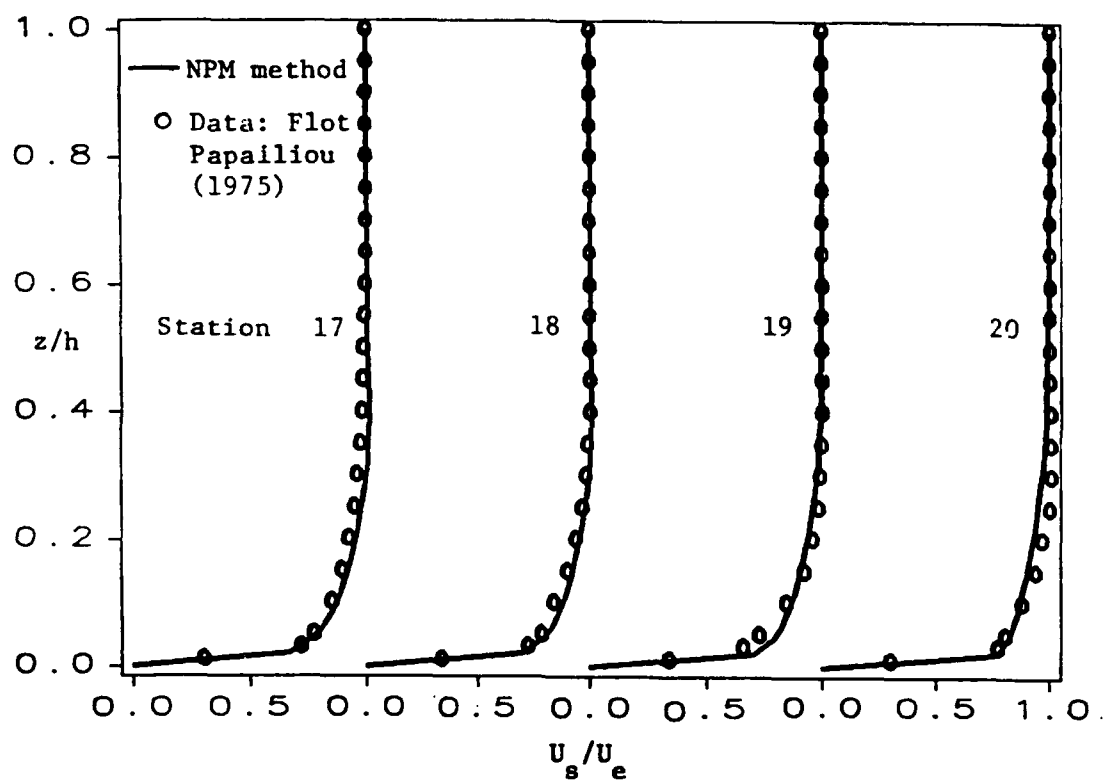Figure 5.13 Pressure Distribution for the End Wall Cascade

Figure 5.14 Streamwise Velocity Profiles at 44% Chord for the
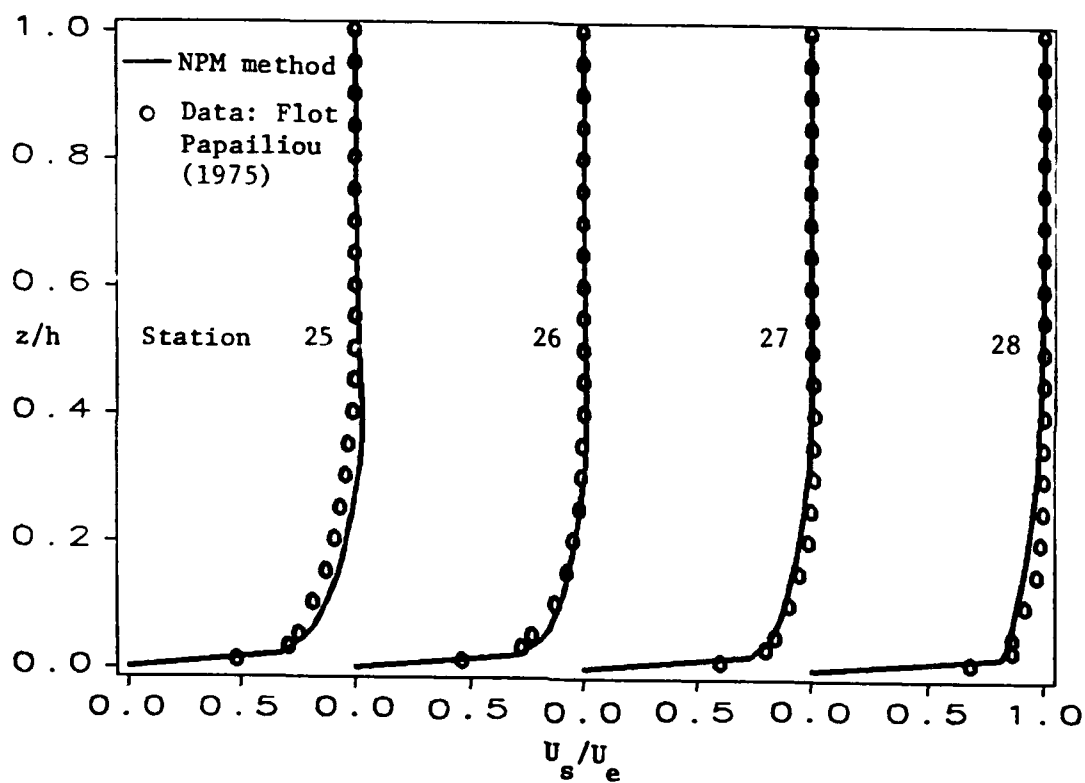End Wall Cascade

Figure 5.15 Streamwise Velocity Profiles at 88% Chord for the
End Wall Cascade

the computed streamwise momentum thickness compared to the the experimental data. The blade to blade variation is well predicted as is the level of the momentum thickness. One can see that the secondary flow is convecting the low momentum fluid to the suction side from the pressure side boundary layers thereby thinning them. The computed secondary end wall velocity profiles are compared to the experimental data at 44% chord and 88% chord in Figures 5.17 and 5.18, respectively. At all locations, the overturning of the flow near the end wall is reasonably well predicted while the flow underturning in the outer reaches of the boundary layer is underpredicted. Since the streamwise profiles were well predicted, one can assert that the error is due to a poor prediction of the transverse pressure gradient near the end wall which drives the secondary flow. Overall, however, the prediction of the secondary flow is good.

The passage vortex is clearly visable from a plot of the computed secondary velocity vectors in Figures 5.19 through 5.21. Careful inspection reveals that the center of the passage vortex is convected from the pressure side to the suction side boundary. Finally, the computed mass averaged secondary flow kinetic energy k_{sec} is presented in Figure 5.22. The secondary flow kinetic energy may be thought of as unrecoverable energy thus it is indicative of the viscous flow losses within the passage. From the results presented in this section, it is apparent that the NPM method is capable of computing the viscous flow in the end wall region of a turbomachinery blade row. The major feature of such a flow, namely the passage vortex system, is well predicted.
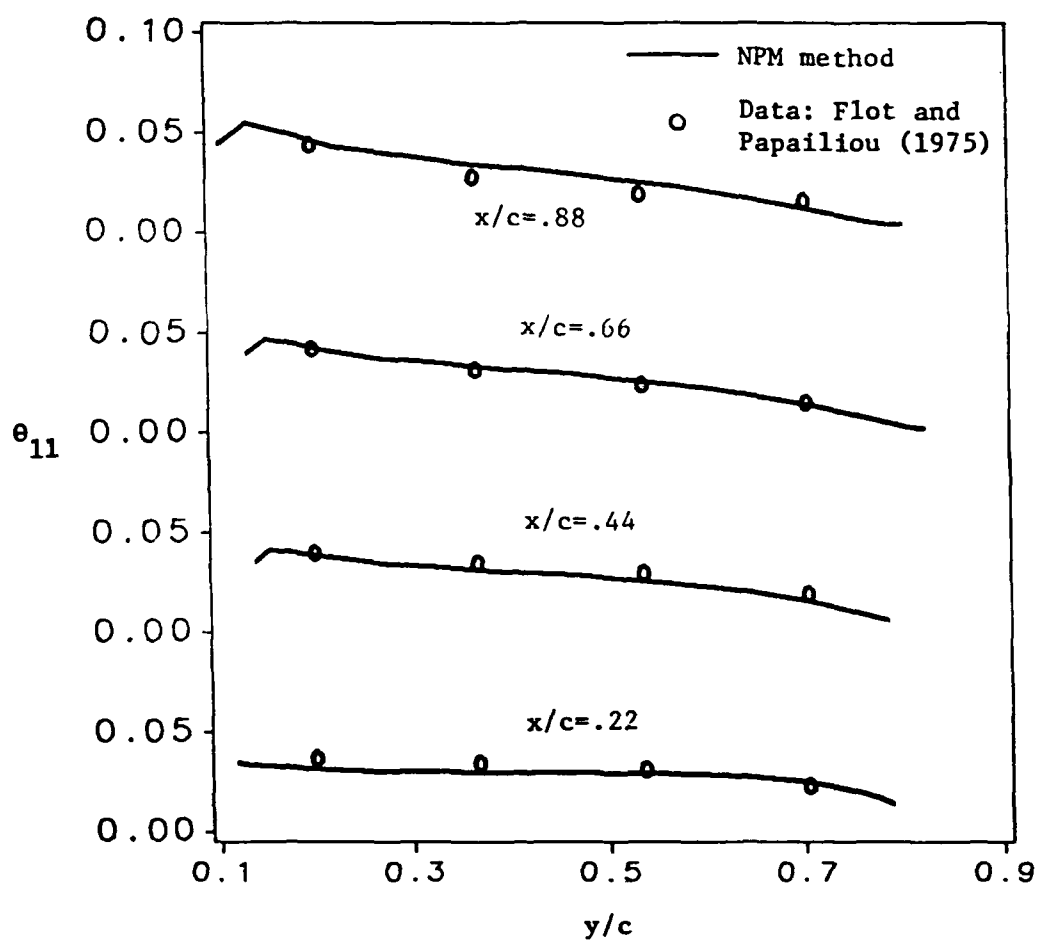
Figure 5.16 Streamwise Momentum Thickness for the End Wall Cascade
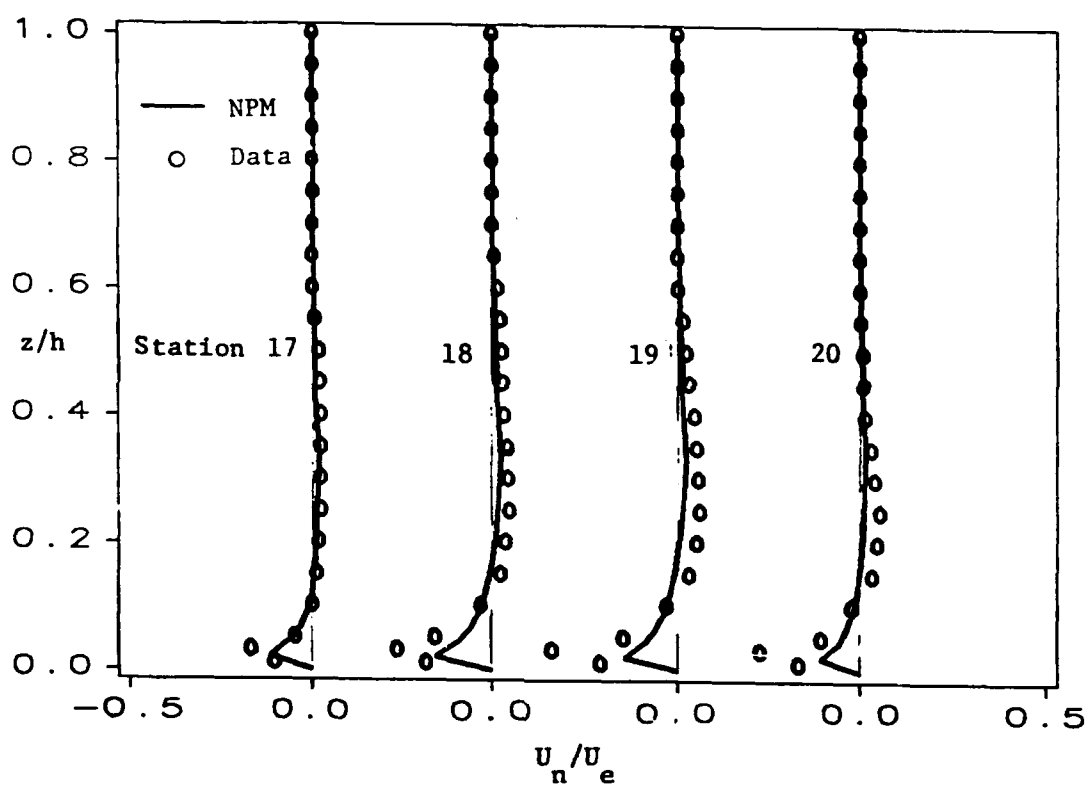
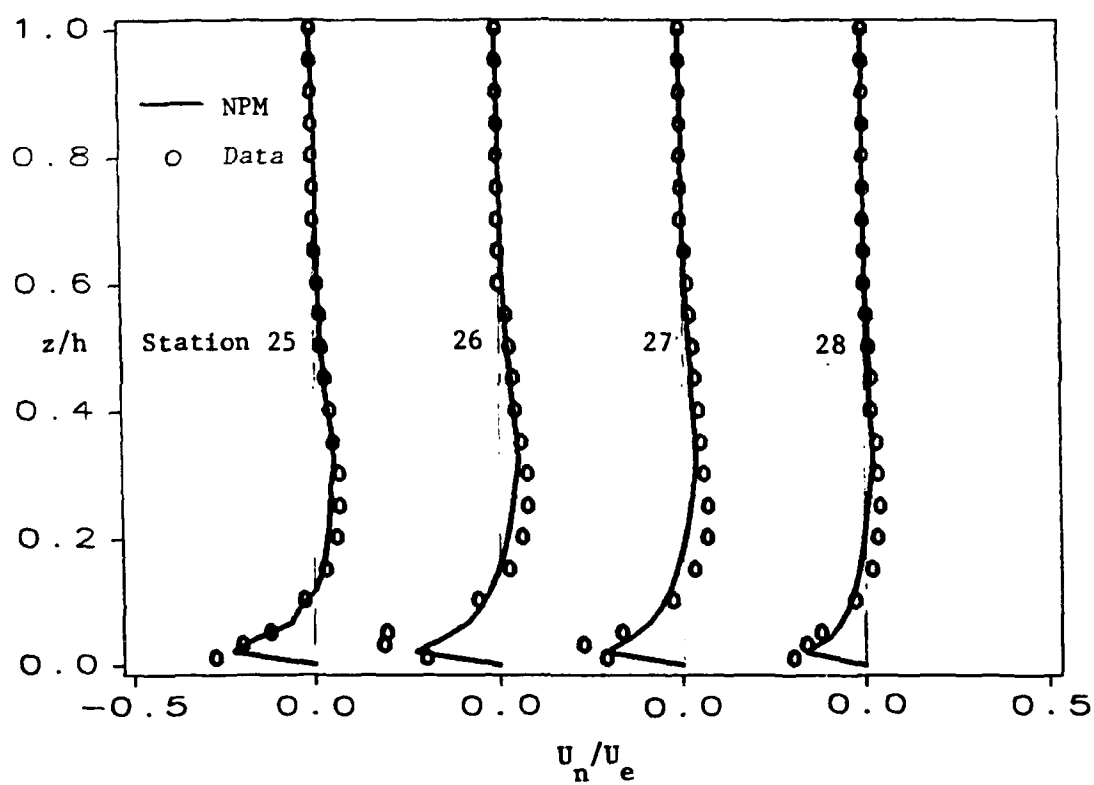Figure 5.17   Transverse Velocity Profiles at 44% Chord for the

End Wall Cascade

Figure 5.18 Transverse Velocity Profiles at 88% Chord for the
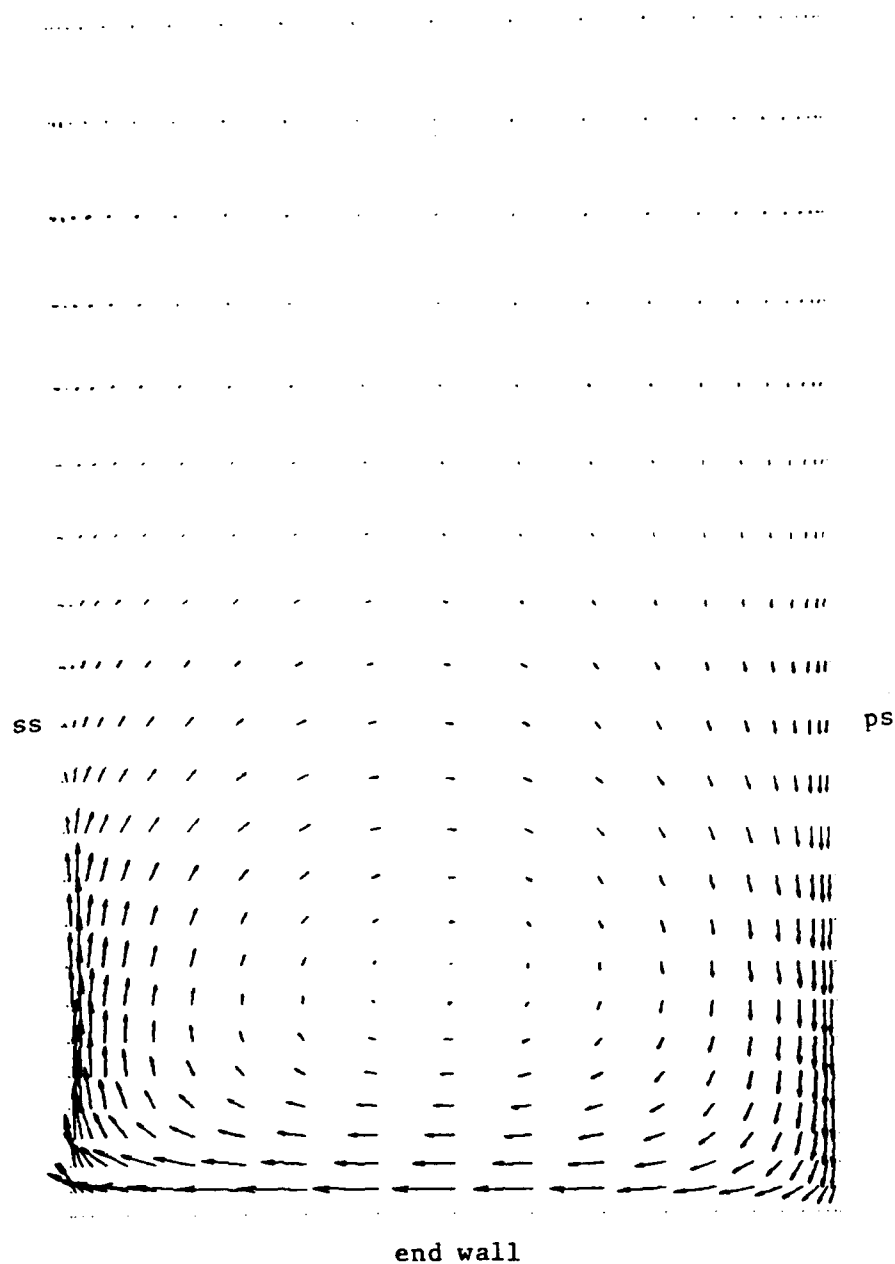End Wall Cascade

ss

ps

end wall

Figure 5.19 Secondary Flow Velocities at 44% Chord for the
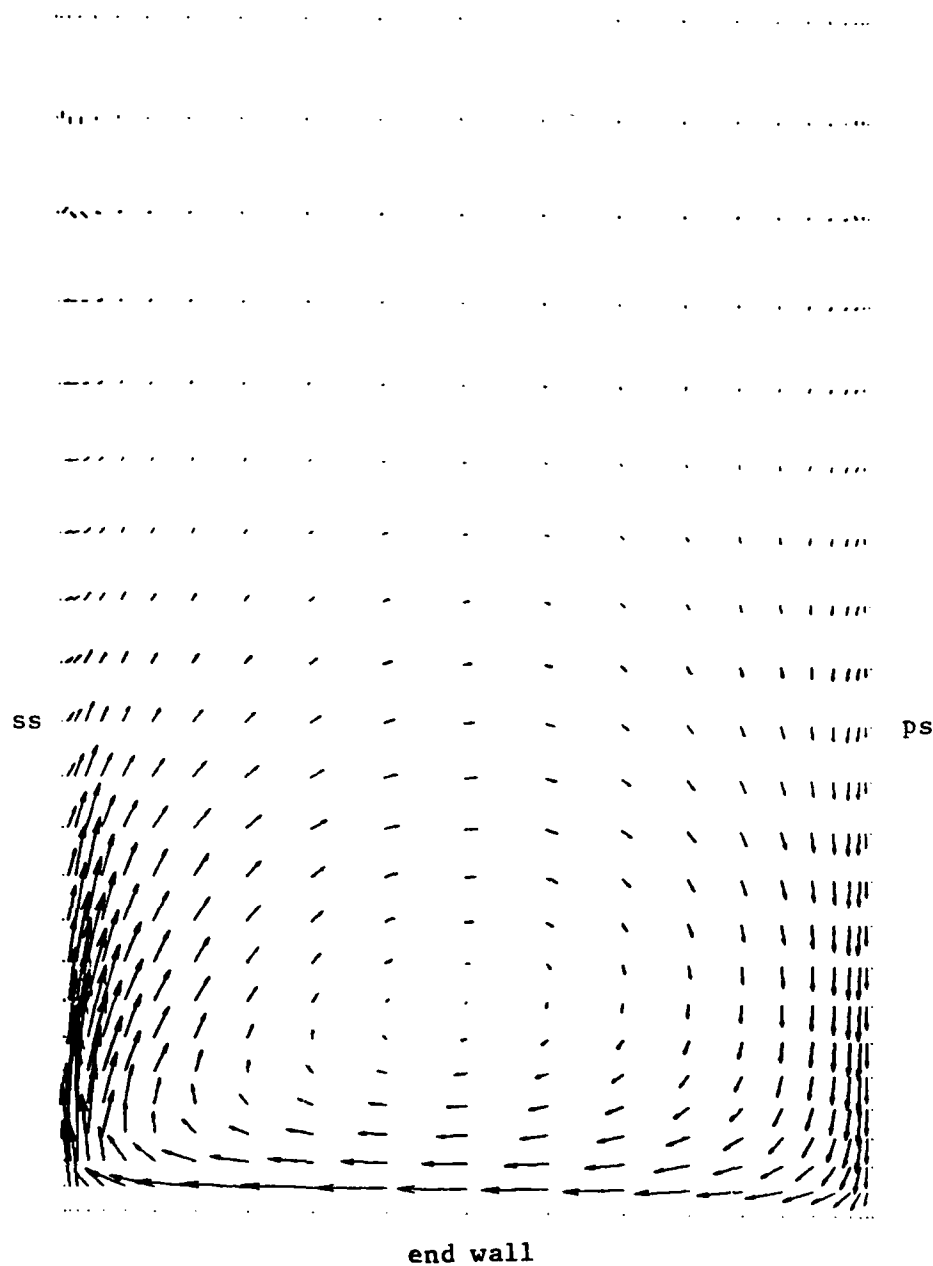
End Wall Cascade

ss ps

end wall

Figure 5.20 Secondary Flow Velocities at 66% Chord for the
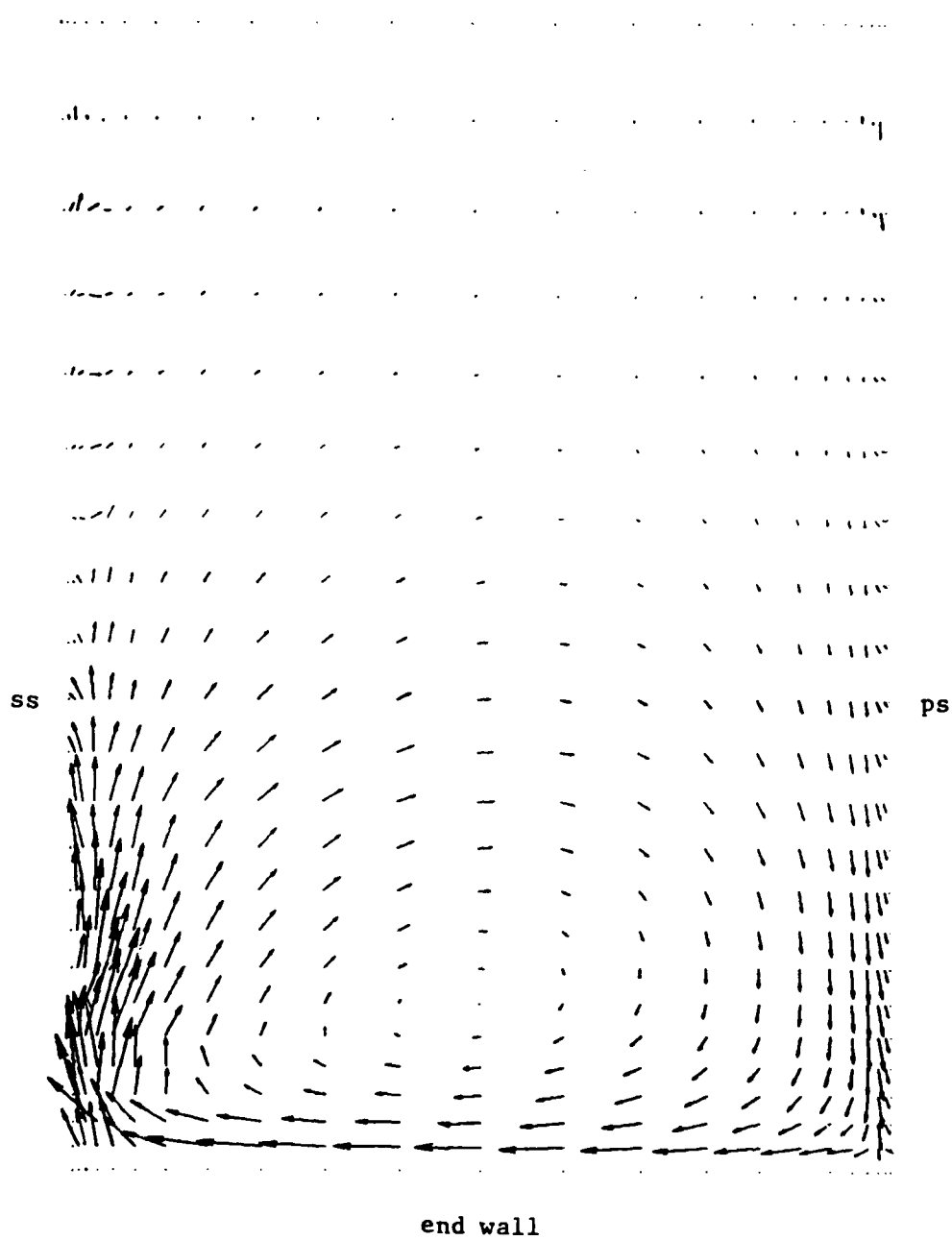
End Wall Cascade

Figure 5.21   Secondary Flow Velocities at 88% Chord for the
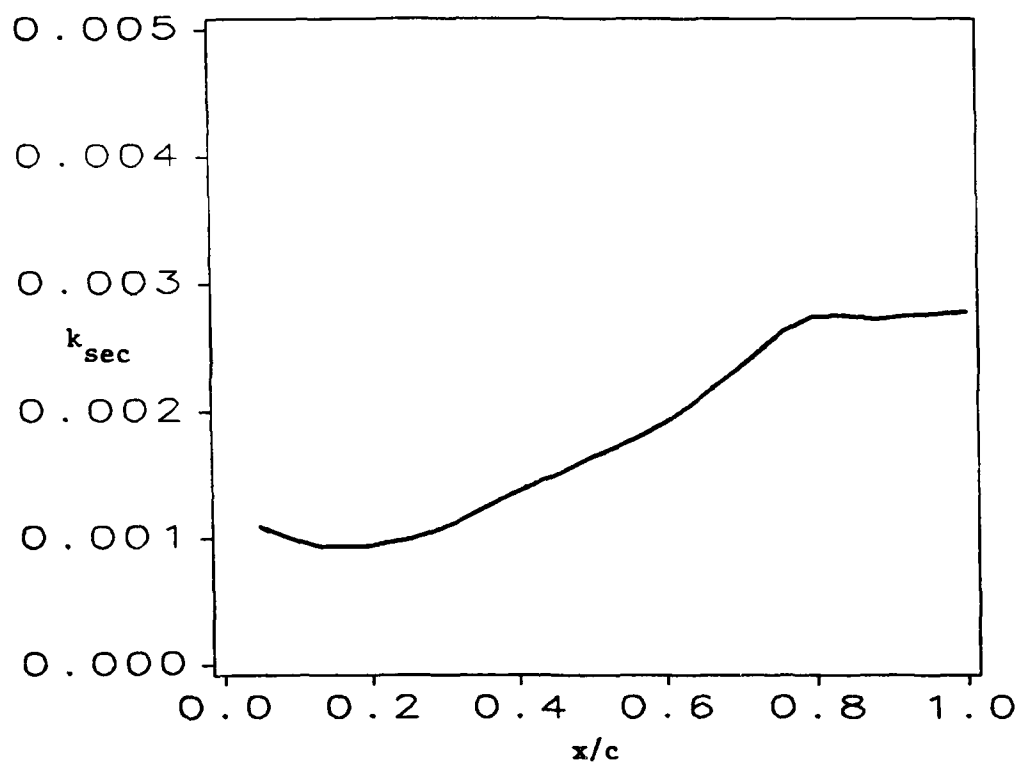End Wall Cascade

Figure 5.22 Mass Averaged Secondary Flow Kinetic Energy

for the End Wall Cascade

5.4 Compressor Cascade Wake Flow

The new parabolic-marching method was used to compute the turbulent wake of a compressor cascade. The flow field was measured by Hobbs et al. (1980) using a hot film probe for the near wake and a five hole probe for the far wake. The blades are double circular arc airfoils with a stagger angle of 20.77°. The space to chord ratio is 0.6 and the flow Reynolds number is 588,000. Although the experimental facility used end wall suction to ensure two-dimensionality, the computation was carried out assuming an end wall was present and only results at the mid-span were considered. The geometry and computational grid at the mid-span is shown in Figure 5.23. The inviscid pressure computed from the panel method code of Giesing (1964) was used as the initial pressure field. The corresponding inviscid velocity at the inlet was used as inlet conditions as was done for the Flot and Papailiou (1975) end wall cascade in section 5.3. In order to save CPU time and since the blade boundary layers are very thin, the inviscid inlet condition was applied near the mid-chord region where the boundary layer thickness of a typical turbulent boundary layer reached a height equal to the distance of the first grid point from the surface. The no-slip condition was used on the blade surfaces and the slip condition was applied on the end wall in an effort to achieve two-dimensionality.

The flow was computed with both the algebraic eddy viscosity model and the two-equation turbulence model. When the algebraic model was used, the best convergence was achieved with a equal to 10 as seen in Figure 5.24. The wake centerline velocity computed with the algebraic eddy viscosity model is compared to the experimental data in Figure 5.25. x is the distance from the trailing edge and Bx is the axial
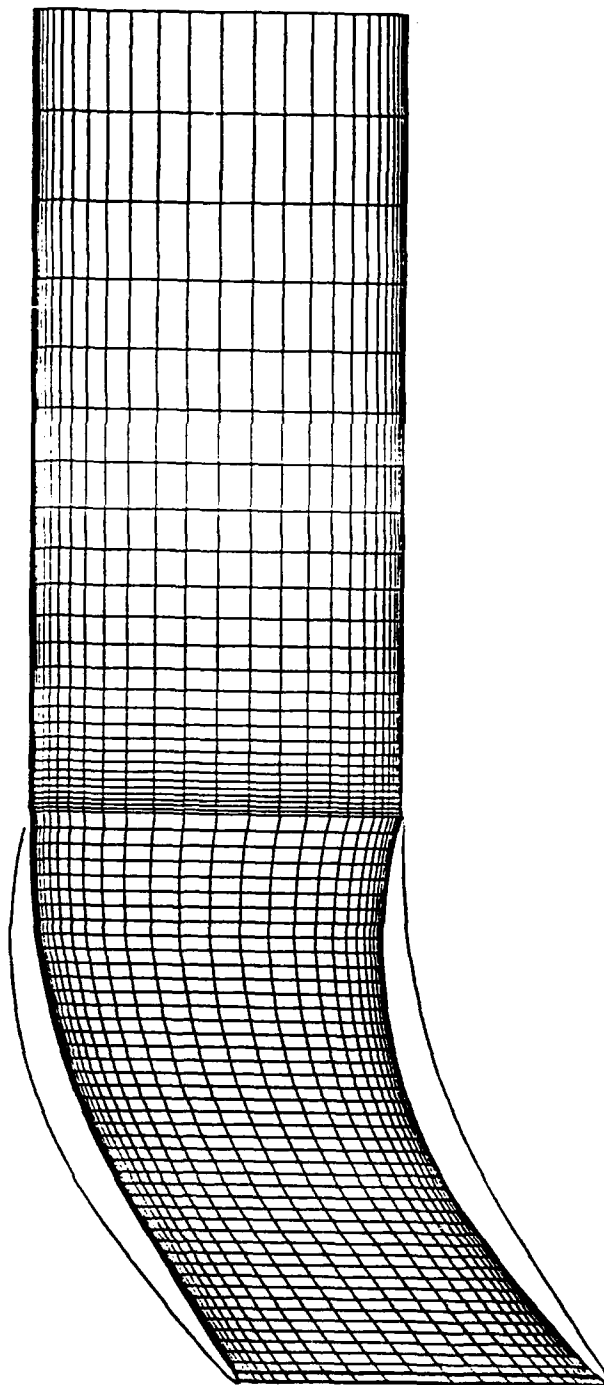
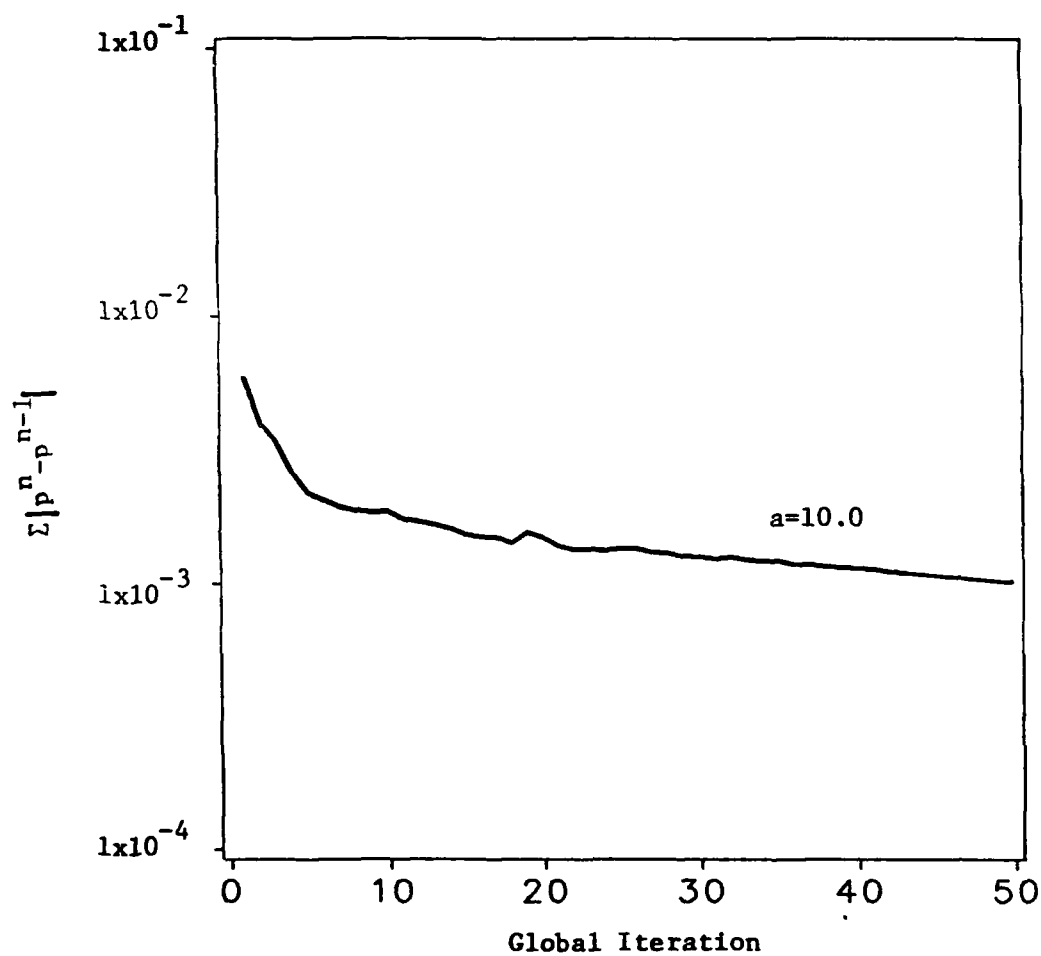Figure 5.23   Geometry for Hobbs Cascade Wake Flow

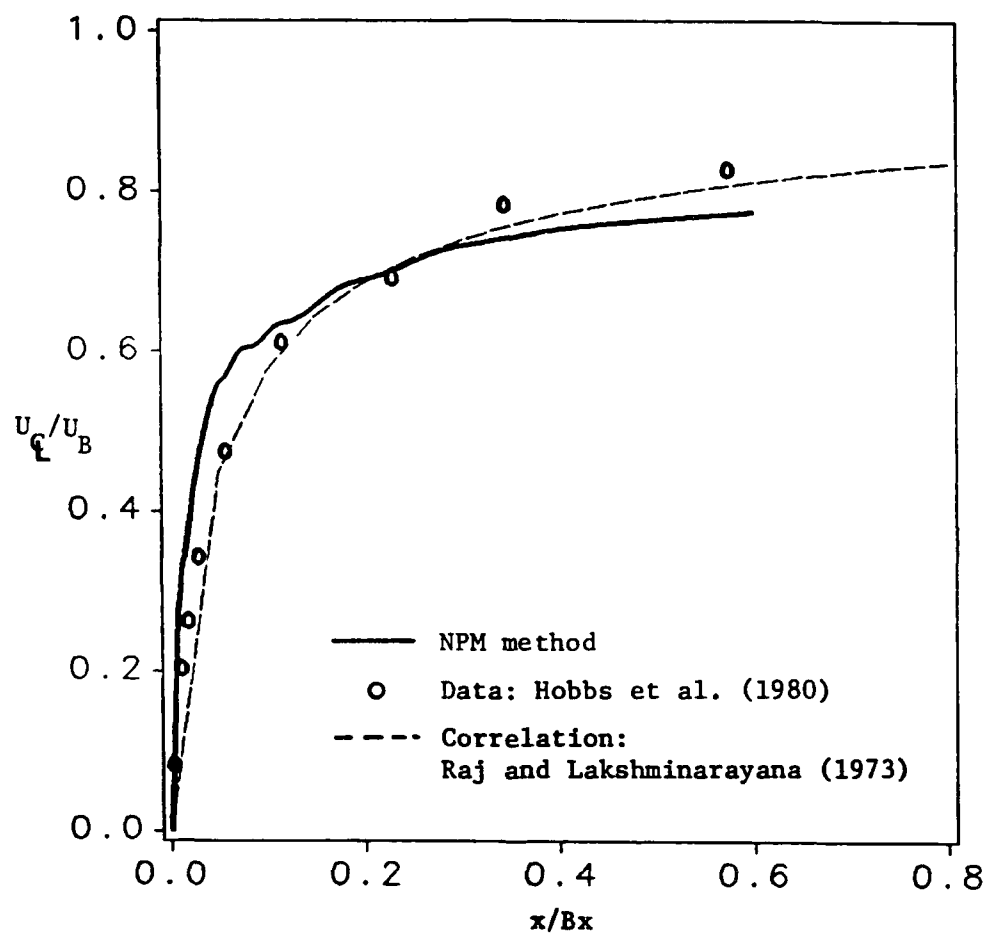Figure 5.24   Convergence History for Hobbs Cascade, Alg. Model

Figure 5.25 Centerline Velocity Distribution in the Wake of

Hobbs Cascade, Alg. Model

chord length. Also displayed is the wake correlation of Raj and Lakshminarayana (1973). The agreement between the computation, experimental data, and correlation is good, however, the computed wake defect is underpredicted in the near wake region while it is overpredicted in the far wake region. The comparison of the computed wake profiles with the experimental data is given in Figure 5.26. In the very near wake, the computed velocity profiles do not compare well with the experimental data near the wake centerline. In this region, the velocity gradients are very large and the NPM method had difficulty computing them. In the outer flow region, the velocity profile is very well predicted owing to the strong influence of the boundary layer which was reasonably well captured. The nature of the turbulence is very complicated near the centerline of the wake and the algebraic turbulence model does not seem to have the power to resolve the strong interaction.

The far wake is only adequately predicted. The wake centerline position is below the measured position and the wake spreading is less than measured. The wake spreading is a strong function of the turbulence and the ad hoc approximations made in the algebraic turbulence model may contribute to the poor prediction.

The two-equation k-ε model, which includes more physical properties in its formulation, was used in an effort to improve the prediction. The convergence history shown in Figure 5.27 is almost identical to that using the algebraic eddy viscosity model. The extra physics included in the k-ε model have indeed improved the prediction of the wake flow. The computed centerline velocity, shown in Figure 5.28, indicates the improved prediction accuracy especially in the far wake region. The wake defect is again underpredicted in the near wake region by a
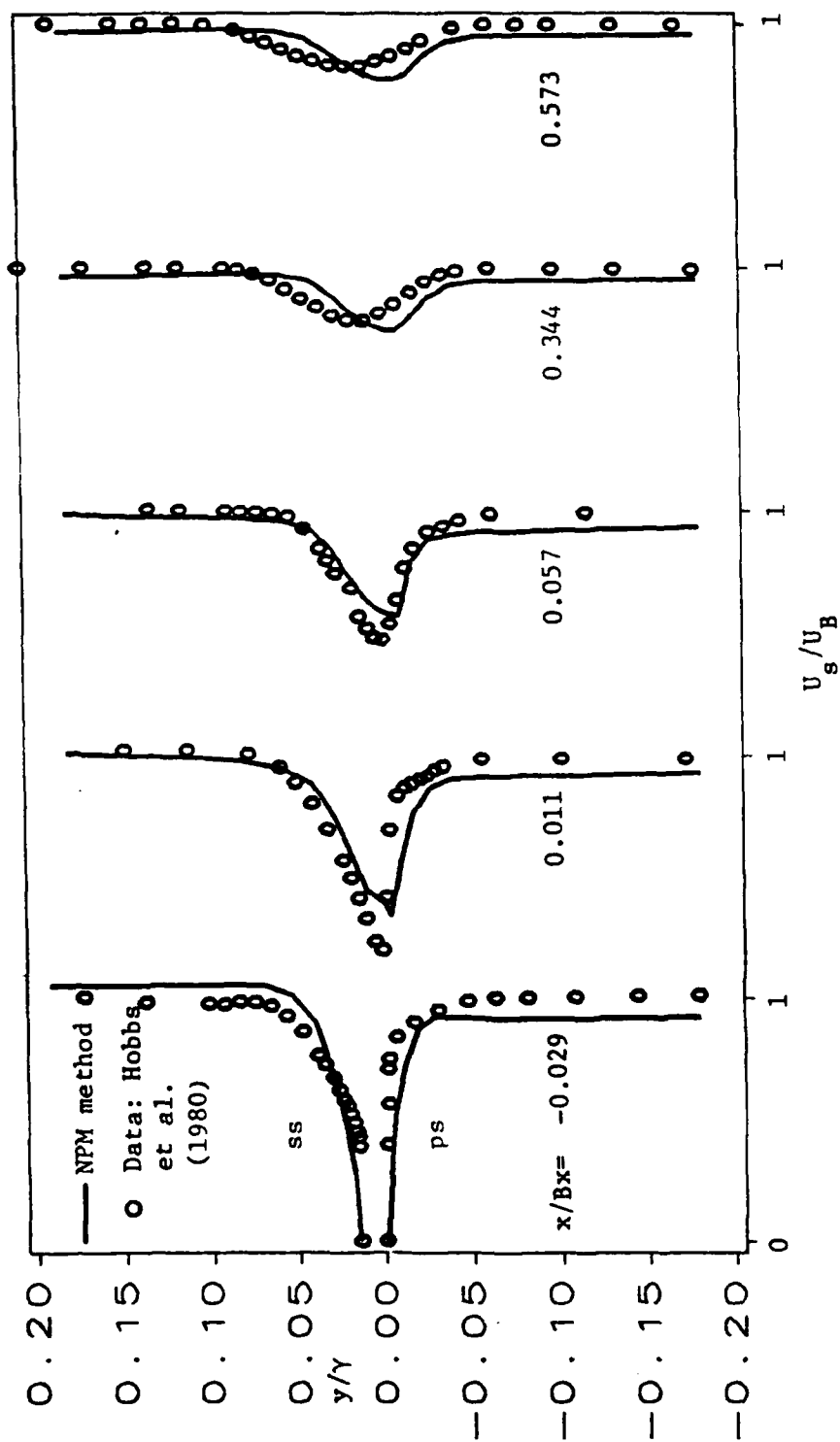
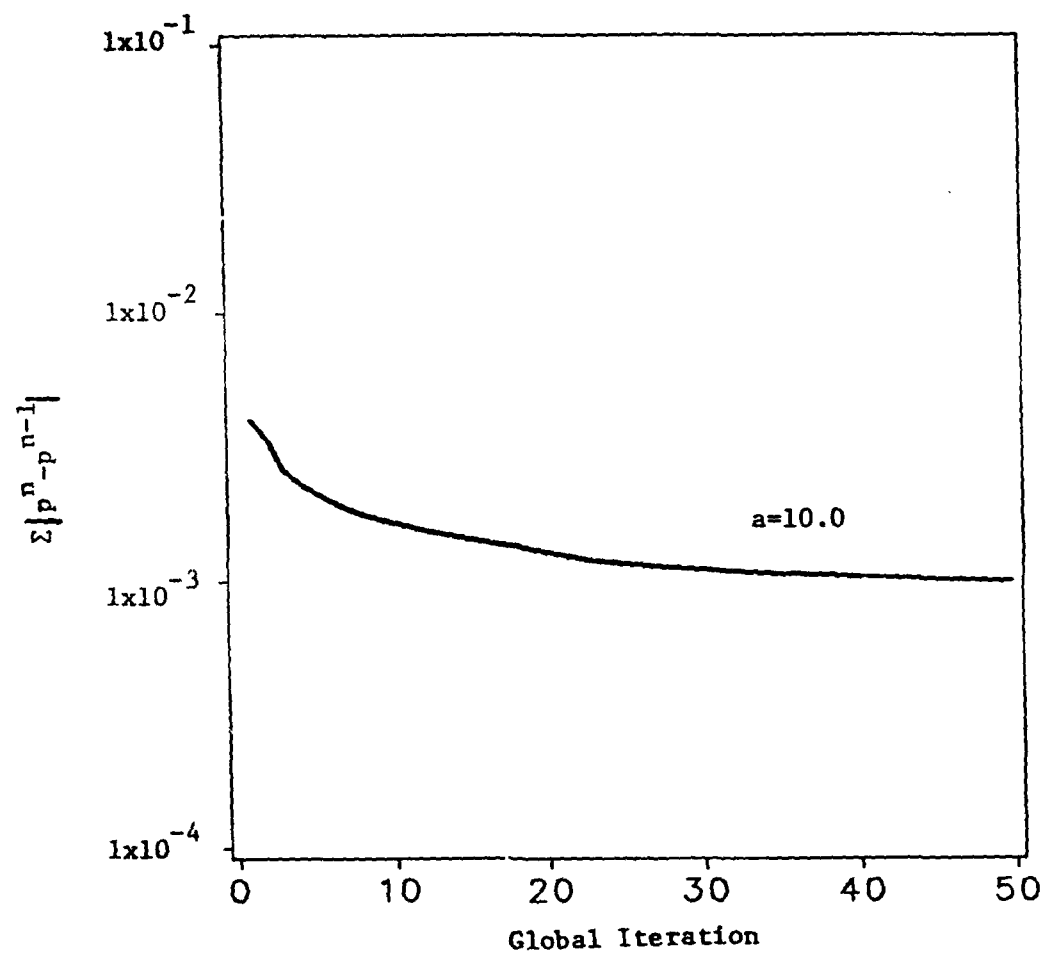Figure 5.26 Wake Profiles for Hobbs Cascade, Alg. Model

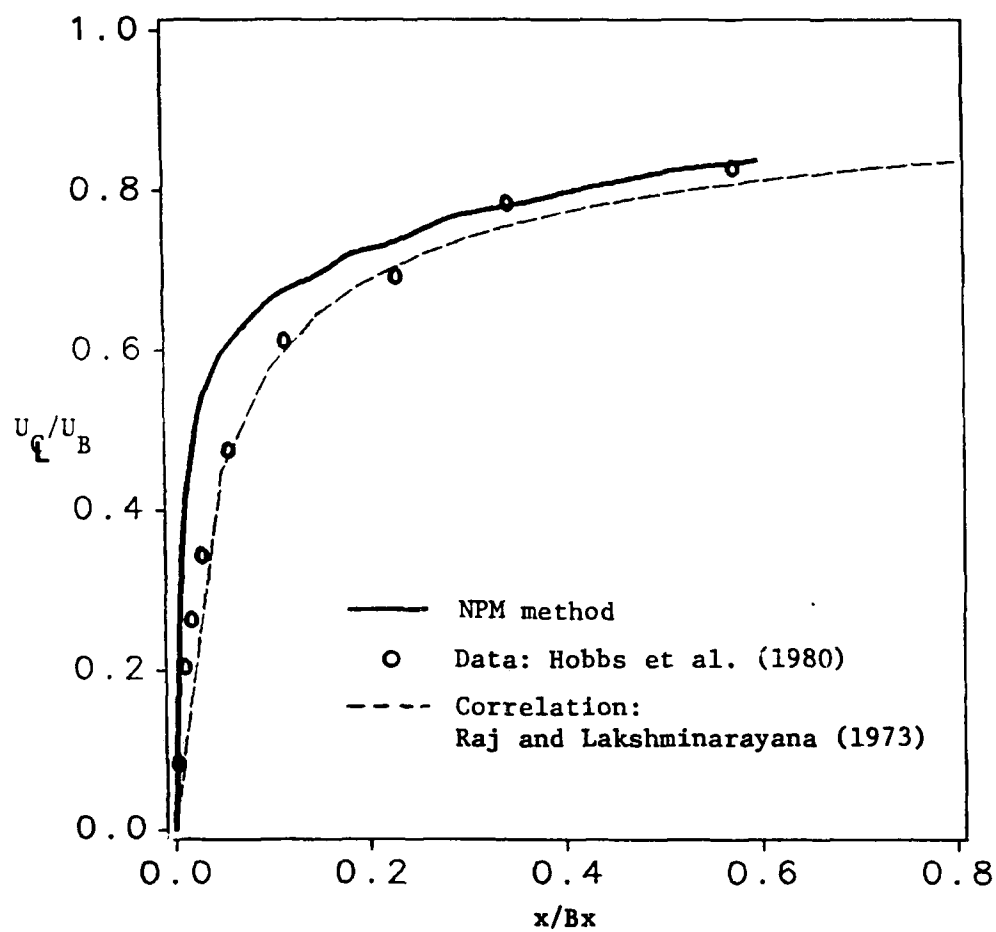Figure 5.27   Convergence History for Hobbs Cascade, k-ε Model

Figure 5.28 Centerline Velocity Distribution in the Wake of Hobbs

Cascade, k-ε Model

substantial amount, however, in the far wake, the defect matches the experimental data almost exactly. The spreading rate is also accurately predicted in the far wake.

The wake velocity profiles computed with the k-ε model are shown in Figure 5.29. Again the boundary layer profiles are reasonably well predicted, however, the near wake profiles show the same lack of agreement with the centerline data as with the computation with the algebraic model. In the far wake, the advantages of the k-ε model are clear with excellent agreement between the computation and the measurements. The wake centerline position as well as the wake spreading is accurately predicted even though the near wake predictions were not as accurate. This leads one to believe that the far wake is not strongly influenced by the near wake. Overall, the prediction using the k-ε model is superior to the prediction using the algebraic model for all regions of the flow. The computed turbulence intensities are compared to the experimental data for the near wake region in Figure 5.30. On the the blade surface, the turbulence intensities compare very well with the data. This is not surprising since the established k-ε model has been 'fine tuned' for wall bounded shear layers. In the near wake region, the peak intensities are not well captured. This can be attributed to the overprediction of the turbulence dissipation. For some coarse grid computations, this turbulence dissipation was so large that no turbulence could be sustained past the near wake region. Thus, there appears to be some grid dependence for this wake flow. It should be noted, though, that for a successful wake computation, special care had to be taken to ensure that the flow did not separate at the trailing edge. Such a situation generated incorrect turbulence kinetic energy
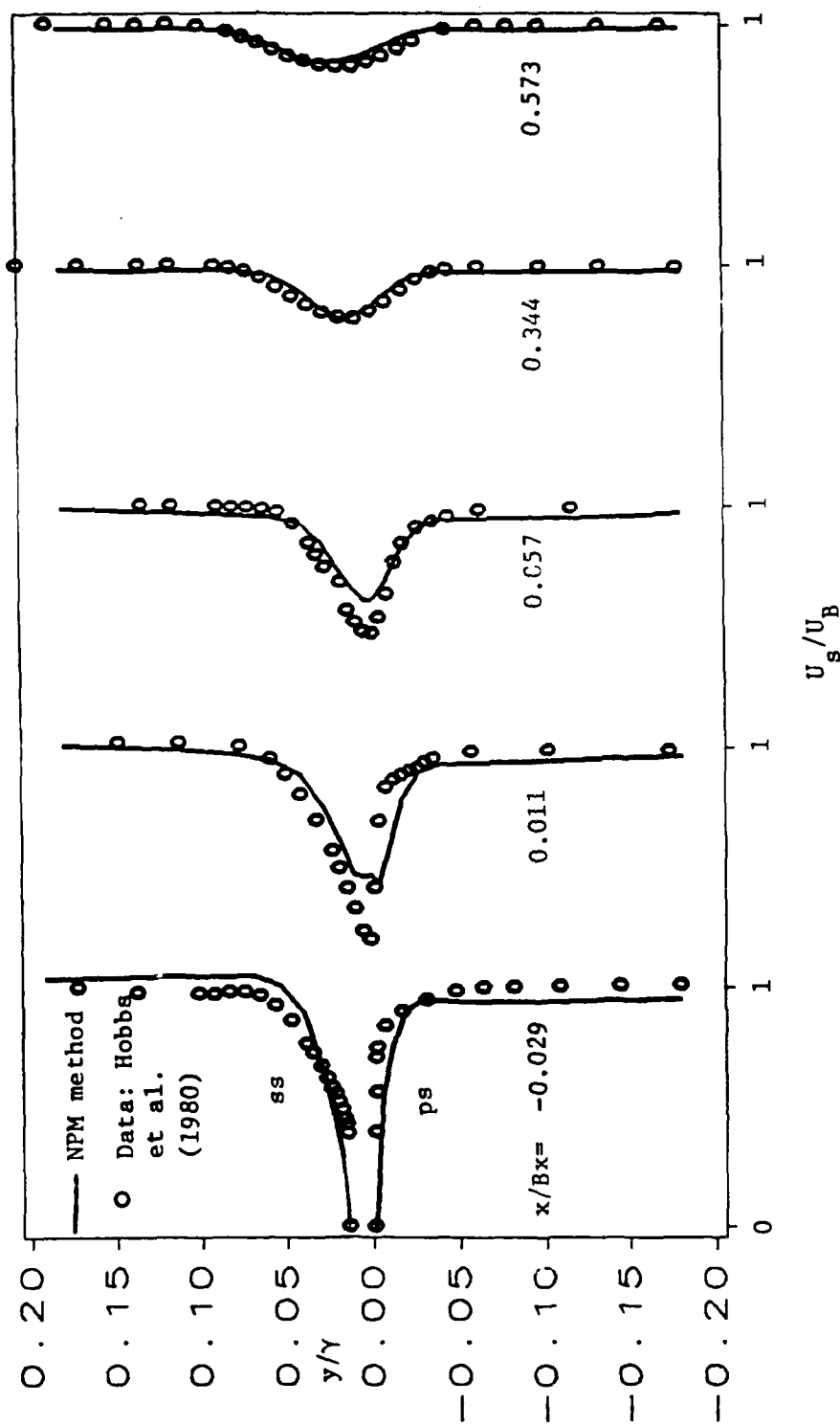
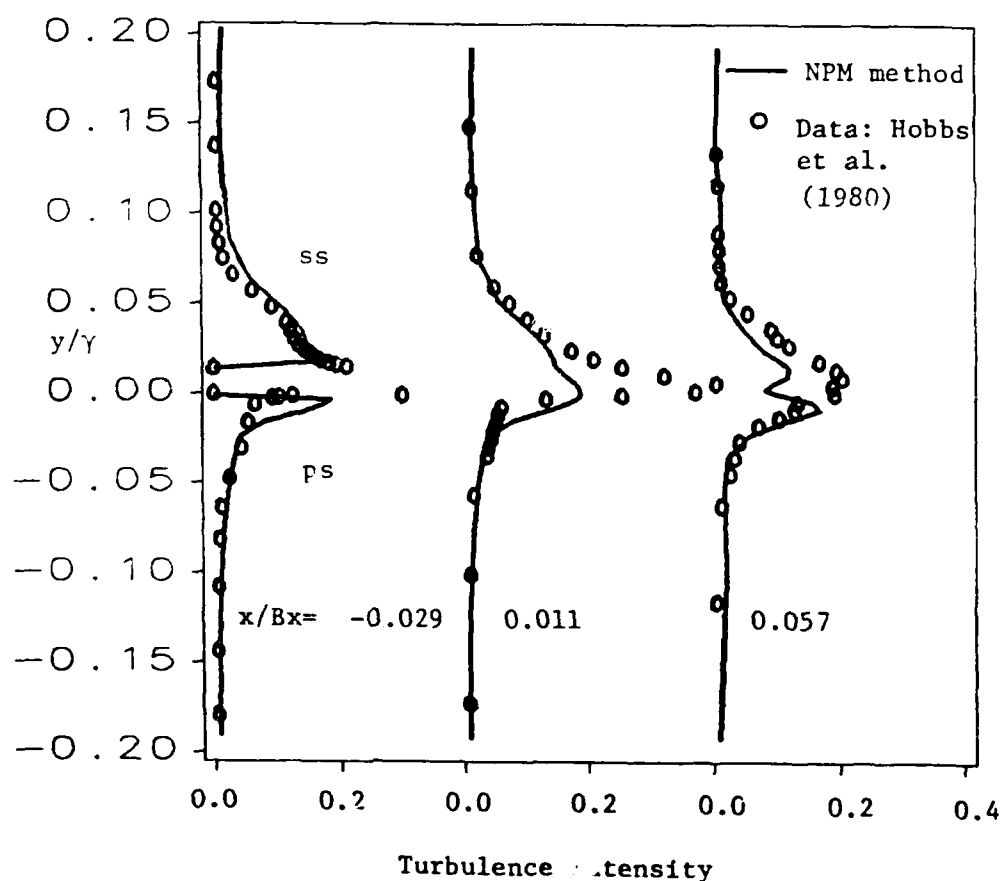Figure 5.29   Wake Profiles for Hobbs Cascade, k-ε Model

Figure 5.30   Turbulence Intensities in the Wake of Hobbs Cascade

and turbulence dissipation distributions in the strong interaction region which generally leads to divergent behavior.

The computed pressure distribution in the wake region is shown in Figure 5.31. The most important observation is that, while the streamwise pressure gradient in the outer flow is nearly constant, the pressure drops dramatically near the wake centerline close to the trailing edge. This localized effect is due to the acceleration of the wake centerline velocities. Thus, the transverse pressure gradient is not constant across the shear layer in the near wake region even for a non curving wake.

5.5 Flow in an Axial Flow Compressor Rotor

The final test of the NPM method was on the PSU axial flow compressor rotor. The facility is described in depth by Lakshminarayana (1980). The hub to tip ratio is 0.5 with the radius of the annulus wall being 0.466 meters. The rotor is made up of 21 NACA 65-010 blades with the stagger angle varying from 22.5^o at the hub to 45° at the tip. The overall performace of this compressor is given in Figure 5.32. The computations performed here were for the design flow coefficient of $\phi=0.56$. Although the tip clearance region is roughly 0.15 cm, the tip clearance effects were not included in the computation. Also, the measured relative inlet Mach number is 0.085 and the Mach number based on tip speed is 0.153 thus the assumption of incompressibility is valid.

The inviscid inlet conditions at the leading edge and the initial inviscid pressure field were generated by stacking several two-dimensional panel solutions using Giesing's (1964) program. Turbulent slip boundary conditions were used on all blade surfaces. Major
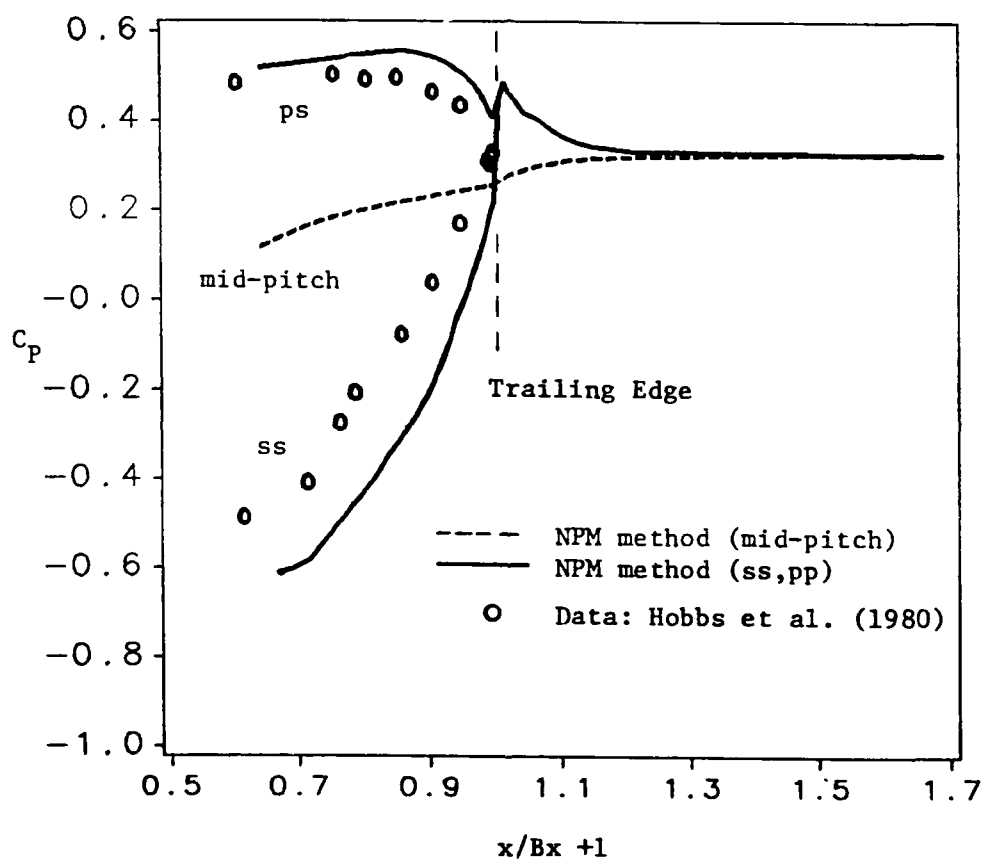
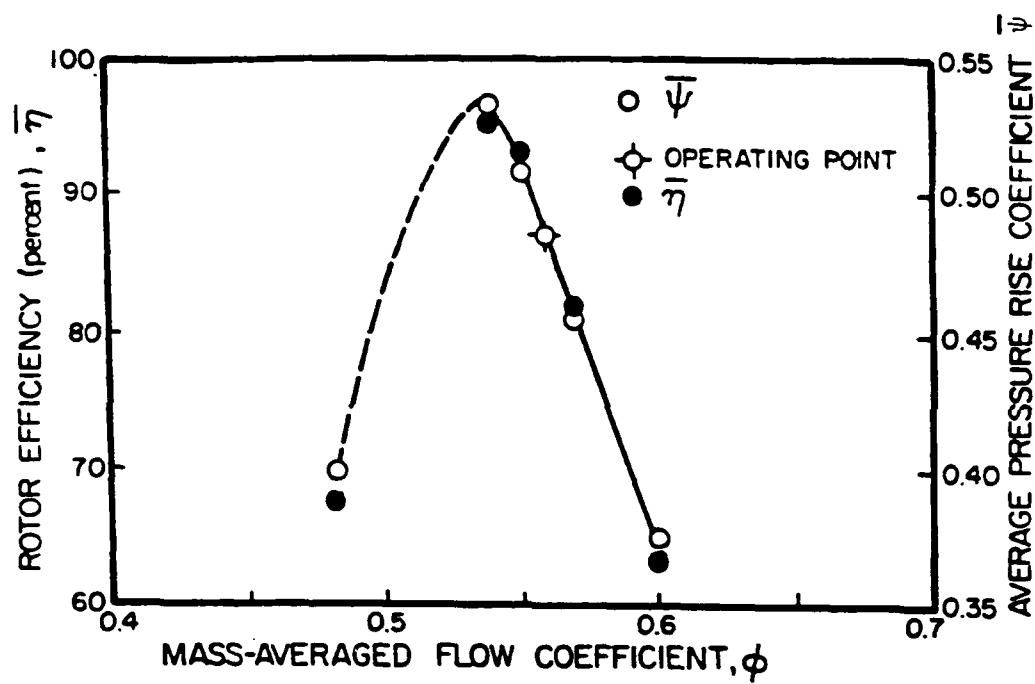Figure 5.31 Pressure Distribution for Hobbs Cascade, Alg. Model

Figure 5.32 Overall Performance for the PSU Compressor Rotor

difficulties were encountered when the k-ε turbulence model was applied to this case, thus the computation was performed using the algebraic eddy viscosity model.

The convergence history for the rotor computation using a equal to 25 can be seen in Figure 5.33. Convergence of one and one half orders of magnitude was achieved in 100 global iterations. The computation was stopped to conserve CPU time. The computed pressure distribution at various radial locations is compared to the experimental data of Sitaram and Lakshminarayana (1983) in Figures 5.34 through 5.37. The suction peak is well captured near the mid-span, however, it is overpredicted in the hub wall region. The suction side pressure distribution agrees favorably with the experimental data. The pressure side C_p agrees well with the data at a hub to tip ratio R=0.832, however, at lower values of R, a hump in the computed distribution is present near the trailing edge. This may have arisen from the fact that the wake region has not been computed and without the interaction of the wake, the flow turns very sharply (locally) to follow the blade trailing edge rather than following the outer inviscid flow. Such turning tends to increase lift which is evident in the computed pressure distribution.

The computed suction side boundary layer profiles are compared to the hot wire data of Pouagare et al. (1985) in Figure 5.38. The agreement with the data is good near the hub and mid-span regions. At R=0.918, the prediction accuracy is less than adequate. It is important to remember that the tip clearance effect has not been included in the computation and the measured data at this location may indeed include the interaction of the leakage jet with the blade boundary layer. Near the trailing edge, the boundary layer profiles are not well predicted
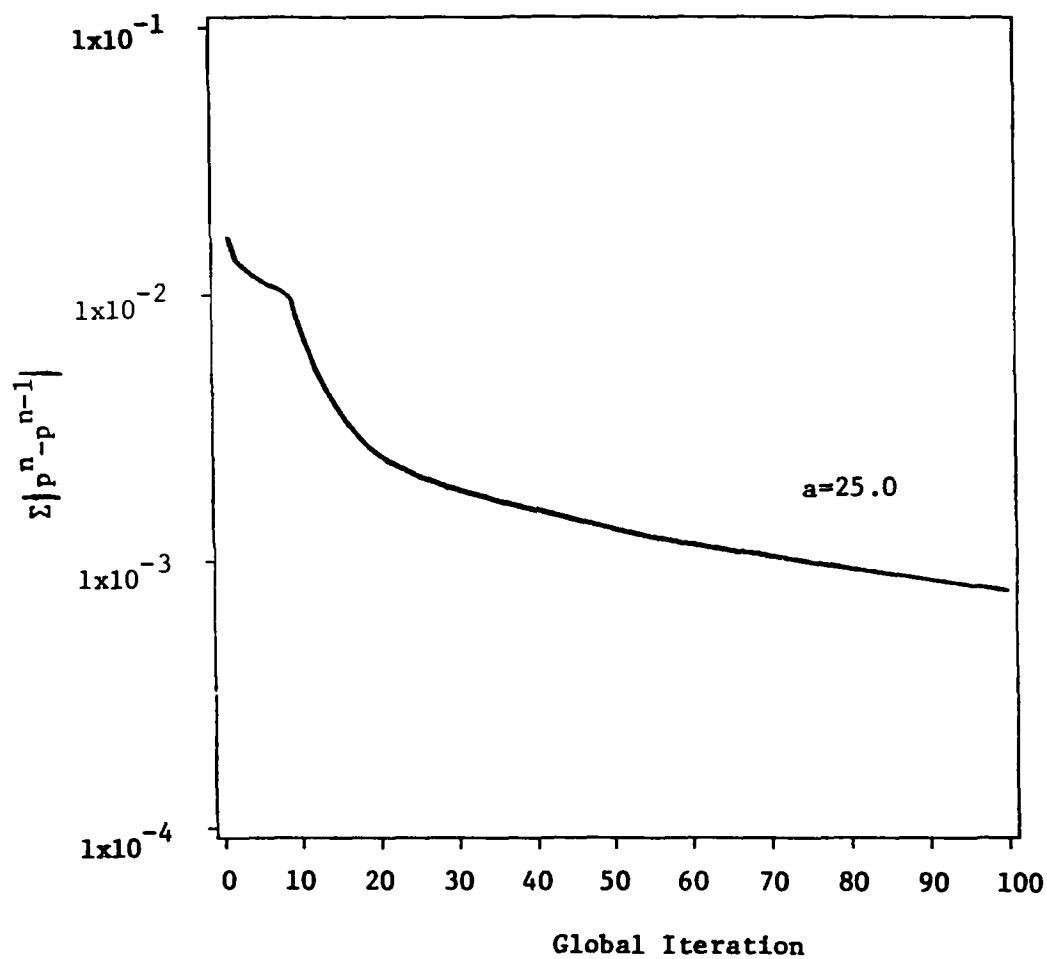
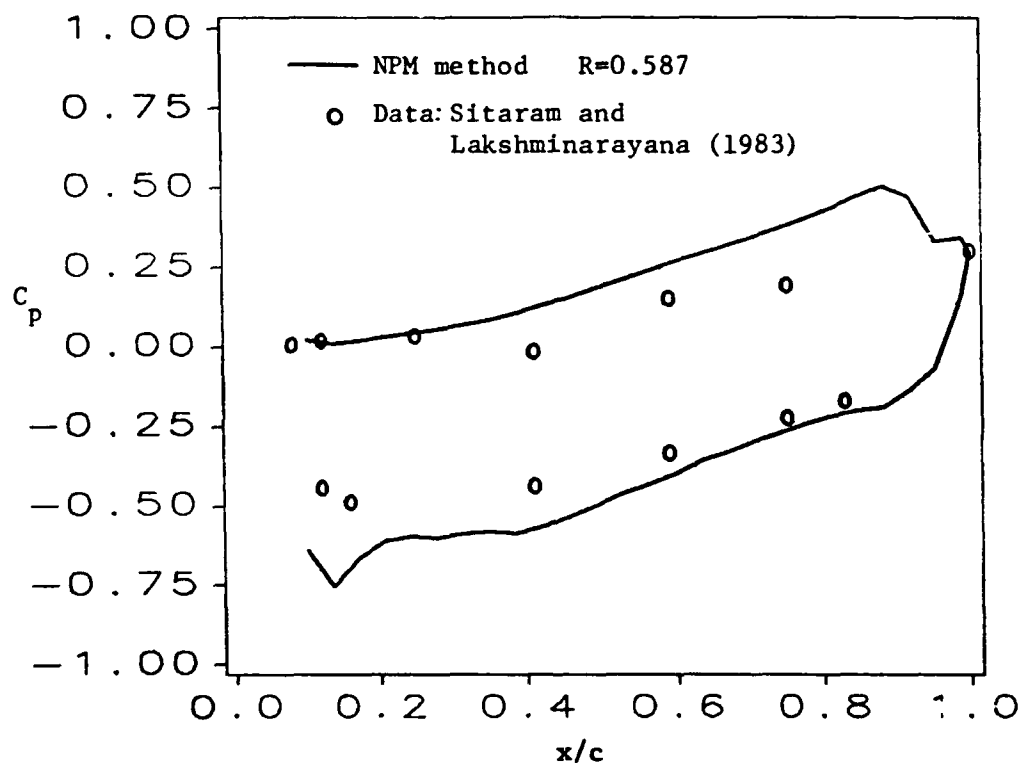Figure 5.33   Convergence History for the Rotor Computation

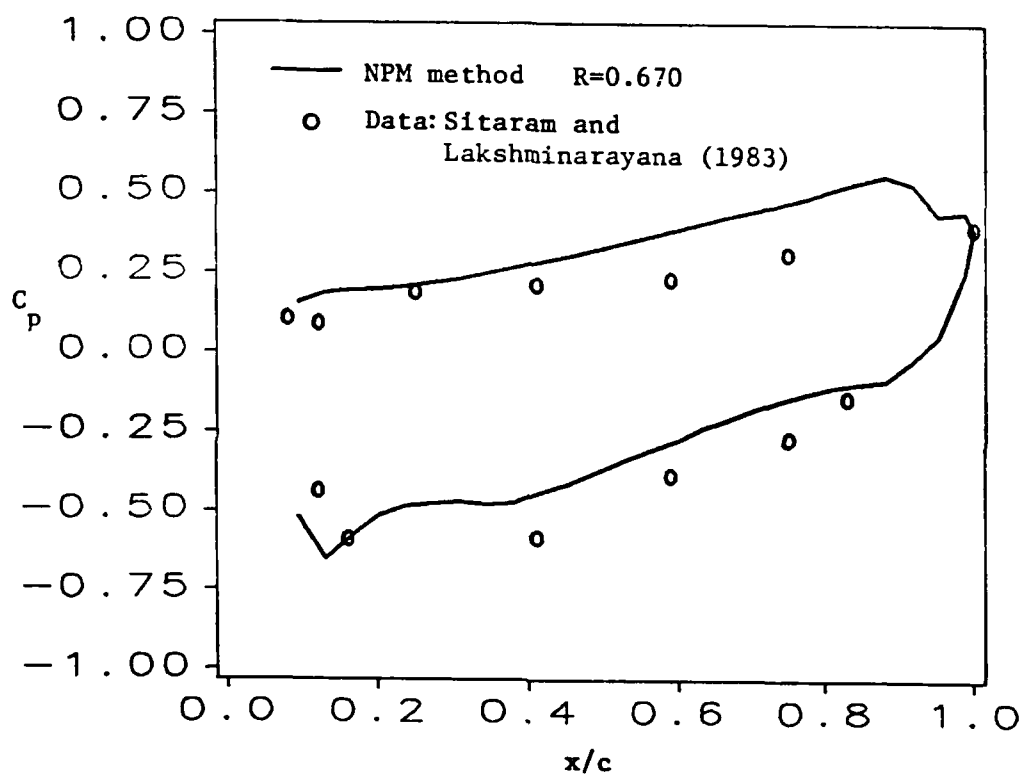Figure 5.34 Pressure Distribution at R=.587 for the Rotor

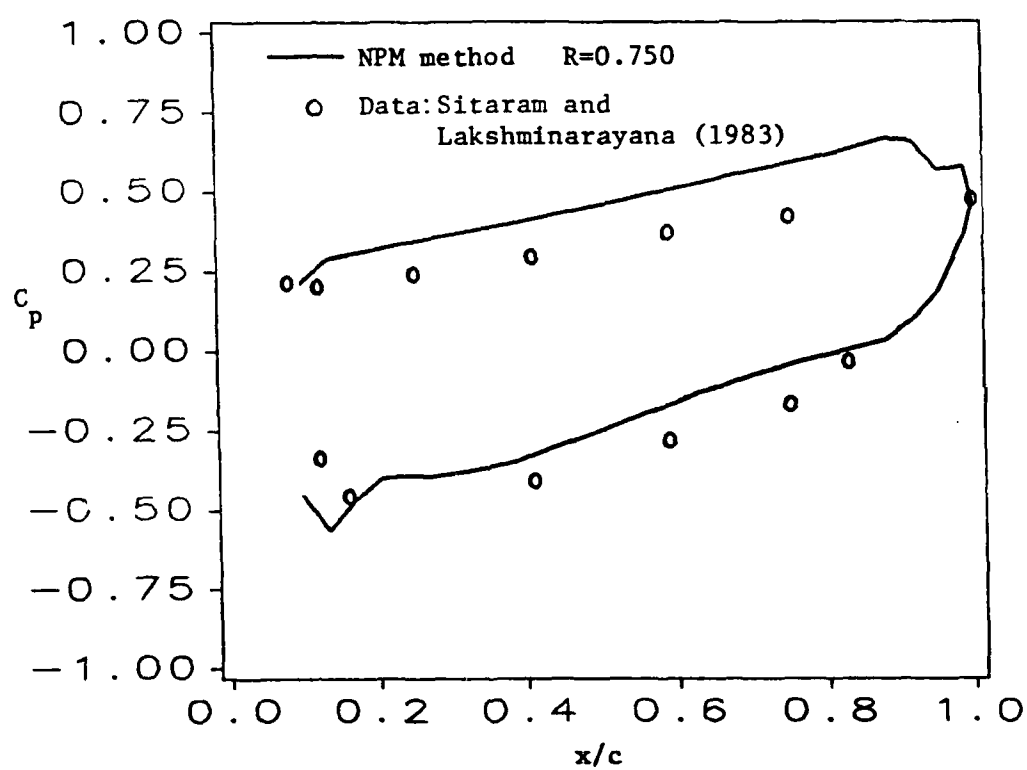Figure 5.35   Pressure Distribution at R=.670 for the Rotor

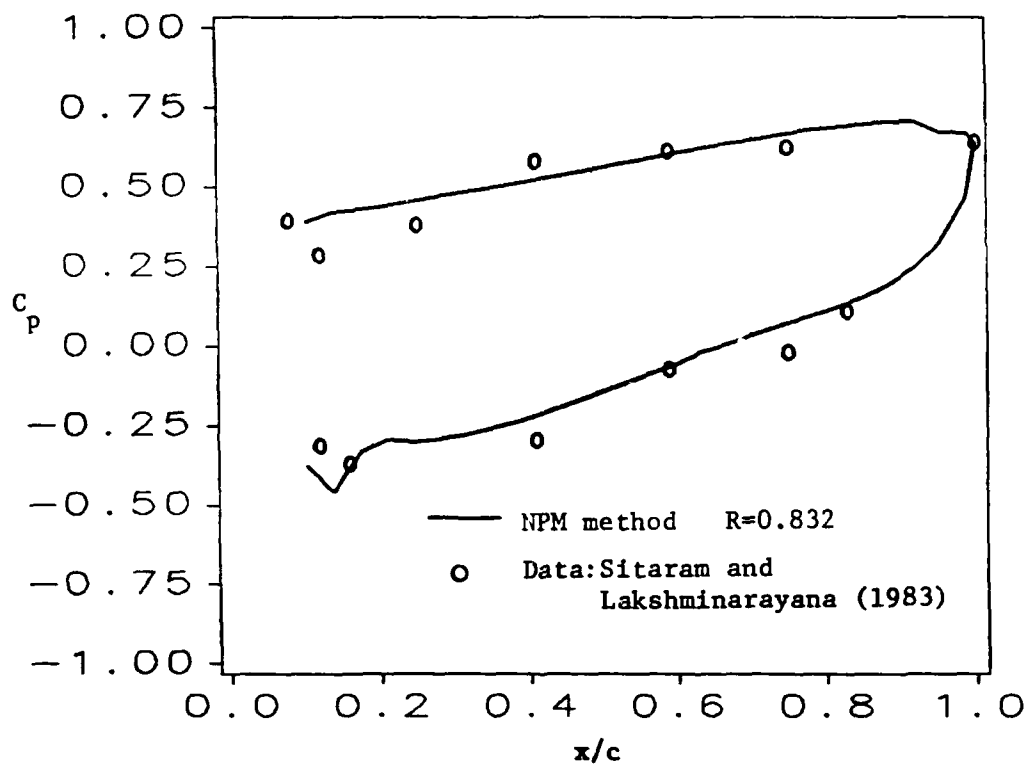Figure 5.36 Pressure Distribution at R=.750 for the Rotor

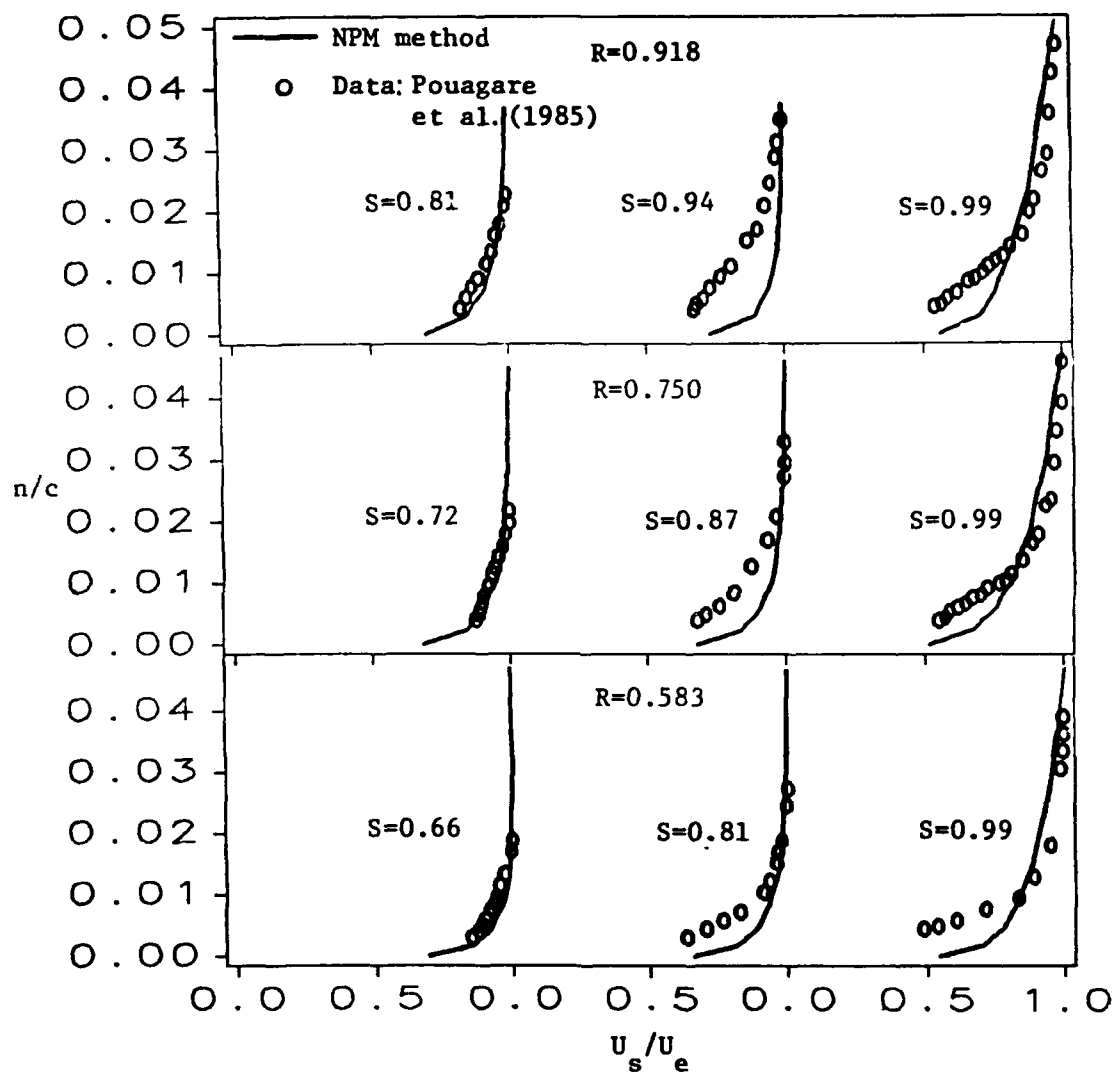Figure 5.37   Pressure Distribution at R=.832 for the Rotor

Figure 5.38   Streamwise Boundary Layer Profiles on the

Suction Side for the Rotor

which may be due to the lack of wake interaction in the computation.

The computed pressure side boundary layer profiles are compared to the experimental data in Figure 5.39. Here, the agreement is not good. These boundary layers are so thin that the measurements must be suspect in the error analysis. Even so, the computed profiles do not show the proper character at R=0.750. This may be due to the poor pressure prediction. The computed radial velocity profiles at S=.99 for the pressure and suction side are compared to the data in Figure 5.40. The results are qualitatively correct, however, the magnitudes are somewhat underpredicted. This may be due to the the use of the turbulent slip boundary condition. The radial flow near the blade surface is driven by the normal gradient of the streamwise velocity. Thus, since the slip condition effectively reduces this gradient, the radial flows will not develop as is the case. The computed hub wall boundary layer is compared to the experimental data in Figure 5.41. The boundary layer growth on the hub wall is well captured as is the actual profile. The computed secondary flow vectors are compared to the experimental data of Murthy and Lakshminarayana (1987) in the hub wall region in Figures 5.42 through 5.44. Overall, the secondary flow has the correct trend near the hub wall, however, the magnitude is slightly overpredicted. Although artificial, due to the lack of tip clearance modelling, a passage vortex can be seen developing near the annulus wall in Figure 5.42a. Radial flows are small at this streamwise station. At S=.58, in Figure 5.43a, the radial flows are stronger as are the secondary flows. The passage vortex near the annulus wall is more strongly developed. Finally, the radial flows are so strong at S=1.0, see Figure 5.44a, that much of the mid-span momentum is convected to the blade tip. This may
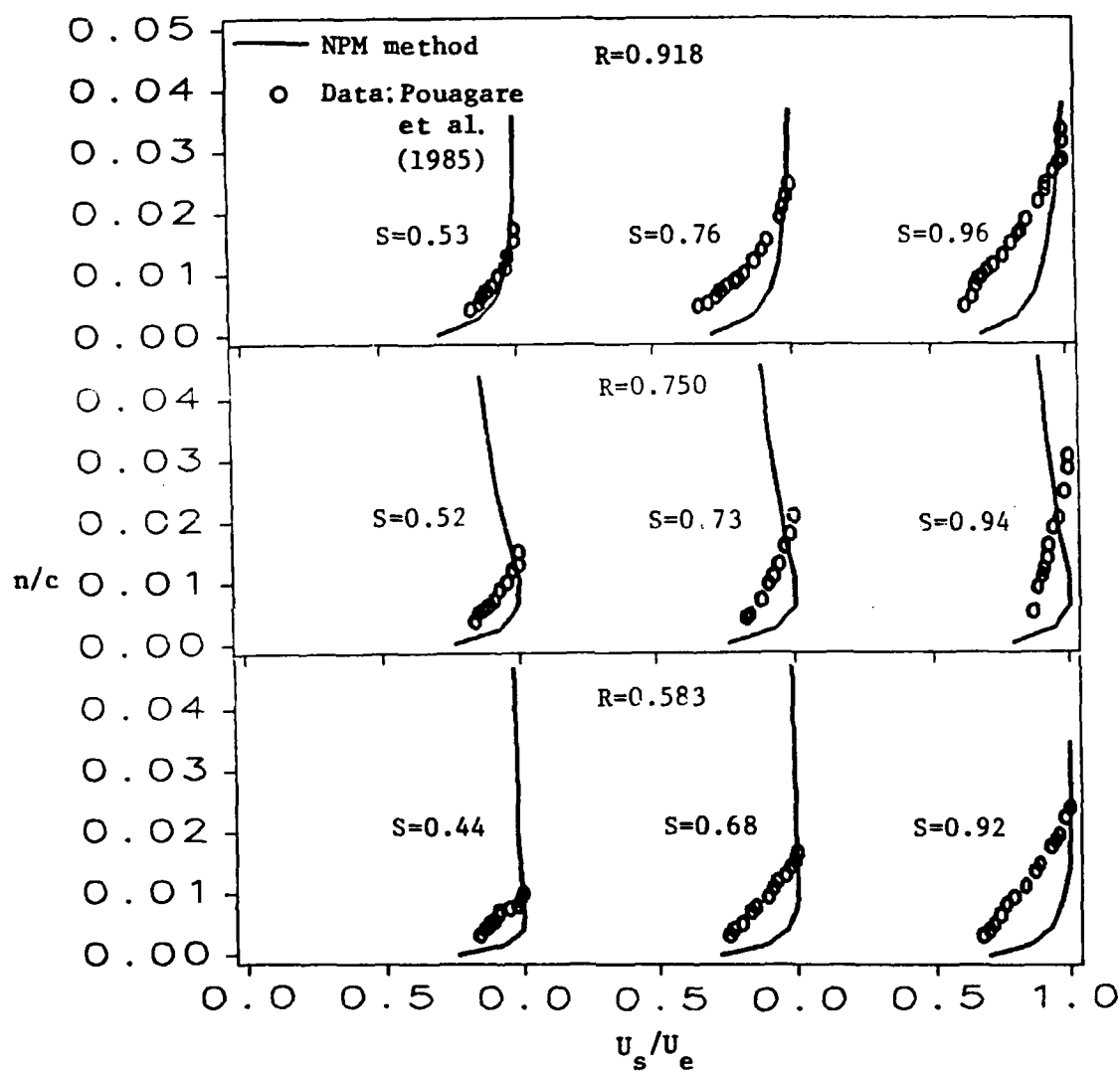
Figure 5.39   Streamwise Boundary Layer Profiles on the
Pressure Side for the Rotor
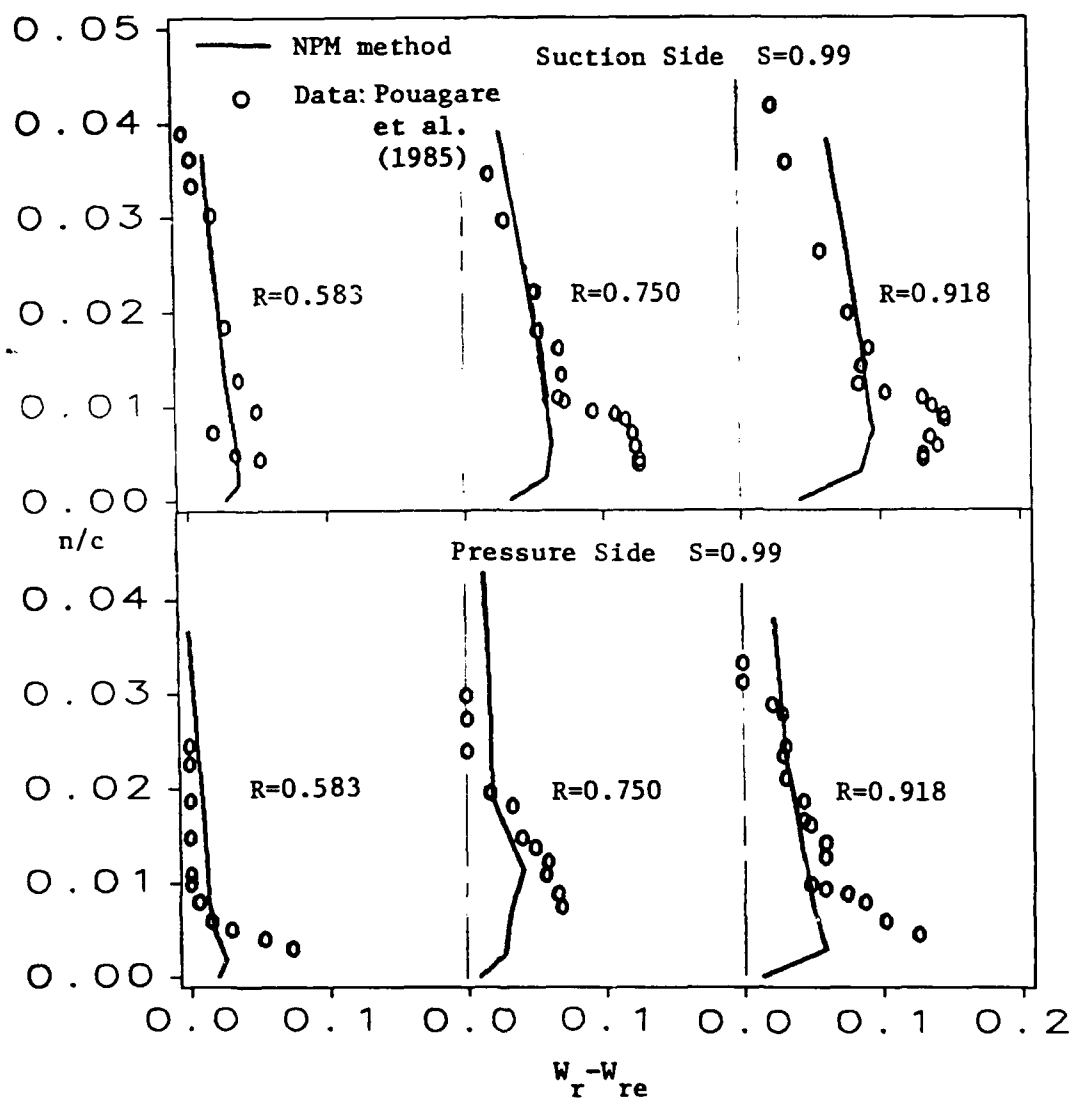
Figure 5.40   Radial Velocity Profiles at S=.99 for the Rotor
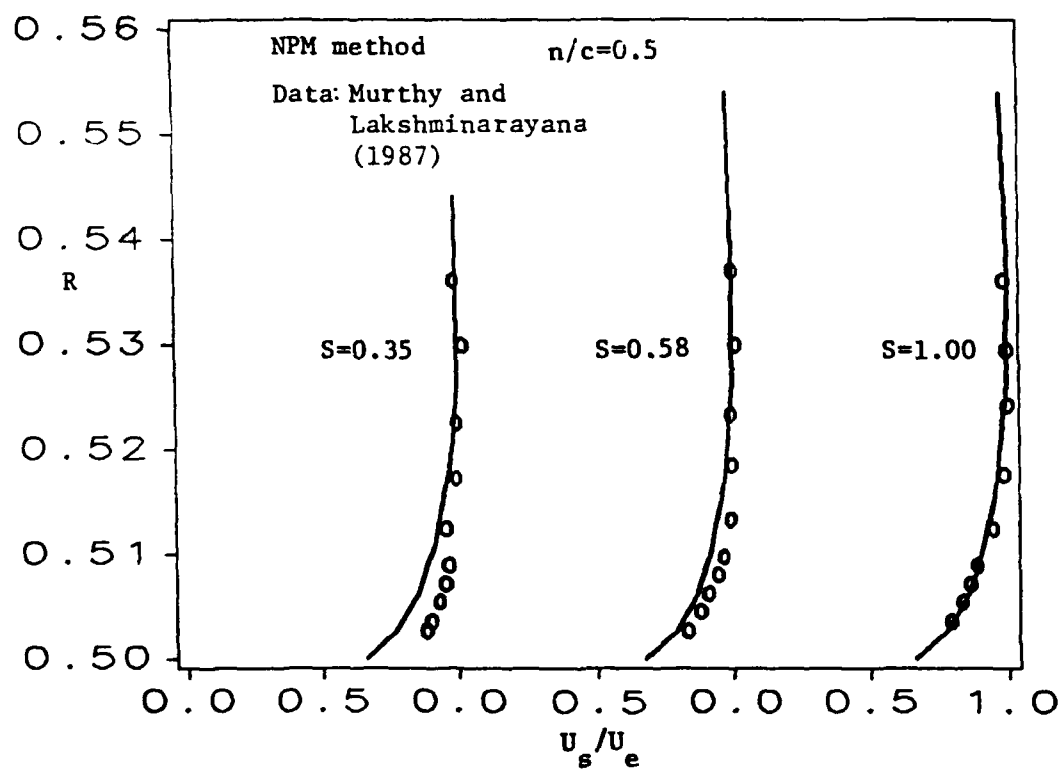
Figure 5.41 Hub Wall Boundary Layer Profiles for the Rotor

annulus wall

ss

ps

.16 Q_t

hub wall
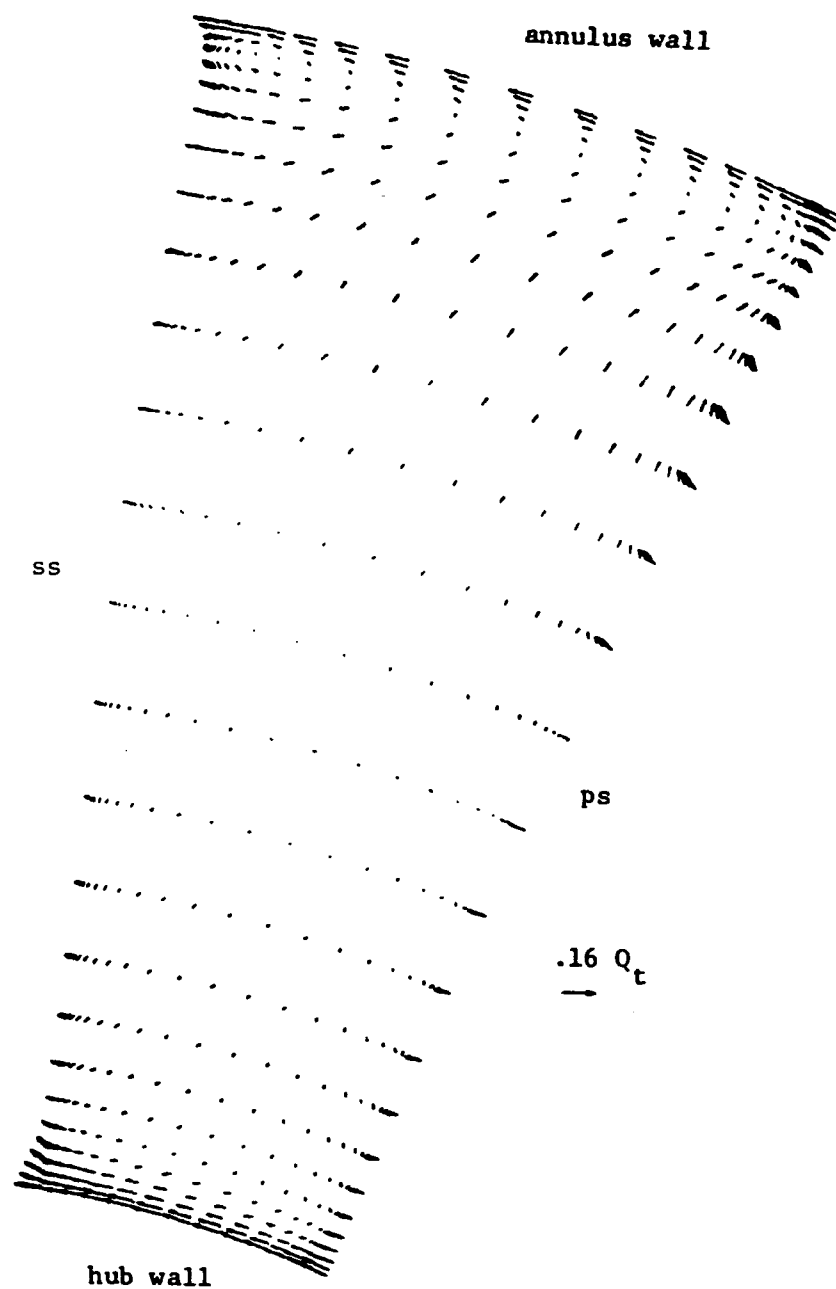
a) Computed

Figure 5.42 Secondary Flow Vectors at X=.35 for the Rotor
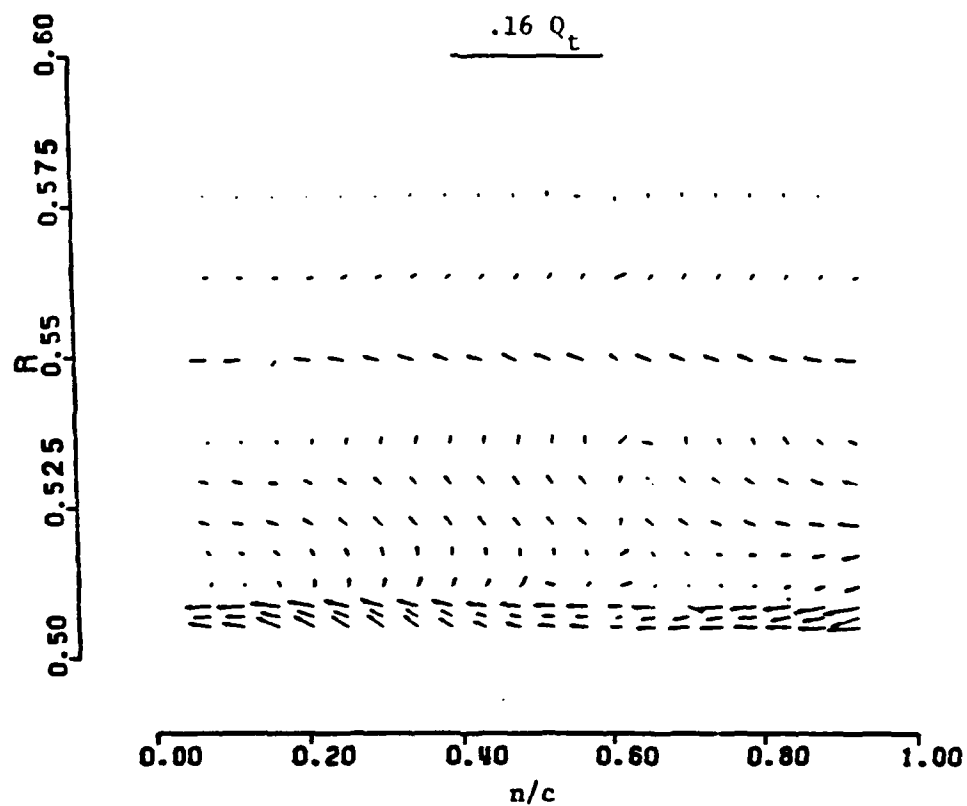
b) Measured: Murthy and Lakshminarayana (1987)

Figure 5.42   Secondary Flow Vectors at X=.35 for the Rotor

annulus wall

ss

ps

.16 Q_t

hub wall
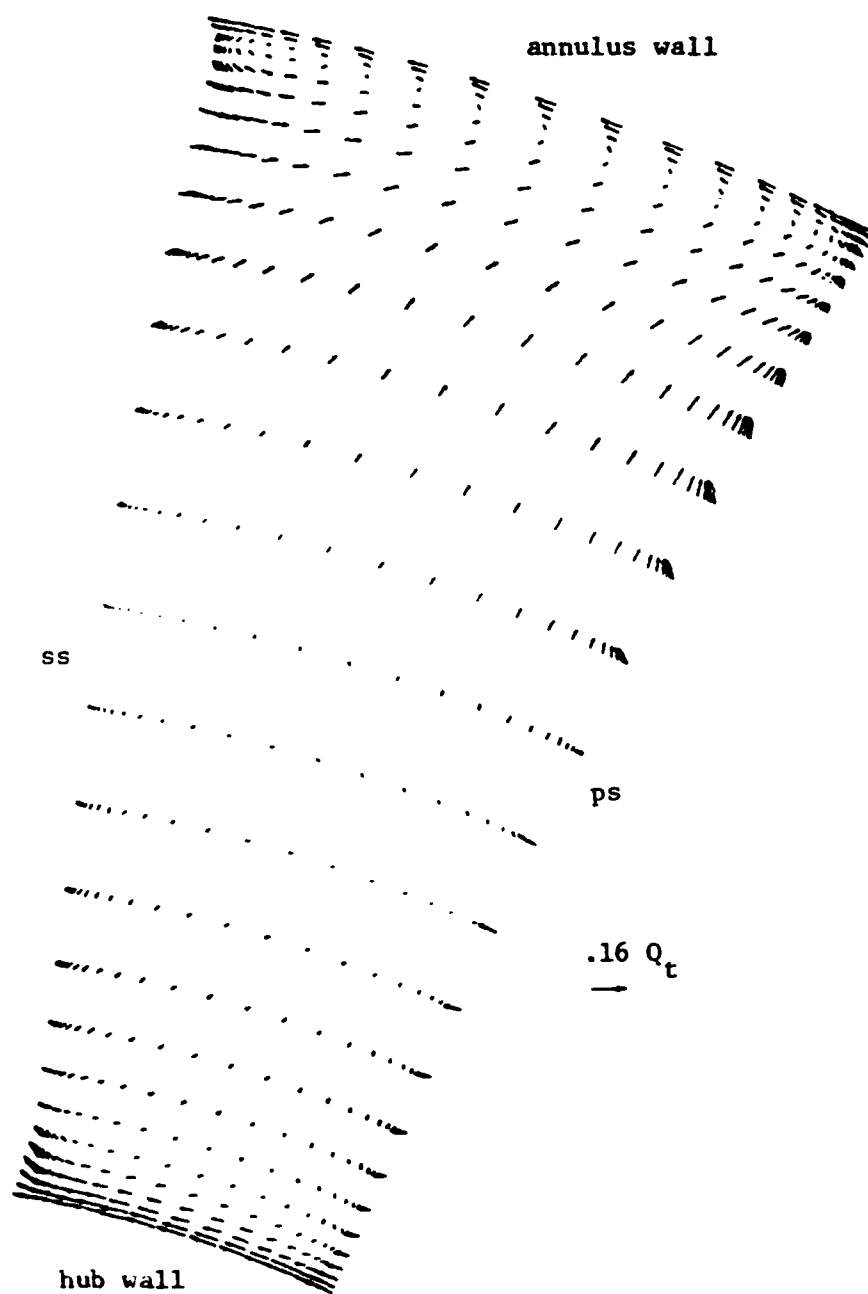
a) Computed

Figure 5.43   Secondary Flow Vectors at X=.58 for the Rotor
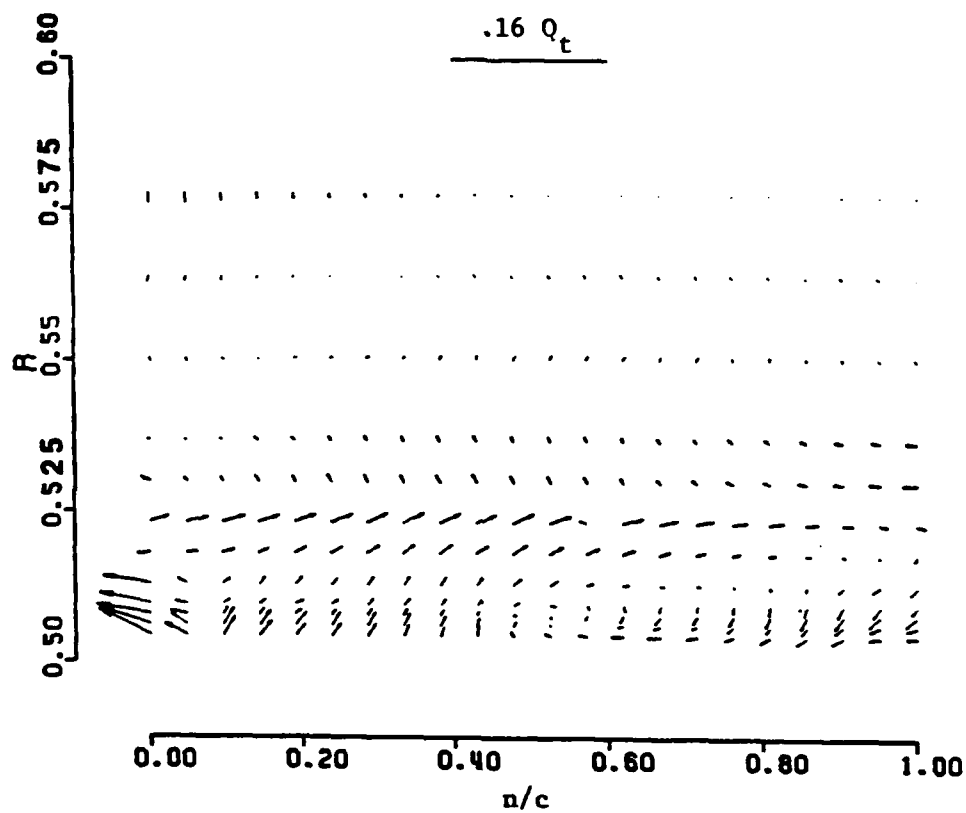
b) Measured: Murthy and Lakshminarayana (1987)

Figure 5.43   Secondary Flow Vectors at X=.58 for the Rotor

annulus wall

ss

ps

.16 Q_t

hub wall
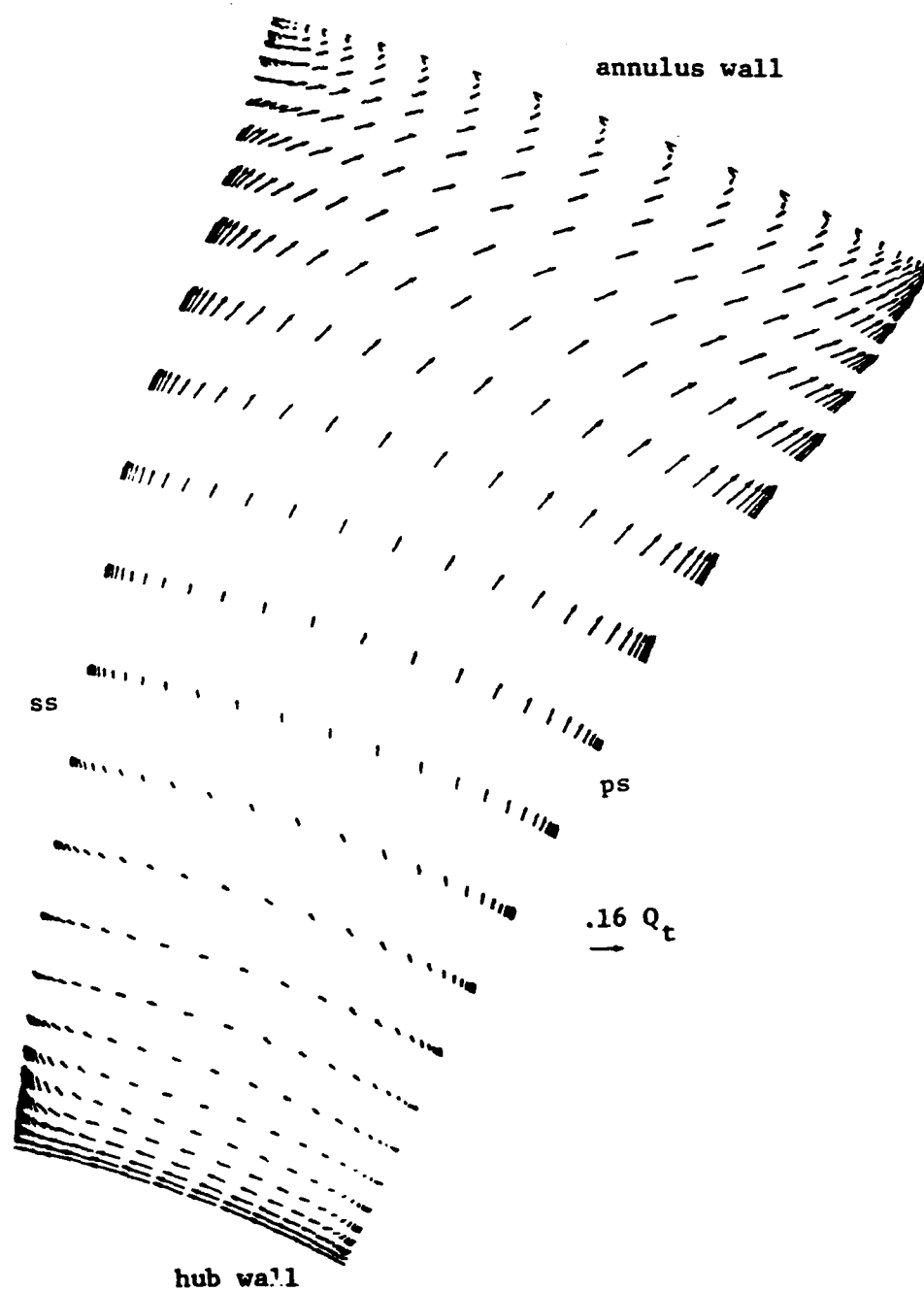
a) Computed

Figure 5.44   Secondary Flow Vectors at X=1.0 for the Rotor
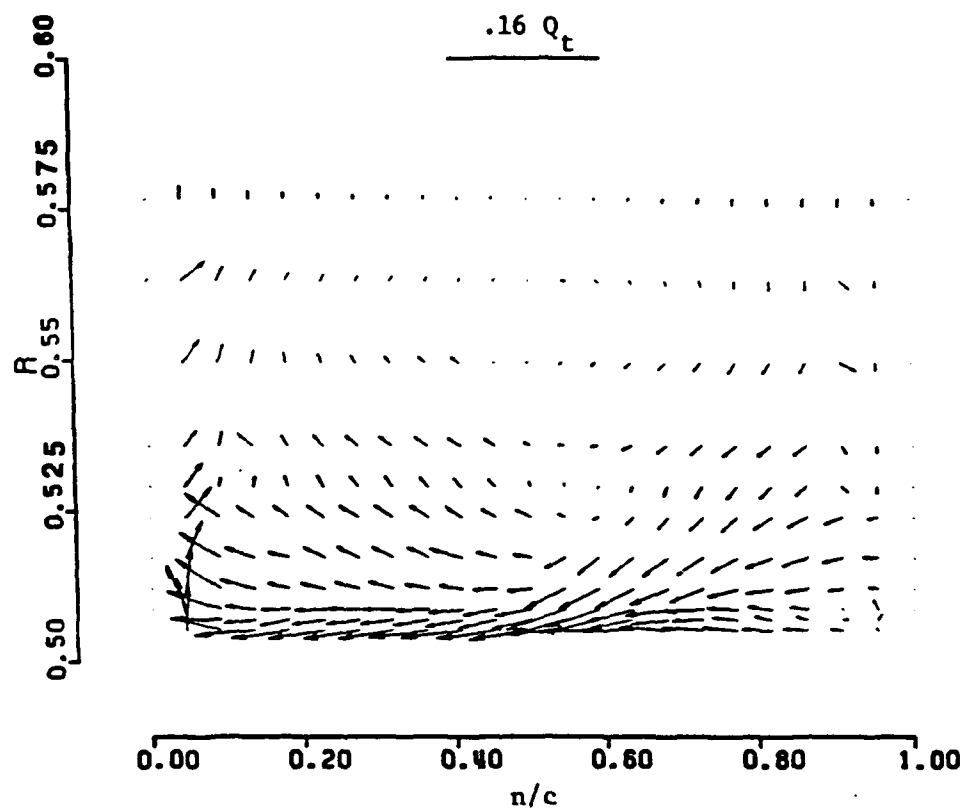
b) Measured: Murthy and Lakshminarayana (1987)

Figure 5.44 Secondary Flow Vectors at X=1.0 for the Rotor

be another reason for the poor boundary layer predictions at S=.99. The interaction of the tip leakage jet tends to slightly reduce these radial flows so perhaps a more accurate computation can be achieved with some tip clearance modelling. In the hub wall region, however, the comparison with the data is very good at this streamwise station. Overall, the major features of the rotor flow have been captured accurately.

Finally, the computed stagnation pressure loss coefficient, ψ_{loss}, based on the blade tip speed is compared to the experimental data at the exit in Figure 5.45. The agreement with the data is surprisingly good. The losses on the pressure side are somewhat underpredicted and the computed loss core, near n/c=0.3, is closer to the suction side than the measured location of n/c=0.4. Still, the stagnation pressure loss is one of the most difficult flow quantities to capture and the NPM method has done a reasonably good job of computing it.
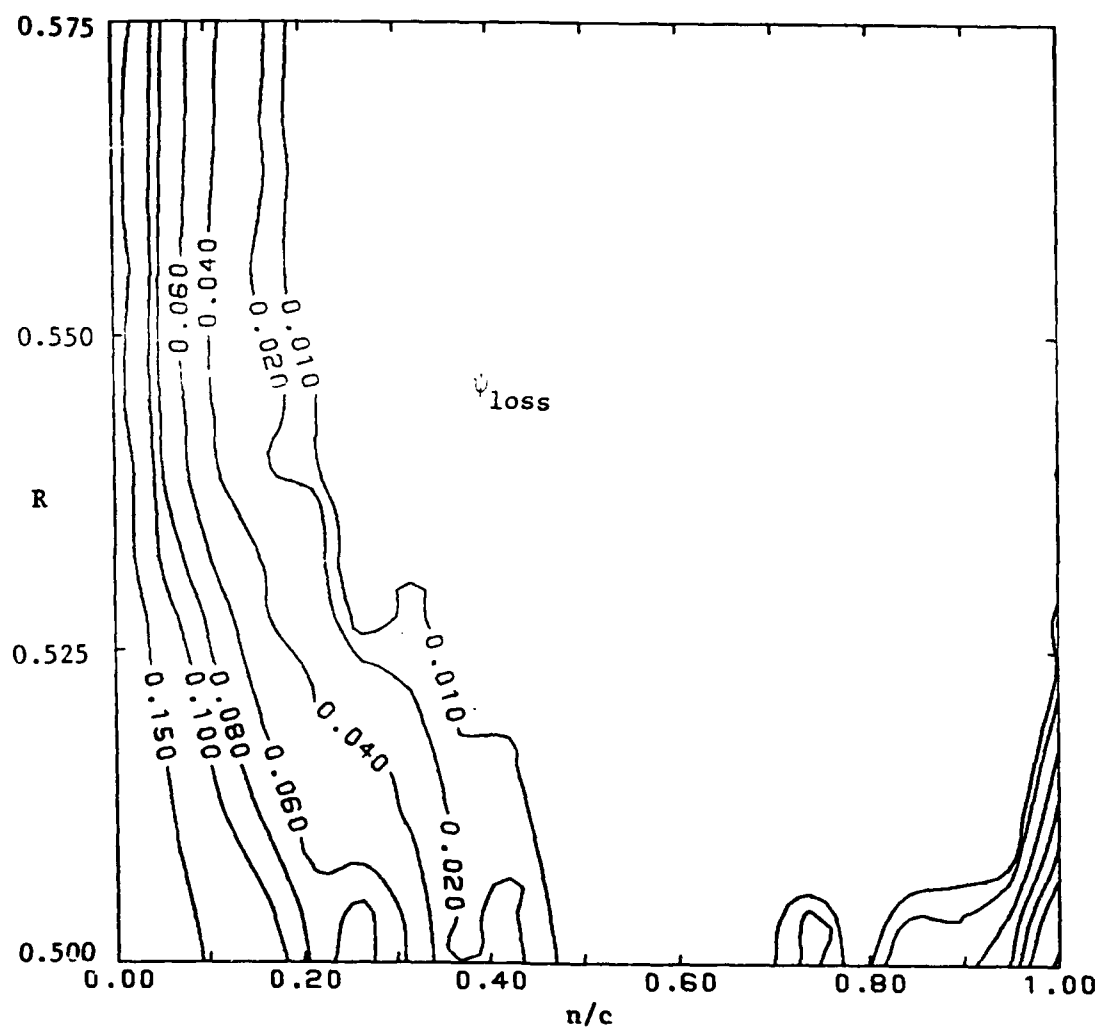
a) Computed

Figure 5.45   Pressure Loss Contours at the Rotor Exit
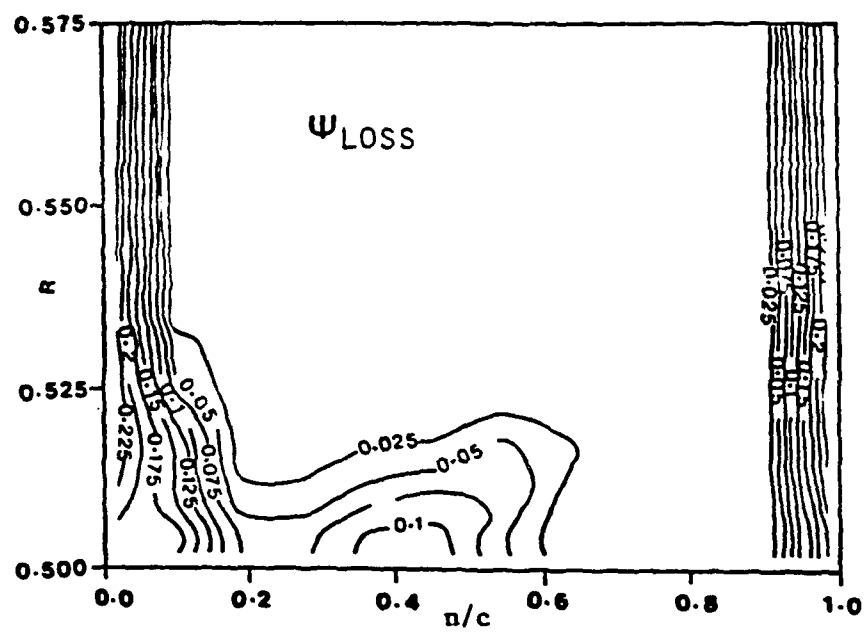
b) Measured: Murthy and Lakshminarayana (1987)

Figure 5.45   Pressure Loss Contours at the Rotor Exit

CHAPTER 6

CONCLUDING REMARKS

6.1 Summary of Conclusions

Existing single pass space-marching methods for solving the partially parabolized Navier-Stokes equation have various drawbacks associated with their use on complex flows. Several require Poisson correction equations which are cumbersome to use and/or do not yield the viscous pressure field. One method in particular due to Pouagare and Lakshminarayana (1986), refered to as the PL method, overcomes many of these drawbacks. The PL method, however, was found through analysis to be unconditionally unstable when used as an iterative, multiple pass, parabolic-marching method. This restricts its usefullness in predicting flows with strong pressure interaction. The PL method was capable of computing many mildly elliptic internal flows because the continuity equation was directly coupled to the momentum equations in the solution process and the streamwise pressure gradient condition was relaxed. This relaxation of the streamwise pressure gradient was the reason for the global instability, where global refers to multiple passes of the domain.

A modification was made to the PL method in an effort to improve its global stability characteristics. The modified PL method, refered to as the MPL method, relaxed the transverse pressure gradients still keeping the continuity equation coupled to the momentum equations. Analysis showed that this system was stable for a forward-marching integration of

the equation yet globally unstable for multiple passes of the domain. Clearly, for global stability, the pressure gradients must not be relaxed. Since some condition must be relaxed for the solution of the coupled form of the Navier-Stokes equation on complex geometries, the continuity equation was determined to be the appropriate condition to relax.

Following pseudocompressibility theory, a pressure term was introduced into the continuity equation giving a system which appears similar to Chorin's ('967) method but with no timewise gradients. The new parabolic-marching method or NPM method was found to be stable when a forward-marching integration was used used as a solution procedure. Most importantly, the NPM method was found to be unconditionally stable for a multiple pass, global iteration procedure. The value of the relaxation parameter in the continuity equation was found to vary from zero to thirty with a general trend of increasing value for increasing flow complexity. In addition, the mass flow was found to be conserved at convergence, however, convergence was generally slow as is typical of parabolic-marching methods.

The LBI scheme used to solve the equation in the cross plane was found to introduce an inconsistent splitting error when used in parabolic-marching methods. This splitting error is strongly dependent upon the way in which the main vector operator in the LBI scheme is split and reduces accuracy significantly. Depending upon the flow under consideration, use of one splitting order over the other can lead to divergent behavior. This was demonstrated for the laminar flow in a strongly curved duct. A new iterative solution procedure was developed which reduces the effect of the splitting error and gives a result which

maintains the formal second order accuracy of the discretization.

The NPM method using the new solution procedure was calibrated by computing the developing flow in a straight square duct as well as the laminar flow in an S-shaped square duct. The agreement with the analysis and the experimental data was excellent in all regions of the flows. Since the streamwise diffusion of momentum was neglected to give the partially parabolized Navier-Stokes equation, the flow 'sees' a change in curvature through the pressure field only. Without proper *transmittion of pressure ellipticity, accurate comparisons with the data* are impossible. The results presented in this work are very accurate for the laminar flow; thus, the S-shaped duct computation showed that pressure ellipticity could be transmitted effectively using the NPM method. Further validation of the NPM method was carried out on several complex, turbulent flows. The turbulent flow in an S-shaped duct was computed with good agreement with the available experimental data. The bulk pressure drop was overpredicted but the transverse gradients due to the duct curvature were well captured. The error in the bulk pressure drop may be due to a poor prediction near the walls. When the accuracy exhibited for the laminar flow is considered, one must suspect the extension to three dimensions of the two-dimensional Baldwin and Lomax (1978) algebraic eddy viscosity model as one reason for the error.

The two equation k-ε turbulence model was used to compute the flow in a rectilinear end wall turbine cascade. The end wall flow computation compared very well to the experimental data. The development of the passage vortex was accurately captured as was the pressure distribution. The wake of a similiar cascade was computed using both the algebraic eddy viscosity model and the k-ε model. The

computed near wake flow compared very well to the experimental data in the outer region and only adequately near the wake centerline. The far wake, however, was not well predicted with the algebraic eddy viscosity model. Indeed, both the location of the wake centerline and the wake decay did not match the data. Recall that the wake spreading is a strong function of the turbulence and the degree of empericism and lack of physical considerations found in the algebraic turbulence model yielded a spreading rate that was too slow. On the other hand, when the k-ε model was used, the far wake computation was extremely accurate.

Finally, the flow in an axial flow compressor rotor was computed using the NPM method. This particular flow proved to be very difficult to compute. The algebraic eddy viscosiy model was used for the simple reason that both the k-ε model and the ARSM showed divergent behavior for reasons unknown to the author. Perhaps the forward-marching solution procedure used for the k and ε equations is not appropriate for this type of flow. The suction side boundary layers as well as the pressure distribution were well predicted. The computed pressure side boundary layers and the exit radial flows did not compare well with the experimental data. The lack of accuracy for the radial flows may be attributed to the use of the turbulent slip condition which tends to reduce the near wall normal gradient of the streamwise velocity. This gradient is the main mechanism driving the radial flows near the blade surfaces. The secondary flows were well predicted near the hub wall as were the stagnation pressure losses at the rotor exit.

Overall, the NPM method showed its usefullness in computing turbulent turbomachinery flows. The rotor computation will require more modelling, a finer grid, and integration of the wake flow if a more

accurate prediction is to be achieved.

6.2 Suggestions for Future Research

Future research into the application of the NPM method should include the development of a method for accelerating the convergence of the scheme. Many iterative methods have incorporated multigrid type algorithms to enhance convergence. Such a method may be successfully incorporated into the NPM method. Since only pressure information needs to be quckly propagated from downstream to upstream, an approximate form of the Poisson equation for the pressure, similar to the one used by Tenpas and Pletcher (1987), may be sufficient to significantly improve the convergence.

Another area where the NPM method can be improved is the iterative LBI method employed at each streamwise station. There may be faster iterative schemes available which will yield the same result.

Finally, the area which needs the most attention and which is vitally important to the successful computation of complex flows is turbulence modelling, or rather the application of existing turbulence models to the unique problems in turbomachinery. Often, ad hoc approximations are required in order to achieve a converged solution. These approximations, e.g., location of transition, have a substantial effect on the outcome of a computation. What is required is a systematic study of the established turbulence models and their extension to three-dimensional turbomachinery flows.

REFERENCES

Abdallah, S. (1987), "Part I: Numerical Solutions for the Pressure Poisson Equation with Neumann Boundary Conditions Using a Non-Staggered Grid," J. Comp. Physics, (to appear).

Abdallah, S. (1987a) private communication.

Baldwin, B. S. and Lomax, H. (1978), "Thin Layer Approximation and Algebraic Model for Separated Turbulent Flows," AIAA Paper 78-257, AIAA 16th Aerospace Sciences Meeting, Huntsville, AL, January 16-18.

Beam, R. M. and Warming, R. F. (1978), "An Implicit Factored Scheme for the Compressible Navier-Stokes Equations," AIAA Journal, Vol. 16, No. 4, April, pp. 393-402.

Brandt, A. (1977), "Multi-Level Adaptive Solutions to Boundary-Value Problems," Math. of Comp., Vol. 31, No. 138, pp. 333-390.

Briley, W. R. (1974), "Numerical Method for Predicting Three-Dimensional Flows in Ducts," J. Comp. Physics, Vol. 14, No. 1, pp. 8-28.

Briley, W. R., Buggeln, R. C. and McDonald, H. (1985), "Solution of the Three-Dimensional Navier-Stokes Equations for a Steady Laminar Horseshoe Vortex Flow," AIAA Paper 85-1520.

Briley, W. R. and McDonald, H. (1979), "Analysis and Computation of Subsonic Primary and Secondary Flows," AIAA Paper 79-1453, AIAA Computational Fluid Dynamics Conference, Williamsburg VA.

Briley, W. R. and McDonald, H. (1980), "On the Structure and Use of Linearized Block Implicit Scheme," J. Comp. Physics, Vol. 34, pp. 54-73.

Chima, R. V. (1986), "Development of an Explicit Multigrid Algorithm for Quasi-Three-Dimensional Viscous Flows in Turbomachinery," NASA TM 87128.

Chorin, A. J. (1967), "A Numerical Method for Solving Incompressible Viscous Flow Problems," J. Comp. Physics, Vol. 2, pp. 12-26.

Dawes, W. N. (1986), "A Numerical Analysis of the Three-Dimensional Viscous Flow in a Transonic Compressor Rotor and Comparison With Experiment," ASME Paper 86-GT-16, ASME 31st International Gas Turbine Conference, Dusseldorf, Federal Republic of Germany, June 8-12.

Dodge, P. R. (1976), "A Numerical Method for 2-D and 3-D Viscous Flows," AIAA Paper 76-425.

Flot, R. and Papailiou, K. (1975), "Couches Limites et Effets D'Estremities Dans les Turbomachines," METRAFLU, contract DR.M.E 73/373.

Ghia, K. N. and Sokhey, J. S. (1977), "Laminar Incompressible Viscous Flow in Curved Ducts of Regular Cross-Sections," ASME J. Fluids Engr., December, pp. 640-647.

Gielda, T. and McRae, D. (1986), "An Accurate, Stable, Explicit, Parabolized Navier-Stokes Solver for High Speed Flows," AIAA Paper 86-1116, AIAA/ASME 4th Fluid Mechanics, Plasma Dynamics and Lasers Conference, Atlanta, GA, May 12-14.

Giesing, J. P. (1964), "Extension of the Douglas-Neumann Program to Problems of Lifting, Infinite Cascades," Douglas Aircraft Company Report No. LB31653.

Govindan, T. R. and B. Lakshminarayana (1987), "A Space-Marching Method for the Navier-Stokes Equations for Internal Flows," J. Comp. Physics, to appear.

Hah, C. (1984), "A Navier-Stokes Analysis of Three-Dimnensional Turbulent Flows Inside Turbine Blade Rows at Design and Off-Design Conditions," ASME J. Engr. for Power, Vol. 106, pp. 421-429.

Hah, C. (1986), "Navier-Stokes Calculation of Three-Dimensional Compressible Flow Across a Cascade of Airfoils with an Implicit Relaxation Method," AIAA Paper 86-0555, AIAA 24th Aerospace Sciences Meeting, Reno, NV, January 6-9.

Hobbs, D. E., Wagner, J. H., Dannenhoffer, J. F., and Dring, R. P., "Experimental Investigation of Compressor Cascade Wakes," ASME paper 82-GT-299.

Khalil, I. M. and Weber, H. G. (1984), "Modeling of Three-Dimensional Flow in Turning Channels," ASME Paper 84-GT-49, ASME 29th International Gas Turbine Conference, Amsterdam, The Netherlands, June 4-7.

Kirtley, K. R. and Lakshminarayana, B. (1985) "Computation of Internal Incompressible Separated Flow Using A Space-Marching Technique," AIAA Paper 85-1624, presented at the AIAA 18th Fluid Dynamics and Plasmadynamics and Lasers Conference, Cincinatti, Ohio, June 16-18.

Kwak, D., Chang, J. L. C., Shanks, S. P., Chakravarthy, S. R. (1984), "An Incompressible Navier-Stokes Flow Solver in Three-Dimensional Curvilinear Coordinate System Using Primative Variables," AIAA Paper 84-0253, AIAA 22nd Aerospace Sciences Meeting, Reno, NV, January 9-12.

Lakshminarayana, B. (1980), "An Axial Flow Research Compressor Facility Designed for Flow Measurement in Rotor Passages," ASME J. Fluids Engr., Vol 102, pp. 402-411.

MacCormack, R. W. (1982), "A Numerical Method for Solving the Equations of Compressible Viscous Flow," AIAA Journal, Vol. 20, No. 9, September, pp. 1275-1281.

Moore, J. and Moore, J. G. (1979), "A Calculation Procedure for Three-Dimensional, Viscous, Compressible Duct Flow," ASME J. Fluids Engr., Vol. 101, December.

Moore, J. and Moore, J. G. (1981), "Calculations of Three-Dimensional Viscous Flow and Wake Development in a Centrifugal Impeller," ASME J. Engr. for Power, Vol. 103, April, pp. 367-372.

Murthy, K. N. S. and Lakshminarayana, B. (1987), "Entwicklung der Nabengrenzschischt und Stromungsverluste im Rotor eines Axialkompressors," Z. Flugwiss. Weltraumforsch, Vol. 11, pp. 1-11.

Patankar, S. V. and Spalding, D. B. (1972), "A Calculation Procedure for Heat, Mass, and Momentum Transfer in Three-Dimensional Parabolic Flows," Int. J. Heat and Mass Transfer, Vol. 15, pp. 1787-1805.

Pouagare, M., Galmes, J. M. and Lakshminarayana, B. (1985), "An Experimental Study of the Compressor Rotor Blade Boundary Layer," ASME J. Engr. for Power, Vol. 107, pp. 364-373.

Pouagare, M. and Lakshminarayana, B. (1986), "A Space-Marching Method for Viscous Incompressible Internal Flows," J. Comp. Physics, Vol. 64, No. 2, June, pp. 389-415.

Pouagare, M. and Lakshminarayana, B. (1987), " Three Dimensional Flow Field Data in a Low Speed Axial Flow Compressor Rotor Passage," (to be published as NASA CR).

Pratap, V. S. and Spalding, D. B. (1976), "Fluid Flow and Heat Transfer in Three-Dimensional Duct Flows," Int. J. Heat and Mass Transfer, Vol. 19, pp. 1183-1188

Pulliam, T. H. and Steger, J. L. (1980), "Implicit Finit-Difference Simulations of Three-Dimensional Compressible Flow," AIAA Journal, Vol. 18, No. 2, February, pp. 159-167.

Raj, R. and Lakshminarayana, B. (1973), "Characteristics of the Wake Behind a Cascade of Airfoils," J. Fluid Mech., Vol. 61, part 4, pp. 707-730.

Rhie, C. M., Delaney, R. A., and McKain, T. F. (1984), "Three-Dimensional Viscous Flow Analysis for Centrifugal Impellers," AIAA Paper 84-1296, AIAA/SAE/ASME 20th Joint Propulsion Conference, Cincinnati, Ohio, June 11-13.

Rhie, C. M. (1983), "Basic Calibration of a Partially-Parabolic Procedure Aimed at Centrifugal Impeller Analysis," AIAA Paper 83-0260, AIAA 21st Aerospace Sciences Meeting, Reno, NV, January 10-13.

Rhie, C. M. (1986), "A Pressure Based Navier-Stokes Solver Using the Multigriu Method," AIAA Paper 86-0207, AIAA 24th Aerospace Sciences Meeting, Reno, NV, January 6-9.

Rodi, W. (1976), "A New Algebraic Relation for Calculating the Reynolds Stresses", ZAMM, Vol. 56, p. 219.

Rodi, W. (1982), "Examples of Turbulence Models for Incompressible Flows," AIAA Journal, Vol. 20, No. 3, March, pp. 872-879.

Rosenfeld, M. and Israeli, M. (1987), "Numerical Solution of Incompressible Flows by a Marching Multigrid Method," AIAA Journal, Vol. 25, No. 5, May, pp. 641-647.

Rubin, S. and Reddy, D. R. (1983), "Analysis of Global Pressure Relaxation for Flows with Strong Interaction and Separation," Computers and Fluids, Vol. 11, No. 4, pp. 281-396.

Shang, J. S., Buning, P. G., Hankey, W. L., and Wirth, M. C. (1980), "Performance of a Vectorized Three-Dimensional Navier-Stokes Code on the Cray-1 Computer," AIAA Journal, Vol. 18, No. 9, September, pp. 1073-1079.

Shiff, L. B. and Steger, J. L. (1979), "Numerical Simulation of Steady Supersonic Viscous Flow," AIAA Paper 79-0130, AIAA 17th Aerospace Sciences Meeting, New Orleans, LA, January 15-17.

Sitaram, N. and Lakshminarayana, B. (1983), "End Wall Flow Characteristics and Overall Performance of an Axial Flow Compressor Stage," NASA CR 3671.

Smith, G. D. (1978), Numerical Solution of Partial Differential Equations: Finite Difference Methods, Oxford Press, pp. 75-107.

Spradley, L. W. and Stalnaker, J. F. (1981), "A Quasi-Parabolic Technique for Computation of Three-Dimensional Viscous Flows," AIAA Paper 81-0113, AIAA 19th Aerospace Sciences Meeting, St. Louis, MO, January 12-15.

Taylor, A.M.K.P., Whitelaw, J. H., and Yianneskis M. (1981), "Measurements of Laminar and Turbulent Flow in a Curved Duct with Thin Inlet Boundary Layers," NASA CR-3367.

Taylor, A.M.K.P., Whitelaw, J. H., and Yianneskis M. (1982), "Developing Flow in S-Shaped Ducts, I-Square Cross-Section Duct," NASA CR-3550.

Tenpas, P. W. and Pletcher, R. H. (1987), "Solution of the NavierStokes Equations for Subsonic Flows Using a Coupled Space-Marching Method," AIAA Paper 87-1173, presented at the 8th Computational Fluid Dynamics Conference, Honolulu, HI, June 9-11.

Vanka, S. P. (1985), "Block-Implicit Calculations of Three-Dimensional Laminar Flow in Strongly Curved Ducts," AIAA Journal, Vol. 23, No. 12, December, pp. 1989-1991.

Vigneron, Y. C., Rakich, J. V. and Tannehill, J. C. (1978), "Calculation of Supersonic Viscous Flow Over Delta Wings with Sharp Subsonic Leading Edges," AIAA Paper 78-1137.

Warfield, M. J. and Lakshminarayana, B. (1986), "Computation of Turbulent Rotating Channel Flow with an Algebraic Reynolds Stress Model," AIAA Paper 86-0214, AIAA 24th Aerospace Sciences Meeting, Reno, NV, January 6-9.

Warfield, M. J. and Lakshminarayana, B. (1987), "Calculation of a Three-Dimensional Locally Elliptic Flow with a Zonal Equation Method," AIAA Paper 87-1141-CP, AIAA 8th Computational Fluid Dynamics Conference, Honolulu, Hawaii, June 9-11.

Weinberg, B. C., Yang, R.-J., McDonald, H., Shamroth, S. J. (1985), "Calculations of Two and Three-Dimensional Transonic Cascade Flow Using the Navier-Stokes Equations," ASME Paper 85-GT-66, ASME 30th International Gas Turbine Conference, Houston, TX, March 18-21.

White, F. M. (1974), <u>Viscous Fluid Flow,</u> McGraw-Hill, New York.

APPENDIX

COMPUTATIONAL GRID GENERATION

The governing equation must be solved on discrete points in the physical domain. For logistical reasons, the distribution of points is not random. Applying the boundary conditions is the most complicated aspect of the numerical method and is simplified by writing the equations in generalized coordinates. What is now required is to generate the distribution of points in the physical domain which is aligned with the generalized coordinates.

There are three types of point distributions or grids. They are O-grids, C-grids, and H-grids. For a parabolic solution procedure for the mean flow equations, the O-grids and C-grids cannot be used. This is because the grid line along which the equations are marched is not necessarily aligned with the streamwise direction. For both grids, in the leading edge region, the marching direction is perpendicular to the streamwise direction. This is also the case in the trailing edge region for O-grids. Thus, only H-grids can be used for the computation of turbomachinery flows with a parabolic marching scheme.

There are several methods for generating these H-grids which can be grouped into partial differential equation methods and algebraic methods. The PDE method, of course, solves partial differential equations to generate the distribution of computational points. With such methods, the user has great control of orthogonality of the grid lines in the physical domain. With algebraic methods, orthogonality of

the grid lines is not always assured. In fact, the grid lines can be highly sheared for periodic grids for cascade geometries with large stagger. This shearing of the grid is detrimental to the accuracy of partially parabolized methods since the second order cross derivatives with respect to the streamwise direction are neglected. These cross derivatives are very important in viscous flows with a non-orthogonal grid. However, if a PDE method is used to generate the grid, large bulges appear in the leading and trailing edge regions due to the enforcement of orthogonality. Experience has shown that this leads to *numerical problems* which inhibit the computation of the flow. Therefore, an algedraic grid is used here for the computation of turbomachinery flows.

The following describes the method used here to generate three-dimensional grids for a turbomachinery rotor in the R-θ-Z coordinate system. First, pseudo-streamsheets must be generated, i.e., two-dimensional grids in the R-θ plane. These streamsheets are refered to as 'pseudo' since they are determined by the geometry of the hub and annulus walls and not by the flow. With the hub boundary and annulus boundary defined from the input data, an arbitrary number of points is chosen along the machine axis to define the pseudo-streamsheets. A uniform distribution is sufficient. Lines are then extended from these points through the hub terminating at the annulus. The corresponding values of R and Z for each line are determined through bilinear interpolation using the input data.

With these lines now generated, a distribution of points in the Z-direction is chosen. Typically, exponential stretching is used to pack grid points near the walls where large flow gradients are anticipated.

When completed for each line, the result is a two-dimensional grid in the R-Z plane where the streamwise grid lines are the cylindrical pseudo-streamsheets. Two-dimensional H-grids are now generated on the pseudo-streamsheets using the following procedure.

First, a new blade profile is interpolated from the input data for a particular streamsheet. This new profile is then split into a lower and upper half and the lower half is shifted in the negative θ direction by an amount equal to 2π/number of blades. This provides an upper and lower bound for the grid. Next, the upper and lower boundaries are extended upstream and downstream of the blades in the Z-direction to the predetermined extents of the domain. Now the axial distribution of points must be generated. Once again, exponential stretching is used to pack grid points near the leading and trailing edges of the blades. Finally, the two-dimensional grid is completed by generating a distribution of points in the θ direction as was done when the pseudo-streamsheets were generated. When completed for each streamsheet, the stacked two-dimensional grids form a smooth three-dimensional algebraic periodic H-grid for a turbomachinery blade row. An example is given in Figure A.1. It should be noted that H-grids have a geometric discontinuity at the leading edge and so the computation in that region may be less accurate. Also, H-grids are not recommended for blunt leading edge airfoils.
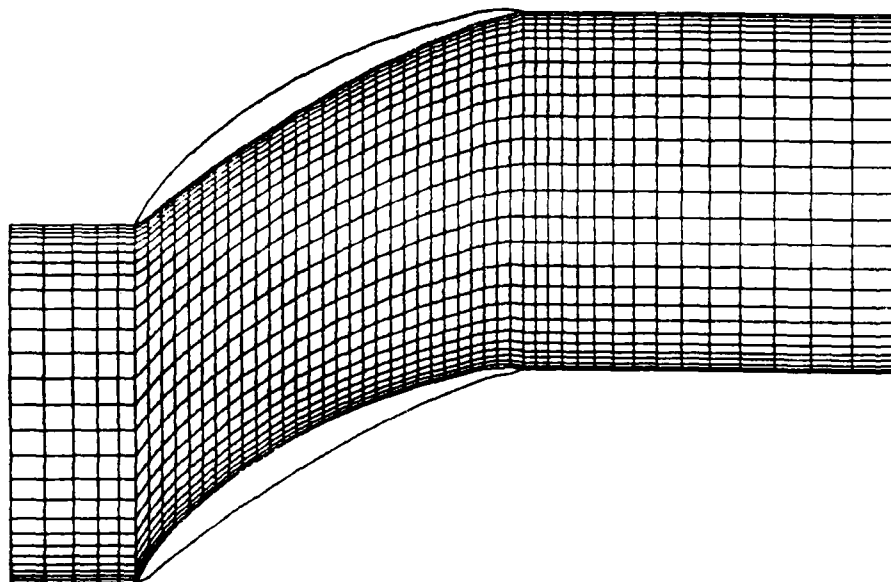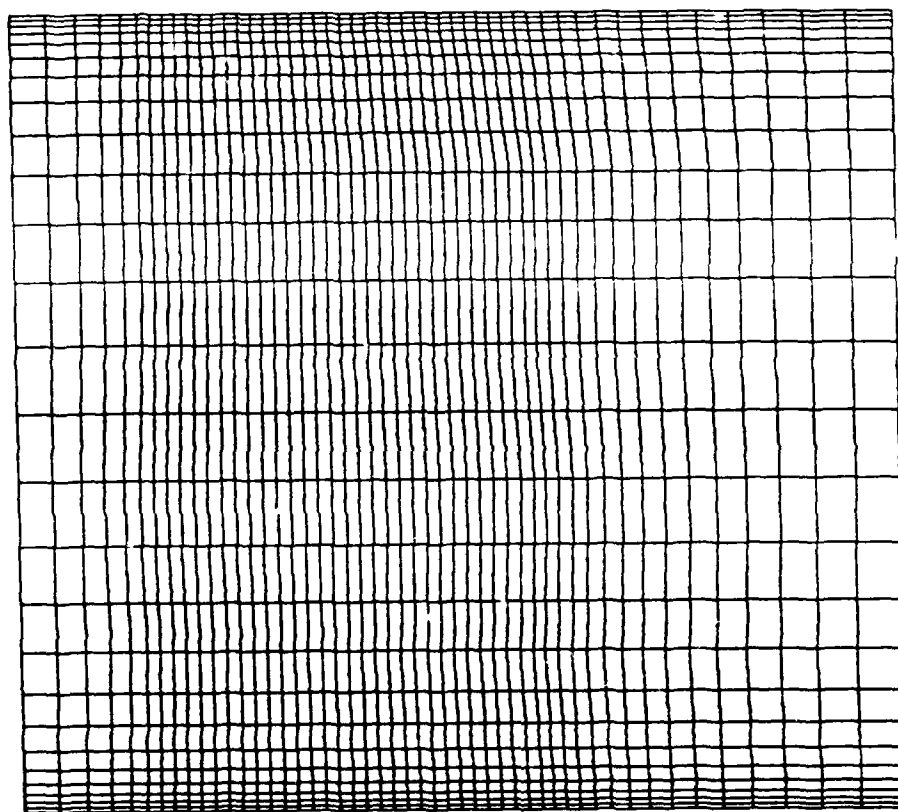
a) θ-Z plane at mid-span.

Figure A.1 Algebraic 3-D Periodic H-Grid
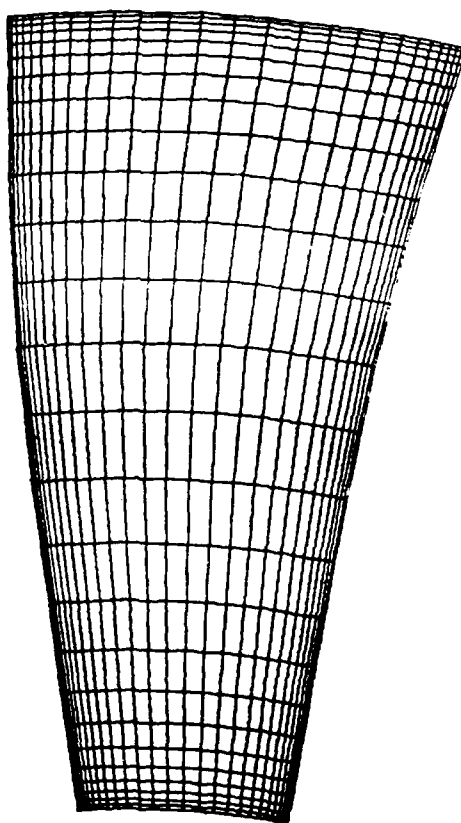
b) R-θ plane at mid-chord.

Figure A.1   Algebraic 3-D Periodic H-Grid

c) R-Z plane at mid-pitch.

Figure A.1   Algebraic 3-D Periodic H-Grid